

TOPICS IN CURRENT CHEMISTRY

287

Volume Editors P. Broekmann · K.-H. Dötz
C.A. Schalley

Templates in Chemistry III

 Springer

287

Topics in Current Chemistry

Editorial Board:

**V. Balzani · A. de Meijere · K. N. Houk · H. Kessler · J.-M. Lehn
S. V. Ley · S. L. Schreiber · J. Thiem · B. M. Trost · F. Vögtle
H. Yamamoto**

Topics in Current Chemistry

Recently Published and Forthcoming Volumes

Templates in Chemistry III

Volume Editors: Broekmann, P., Dötz, K.-H.,
Schalley, C. A.
Vol. 287, 2009

Tubulin-Binding Agents:

Synthetic, Structural and Mechanistic Insights
Volume Editor: Carlomagno, T.
Vol. 286, 2009

STM and AFM Studies on (Bio)molecular Systems: Unravelling the Nanoworld

Volume Editor: Samori, P.
Vol. 285, 2008

Amplification of Chirality

Volume Editor: Soai, K.
Vol. 284, 2008

Anthracycline Chemistry and Biology II

Mode of Action, Clinical Aspects and New Drugs
Volume Editor: Krohn, K.
Vol. 283, 2008

Anthracycline Chemistry and Biology I

Biological Occurrence and Biosynthesis,
Synthesis and Chemistry
Volume Editor: Krohn, K.
Vol. 282, 2008

Photochemistry and Photophysics of Coordination Compounds II

Volume Editors: Balzani, V., Campagna, S.
Vol. 281, 2007

Photochemistry and Photophysics of Coordination Compounds I

Volume Editors: Balzani, V., Campagna, S.
Vol. 280, 2007

Metal Catalyzed Reductive C–C Bond Formation

A Departure from Preformed Organometallic
Reagents
Volume Editor: Krische, M. J.
Vol. 279, 2007

Combinatorial Chemistry on Solid Supports

Volume Editor: Bräse, S.
Vol. 278, 2007

Creative Chemical Sensor Systems

Volume Editor: Schrader, T.
Vol. 277, 2007

In situ NMR Methods in Catalysis

Volume Editors: Bargon, J., Kuhn, L. T.
Vol. 276, 2007

Sulfur-Mediated Rearrangements II

Volume Editor: Schaumann, E.
Vol. 275, 2007

Sulfur-Mediated Rearrangements I

Volume Editor: Schaumann, E.
Vol. 274, 2007

Bioactive Conformation II

Volume Editor: Peters, T.
Vol. 273, 2007

Bioactive Conformation I

Volume Editor: Peters, T.
Vol. 272, 2007

Biom mineralization II

Mineralization Using Synthetic Polymers and
Templates
Volume Editor: Naka, K.
Vol. 271, 2007

Templates in Chemistry III

Volume Editors: Peter Broekmann · Karl-Heinz Dötz ·
Christoph A. Schalley

With contributions by

R. Aguilar-Sanchez · J. V. Barth · C. Becker · S. De Feyter
S. Furukawa · B. Han · U. Jonas · W. Knoll · C. Li · Q. Li · Z. Li
N. Lin · I. Pobelov · M. Retsch · M. Ruben · S. Stepanow · G. Su
K. Wandelt · T. Wandlowski · J. Wang

The series *Topics in Current Chemistry* presents critical reviews of the present and future trends in modern chemical research. The scope of coverage includes all areas of chemical science including the interfaces with related disciplines such as biology, medicine and materials science. The goal of each thematic volume is to give the nonspecialist reader, whether at the university or in industry, a comprehensive overview of an area where new insights are emerging that are of interest to a larger scientific audience.

As a rule, contributions are specially commissioned. The editors and publishers will, however, always be pleased to receive suggestions and supplementary information. Papers are accepted for *Topics in Current Chemistry* in English.

In references *Topics in Current Chemistry* is abbreviated Top Curr Chem and is cited as a journal. Visit the TCC content at springerlink.com

ISBN 978-3-540-89691-3

ISBN 978-3-540-89692-0 (eBook)

DOI 10.1007/978-3-540-89692-0

Topics in Current Chemistry ISSN 0340-1022

© 2009 Springer-Verlag Berlin Heidelberg

This work is subject to copyright. All rights are reserved, whether the whole or part of the material is concerned, specifically the rights of translation, reprinting, reuse of illustrations, recitation, broadcasting, reproduction on microfilm or in any other way, and storage in data banks. Duplication of this publication or parts thereof is permitted only under the provisions of the German Copyright Law of September 9, 1965, in its current version, and permission for use must always be obtained from Springer. Violations are liable to prosecution under the German Copyright Law.

The use of general descriptive names, registered names, trademarks, etc. in this publication does not imply, even in the absence of a specific statement, that such names are exempt from the relevant protective laws and regulations and therefore free for general use.

Cover design: WMXDesign GmbH, Heidelberg

Typesetting and Production: le-tex publishing services oHG, Leipzig

Printed on acid-free paper

9 8 7 6 5 4 3 2 1 0

springer.com

Volume Editors

Dr. Peter Broekmann

Interfacial Electrochemistry Group
Department of Chemistry and Biochemistry
University of Berne
Freiestrasse 3
3012 Berne, Switzerland
peter.broekmann@iac.unibe.ch

Prof. Dr. Christoph A. Schalley

FU Berlin
Institut für Chemie und Biochemie
Organische Chemie
Takustr. 3
14195 Berlin, Germany
schalley@chemie.fu-berlin.de

Prof. Dr. Karl-Heinz Dötz

Universität Bonn
Kekulé-Institut
für Organische Chemie und Biochemie
Gerhard-Domagk-Str. 1
53121 Bonn, Germany
doetz@uni-bonn.de

Editorial Board

Prof. Vincenzo Balzani

Dipartimento di Chimica „G. Ciamician“
University of Bologna
via Selmi 2
40126 Bologna, Italy
vincenzo.balzani@unibo.it

Prof. Dr. Horst Kessler

Institut für Organische Chemie
TU München
Lichtenbergstraße 4
86747 Garching, Germany
kessler@ch.tum.de

Prof. Dr. Armin de Meijere

Institut für Organische Chemie
der Georg-August-Universität
Tammanstr. 2
37077 Göttingen, Germany
ameijer1@uni-goettingen.de

Prof. Jean-Marie Lehn

ISIS
8, allée Gaspard Monge
BP 70028
67083 Strasbourg Cedex, France
lehn@isis.u-strasbg.fr

Prof. Dr. Kendall N. Houk

University of California
Department of Chemistry and
Biochemistry
405 Hilgard Avenue
Los Angeles, CA 90024-1589
USA
houk@chem.ucla.edu

Prof. Steven V. Ley

University Chemical Laboratory
Lensfield Road
Cambridge CB2 1EW
Great Britain
Svl1000@cus.cam.ac.uk

Prof. Stuart L. Schreiber

Chemical Laboratories
Harvard University
12 Oxford Street
Cambridge, MA 02138-2902
USA
sls@slsiris.harvard.edu

Prof. Dr. Joachim Thiem

Institut für Organische Chemie
Universität Hamburg
Martin-Luther-King-Platz 6
20146 Hamburg, Germany
thiem@chemie.uni-hamburg.de

Prof. Barry M. Trost

Department of Chemistry
Stanford University
Stanford, CA 94305-5080
USA
bmtrost@leland.stanford.edu

Prof. Dr. F. Vögtle

Kekulé-Institut für Organische Chemie
und Biochemie
der Universität Bonn
Gerhard-Domagk-Str. 1
53121 Bonn, Germany
voegtle@uni-bonn.de

Prof. Dr. Hisashi Yamamoto

Department of Chemistry
The University of Chicago
5735 South Ellis Avenue
Chicago, IL 60637
USA
yamamoto@uchicago.edu

Topics in Current Chemistry Also Available Electronically

For all customers who have a standing order to Topics in Current Chemistry, we offer the electronic version via SpringerLink free of charge. Please contact your librarian who can receive a password or free access to the full articles by registering at:

springerlink.com

If you do not have a subscription, you can still view the tables of contents of the volumes and the abstract of each article by going to the SpringerLink Homepage, clicking on “Browse by Online Libraries”, then “Chemical Sciences”, and finally choose Topics in Current Chemistry.

You will find information about the

- Editorial Board
- Aims and Scope
- Instructions for Authors
- Sample Contribution

at springer.com using the search function.

Color figures are published in full color within the electronic version on SpringerLink.

Preface

The first two volumes in this “Templates in Chemistry” series have focused on templates that control solution-phase reactions. Among the templates discussed in these two volumes were convex and concave templates that mediate the formation of (macro)cyclic molecules and mechanically bound molecules with their intriguing intertwined topology. Also, three-dimensional templates that are used to imprint polymers and that organize compounds in the solid state for predestined reactions have been included in the earlier volumes.

In the present volume, we extend the template topology to surfaces that act as matrices for the controlled growth of two-dimensional arrays. Naturally, the typical methods for the characterization of surfaces such as scanning probe microscopy are prominently represented in this volume.

Different lateral interactions such as coordinative bonds or hydrogen bonding play a major role in assembling the 2D networks on surfaces in addition to the interaction of the samples with the underlying substrates. Many phenomena that are also encountered in solution can be directly visualized on surfaces: Reversible self-assembly processes lead to the formation of large structures through multiple recognition of small building blocks and culminate in the engineering of crystals in two dimensions. Self-sorting processes drive the formation of highly ordered arrays through the geometric fit of the available components. Either the surface itself is the template, for example, when clusters grow on metal oxide films, or colloidal templates control the formation of macroporous networks on the substrate.

This volume highlights a selection of actual complementary aspects of surface templates. We believe that the scope and the variety of topics covered in this volume will attract readers from different communities such as supramolecular chemistry, material sciences, surface chemistry, surface physics and surface technology and we hope they will enjoy this new volume on Templates in Chemistry.

Bonn, Bern, Berlin, autumn 2008

Peter Broekmann
Karl-Heinz Dötz
Christoph A. Schalley

Contents

Surface-Confined Supramolecular Coordination Chemistry N. Lin · S. Stepanow · M. Ruben · J. V. Barth	1
Surfaces: Two-Dimensional Templates C. Becker · K. Wandelt	45
Two-Dimensional Crystal Engineering at the Liquid–Solid Interface S. Furukawa · S. De Feyter	87
Porous Networks Through Colloidal Templates Q. Li · M. Retsch · J. Wang · W. Knoll · U. Jonas	135
From Self-Assembly to Charge Transport with Single Molecules – An Electrochemical Approach B. Han · Z. Li · C. Li · I. Pobelov · G. Su R. Aguilar-Sanchez · T. Wandlowski	181
Subject Index	257

Contents of Volume 248

Templates in Chemistry I

Volume Editors: Schalley, C. A. · Vögtle, F. · Dötz, K.-H.

ISBN: 3-540-22547-1

Spacer-Controlled Multiple Functionalization of Fullerenes

C. Thilgen · S. Sergeyev · F. Diederich

Chromium-Templated Benzannulation and Haptotropic Metal Migration

K.-H. Dötz · B. Wenzel · H. C. Jahr

Supramolecular Templating in the Formation of Helicates

M. Albrecht

**Hydrogen-Bond-Mediated Template Synthesis
of Rotaxanes, Catenanes, and Knotanes**

C. A. Schalley · T. Weilandt · J. Brüggemann · F. Vögtle

Template-Controlled Synthesis in the Solid State

L. R. MacGillivray · G. S. Papaefstathiou · T. Friščić · D. B. Varshney ·
T. D. Hamilton

Gels as Templates for Nanotubes

J. H. Jung · S. Shinkai

Contents of Volume 249

Templates in Chemistry II

Volume Editors: Schalley, C. A. · Vögtle, F. · Dötz, K.-H.

ISBN: 3-540-23087-4

First Considerations: Principles, Classification, and History

D. H. Busch

Macrocyclic Synthesis Through Templatation

Z. R. Laughrey · B. C. Gibb

Macrocycles and Complex Three-Dimensional Structures

Comprising Pt(II) Building Blocks

A. Kaiser · P. Bäuerle

Templated Synthesis of Interlocked Molecules

F. Aricó · J. D. Badjic · S. J. Cantrill · A. H. Flood · K. C.-F. Leung · Y. Liu ·
J. F. Stoddart

Molecular Knots

C. Dietrich-Buchecker · B. X. Colasson · J.-P. Sauvage

Templatation in Noncovalent Synthesis of Hydrogen-Bonded Rosettes

M. Crego-Calama · D. N. Reinhoudt · M. G. J. ten Cate

Imprinted Polymers

A. J. Hall · M. Emgenbroich · B. Sellergren

Surface-Confined Supramolecular Coordination Chemistry

Nian Lin¹ (✉) · Sebastian Stepanow² (✉) · Mario Ruben³ (✉) ·
Johannes V. Barth^{4,5} (✉)

¹Department of Physics, The Hong Kong University of Science and Technology,
Clear Water Bay, Hong Kong, P.R. China
phnlin@ust.hk

²Centre d'Investigacions en Nanociència i Nanotecnologia (CIN2-ICN), UAB Campus,
08193 Bellaterra, Spain
sebastian.stepanow.ICN@uab.es

³Institut für Nanotechnologie, Karlsruhe Institute of Technology, P.O. Box 3640,
76021 Karlsruhe, Germany
mario.ruben@int.fzk.de

⁴Physik Department E20, Technische Universität München, James Franck Str.,
85748 Garching, Germany

⁵Department of Physics & Astronomy – AMPEL, The University of British Columbia,
2355 East Mall, Vancouver, V6T 1Z4, Canada
jvb@ph.tum.de

1	Introduction	2
2	Concepts	5
3	In vacuo Metallo-supramolecular Engineering at Solid Surfaces	8
3.1	Principles	8
3.2	STM Observations	11
3.3	Computational Modeling	26
4	Metal Ion–Ligand Assemblies at the Solid–Liquid Interface	30
5	Résumé and Perspectives	36
	References	37

Abstract The non-covalent synthesis of coordination compounds and networks provides promising avenues towards metal-containing supermolecules and nanostructured materials with ultimate feature definition. An important factor for their further development, and their integration and exploitation in nanoscale functional systems, is the capability to prepare or organize them at well-defined substrates or templated environments. Supramolecular engineering on atomistically controlled surfaces has been propelled by the direct insight into low-dimensional coordination systems provided by scanning tunneling microscopy observations. Here we discuss the principles of *surface-confined supramolecular coordination chemistry*, emphasizing self-assembly protocols conducted on surface atomic lattices employing metal centers to direct the organization of molecular ligands and the template-induced organization of prefabricated metallo-supramolecular species. The presented exemplary molecular-level studies elucidate the arrangement of organic

adsorbates and transition metal adatoms on low-index metal and graphite surfaces. They reveal the interplay between molecule–adatom, intermolecular, and adsorbate–substrate interactions, which need to be balanced for the fabrication of low-dimensional nanostructures. The control and understanding of both the nature of metal–ligand interactions and the resulting supramolecular organization on solid surfaces is decisive for the design of advanced architectures with concomitant functions. The realized metallosupramolecular compounds and arrays combine the properties of their constituent metal ions and organic ligands, and feature versatile structural characteristics as well as attractive functional aspects: their redox, magnetic, spin-state, and electronic transitions.

Keywords Interface science · Metal surfaces · Metal-directed assembly · Scanning tunneling microscopy · Supramolecular engineering · Surface coordination chemistry

1

Introduction

The foundations of coordination chemistry were laid in 1892 by Werner, who expounded in a landmark publication the constitution of inorganic compounds where metal centers are surrounded by a specific number of ligands in a symmetrical geometric arrangement [1]. He notably introduced the concept of *Hauptvalenz* and *Nebervalenz* for metal ions and analyzed the isomerism of optically active complexes [2]. This eventually led to the acceptance of his views, that were confirmed by X-ray diffraction studies [3, 4]. Their description in terms of quantum mechanical modeling led to the formulation of ligand field theory [5–7]. At the same time, the intriguing magnetic properties of the metal centers in different environments were analyzed [8, 9]. In the following decades the science of coordination compounds became a mature research field and independent chemistry discipline [10, 11].

On the other hand, the first systematic surface science investigations were conducted in the 1910–1920s, notably focusing on phenomena like chemisorption, diffusion of adsorbed species, heterogenous catalytic reactions, growth of thin films or thermionic electron emission [12–26], and the “life history of adsorbed atoms and ions”, dubbed adatoms [27]. Important feats were the derivation of the Langmuir isotherm relating the concentration of adsorbed molecules on a solid surface to their gas phase pressure at fixed temperature – named after the leading surface chemist of the time who formulated it [12]; and the first demonstration of electron diffraction from a crystal surface [28], which was equally important in proving the electron’s wave nature and in the later development of a major surface science tool, low-energy electron diffraction [29, 30].

Coordination and surface chemistry represent scientific movements with rather disparate origins and accordingly there was hardly any crosstalk during their initial development. The situation changed when in the 1960s the era of *modern surface science* was entered, triggered by the widespread availability of ultra-high vacuum systems and the development of sensitive tools for the structural and chemical characterization of solid surfaces and adsorbates thereon [31]. This notably led to an improved understanding regarding the bonding and chemical reactions of molecular ligands on metals [32, 33]. Based on the experimental evidence, analogies between coordination chemistry and surface chemical bond formation and reactions were delineated [34–41]. This relation between the chemistry of adsorbates on metals and coordination compounds is expressed in the term *surface coordination chemistry*. Similar considerations hold regarding the surfaces of metal oxide catalysts, where surface atoms are characterized by a ligand sphere differing from that in the bulk, whence the metal centers have reduced coordination numbers and can be designated *coordinatively unsaturated sites* (abbreviated *cus*) [42]. Their coordination sphere may be completed by adsorbed molecular species, and these may be activated for catalytic transformations [43–47]. Thus there is an analogy between surface processes on oxides and those occurring in homogenous catalytic reactions mediated by metal complexes in both natural and synthetic metal-containing systems [48, 49]. The derived *surface organometallic chemistry* [48], aiming at the rational design of single-site heterogeneous catalysts by anchoring catalytically active complexes on surfaces to achieve novel reaction pathways bears much promise [50–52], also in view of its potential to eventually mimic the function of metallobiomolecules [53–56]. Further recent applications of surface coordination chemistry encompass the control of superconductor surfaces [57], corrosion inhibition [58], the magnetochemistry of nanoparticles [59], as well as the anchoring of functional metal–organic species on Si surfaces [60–62] and – last but not least – on titanium oxide nanoparticles as dyes for photovoltaic cells [63].

During the 1980s the chemistry of large supermolecules and networks stabilized by metal–ligand interactions moved, at least partially, under the auspices of supramolecular science [64, 65]. Thus supramolecular coordination (or metallosupramolecular) chemistry evolved, relying on the paradigms of molecular recognition and metal-directed assembly, which represent a key strategy for the engineering of highly organized systems using discrete molecular building blocks (sometimes designated *tectons*). The intense research efforts revealed tremendous potential in the areas of catalysis, molecular electronics, molecular magnetism, sensor design, and optics [66]. The use of metal ions offers a set of directional bonds of intermediate strength that is exploited to realize distinct geometric shapes. Supramolecular coordination chemistry has gathered a vast database of metal–ligand pairs with a huge variety of specific binding schemes giving the possibility to program selectivity

and directionality directly into the binding motif. This allows for the self-assembly of supramolecular architectures as diverse as polygonal clusters, polyhedra, cages, and grids [64, 67–72]. Moreover, the synthesis of highly porous solid frameworks and coordination polymers has reached a mature level [73–81]. Therefore, the use of transition metal centers, or in general secondary building blocks, and coordination chemistry for directing the formation of complex structures has evolved into one of the most widely used strategies for organizing molecular building blocks into supramolecular arrays. The formation of a given supramolecular shape is driven by the inherent symmetry of the available metal orbitals and the spatial organization of the donor atoms in the organic ligand system. Therefore, careful consideration must be given to the preferred coordination environment of the metal to be used and the binding mode of the linkers, in particular chelating ligands. Given such a coordination environment around the metal centers, the symmetric and rigid extension of the ligand system from mono- to multitopicity will automatically lead to a infinite grid-like one-, two-, or three-dimensional coordination network with regularly arrayed metal ions. The supramolecular organization is encoded in the electronic structure of both the metal ions and in the organic ligands. The interpretation of this information during the self-assembly process leads to a mutually acceptable structure. The principle of using metals with predetermined coordination numbers and angles as building blocks and functional units is not only an appealing method from the synthetic chemistry point of view. The transition metal ions incorporated into such structures do not merely act as stabilizing agents of the structures but remain accessible for the construction of more complex structures [82], featuring modular, hierarchic, or even dynamic behavior. Furthermore, they possess multiple electronic/spin states and a related variety of redox, photochemical, and magnetic properties, which can be tuned by the specific coordination environment. Thus the potential applications of these complex systems lie in the scientific fields of chemistry, biology, and materials science, including, e.g., catalysis, sensing, and construction of various devices on the molecular level [83–85].

In parallel, modern surface science was revolutionized over the years following the introduction of scanning tunneling microscopy (STM) in the early 1980s [86]. STM and related techniques proved to be extremely versatile tools for the direct observation of surface phenomena. Moreover, the controlled manipulation of individual adsorbed species to write at the atomic scale or create quantum confinement structures symbolized the striking advance and highlighted the promise of nanoscale science and technology [87, 88]. While many research groups explored single-molecule chemistry experiments [89–92], molecular-level nanoscience simultaneously provided the basis to explore concepts from supramolecular chemistry for the fabrication of molecular architectures on well-defined planar substrates [93–97]. It became clear that surfaces represent unique platforms on which a novel 2D supra-

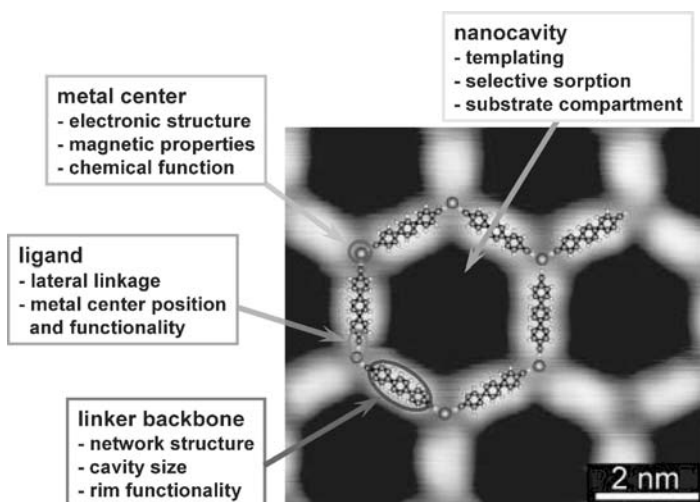
molecular chemistry can be explored to realize distinct low-dimensional molecular arrangements employing adsorbed molecules with functionalities for selective non-covalent interactions, mediated by polar exodentate moieties [98–100], hydrogen bonding groups [101–105] or zwitterionicity [106]. In addition, the significant potential of surface-confined supramolecular coordination chemistry emerged [94, 95, 107–124], as detailed in the following section.

2 Concepts

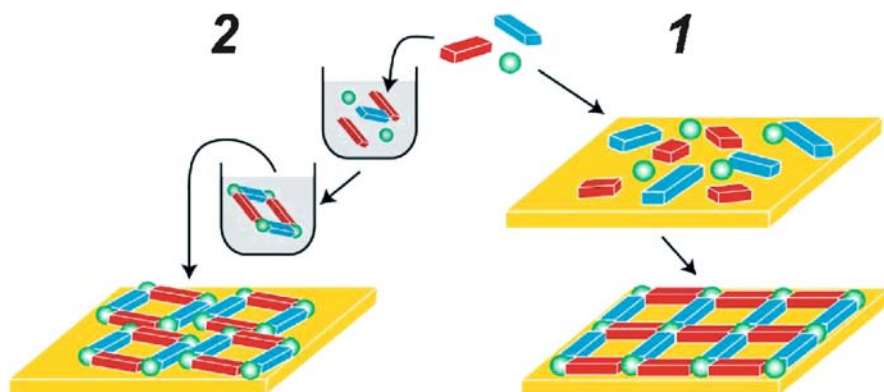
In the present context it is important to fully appreciate that a molecule's spatial confinement imposes steric constraints for molecular recognition and that the coupling of the adsorbates to the surface plays a role of comparable importance with that of the non-covalent bonds typical of supramolecular complexes, and even may entirely dominate the investigated systems [123]. Thus, one demands the development of a conceptual framework for using the surface as an assistance to guide metal-directed self-assembly processes, i.e., to address the concomitant positioning of molecules with surface-adapted functional units and metal centers. Such a scheme is similarly of interest for the deposition of pre-assembled metallosupramolecular entities. Moreover, the surface plays an important role regarding the functional properties of the low-dimensional coordination systems it supports. In particular, the properties of transition metal centers embedded in the organic layer can be affected by the intricate interplay between the present interactions, e.g., the substrate electrons can influence their magnetic moments [125–127]. The balance between metal–ligand, intermolecular, and surface interactions assumes therefore a critical role in determining the chemical and electronic properties of supramolecular layers [123, 128]. At the same time, the adsorbed ligand's chemical state [104, 129–131] and conformation [132–140] need to be assessed because they affect both the functional properties and organizational behavior of adsorbed molecular nanosystems.

The control and fabrication of single compounds, and the organization of metal–organic units in 1D coordination polymers or 2D coordination arrays is of interest in metallosupramolecular engineering on surfaces. The key features and their role in the potential functionality of the particularly versatile nanoporous networks achieved by metal-directed assembly in vacuum are illustrated in Scheme 1. The work on the formation of supramolecular architectures on surfaces containing metal centers will here be divided into the two approaches illustrated in Scheme 2.

1. On the one hand, the ultra-high vacuum (UHV) approach has been pioneered over the last decade because of its exquisite surface control and



Scheme 1



Scheme 2

cleanness rendering submolecular level resolution in scanning tunneling microscopy (STM) imaging. By using the UHV approach, the assembly process of metallosupramolecular architectures can be directly conducted following the deposition of the components, i.e., organic linkers and metal atoms (Scheme 2, right). For the realization of low-dimensional coordination systems one has to take care about the different mobility characteristics of the adsorbates, i.e., organic molecules and metal adatoms, which can differ by several orders of magnitudes [123, 141–143]. Apart from the non-covalent lateral interactions between the adsorbates, there can be strong and irreversible interactions with the surface, e.g., the alloying of metal adatoms [144–148] or chemical reactions of the organic species with the surface that alter their chemical state [104, 129–131]. The point of in-

terest for their potential functional properties in the 2D metal–organic architectures are their versatile structural characteristics with the common feature of metal centers [149, 150]. STM studies of organic building blocks adsorbed on metal surfaces revealed that their supramolecular ordering is governed by the competition of intermolecular hydrogen, π – π -, van der Waals interactions, and dipolar bonds with site-selective substrate bonding. As a consequence of the linker’s surface confinement, also with metal centers employed as steering agents, the reduction to two dimensions is quite generally accompanied by coordinatively unsaturated sites. This opens the way to realize unique compounds and study a novel class of metallosupramolecular systems. Thus, the choice of donor atoms, bridging groups, metal ions, and systematic synthetic design strategies might render these systems ideal for designing perfectly surface-adapted receptor sites with tailorable molecular recognition properties, and catalysts with tunable reactivities.

2. On the other hand, systematic studies have been performed at the solid–liquid interface and representative examples will be discussed in Sect. 4. Frequently the molecular building blocks are pre-assembled into entities stabilized themselves by metal coordination centers (see Scheme 2, left). Such so-called *supermolecules* are brought to the surface by drop-casting, spin-coating, or other methods, where they bind and form specific patterns (cf. [118, 151, 152]). The involved coordinated metal ions assure the integrity of the molecules and are not directly involved in the surface linkage of the molecules. Alternatively, layers from the ligands can be pre-organized on the surface by self-assembly or by tethering techniques and subsequently modified with the addition of metal atoms, i.e., by in-situ complexation, or by interfacial reactions in electrochemically controlled environments. A further important advantage when using a solution-based surface approach with electrochemical methods is the possibility of combined self-assembly–molecular electronics studies [153–155].

A special situation is encountered with metal–porphyrin or metal–phthalocyanine molecules that can be either deposited by sublimation under UHV conditions or in solution environments. For these macrocyclic compounds, free-base species exist, i.e., the metal centers are not required per se as a construction unit. The building of supramolecular structures that incorporate porphyrin subunits is of great interest to many research groups. The rich photochemistry and redox properties (e.g., photoinduced electron transfer, luminescence, and light harvesting) of porphyrins have driven this interest. Porphyrins or phthalocyanines have a rich coordination chemistry that allows the inclusion of many different metal centers at their macrocycle. They serve in many respects as a model system since this constitutes a low-coordination complex. Recent STM studies report on the organization of metal-coordinated or free-base porphyrins as well as phthalocyanines on

various metal surfaces. In particular, chemically modified molecules with additional functional groups as *meso*-substituents, (e.g., pyridyl or other bulky groups) were at the focus of investigation. These additional exodentate ligands play a similar role in the determination of the adlayer structure as the metal-containing macrocycle and can be used to effectively control the arrangement of the functional molecules on the surface. Such systems have also been studied for their complexation chemistry that takes place directly at the surface in vacuo. Upon exposure of free-base porphyrins to a beam of transition metal atoms, selective complexation of the porphyrin macrocycle occurs leaving the template structure preserved [156, 157]. This approach can be even employed for rare-earth centers [158]. Although the complexation reaction is not involved in the formation of the adlayer structure, the controlled in-situ metalation of adsorbed porphyrins provides a novel route toward high-purity metalloporphyrin architectures and patterned surfaces. Many aspects regarding metal–porphyrin or metal–phthalocyanine adlayer systems are discussed elsewhere (cf. [140, 159–171]; see also the review [172] and references therein) and thus not developed here in detail.

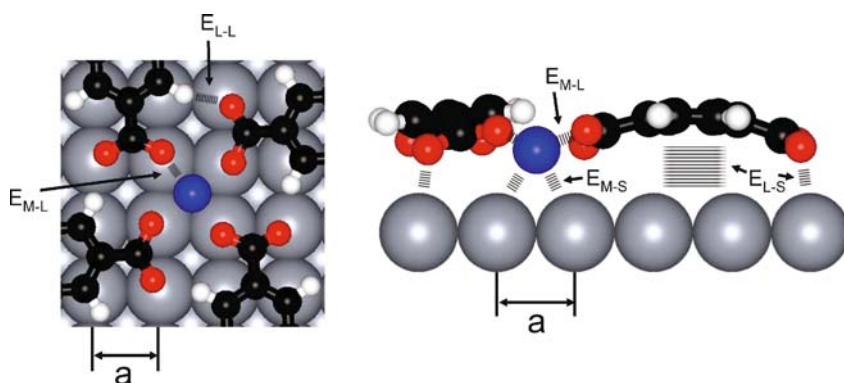
3

In vacuo Metallosupramolecular Engineering at Solid Surfaces

3.1

Principles

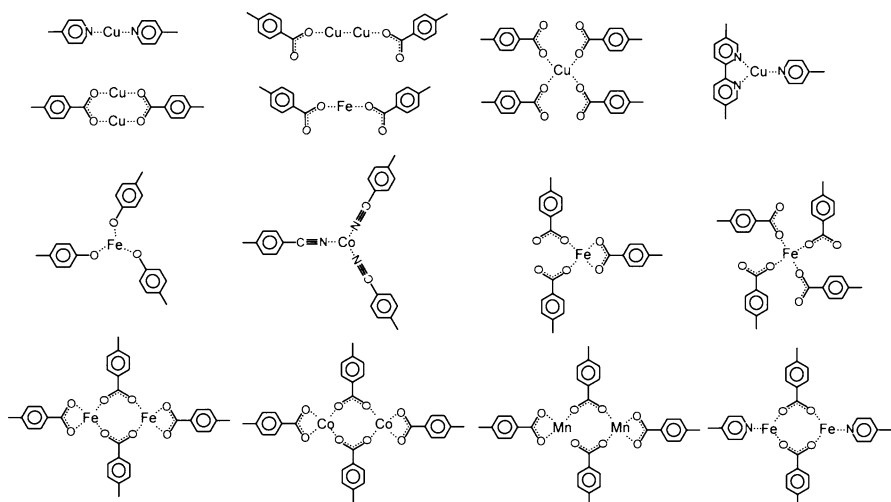
In this section we provide a status report on the modular assembly of metal–organic compounds, polymers, and networks using molecular linkers with aromatic backbones in UHV conditions on clean metallic surfaces, i.e., without any solvent or atmospheric molecular concomitants. Attractive interactions between aromatic bricks with the metal substrate frequently favors a flat adsorption configuration, i.e., with the ligands' π -systems parallel to the surface plane. This is illustrated in Scheme 3, that also depicts the multiple and competing interactions between adsorbed metal centers, functional molecular groups, and the substrate atoms arranged in a lattice with periodicity a . A direct consequence of the ligand's 2D confinement is that steric restrictions prevent the expression of many 3D coordination motifs. Moreover, the surface bonding of both admetal centers and organic linkers is typically at specific sites on the substrate atomic lattice (labeled E_{M-S} and E_{L-S} in Scheme 3, respectively). The easiest translational (rotational) path between two equivalent bonding sites is separated by the so-called migration (rotation) energy barrier, that can be a sizable fraction of the bonding energy [123, 141–143] and thus comes close to the energy gain from a potential coordination bond. When the site-specific bonding prevails thus only discrete configurations for

**Scheme 3**

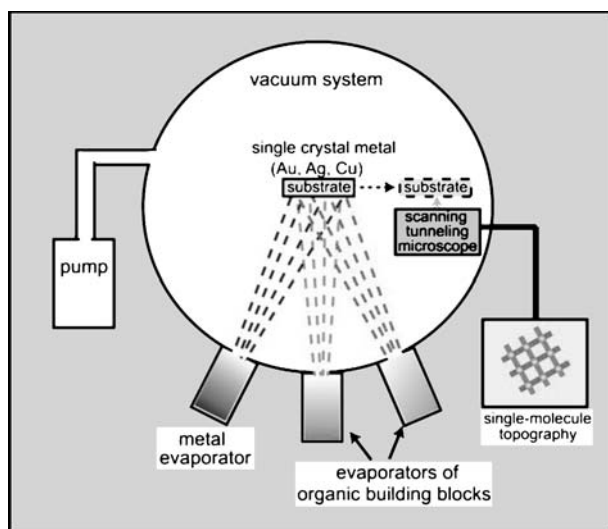
the formation of lateral bonds are possible. Consequently the metal center–ligand interactions (labeled E_{M-L}) compete with the substrate interactions (for a more detailed discussion, see [123]). In addition, their nature is affected by the modified electronic structure of the metal centers and ligands resulting from the surface chemical bonding. Furthermore, lateral interactions between the ligands (labeled E_{L-L} – for instance hydrogen bonds or substrate-mediated interactions) may play a secondary role in the 2D supramolecular organization.

The ligand functionalities explored to date include carboxylate, pyridine, hydroxyl, and carbonitrile groups. Carboxylates in particular represent a versatile class of building blocks for engineering robust 3D metal–organic frameworks or functional coordination polymers [79, 80]. One can similarly use metal–carboxylate coupling schemes on appropriate substrates to tailor coordination architectures in two dimensions. A series of systematic investigations demonstrated the construction of mononuclear metal–carboxylate clusters, polymeric coordination chains, and fully reticulated networks based on polyfunctional exodentate benzoic-acid species. These findings give insight into the principles underlying the complexation of organic ligands and transition metal centers on surfaces and illustrate their potential for rational 2D metallosupramolecular engineering. Scheme 4 shows the coordination modes that have been explored so far, and we shall discuss how the intricate interplay between the driving forces in the self-assembly process leads to specific arrangements.

A typical experimental setup is sketched in Scheme 5. Organic precursor layers are deposited on the atomically clean surfaces by sublimation of the molecular linkers, typically present in high-purity powder form. The temperature of the substrate is controllably varied from cryogenic conditions (~ 10 K) to elevated temperatures (~ 500 K) in order to achieve thermodynamically metastable or equilibrated products. In the surface-assembled systems the coordination centers are evaporated using electron beam or re-



Scheme 4



Scheme 5

sistive heating sources. The assembly conditions are set by the substrate temperature, evaporation rate or sequence, and surface concentrations of the adsorbates.

Because under vacuum conditions the sublimation of entire complexes stabilized by coordination interactions may correlate with decomposition (see [173, 174], but also note that coordinatively enhanced stability has been reported [175]), more sophisticated techniques are of interest for the handling of thermolabile species, such as pulse-deposition or electro spray methods

where fragile compounds are directly released into vacuum [176–183]. Notably, a straightforward combination of solution-based supramolecular self-assembly techniques with UHV-based STM imaging by means of pulse injection onto an Au(111) surface was the key for the successful observation of ring-like molecular structures containing up to 30 Zn^{II} metal ions and exhibiting an internal diameter of ~ 10 nm [184].

3.2

STM Observations

A direct illustration of the capturing of transition metal centers by the terminal pyridyl groups of a surface anchored porphyrin species is provided by the experiment depicted in Fig. 1 [138]. The isolated tetra-pyridyl-porphyrin (TPyP) molecules are immobile following adsorption on a Cu(111) substrate at 300 K. Single Fe atoms were added in situ at 8 K, where thermal diffusion is frozen. Figure 1a accordingly shows randomly distributed Fe monomers appearing as round protrusions coexisting with TPyP. In a next step, the sample temperature was slightly increased to about 15 K, which allows the Fe adatoms to freely migrate on the surface, while the TPyP remains stationary. Subsequently, the sample was cooled down again. As a result, Fe is selectively captured by the pyridyl groups (Fig. 1b). Once attached the adatoms stick, whereby the modified imaging characteristics of both Fe and TPyP-endgroups indicate marked chemical interaction. These findings confirm that the N-containing ligands retain their affinity towards metal centers despite the simultaneously observed conformational adaptation of the porphyrin unit, implying a non-planar orientation of pyridyl groups.

The measurements visualize the impact of metal–ligand interactions and a metallosupramolecular self-assembly process in two dimensions, where the

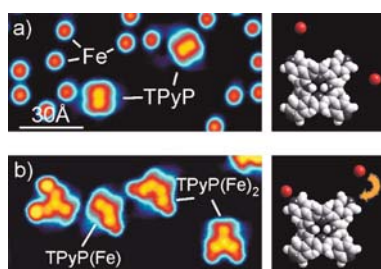


Fig. 1 Selective attachment of Fe adatoms to the pyridyl groups of TPyP adsorbed on Cu(111) (images are of identical size). The porphyrin species is immobile following deposition at 300 K. **a** Upon codeposition of Fe at very low temperatures ($T = 8$ K), there is a random distribution of Fe monomers. They become mobile at $T = 15$ K and are irreversibly attached to the pyridyl ligands of the porphyrins (**b**). Two main steps of this experiment are schematically illustrated in the column on the right. Adapted from [138]

organic linkers are spatially anchored. Furthermore, additional incoming Fe monomers can be trapped by the metal–ligand complex, resulting in small metal clusters pinned to the pyridyl groups of the TPYP (Fig. 1b, complex on the left). Such changes could be equally achieved by single atom manipulation experiments, i.e., by positioning Fe atoms at the pyridine ligands with the STM tip [168]. In a related manipulation experiment, the bonding between a single Au atom and pentacene molecules was induced [185]. At higher temperatures, where surface adatoms are supplied from step edges and the TPYP molecules become mobile, pairing and chaining of TPYP is encountered, mediated by Cu-directed coupling of the pyridyl endgroups [186]. Surprisingly, the pairing of two molecules interconnected with just one metal–organic linkage strongly increases the mobility of the dimers formed, i.e., their diffusion rates exceed those of monomers by more than one order of magnitude. Furthermore, indications exist that the Cu adatom dimers can also mediate the coupling of the pyridine ligands [186]. Such pairs were similarly identified in the structure-determining element of 2D metal–organic oligopyridine networks recently realized on a graphite substrate [187]. The copper–nitrogen affinity was also exploited to create coordination dumbbells in Cu-directed assembly of mixed bipyridine and pyridyl linkers [188]. Moreover a tetraazaperopyrene on Cu(111) was used to realize a porous network where the dye molecules coordinate to Cu adatoms through their N atom lone pairs in a cyclic arrangement [189]. In this case the coordination network could even be employed as a precursor structure to mediate the formation of covalent bonds following thermal annealing.

In a different reaction scheme, one can take advantage of the functional porphyrin macrocycle to create metalloporphyrin compounds and nanoarchitectures in 2D. Upon exposure of regular TPYP arrays self-assembled on Ag(111) to iron monomers supplied by an atomic beam, selective complexation occurs whereby the template structure is strictly preserved [156]. This expands the diversity of metalloporphyrin layers conventionally realized by evaporation of integral species, because in-situ metalation provides a route towards novel metalloporphyrin nanoarchitectures and patterned surfaces [156–158]. In a related reaction pathway, evidence could be obtained for in-situ complexation and metal center-induced switching of phenanthroline-based catenane units deposited the Ag(111) surface [182].

Early evidence of lateral metal–ligand bonding in molecular systems at vacuum–solid interfaces was found for low-coverage benzoic acid adlayers on Cu(110) [190–192]. The proposed model contained two Cu adatoms bridging two opposing benzoate moieties. In this study it was concluded that the Cu adatoms play a specific role for the adsorption geometry of the molecules, where the π -interaction of the aromatic backbone favors a flat geometry and the carboxylate group favors an upright configuration. The necessary deprotonation of the acid group is thermally activated on the Cu surface. The reaction is partially accompanied by the formation of upright species.

The same mechanism for the formation of molecular pairs at elevated temperatures (425 K) was proposed for 4-[*trans*-2-(pyrid-4-ylvinyl)]benzoic acid (PVBA) adsorbed on Cu(111) (see Fig. 2a) [94]. The Cu adatoms are provided by the continuous evaporation/condensation from the surface atomic steps [193]. The rate of detachment from the kink sites on the terraces on Cu(111) is lower than on Cu(110), which is the reason for the requirements of thermal activation for the complex formation in the case of PVBA compared to the benzoate structures mentioned above. By comparison, on the less reactive Ag(110) substrate no similar compounds evolve; however, there is a reshaping of the substrate steps induced by the functional carboxylate group [194].

The first unambiguous identification of distinct metal–organic coordination complexes formed on a surface was demonstrated by the Cu-TMA (1,3,5-benzoic tricarboxylic acid) system. Two types of complexes, $\text{Cu}(\text{TMA})_4$ and $\text{Cu}_2(\text{TMA})_6$ were observed when TMA molecules were deposited on Cu(100) (Fig. 2b). Again, the metal centers are provided by the Cu substrate via thermally activated step evaporation. The energetics of the surface chemical processes permits monitoring of the metal–ligand bonding by STM imaging. For instance, the complexation reaction of clover-leaf shaped $\text{Cu}(\text{TMA})_4$ enti-

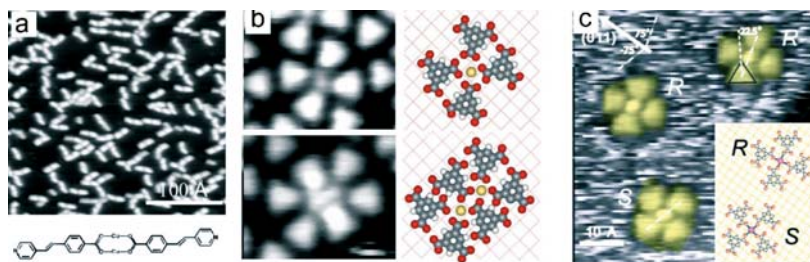


Fig. 2 Metal–carboxylate compounds on copper surfaces. **a** Pairing of PVBA molecules upon deposition on Cu(111) at elevated temperatures (adsorption at 425 K, imaged at 77 K). The corresponding tentative model shows the copper–carboxylate bonding with a head-to-head coupling of two PVBA molecules. **b** STM topographs and corresponding models of trimesic acid–copper complexes spontaneously assembling on Cu(100) at 300 K. The molecules’ triangular shape reflects a flat-lying adsorption geometry. The *upper panel* shows a cloverleaf-shaped arrangement of four TMA molecules with a central Cu adatom protrusion. The *lower panel* depicts a STM image and model of the Cu_2TMA_6 coordination compound with four unidentate and two *syn,syn* coordination bonds. **c** High-resolution image showing the two FeTMA_4 stereoisomers on the Cu(100) surface, labeled *R* and *S*, representing mirror-symmetric species with respect to the [011] substrate direction. The corresponding model depicts a unidentate coordination of the carboxylate ligands to the central Fe atom (placed on the hollow site) with a bond length of about 2 Å (*solid lines*). The corresponding rotation of the carbon backbone is strictly correlated for all TMA molecules in a given complex. The resulting symmetry break accounts for the chirality of the complexes. Adapted from [94, 110, 111]

ties allows one to gain quantitative information of the formation, energetics, and dynamics of individual complexes on Cu(100) [110]. Notably the energy barrier for the 2D dissociation reactions was determined to be 0.31 eV. The lifetime of the complexes increases significantly when stabilized by the surroundings being either other molecules or surface step edges. Besides being engaged in the complexation, the Cu adatoms are simultaneously potential agents for the deprotonation of the carboxylic moieties [195]. At low temperatures where the deprotonation reaction is inhibited, stable hydrogen-bonded networks are observed whereas at elevated temperatures metal-organic arrangements evolve due to the catalytic activity of the substrate [129]. To verify this concept it was shown that TMA molecules adsorbed on a Ag(111) surface do not undergo deprotonation reactions at ambient temperatures [195], whereas at elevated temperatures [196] or in the presence of Cu adatoms made available by codeposition the reactive carboxylate linkers evolve.

The Cu-TMA complexes described above are intrinsically 0D entities because they do not organize as extended metal-organic arrays. In order to realize compounds where the supply of all constituents is controlled by the experimentalist, the coordination interaction of TMA with Fe adatom centers was probed (Fig. 2c) [111]. The iron was codeposited at low temperatures in order to inhibit intermixing reactions with the surface. The resulting complexes appear exclusively in the presence of Fe on the surface and are distinct from their Cu-based counterparts, notably featuring reduced bonding distances and 2D chirality. The STM observations at room temperature reveal two mirror-symmetric square-planar $\text{Fe}(\text{TMA})_4$ complexes where the correlated attachment of the ligands defines the handedness of the entity. In contrast to the Cu-TMA cloverleaves, isolated Fe complexes are thermally stable at 300 K. Upon annealing the surface decorated with $\text{Fe}(\text{TMA})_4$ complexes to 350 K, they aggregate in a 4×4 grid pattern comprising 16 TMA and 9 Fe [114]. These grid-like structures inherit the chiral nature of the central $\text{Fe}(\text{TMA})_4$ complexes and are randomly distributed at the surface (vide infra).

In subsequent systematic investigation it was shown that by employing the symmetric linker 1,4-benzoic dicarboxylic acid (terephthalic acid, TPA), the linear analogue of TMA, one can achieve distinct regular 2D structures consisting of coordination complexes interconnected by hydrogen bonds on a Cu(100) surface in the low Fe concentration regime [197]. The molecules form mononuclear iron complexes $\text{Fe}(\text{TPA})_4$ where four molecules coordinate each with one carboxylate oxygen to the Fe center, and the ligands assume two different mirror symmetric senses of rotations around the Fe center. The individual Fe centers span a (6×6) -superstructure commensurate with the Cu(100) lattice (Fig. 3a), and this square array extends over entire substrate terraces. The high degree of long-range organization is presumably mediated by secondary intercomplex carboxylate-phenyl hydrogen bonds (see model in Fig. 3b). This rather unusual hydrogen bond has been identified in related adlayer systems [130, 131, 198, 199] and analyzed by theoretical means [196].

It represents a particular member of the class of ionic hydrogen bonds [200]. A domain of complexes contains only one type of handedness signaling the chiroselectivity of the intercomplex interaction. The lower-symmetry derivative 1,3,4-benzoic tricarboxylic acid (trimellitic acid, TMLA) forms isomorphological structures, i.e., the remaining carboxylate side group of the TMLA molecule is not directly involved in the network formation [201].

At intermediate Fe concentrations for both TPA and TMLA, 1D ladder structures can be realized comprising rows of coordinated molecules along the $[011]$ or $[0\bar{1}1]$ substrate directions (Fig. 3c,d) [113, 197]. The ligands binding laterally to the rows and either bridge directly two coordination centers or interdigitate and presumably form hydrogen bonds. The number of the two different links accounts for the Fe–ligand concentration ratio present in the self-assembled structure. This suggests that the formation of true coordination bonds, as confirmed recently by X-ray photoemission measurements of oxygen and iron electronic core levels in such systems [202]. Each Fe center is coordinated to three ligands in a distorted square-planar geometry. Also, this structure is commensurate to the underlying substrate atomic lattice.

The formation of 1D structures was deliberately steered through two strategies: (i) applying anisotropic surfaces and (ii) utilizing linear coordination modes. An example illustrating the first strategy is shown by depositing TMA molecules on an anisotropic Cu(110) surface [203]. Despite the triangular arrangement of the reactive carboxylate linker moieties, which

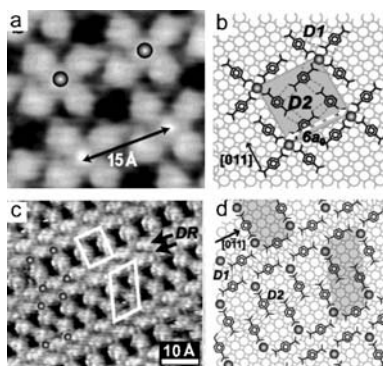


Fig. 3 Arrays of mononuclear Fe–carboxylate compounds and coordination polymers. **a** High-resolution STM image of the FeTPA cloverleaf phase on Cu(100). **b** Geometrical model of the coordination structure shown in **a**. Each Fe atom (*gray spheres*) coordinates four carboxylate ligands unidentately in a square-planar configuration. Lateral potential C–H···O hydrogen bonds are indicated. The distances $D1 = D2$ amount to 3.5 \AA . The $15 \times 15 \text{ \AA}^2$ superstructure unit cell is shown as a *gray square*. **c** STM image of the FeTPA ladder phase on Cu(100). The Fe atoms are marked by *gray spheres* and a double row by *DR*. **d** Geometrical model of **c**. *Dashed lines* indicate potential C–H···O hydrogen bonds. $D1 = D2 = 3.0 \text{ \AA}$. Adapted from [27]

would favor 2D assemblies, the molecules form 1D strings, demonstrating the strong templating effect of the substrate. The intermolecular interactions are overcome by the strong coupling to the substrate, effectively controlling the 1D character. Again mobile Cu adatoms are found to link adjacent TMA molecules along the close-packed $[1\bar{1}0]$ direction. Notably, it was shown by DFT calculations that the misleading and tempting single protrusion observed by STM could be modeled by a dimeric Cu center, confirming the geometric analysis of the structures. The intrinsic Cu–TMA linear nanostructures can be transformed into the Fe–TMA chains by preventing the formation of Cu–TMA complexes at low temperatures and subsequent deposition of Fe. The observed chains exhibit a shorter periodicity where only single Fe ions are found as the coordination centers (Fig. 4a). Thus the different chemical nature of the coordinating metal is reflected in the composition of the structures. A recent study follows the second strategy: two linear aromatic bipyridyl linkers were investigated on the isotropic Cu(100) surface [204]. Upon deposition on the substrate held at room temperature, chains evolve where the molecules are linked by a linear coordination motif of pyridine–Cu–pyridine (Fig. 4b). The Cu centers are not imaged, presumably due to an electronic effect (cf. [203]). The unconventional twofold coordination of Cu centers has not been observed in bulk coordination compounds. Similar chaining features were encountered in Cu-linked TPYP assemblies [186].

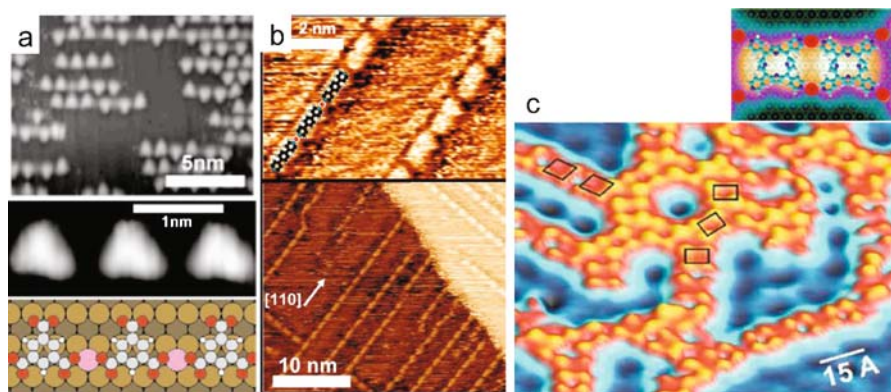


Fig. 4 Linear coordination systems. **a** STM image of Fe–TMA chains on the anisotropic Cu(110) substrate. The high-resolution topography and the corresponding model are depicted below. **b** STM images of 1,4-bis(4-pyridyl)benzene adsorbed on Cu(100) at 300 K. The structural model overlaid on the image illustrates the N–Cu–N coordination bonding. The lower STM topograph shows an overview of the chains attached to the lower side of the terrace step or running parallel on the upper side of the step. **c** Chains of self-assembled TPYP molecules on Cu(111) with the pyridyl endgroups interconnected by Cu adatoms. Individual TPYP are marked as rectangles in the large-scale image; the inset shows the coupling motif. A substrate standing wave pattern is generated by surface state electrons scattered at the metallosupramolecular strings. Adapted from [186, 203, 204]

(In this arrangement the confinement of the substrate's surface state quasi-2D electron gas moreover leads to an electron standing wave pattern at the undecorated surface areas [205]). A related chaining coordination scheme was encountered in tetracyanoethylene chains observed on the Cu(100) surface [206].

Regular 2D metal–organic coordination networks (MOCNs) were realized by the direct reticulation of coordination networks in two dimensions. In this approach distinct levels of hierarchies and complexity can be encountered. This intriguing issue, which is abundant in biological systems, was observed in Fe–TMA self-assembled layers on Cu(100) and is schematically depicted in Fig. 5a. As reported above, the TMA molecules and Fe adatoms initially form mononuclear chiral complexes at room temperature and these entities are antecedents for the higher level polynuclear 4×4 grids at evolving 350 K (Fig. 5b) [114]. At the final stage, after annealing at 400 K, the 4×4 grids are interconnected by hydrogen bonds, forming mesoscale networks comprising a regular arrangement of homochiral nanocavities. (Fig. 5c) The only control parameters in the assembly are the temperature and surface concentration. Such nanofabrication schemes involving hierarchical structures represent an

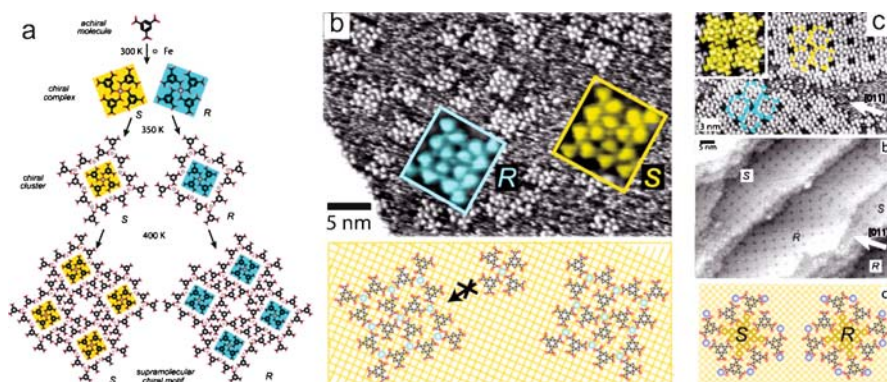


Fig. 5 *Aufbau* of dissymmetric supramolecular motifs mediated by hierarchical assembly of simple achiral species on Cu(100). **a** TMA molecules and Fe atoms represent the primary units, which are employed for the formation of secondary chiral complexes. The complexes are antecedents for tertiary polynuclear nanogrids, which are in turn the supramolecular motifs for the assembly of homochiral nanocavity arrays. The respective mirror-symmetric configurations (labeled S and R) are indicated with shaded backgrounds. **b** Assembly of tertiary stage: square-shaped polynuclear nanogrids evolve upon annealing at 350 K. The *magnified insets* and *model* below reveal that the respective core units of the dissymmetric metal–organic motifs are related to the chiral secondary FeTMA compounds. **c** Formation of extended nanocavity arrays triggered by 400 K annealing. Two homochiral domains are assembled consisting of pure enantiomers (labeled R and S), marked by *shaded rectangles*. The central opening of the domains, modeled in the *bottom panel*, is functionalized by eight surrounding carboxylate groups. Adapted from [114]

appealing possibility for the bottom-up fabrication of complex functional materials.

With both TPA and TMLA linkers, regular 2D network structures can be realized by complexation with appreciable amounts of Fe. One achieves a fully reticulated structure comprising arrays of diiron coordination centers [113, 197]. A drawback is the existence of two equivalent isomeric structures that differ in the orientation of the Fe pairs in the network nodes, i.e., they are either equally oriented or alternate as shown in Fig. 6a,b. The Fe–Fe spacing within a dimer amounts to about 4.7 Å, slightly less than twice the substrate lattice constant (2.55 Å). The coordination geometry for each Fe ion assumes a distorted square-planar geometry. Both isomeric networks reside commensurate on Cu(100) with a (6×4) and (5×5) -unit cell, respectively. These structures possess cavities of well-defined size and shape exposing the underlying Cu surface [113, 197]. Two longer analogues of TPA, 4,4'-biphenyl dicarboxylic acid (BDA) and 4,1',4',1''-terphenyl-1,4''-dicarboxylic acid (TDA), having two and three phenyl groups in the molecular backbone, respectively, form networks with increasing size similarly containing diiron centers as the essential coupling motif of the carboxylate groups (Fig. 6c,d) [115, 207]. The dimensionality dependence on the metal-to-ligand concentration ratio is absent for the longer molecules and instead coexistence of network and pure molecular domains are observed at Fe deficiency. Recently, it has been

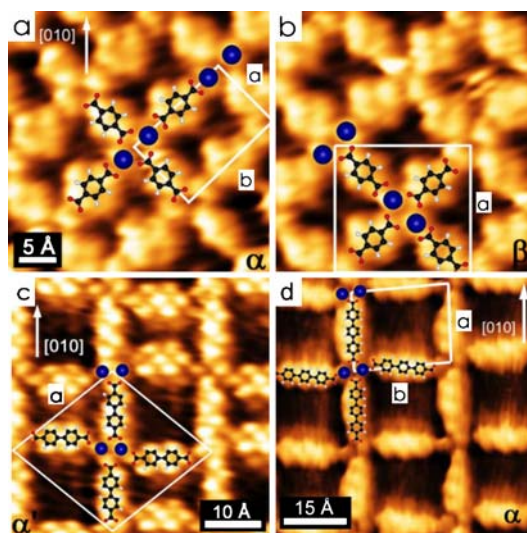


Fig. 6 Fully reticulated nanoporous Fe–carboxylate networks comprising diiron centers as coordination motif. **a,b** STM topographs of isomeric FeTPA network phases: **a** identical and **b** alternating Fe dimer arrangement. **c** High-resolution STM image of the FeBDA network. **d** STM image of the FeTDA network phase. Tentative models are superimposed on the STM images. Adapted from [207]

demonstrated that manganese–carboxylate interactions can be similarly employed to engineer 2D metal–organic lattices comprising the same dimetal centers as the Fe–carboxylate polymers and lattices presented above [208].

The replacing of the linear C–C bridge between the two aromatic rings of the BDA molecule by an ethenyl or azo group, namely 4',4''-*trans*-ethene-1,2-diyl-bisbenzoic acid and 4,4'-azobenzene dicarboxylic acid, alters significantly the appearance of the network structure. Again, the diiron coordination motif prevails [128]. But compared to the linear polybenzene dicarboxylic linkers, the network domain sizes are significantly smaller, i.e., the domains do not exceed 10 nm in size, and the structures exhibit many structural defects. Moreover, the cavity sizes and shapes span a variety of geometries and the axial orientation of the Fe pairs appears to be arbitrary. These differences can be attributed to the prochirality of the ligands, which accounts for the presence of two enantiomers on the substrate. This lack of enantioselectivity in the self-assembled structures is in contrast to the chirally resolved hydrogen-bonded pure molecular adlayers. The inclusion of both types of adsorbates in the coordination assemblies prevents the development of a perfect periodic structure that is commensurate to the Cu(100) substrate. It signals the prevailing strength of the Fe–carboxylate bond in these systems [209].

The series of the presented studies show that the carboxylate functional group frequently assumes a coordination motif with a diiron center. The carboxylate moieties are either bridging the two Fe centers or are engaged in the axial binding, being either chelating bidentate or monodentate, which also results in the evolution of isomeric phases. By replacing the symmetric linkers to dissymmetric carboxylpyridyl ligands, namely PVBA, one can eliminate the isomeric structures [210]. The carboxylate moiety acts in these system solely as an equatorial linker, whereas the pyridyl group binds strictly axially to the diiron motif resulting in a threefold coordination geometry for the metal centers. As a consequence, the orientation of the diiron centers must alternate. The realization of this structure provides the conceptual grounds that equatorial and axial ligands might be employed independently, leading to more control over the design of the network structure. Indeed, subsequent studies revealed that with the mixture of complementary carboxylate and bipyridine ligands, self-selection processes steer the size and aspect ratio of rectangular coordination networks on Cu(100), incorporating Fe centers [211].

Threefold coordination motifs, leading to such complex structures as honeycomb or kagomé lattices, are scarce in 3D compounds since low-dimensional coordination modes are less frequent. In fact, small coordination numbers were only found to occur in complexes where the steric hindrance originating from bulky ligands results in such arrangements. At surfaces, the imposed 2D confinement of the ligands and metal ions substantially influences the metal-to-ligand binding modes. In a recent study, networks

comprising trigonal mononuclear coordination nodes have been achieved by the Co- and Fe-directed assembly of ditopic dicarbonitrile- and hydroxyl-terminated polyphenyl linkers, respectively [122, 124]. This is illustrated by the hexagonal Fe-biphenolate and Co-dicarbonitrile superlattices realized on Ag(111) (Fig. 7).

The hexagonal Fe-biphenolate network could be similarly realized on the square Cu(100) substrate. The occurrence of threefold coordination motifs on substrates with different symmetries signifies that the binding motif is an intrinsic characteristic of the metal coordination and is not induced by the symmetry of the supporting surface. The two binding modes of the different functional groups differ with respect to the orientation of the ligand termination. The carbonitrile moiety points directly towards the metal center, whereas the hydroxy ligands are directed slightly off center, which accounts for the chirality of the binding motif in the latter case. These features are intrinsic properties of the ligand system and have to be taken into account when designing coordination architectures. The results demonstrate that surface-assisted assembly can lead to unusual coordination motifs that are generally not found in conventional 3D bulk phases. This effect is attributed to the presence of the surface, where hybridization of the metal orbitals with the metal states of the substrate causes unusual redox states (see Sect. 3.3). In addition, the preferred flat bonding of the aromatic system favors such unusual binding modes.

In a systematic study, the engineering of a series of honeycomb networks assembled from a series of the ditopic dicarbonitrile molecular bricks and Co atoms on Ag(111) was reported [124]. This approach enabled fabrica-

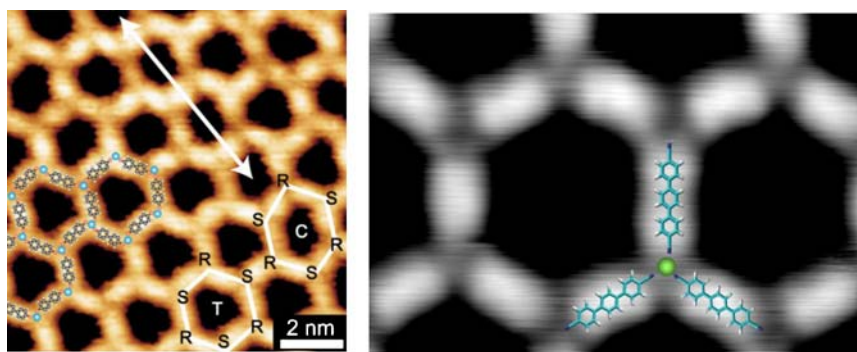


Fig. 7 Surface coordination motifs with threefold symmetry. *Left*: STM topograph displaying the hexagonal Fe-biphenolate network assembled on Ag(111). Different cavity types are highlighted in *white frames* and the handedness of the coordination centers are indicated by *S* and *R*. *Right*: high-resolution image of the Co-NC-Ph₃-CN honeycomb network assembled on Ag(111). Tentative models are superimposed over the data. Adapted from [122, 124]

tion of size- and shape-controlled open nanomeshes with pore dimensions up to 5.7 nm. For the investigations, linear dicyanitrile–polyphenyl molecular linkers (abbreviated NC–Ph_{*n*}–CN, whereby *n* can be 3, 4, or 5) were synthesized [100], motivated by the fact that carbonitrile compounds are known to coordinate strongly to transition metal centers [212, 213]. All ditopic molecular bricks have the same functional endgroups, while their lengths increase with *n* from 1.66 via 2.09 up to 2.53 nm. Indeed, the STM data reproduced in Figs. 7 and 8 demonstrate that by the controlled reaction of cobalt centers with preadsorbed linker molecules, a series of open nanomeshes with a tunable cavity size can be realized. The area of the enclosed hexagons increases stepwise with the number of phenyl rings incorporated into the molecular linker's backbone. Accordingly, the cell size expands stepwise from ≈ 10 via 15 up to 20 nm² for *n* = 3, 4, 5, respectively. While the 20 nm² nanopores achieved with NC–Ph₅–CN linkers represented a record for the most open surface-confined nanomesh realized by self-assembly, in more recent studies the limits were extended even further with a NC–Ph₆–CN linker [214].

It is known from the well-documented inorganic epitaxy studies that substrates play a crucial role in determining the adlayer structures. Related rules have been established for organic layers [215]. Parameters like the atomic lattice constant, crystalline orientation, and atomic steps have to be taken into

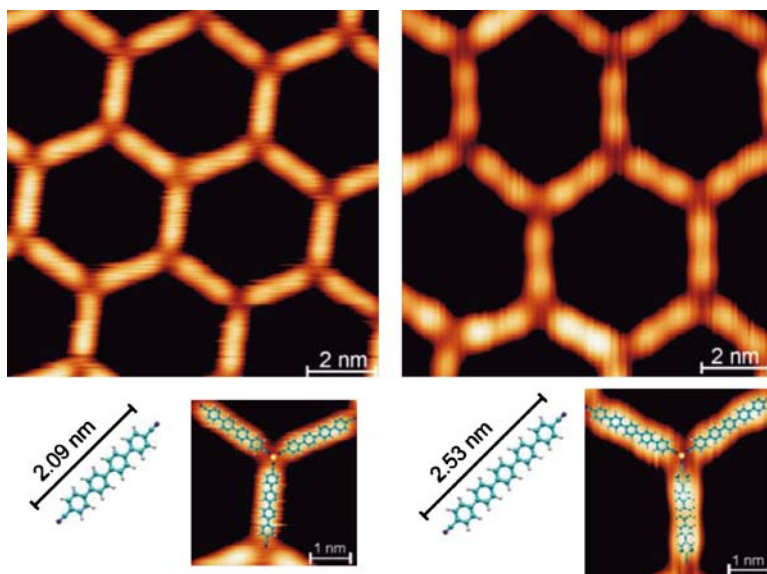


Fig. 8 Tunable metal–organic honeycomb nanomeshes with designed dicyanitrile linear linkers. *Upper panel:* STM images show the result of Co-directed assembly of NC–Ph₄–CN, and NC–Ph₅–CN. *Lower panel:* molecular structure and length along with models of the threefold Co–carbonitrile coordination motif. Adapted from [124]

account. For the metal-directed organization, the substrate influence is also of importance and needs to be assessed. Detailed investigation of the structural parameters of TPA, BDA, and TDA networks reveals the templating effects of the underlying substrate [207]. Besides the common feature of diiron coordination centers in fully reticulated network domains, the structures of the three molecules differ markedly in the coordination configuration and network geometries. These differences are attributed to the adsorbate–substrate coupling that plays a decisive role in the determination of the local coordination geometry. For instance, the Fe–Fe spacing in the BDA structure amounts to only 3.7 Å, thus being considerably smaller than in the TPA networks. In addition, the coordination configuration of BDA and TDA is different from the distorted square-planar geometry found for the Fe–TPA structure. Although the exact configuration cannot be deduced from the STM images, the spatial attachment of the ligands suggests either a planar trigonal geometry or a distorted tetrahedral coordination, whereby the former has been indeed observed for hydroxy functional moieties on the same surface. Besides the local coordination geometry, the network orientation with respect to the substrate lattice is different for the three molecules. In particular, the BDA and TDA molecules align along the [010] and [001] directions, whereas the TDA network orientation deviates slightly from the high symmetry [010] and [001] directions, implying that the structure is not precisely commensurate to the surface lattice. The influence of the substrate also has consequences for the shape of the cavities, whose size reflects the length of the linkers. It is proposed that the network structures are dominated by three different factors, the molecular adsorption energy, the Fe adsorption energy, and the Fe–carboxylate binding energy. The competition between the most favored molecular and metal adsorption sites and optimal coordination bonds determines the final topology. Thus the change of the molecule backbone strongly affects the geometries.

This mechanism is expressed explicitly when a symmetry mismatch between networks and substrate atomic lattices is present [122]. On the (100) facet the hexagonal Fe–hydroxyl networks are strongly distorted, resulting in a complicated arrangement of different cavity types but preserving the honeycomb topology. This ultimately limits the domain size. In contrast to the (100) surface, the networks grow continuously over entire terraces of the Ag(111) surface. The formation of highly symmetric hexagons is a consequence of the matching symmetry of the underlying substrate. Moreover, the achiral coordination nodes of the dicarbonitrile networks facilitate the growth of extended domains. The observed templating effects are a consequence of the preferred adsorption sites of the molecules and metal adatoms. Especially on the (100) surface, the network nodes of the honeycomb structure cannot adsorb on identical sites and therefore slight displacements are caused and the network is deformed. Nevertheless the metal–ligand bonding dictates the symmetry of the coordination motif.

In the case of rectangular Fe-TPA- or Co-TPA-coordination grids grown on the threefold Au(111) quasihexagonal substrate [121], the mismatch of the symmetries is merely reflected in limited domain sizes, which is significantly smaller than that of pure organic layers on the same substrate [216]. In conjunction with model calculations (see discussion below), the formation of the network is a result of the intrinsic properties of the binding mode between the transition metal ions and the carboxylate linkers. This linkage can overcome the templating influence of the rather low corrugated Au(111) surface. The driving forces for metal-terephthalate formation on Au(111) are determined primarily by the strength of the metal-carboxylate bond. Similar behavior was encountered in Mn-coordinated carboxylate lattices on the same surface [208], although much larger domains could be obtained.

To date, the networks based on dicyanitrile coordination of Co centers on the smooth Ag(111) substrate are of the highest structural quality. The honeycomb nanomeshes are thermally robust while extending over μm^2 large areas as single domains. Their high degree of regularity is visualized by the large scale STM topography in Fig. 9b. Histograms of the size distribution of the hexagonal cell underline the nearly perfect geometric order within the metal-organic networks (cf. [124]).

In sharp contrast, the twofold pyridine-Cu-pyridine coordination is not strong enough to overcome the adsorbate-substrate interaction. It was shown that by adjusting the chain structure commensurability with the substrate, the stability and structure of the chains is strongly affected, i.e., the epitaxial fit of the molecular structure with the substrate lattice has profound effects on the assembly and stability of the structures. The discussion of the commensurability of the structures in [204] as well as the dynamics of the chain formation highlights once again the importance of the adsorbate-substrate interaction and their implications for the construction of such low-dimensional architectures.

There is yet another approach to surface patterning, which involves the spatial confinement of reactions on surfaces, e.g., by controlling the formation of clusters or assembly of metal-organic complexes on a restricted area on the substrate. For instance, the dislocation pattern provided by the reconstructed Au(111) surface [217] provides a means to create transition-metal island arrays via self-organized growth of Fe or Co [120]. By tuning the local-reaction conditions with codeposited terephthalate linker molecules, one can follow coordination reactions [120, 121, 218, 219] and synthesize distinct low-dimensional metallosupramolecular systems, including regularly spaced Fe-terephthalate ribbons. With a careful exploitation of kinetic limitations, the corresponding gratings reflect the substrate chevron pattern, with their extension only limited by the terrace morphology rendering a mesoscopically ordered template structure [120].

One of the first intentions to test the usability of the described nanoporous superlattices was the study of inclusion of guest molecules into the open cavi-

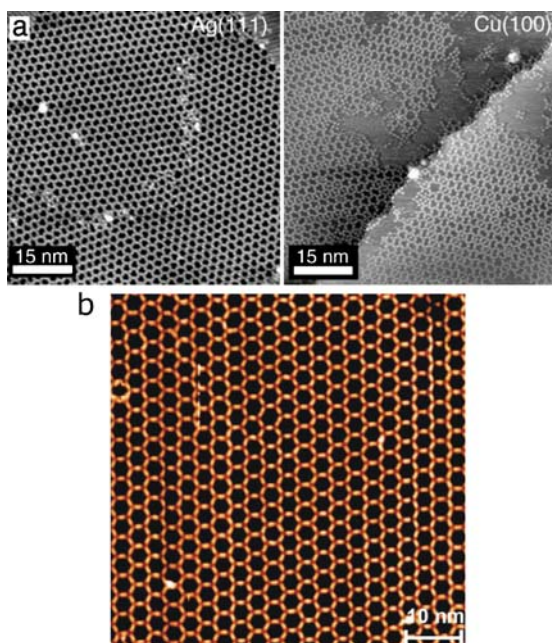


Fig. 9 Mesoscopic order of metallosupramolecular networks. **a** STM overview images showing the Fe-biphenolate networks assembled on Ag(111) (*left image*) and Cu(100) (*right image*). Two large domains on the Ag(111) surface are separated by a domain boundary. Three different domains are discernible on the Cu(100) surface. The size of the domains is considerably smaller on Cu(100) than on Ag(111). **b** The high lattice regularity extending in μm domains of Co-dicarbonitrile networks is shown by the large-scale STM image for the NC-Ph₃-CN linker. Adapted from [122, 124]

ties of the arrays revealing the underlying substrate. The appreciable thermal stability and overall robustness of the metal-organic networks makes them ideal templates for the (selective) adsorption of guest molecules and their templating on the surface. The cavities of the polybenzene carboxylate networks, as reported above, can be controlled by the backbone length of the linker molecules. The surrounding cavity consists of rather inert phenyl rings, weakly interacting with other functional groups. The size of the cavities was used to steer the interaction of C₆₀ molecules with the copper substrate and also the number of interacting C₆₀ molecules per pore (Fig. 10a,b) [115]. Furthermore, it was shown that besides the effect on the adsorbate-substrate interactions of the different pore sizes, the functionalization of the cavity rim by replacing the rod-like TPA molecule with TMLA (featuring an additional carboxylate side group available for interactions with guest species) can significantly alter the effective interaction of the C₆₀ with the pores and substrate. Recently open Mn-based carboxylate networks were also used to capture C₆₀ dimers [220].

The cavities of the FeTMA arrays presented above, emerging from the hierarchical self-assembly of TMA molecules in the presence of Fe adatoms, feature identically shaped hosts of about 1 nm, equally spaced by 3.43 nm and functionalized by eight carboxylate groups. It was successfully demonstrated that this network is capable of selective and reversible adsorption of a series of guest species, including C_{60} and small biomolecules (Fig. 10c) [221].

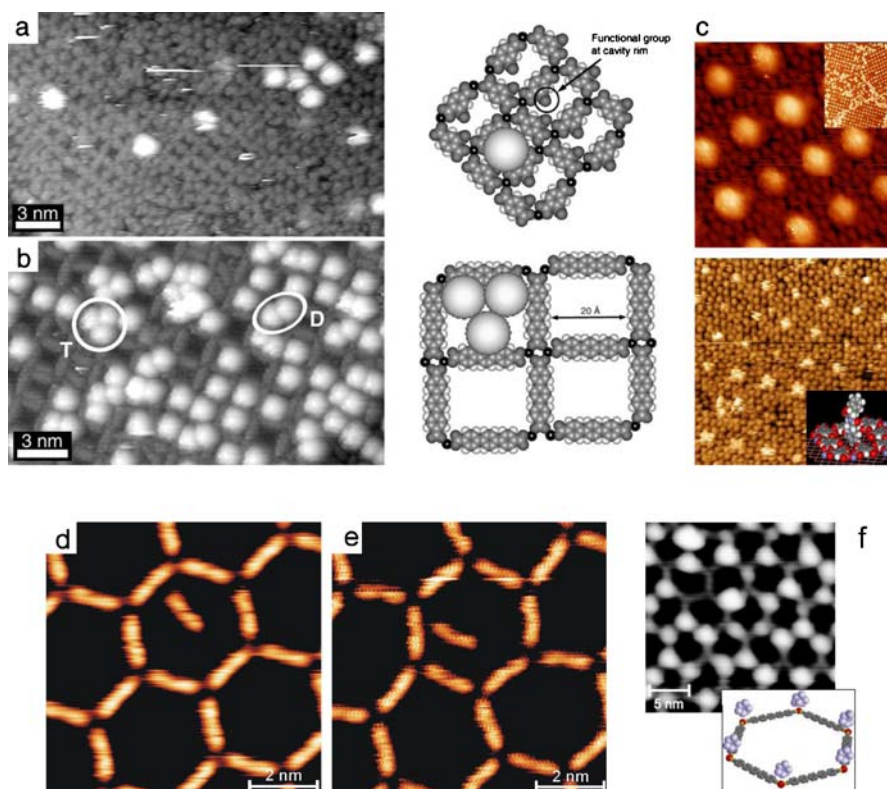


Fig. 10 Host-guest interactions and selective decoration at nanoporous coordination networks. **a,b** STM data and models showing the accommodation of C_{60} in nanoporous FeTMLA (**a**) and FeTDA (**b**) networks. Similar to the FeTPA grids, FeTMLA networks exclusively host C_{60} monomers. The indicated functional side-group strongly affects the chemical reactivity of the cavity. The mesoscale cavities in FeTDA networks can host C_{60} monomers, dimers (*D*) and trimers (*T*). **c** Binding of C_{60} (*upper image*) and diphenylalanine (*lower image*) in FeTMA nanocavities. The apparent fuzzy protrusions of the Phe-Phe is associated with molecular conformational changes during the STM imaging process. **d,e** Host cavities, formed by the metal-organic network of NC-Ph₃-CN linkers and CO₂ where a single dicarbonitrile guest molecule is trapped. The confined species can be switched between two configurations by the STM tip. **f** Preferential decoration of network nodes by Fe clusters following exposure of the same nanomesh to a beam of Fe atoms at $T \sim 200$ K; the *inset* shows a schematic model. Adapted from [115, 124, 214, 221]

Metal–organic open networks similarly represent templates for the study of molecular motion processes in confined environments, as illustrated with the confined guest species in the dicyanitrile-based nanomeshes depicted in Fig. 10d,e. Individual dicyanitrile linkers confined in the cavities formed by $[(\text{NC-Ph}_3\text{-CN})_{3/2}\text{Co}]_n$ nanomeshes, can be, for instance, rotated back and forth between two metastable positions. On the other hand, the honeycomb nanomeshes qualify as templates to steer the formation of Fe and Co nanostructures by offering nucleation sites at their rims and nodes. They notably can be used to control the surface distribution of Fe clusters that comprise a small number of atoms. The preferential nucleation sites are the ligands of the networks for temperatures in the range 90–120 K and the networks nodes for temperatures in the range 190–220 K (cf. Fig. 10f) [214].

3.3

Computational Modeling

The theoretical analysis of metal–organic complexes in contact with solid metal substrates has been addressed by ab initio calculations based on density functional theory (DFT). The reported results of the Fe- and Co-terephthalate dinuclear grids [121, 222], the Fe–TMA chains [203], and isolated adsorbed porphyrins on noble metal surfaces [127, 165, 223] reveal the interplay of the involved interactions between ligands and metal ions as well as adsorbates and substrate in the determination of the electronic and magnetic properties of the metal centers. For the $3d$ metal-carboxylate systems presented above the molecules are rather flat on the surfaces with their carboxylate groups bending towards the surface, such that oxygen atoms reside on top of the Cu surface. This signifies the strong interaction of the carboxylate groups with the substrate, which has been suggested by earlier findings and accounts for the strong templating effects.

Besides the elucidation of the adsorbate structure of the metal–TMA chains, DFT calculations give also insight into the electronic structure of the coordination centers, in particular the spin states [203]. It was found that the projected density of states displays an appreciable splitting between the majority and minority spin electronic d states. Moreover, the spin polarization of $3.3 \mu_{\text{B}}$ is comparable to the polarization of an isolated Fe adatom ($3.2 \mu_{\text{B}}$). Consequently the coordination to the carboxylate groups does not affect the electron localization at the coordination center, i.e., does not quench the spin magnetic moment.

For the diiron FeTPA system, DFT charge density calculations reproduce the main features appearing in the STM data (see Fig. 11a) and provide an atomistic description of the respective electronic and geometric structure [222]. The corresponding model in Fig. 11a shows a close-up view of the carboxylate-bridged diiron center. DFT indicates Fe–O bond lengths of

2.01 Å (equatorial) and 2.24 Å (axial), respectively, close to values in 3D Fe-carboxylates [54].

A further striking consequence of the strong lateral Fe-carboxylate coupling is the modified Fe-substrate bonding distance upon embedding of the Fe centers in the metal-organic array. Compared with isolated Fe adatoms in a fourfold hollow position, those in the Fe-TPA grid are vertically lifted by 0.6 Å, and in addition the Fe atoms are laterally displaced from the high-symmetry substrate positions (Fe-Fe spacing of 4.4 Å). Comparative calculations for the freestanding isostructural 2D Fe-TPA layer signal that the unsupported metal-organic array's properties are close to those of the adsorbed grid; i.e., the Cu(100) square atomic lattice represents an excellent template. The strong hybridization between the Fe and Cu states prevents a conclusive analysis of the Fe oxidation state. Nevertheless, there also is a marked splitting between the spin majority and minority states in this system, as observed in the projected density of states presented in Fig. 11b. The resulting spin polarization accounts for strongly magnetized Fe centers bearing a magnetic moment of $3.4 \mu_B$, coming close to the spin moment

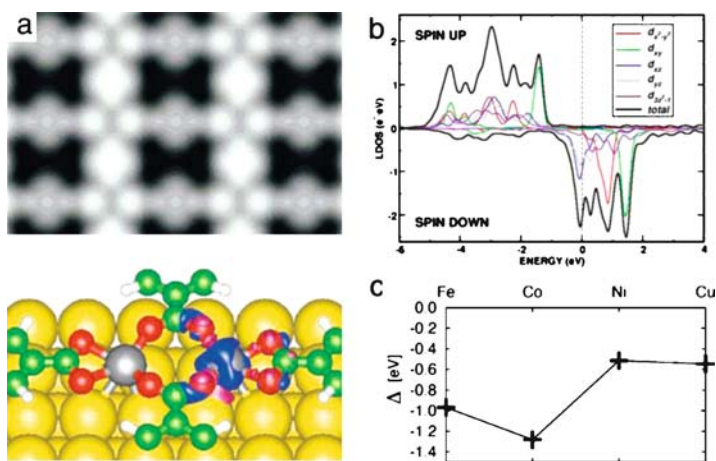


Fig. 11 Modeling of Fe-carboxylate dinuclear bond motif by ab initio methods. **a** STM image simulation showing contours of constant local density of states (LDOS) at the sample Fermi level derived from the DFT modeled Fe-diterephthalate grids on Cu(100). The graph below shows a perspective view of the diiron unit. The substrate square atomic lattice is represented by large spheres, the linkers and the Fe centers of the grid by spheres with rods symbolizing the chemical bonding. Fe charge rearrangement contour levels are indicated for the center at the right, drawn with respect to a removed iron atom, at $\pm = 0.004 e^-/\text{\AA}^3$, whereby the intensity indicates increased (dark) and decreased (light) electron density, respectively. **b** Spin-polarization of Fe centers as evidenced in the projected density of electronic states on the Fe atomic *d* orbitals. **c** Driving force Δ for metal-carboxylate formation on Au(111) as a function of different transition-metal species. Adapted from [222] **a,b** and [121] **c**

in the mononuclear Fe trimesate chains grown on the Cu(110) substrate. Moreover, the DFT results reveal a magnetic coupling between the Fe centers in diiron units. This is in line with the previously observed magnetic coupling in 3D oxygen-bridged dinuclear iron complexes [224], but in the present case its nature (ferro- or antiferromagnetic) could not be conclusively determined.

The dependence of the metal–ligand formation on the nature of the coordination center was addressed by DFT calculations for the metal–TPA system on Au(111) [121]. The energetics of the process involve the chemisorption energy of the adsorbed metal–TPA complex, the individual adsorbates, i.e., metal adatom and molecule, and the gas phase molecules/products. It was assumed that the major contribution is given by the metal–surface and metal–carboxylate interaction, whereas the molecule–surface interaction does not vary strongly with different metals bound to the molecule. The interaction energy is further divided into the binding energy in the gas phase, the adhesion energy of the metal adatom on the surface and the cohesion energy of the bulk metal, i.e., the energy gain of a gas phase atom incorporated into an island. It was found in the study of four metal centers (Fe, Co, Ni, and Cu) that the strongest binding energy in the gas phase exists for Co, followed by Fe and, by some distance, the less reactive Ni and Cu atoms. The transition metals generally have a strong tendency to form clusters and islands, so the binding energy to the carboxylate group determines the driving force for the complexation of the metals. The relatively low cohesive energy of Cu compared to the other metals makes it easily available on the surface for metal–ligand bonding, although the binding energy to the carboxylate groups is rather low (Fig. 11c).

The theoretical treatment of the interesting class of macrocyclic four-dentate ligands like porphyrins and phthalocyanines has also been performed with DFT calculations. On metal surfaces in the submonolayer regime the molecules are found to chemisorb parallel to the surface, in accordance with STM observations, with rather weak binding energies on Au or Ag substrates [125, 127, 165, 223]. The identification of binding sites, especially for the metal center, and the charge transfer between molecule and surface provide information in great detail about the spin-state and magnetic properties of the adsorbates. The deformation and conformational changes of the molecules upon adsorption affects the hybridization of the metal *d*-states with the surface and has consequences for the spin-polarization of the coordination centers [126, 223, 225].

Also, the threefold coordination of the Co centers in the dicarbonitrile nanomeshes described above could be rationalized with the help of DFT calculations. For the modeling, the molecular linkers were simplified as NC–Ph₁–CN retaining the carbonitrile endgroups that interact with the Co centers. In addition, the molecules were confined in a plane in accordance with the STM data, showing that the aromatic polyphenylene linkers are ad-

sorbed in a flat configuration with the molecular axis parallel to the metal substrate [124]. To assess the interaction of the Co center with the underlying surface, calculations were performed of both free planar compounds and complexes where a cluster of four Ag atoms was placed underneath the coordinated Co atom (cf. Fig. 12). A comparison between threefold and fourfold coordination without and with an Ag cluster placed below the coordination node shows that including an Ag cluster leads to a preferred threefold coordination (Fig. 12). Consideration of the binding energies within the node indicates that the interaction of the cobalt atoms with the surface is a key factor in favoring a 2D network with a threefold coordination of the organic

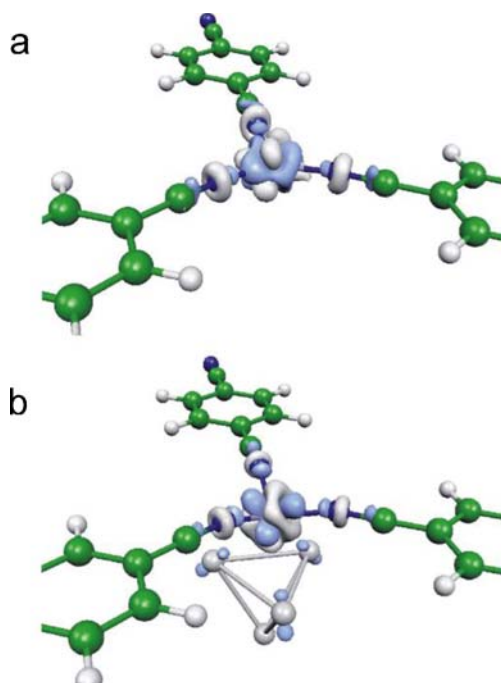


Fig. 12 DFT calculations addressing the threefold coordinated Co centers in the honeycomb nanomeshes obtained with dicarbonitrile linkers on Ag(111). **a,b** Plots of the induced charge density around the cobalt atom in threefold coordination of a model compound (NC-Ph₁-CN) without (**a**) and with (**b**) the presence of an Ag₄ cluster underneath the transition metal center. The image displays the electron density redistribution around the Co atom due to the bond formation with the ligands. *Dark shading* means charge depletion, and *light shading* charge accumulation ($0.01 e/\text{\AA}^3$). Without an Ag cluster the binding energy within the node for fourfold coordination exceeds threefold by 460 meV (energy per ligand: 1.82 eV threefold and 1.48 eV fourfold). With an Ag cluster placed below the coordination node threefold exceeds fourfold by 70 meV (energy per ligand: 1.65 eV threefold and 1.22 eV fourfold). Adapted from [124]

ligands. Accordingly an appreciable electronic hybridization between the Co and Ag atoms occurs, as visualized in Fig. 12.

4

Metal Ion–Ligand Assemblies at the Solid–Liquid Interface

Initial work on coordination-controlled self-assembly at interfaces was inspired from the field of self-assembled monolayers (SAMs) [226, 227]. This means the fabrication of an organized molecular layer, where the reactive group at one end of the molecule (e.g., a carboxylate, reactive silane, or thiol) is anchored to the surface, and non-covalent intermolecular interactions mediate an in-plane ordering. The functional group at the other end of the molecule can be chosen to be an appropriate ligand (e.g., hydroxamate, phosphonate, carboxylate) for the coordination of metal ions provided by a solution or an atomic beam. Thus coordination-controlled multilayers can be engineered by sequential adsorption (cf. [62, 228–230] and references therein). The control of such systems is also of interest for electronic nanoscale devices [230–233]. On Au-supported self-assembled monolayers, coordination cages based on cavitands complexed with pyridine-coordinated Pd ions were realized [234]. More recently, the SAM-template approach was refined to direct the growth of metal–organic frameworks [235, 236]. These findings bear promise for the interfacing of 2D to 3D systems [237] and the development of novel functional materials based on 3D metal–organic framework or metallocsupramolecular synthesis protocols.

An early report involving metal complexes on surfaces deals with the *in-situ* coordination reaction of deposited 2,2'-bipyridine ligands with Pd(OAc)₂ at the phenyloctane graphite interface, which results in a complete reorganization of the organic monolayer [112, 117], whereby the coordination reaction presumably takes place in the concomitant solvent volume after detaching the 2,2'-bipyridine ligands from the surface and redeposition of the formed 2,2'-bipyridine ligands–palladium acetate complexes [96]. Pyridine ligands were similarly employed for a bimodal self-assembly procedure for the organization of either cavitand dimers or oligomers on graphite [238]. A related protocol was used to coordinate 4-pyridyl-substituted terpyridyl ligands with Co(II) and Pd(II) metal ions, leading in both cases to strictly 1D structures on graphite [239], whereas the same ligand preassembled with Ru(II) and Os(II) metal ions and drop-casted on Pt(100) leads to molecular arrays exhibiting relatively low internal order but a high degree of internal freedom and mobility [240]. Also the metal-directed assembly of terpyridine-containing dendrimers could be achieved in an interfacial reaction [241]. A more sophisticated synthetic design based on the terpyridine motif features two enantiomerically pure bridging ligands giving controlled access to domains of highly ordered chiral coordination polymers. Thereby, each enan-

tiomorphic ligand is mixed with Fe(II) metal ions in CH₂Cl₂/water mixture and deposited on an HPOG substrate yielding domains of interfacially stabilized helical coordination polymers of opposite sense of rotation, detectable directly by STM imaging [108, 242].

Being another classical ligand system, a series of salophen complexes [salophen = *N,N'*-(*o*-phenylene)bis(salicylideneimine)] of Cu(II), Ni(II), and Co(II) metal ions was prepared and their 2D assemblies investigated at the liquid–solid interface by STM. Depending on the chain lengths of the alkyl substituents, two different adlayer organizations, parallelogram and honeycomb, were observed [243]. However, only isolated mononuclear complexes are formed by the distinctive metal ion–ligand interactions, while the intermolecular complex-to-complex interaction is mediated by van der Waals interactions and hydrogen bonds. A recent study reported an even more intricate 2D assembly scheme for surface-supported metal–organic clusters: a single nanoporous coordination structure, in which a fractal polymeric macromolecule (recognized as Sierpinski gasket) is composed of bis-terpyridine tectons coordinating 36 Ru and six Fe atoms [244].

The formation of highly-ordered 2D monolayers from preassembled [$n \times n$] metal ion arrays on surfaces represents a two-tiered self-assembly process (see Scheme 2, left): (i) The [$n \times n$] metal ion arrays are formed in a bulk self-assembly step in solution from their constituents (organic ligands and metal ions). (ii) Subsequently, the [$n \times n$] metal ion arrays are self-assembled themselves to densely packed domains of monolayers on the graphite surface [118]. The first self-assembly process relies on the read-out of the coordination instructions stored in the ligands and the metal ions, while the second is steered by van der Waals forces between the metal ion arrays on the one side and between arrays and graphite surface on the other side. Due to the flat, square-like geometry of the [$n \times n$] metal ion arrays, this second self-assembly process automatically results in a highly-ordered “grid-of-grids” superstructure under 2D confinement. Thus, monolayers of [$n \times n$] metal ion arrays exhibit a twofold supramolecular matrix-structure: (i) internally by the ligand-directed coordinative positioning of the metal ions and (ii) externally by the van-der-Waals directed formation of the “grid-of-grids” superstructure. Single metal ion addressing the inside of isolated metal ion arrays could be achieved electronically by use of scanning tunneling spectroscopy technique called current-induced tunneling spectroscopy (CITS) [150].

Different supramolecular bi- and tetranuclear Pd(II) and Pt(II) complexes of square- or rhomb-like shape were deposited under potential control from aqueous electrolyte on a Cu(100) electrode surface, which was precovered by tetragonal pattern of chloride anions (Fig. 13) [116, 151, 245]. Although, partial decomposition was observed, it could be concluded that contact with the surface does not affect the metal coordination algorithms, but actively steers the adsorption parameters (relative orientation, internal conformations, etc.)

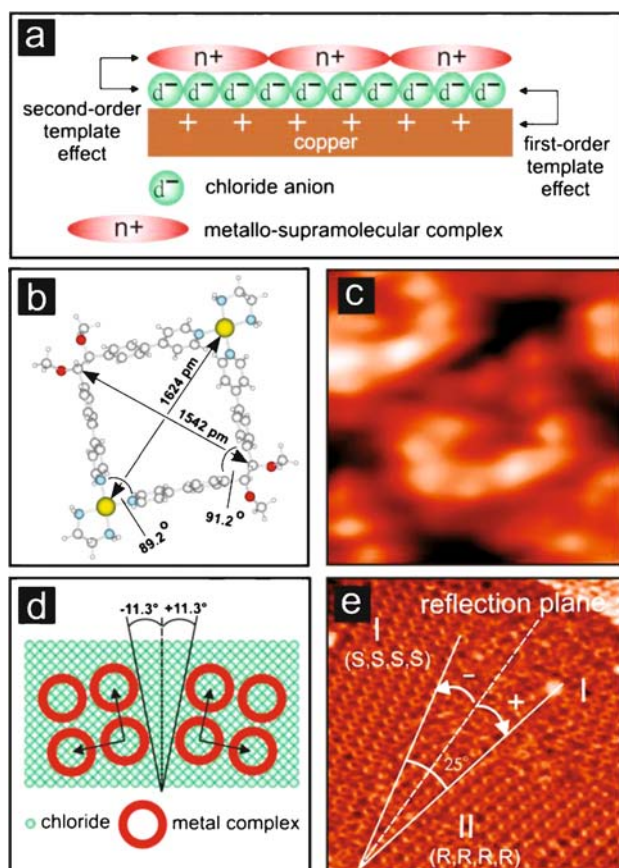


Fig. 13 Binuclear Pt^{II} -square complexes on surfaces. **a** Scheme showing the different tiers of template steering the self-assembly of the supramolecular $\text{Pt}^{\text{II}}(\text{L})_2$ complex on a $\text{Cu}(100)/\text{Cl}^-$ -substrate. **b** Molecular structure and dimensions of a $[\text{Pt}^{\text{II}}(\text{L})_2]^{4+}$ cation. For comparison, **c** STM data showing a single complex. **d** Schematic and **e** experimental representation of the segregation of a racemic mixture of $[\text{Pt}^{\text{II}}(\text{L})_2]^{4+}$ molecules exhibiting surface-confined resolution into 2D enantiopure domains. Adapted from [245]

of the supramolecules on the metallic surface. The introduction of chirality into the ligand systems induces the formation of single domain orientation, or, if racemic mixtures are used, segregation into enantiomerically pure surface-confined domains (Fig. 13d,e). By a similar approach, the organization of previously self-assembled supramolecular metallacyclic $\text{Pt}(\text{II})_4$ rectangles was investigated on graphite and $\text{Au}(111)$ surfaces. The rectangles adsorb on both substrates in a different way: On graphite, they stand on the long edge, while on $\text{Au}(111)$ they lay flat on the surface forming linear chains [152, 246]. More recently, their ordering in monodisperse islands could be achieved with the help of a molecular template providing an array

of nanocavities [247]. Additionally, trimeric Zn(II) complexes of polypyrrolimine ligands with distinct triangular shape were studied on a Au(111) surface [248].

Monolayers of tetranuclear $[2 \times 2]$ Co_4^{II} metal ion arrays were generated by drop-casting the supramolecules on an atomically flat graphite surface (HOPG). The highly ordered supramolecular surface structures consisting of densely-packed flat-lying $[2 \times 2]$ Co_4^{II} metal ion arrays (MIAs) of rectangular shape are formed spontaneously from dilute acetone solution as almost defect-free domains of up to $0.5 \mu\text{m}^2$ (Fig. 14). The domain formation proceeds outwards from single nucleation points, a process which might be considered 2D crystallization.

Certain substitution patterns at the organic ligands also provoke “on-the-edge” orientation of the metal ion arrays with respect to the surface. But, most of the observed metal ion $[2 \times 2]$ arrays result in flat tiles forming a “grid-of-grids” superarray, in which the presence of the $[2 \times 2]$ metal ion grids is reflected by the $2.5 \times 2.4 \text{ nm}$ periodicity in agreement with the molecule size determined by X-ray crystallography [107, 249]. In a similar way, $[3 \times 3]$ Mn_9^{II} metal ion arrays were studied on both HOPG and Au(111) surfaces [250, 251].

By application of a voltage pulse through the STM-tip on the monolayer of metal ion arrays, a single $[2 \times 2]$ Co_4^{II} metal ion array could be lifted, leaving a square-like hole of the dimension of the molecule (see Fig. 14b). The migration rate of the hole was measured to be 200 times slower than in a monolayer of cycloalkanes, reflecting the degree of adsorption of the molecules to the

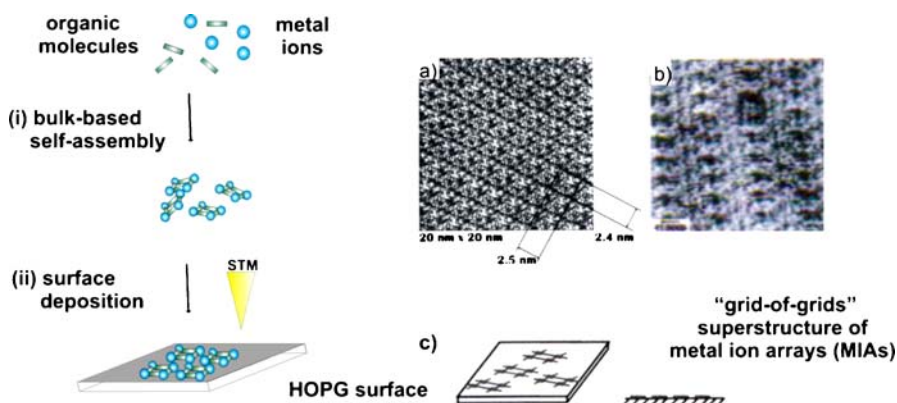


Fig. 14 Schematic representation of the deposition of metal ion arrays (MIAs) on surfaces. **a** STM-image of the monolayer of $[2 \times 2]$ Co_4^{II} metal ion arrays on graphite. The 2D periodicity of the “grid-of-grids” network is shown with $2.5 \times 2.4 \text{ nm}^2$. **b** A hole in the supramolecular monolayer is produced by potential induced lifting of a single $[2 \times 2]$ Co_4^{II} molecule with the STM-tip. **c** Schematic representation of the disposition of the MIAs at the surface (*top and side view*). Images adapted from [107]

graphite surface [107]. Further insight into the intramolecular electronic situation of isolated single $[2 \times 2]$ Co^{II} metal ion arrays at room temperature and ambient conditions was gained by CITS [119]. These experiments allowed, by selective mapping of the highest occupied molecular orbitals (HOMOs), the localization of the positions of the incorporated Co^{II} ions. First-principle DFT calculations confirmed that in these type of molecules the HOMOs possess a large d -character such that they are strongly localized around the positions of the metal ions. Consequently, the projection of the CITS maps at certain negative tunneling biases indicates electronically the cornerstone positions of the four Co^{II} metal ions (Fig. 15a,b) [118] (for a related discussion of the imaging of Cu-complexes on graphite see [252]). The same technique was successfully applied to visualize the metal ions in the higher homologous $[3 \times 3]$ Mn_9^{II} and $[4 \times 4]$ $\text{Mn}_{16}^{\text{II}}$ MIAs aligning nine and 16 manganese ions, respectively. The obtained CITS maps mirror the structural situation within the metal ion arrays since, although very regularly arranged, the metal ions in these higher homologues display a more lozenge-like structure (Fig. 15c). This structural deviation from the optimal square-like arrangement can be attributed to the “pinching-in” of the organic ligands during metal ion coordination, reflecting the importance and the consequences of sufficiently instructed metal-ligand interactions for the outcome the self-assembly processes [251].

Cage compounds were also studied at surfaces. In particular polyoxometallates (POMs), which are early-transition-metal oxygen clusters, give rise to a certain interest in view of their potential applications due to the very robust cage scaffold and broad variety in shape, size, and composition [253]. This class of compounds, often described as soluble metal-oxide fragments, receives increasing attention mostly due to its multitude of interesting catalytic, electronic, magnetic, medical, thermal, and optical properties [254]. Recently, the synthesis of an unprecedented Cu_{20} -containing polyoxotungstate of large

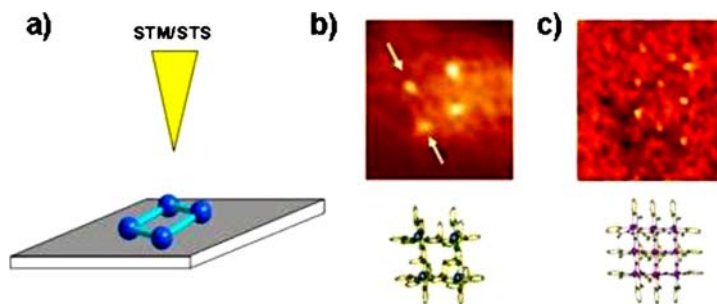


Fig. 15 **a** Schematic principle showing the metal ion array on a graphite surface; **b** and **c** show the results of the locally resolved current-induced tunneling spectroscopy (CITS) measurements of a $[2 \times 2]$ Co_4^{II} and $[3 \times 3]$ Mn_9^{II} indicating the position and arrangement of the respective metal ions. Adapted from [150]

size and high symmetry by self-assembly techniques was reported [255]. The wheel-shaped $[\text{Cu}_{20}\text{Cl}(\text{OH})_{24}(\text{H}_2\text{O})_{12}(\text{P}_8\text{W}_{48}\text{O}_{184})]^{25-}$ represents a transition metal-substituted derivative of $[\text{H}_7\text{P}_8\text{W}_{48}\text{O}_{184}]^{33-}$ and incorporates more Cu^{2+} ions than any other polyoxometalate known to date. The present Cu_{20} wheel can be considered an oxygen-copper cage sitting as a hub in the center of a large polyoxotungstate wheel. The Cu_{20} cluster is therefore effectively shielded from the environment but sufficiently open for investigations with the STM [256]. A second supramolecular cage compound, a self-assembled cuboctahedron comprising 12 Pd(II) metal ions and 24 organic ligands of pyridine type, was studied on a HOPG surface. The investigations have proven that this cage also maintains its integrity under near-surface conditions, despite the relative lability of the constituent Pd(II)-N bond [257]. More recently, the assembly of nanosize coordination cages on Si(100) was achieved using a two-step procedure [258].

1D coordination polymer assemblies have attracted much attention in the development of new functional materials owing to such properties as zeolitic behavior, conductivity, luminescence, magnetism, spin-crossover, and non-linear optical effects [76]. 1D coordination chains in solution were obtained from Fe and ditopic bis-terpyridines on graphite [109]. Also, polymeric rotaxane chains consisting of cyclodextrins-dipyridine units connected by coordination with Ni ions [259], and $[\text{CuBr}-(\text{isonicotinic acid})]_n$ polymeric chains [260] were investigated regarding their surface assembly behavior.

In related investigations, a series of structurally similar polymers containing different aromatic amino acid ligands were investigated in order to estimate the influence of the substituents on the local surface properties. Towards this end, the cationic coordination polymer $[[\text{Zn}(\text{L})]_n] (\text{CF}_3\text{SO}_3)_n$ (L = dipicolylglycyl tyrosine) was deposited on HOPG and investigated with regard to its local tunneling properties (Fig. 16) [261]. More recently, fibres of $[\text{Ru}_2\text{Br}(\mu\text{-O}_2\text{CET})_4]_n$ polymers have also been isolated on different surfaces [262].

Samples of $[[\text{Zn}(\text{L})]_n] (\text{CF}_3\text{SO}_3)_n$ on HOPG were prepared by allowing 10^{-9} M aqueous solutions of pH 5 to 6 to evaporate under air. It was shown by topographic STM investigations that the polymer adopts two different structures depending on the local environment of the substrate: (i) a double-helical plait is formed on undisturbed flat surface areas, and (ii) linearly stretched polymer strands are formed along the steps of the substrate (see Fig. 16b). Apparently, the structure change is a consequence of different strength polymer-substrate interactions between $[[\text{Zn}(\text{L})]_n] (\text{CF}_3\text{SO}_3)_n$ and the HOPG substrate.

Furthermore, a 1D ribbon-like coordination polymer could be obtained by the coordination of 2,5-dihydroxybenzohydroquinone (DHBQ) with Cu(II) ions in aqueous solution directly at the solid-liquid interface on an Au(111) substrate. The authors advocate a "surface-assisted self-organized" growth mechanism, which involves in-situ deprotonation and metal coordination

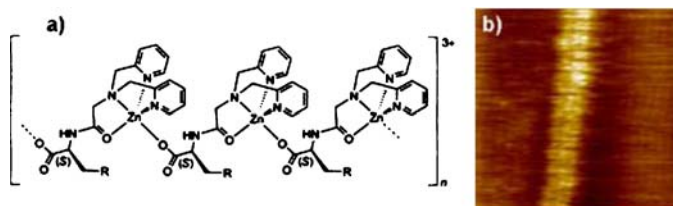


Fig. 16 The cationic coordination polymer $[[\text{Zn}(\text{L})]_n] (\text{CF}_3\text{SO}_3)_n$: **a** representation of the molecular structure, $\text{R} = \text{Ph-OH}$; **b** topographic STM image on HOPG revealing the 1D character under near-surface conditions. Adapted from [261]

processes under the steering influence of the Au(111) surface. Since these processes seem to yield ordered monolayers of 1D $[\text{Cu-DHBQ-}]_n$ ribbons if the gold substrate is preheated, an activation barrier seems to be involved in the formation of the supramolecular structure; indeed an argument in favor of in-situ coordination processes under surface confinement [263].

5 Résumé and Perspectives

The presented double road map towards surface-confined metallosupramolecular nanostructures constitutes part of the future toolkit needed to put into reality steered *aufbau* and controlled manipulation of functional interfaces or operational surfaces. The described findings reveal that both methodologies (i.e., direct surface-assisted complexation and deposition of pre-fabricated species) employ metal-directed assembly protocols to achieve unique coordination systems in environments of reduced dimensions. They are conceivable for a great variety of molecular systems and can be applied to substrates with different symmetries and with different physical and chemical nature. The intrinsic physicochemical properties of the metal centers (e.g., unsaturated coordination spheres, their redox, spin, magnetic, and electronic states) present a formidable playground for many exciting further developments, ranging from molecular electronics and magnetism to single-site heterogeneous catalysis. The templating of specific host-guest interactions foreshadows the use of nanoporous metal-organic coordination networks for both patterning purposes or investigations of surface chemical reactions in controlled surroundings. Furthermore, they may serve as scaffolds for the organization of separated, regularly distributed magnetic nanoclusters and bear the potential to confine complex synthetic or biological guest molecules in tuneable spaces where their motion or switching can be regulated.

Acknowledgements The work reviewed here has been partially supported through several funding schemes, as mentioned in the original papers. It would not have been possible

without the dedication and talent of the involved students, researchers, and cooperating scientists to whom the authors are very thankful.

References

1. Werner A (1893) *Z Anorg Chem* 3:267
2. Werner A (1912) *Annu Chem* 386:1
3. Wyckoff RWG, Posnjak E (1921) *J Am Chem Soc* 43:2292
4. Dickinson RG (1921) *J Am Chem Soc* 44:2404
5. Bethe H (1929) *Ann Phys* 395:133
6. Bethe H (1930) *Z Phys* 60:218
7. Bersuker IB (1996) *Electronic structure and properties of transition metal compounds: introduction to the theory*. Wiley, New York
8. Becquerel J (1929) *Z Phys* 58:205
9. Van Vleck JH (1932) *J Chem Phys* 3:807
10. Cotton FA, Wilkinson G (1988) *Comprehensive inorganic chemistry*. Wiley, New York
11. Wilkinson G, Gillard RD, McCleverty JA (1989) *Comprehensive coordination chemistry*. Pergamon, Oxford
12. Langmuir I (1916) *J Am Chem Soc* 38:2221
13. Taylor HS (1925) *Proc R Soc London A* 108:105
14. Volmer M, Adhikari G (1925) *Z Phys* 35:170
15. Becker JA (1926) *Phys Rev* 28:341
16. Cassel H (1926) *Naturwissenschaften* 14:103
17. Moll F (1928) *Z Phys Chem* 136:183
18. Schottky W (1928) *Z Phys* 14:63
19. Langmuir I (1932) *J Am Chem Soc* 16:2798
20. Langmuir I, Taylor JB (1932) *Phys Rev* 40:463
21. Lennard-Jones JE (1932) *Trans Faraday Soc* 28:333
22. Rideal EK (1932) *Trans Faraday Soc* 28:139
23. Volmer M (1932) *Trans Faraday Soc* 28:359
24. Becker JA (1933) *Trans Faraday Soc* 28:148
25. Langmuir I (1933) *Chem Rev* 13:147
26. Taylor JB, Langmuir I (1933) *Phys Rev* 44:423
27. Becker JA (1929) *Trans Am Electrochem Soc* 55:153
28. Davisson C, Germer LH (1927) *Phys Rev* 30:705
29. Lander JJ, Morrison J, Unterwald F (1962) *Rev Sci Instrum* 33:782
30. Ertl G, Küppers J (1985) *Low energy electrons and surface chemistry*. VCH, Weinheim
31. Duke CB (ed) (1994) *Surface science: the first thirty years*. *Surf Sci* 299/300:1–1039
32. Ertl G (1990) *Angew Chem Int Ed* 29:1219
33. Somorjai GA (1996) *Chem Rev* 96:1223
34. Ugo R (1975) *Catal Rev Sci Eng* 11:225
35. Plummer EW, Salaneck WR, Miller JS (1978) *Phys Rev B* 18:1673
36. Johnson KH, Balasz AC, Kolari HJ (1978) *Surf Sci* 72:733
37. Muetterties EL, Rhodin TN, Band E, Brucker CF, Pretzer WR (1979) *Chem Rev* 79:91
38. Nitschké F, Ertl G, Küppers J (1981) *J Chem Phys* 74:5911
39. Gavin RM, Reutt J, Muetterties EL (1981) *Proc Natl Acad Sci USA* 78:3981
40. Soriaga MP (1990) *Chem Rev* 90:771

41. Gibson DH (1999) *Coord Chem Rev* 185-186:335
42. Burwell RL Jr, Haller GL, Taylor KC, Read JF (1969) *Adv Catal* 20:1
43. Ferrari AM, Huber S, Knözinger H, Neyman KM, Rösch N (1998) *J Phys Chem B* 102:4548
44. Freund HJ (1997) *Angew Chem Int Ed* 36:452
45. Over H, Kim YD, Seitsonen AP, Wendt S, Lundgren E, Schmid M, Varga P, Morgante A, Ertl G (2000) *Science* 287:1474
46. Gong X-Q, Raval R, Hu P (2004) *Phys Rev Lett* 93:106104
47. Wang J, Fan CY, Sun Q, Reuter K, Jacobi K, Scheffler M, Ertl G (2004) *Angew Chem Int Ed* 42:2151
48. Copéret C, Chabanas M, Saint-Arroman RP, Basset J-M (2003) *Angew Chem Int Ed* 42:156
49. Thomas JM, Raja R, Lewis DW (2005) *Angew Chem Int Ed* 44:6456
50. Nozaki C, Lugmair CG, Bell AT, Tilley TD (2002) *J Am Chem Soc* 124:13194
51. Avenier P, Taoufik M, Lesage A, Solans-Monfort X, Baudouin A, de Mallmann A, Veyre L, Basset J-M, Eisenstein O, Emsley L, Quadrelli EA (2007) *Science* 317:1056
52. Tada M, Coquet R, Yoshida J, Kinoshita M, Iwasawa Y (2007) *Angew Chem Int Ed* 46:7220
53. Holm RH, Kennepohl P, Solomon EI (1996) *Chem Rev* 96:2239
54. Merckx M, Kopp DA, Sazinsky MH, Blazyk JL, Müller J, Lippard SJ (2001) *Angew Chem Int Ed* 40:2783
55. Groves JT (2003) *Proc Natl Acad Sci USA* 100:3569
56. Woggon W-D (2005) *Acc Chem Res* 38:127
57. Chen K, Mirkin CA, Lo R-K, Zhao J, McDevitt JT (1995) *J Am Chem Soc* 117:6374
58. Thorpe JM, Beddoes RL, Collison D, Garner CD, Helliwell M, Holmes JM, Tasker PA (1999) *Angew Chem Int Ed* 38:1119
59. Vestal CR, Zhang ZJ (2003) *J Am Chem Soc* 125:9828
60. Maeda Y, Okumura M, Daté M, Tsubota S, Haruta M (2002) *Surf Sci* 514:267
61. Aurora A, Cattaruzza F, Coluzza C, Della Volpe C, Di Santo G, Flamini A, Mangano C, Morpurgo S, Pallavicini P, Zanoni R (2007) *Chem Eur J* 13:1240
62. Condorelli GG, Motta A, Bedoya C, Di Mauro A, Pellegrino G, Smecca E (2007) *Inorg Chim Acta* 360:170
63. Hagfeldt A, Grätzel M (2000) *Acc Chem Res* 33:269
64. Lehn J-M (1995) *Supramolecular chemistry, concepts and perspectives*. VCH, Weinheim
65. Lehn JM (2002) *Proc Natl Acad Sci USA* 99:4763
66. Atwood JL, Davies JED, MacNicol DD, Vögtle F, Lehn J-M (1996) *Comprehensive supramolecular chemistry*. Pergamon, New York
67. Lawrence DS, Jiang T, Levett M (1995) *Chem Rev* 95:2229
68. Philp D, Stoddart JF (1996) *Angew Chem Int Ed* 35:1154
69. Swieggers GF, Malefetse TJ (2000) *Chem Rev* 100:3483
70. Fujita M, Umemoto K, Yoshizawa M, Fujita N, Kusakawa T, Biradha K (2001) *Chem Commun*, p 509
71. Leininger S, Olenyuk B, Stang PJ (2000) *Chem Rev* 100:853
72. Holiday BJ, Mirkin CA (2002) *Angew Chem Int Ed* 40:2022
73. Cheetham AK, Férey G, Loiseau T (1999) *Angew Chem Int Ed* 38:3268
74. Moulton B, Zaworotko MJ (2001) *Chem Rev* 101:1629
75. Férey G (2001) *Chem Mater* 13:3084
76. Janiak C (2003) *Dalton Trans*, p 2781
77. Maspoch D, Ruiz-Molina D, Veciana J (2004) *J Mater Chem* 14:2173

78. Maspoch D, Ruiz-Molina D, Wurst K, Domingo N, Cavallini M, Biscarini F, Tejada J, Rovira C, Veciana J (2003) *Nat Mater* 2:190
79. Yaghi OM, O'Keefe M, Ockwig NW, Chae HK, Eddaoudi M, Kim J (2003) *Nature* 423:705
80. Kitagawa S, Kitaura R, Noro S (2004) *Angew Chem Int Ed* 43:2334
81. Hosseini MW (2005) *Acc Chem Res* 38:313
82. Gianneschi NC, Masar MS, Mirkin CA (2005) *Acc Chem Res* 38:825
83. Badjic JD, Nelson A, Cantrill SJ, Turnbull WB, Stoddart JF (2005) *Acc Chem Res* 38:723
84. Balzani V, Credi A, Raymo FM, Stoddart JF (2000) *Angew Chem Int Ed* 39:3348
85. Sauvage J-P (1998) *Acc Chem Res* 31:611
86. Binnig G, Rohrer H (1987) *Rev Mod Phys* 59:615
87. Eigler DM, Schweizer EK (1990) *Nature* 344:524
88. Crommie MF, Lutz CP, Eigler DM (1993) *Science* 262:218
89. Avouris P (1995) *Acc Chem Res* 28:95
90. Gimzewski JK, Joachim C (1999) *Science* 283:1683
91. Hla S-W, Bartels L, Meyer G, Rieder K-H (2000) *Phys Rev Lett* 85:2777
92. Ho W (2002) *J Chem Phys* 117:11033
93. De Feyter S, De Schryver FC (2003) *Chem Soc Rev* 32:139
94. Barth JV, Weckesser J, Lin N, Dmitriev S, Kern K (2003) *Appl Phys A* 76:645
95. Barth JV, Costantini G, Kern K (2005) *Nature* 437:671
96. De Feyter S, De Schryver FC (2005) *J Phys Chem B* 109:4290
97. Wan L-J (2006) *Acc Chem Res* 39:334
98. Böhrringer M, Morgenstern K, Schneider W-D, Berndt R, Mauri F, Vita AD, Car R (1999) *Phys Rev Lett* 83:324
99. Yokoyama T, Yokoyama S, Kamikado T, Okuno Y, Mashiko S (2001) *Nature* 413:619
100. Schlickum U, Decker R, Klappenberger F, Zoppellaro G, Klyatskaya S, Auwärter W, Nepl S, Kern K, Brune H, Ruben M, Barth JV (2008) *J Am Chem Soc* (in press)
101. Barth JV, Weckesser J, Cai C, Günter P, Bürgi L, Jeandupeux O, Kern K (2000) *Angew Chem Int Ed* 39:1230
102. Barth JV, Weckesser J, Trimarchi G, Vladimirova M, Vita AD, Cai C, Brune H, Günter P, Kern K (2002) *J Am Chem Soc* 124:7991
103. Theobald JA, Oxtoby NS, Phillips MA, Champness NR, Beton PH (2003) *Nature* 424:1029
104. Stöhr M, Wahl M, Galka CH, Riehm T, Jung TA, Gade LH (2005) *Angew Chem Int Ed* 44:7394
105. Cañas-Ventura ME, Xiao W, Wasserfallen D, Müllen K, Brune H, Barth JV, Fasel R (2007) *Angew Chem Int Ed* 46:1814
106. Schiffrin A, Riemann A, Auwärter W, Pennec Y, Weber-Bargioni A, Cvetko D, Cosaro A, Morgante A, Barth JV (2007) *Proc Natl Acad Sci USA* 104:5279
107. Semenov A, Spatz JP, Möller M, Lehn J-M, Sell B, Schubert D, Weidl CH, Schubert US (1999) *Angew Chem Int Ed* 38:2547
108. Bernhard S, Takada K, Díaz DJ, Abruña HD, Mürner H (2001) *J Am Chem Soc* 123:10265
109. Kurth DG, Severin N, Rabe JP (2002) *Angew Chem Int Ed* 41:3681
110. Lin N, Dmitriev A, Weckesser J, Barth JV, Kern K (2002) *Angew Chem Int Ed* 41:4779
111. Messina P, Dmitriev A, Lin N, Spillmann H, Abel M, Barth JV, Kern K (2002) *J Am Chem Soc* 124:14000
112. Abdel-Mottaleb MMS, Schuurmans N, Feyter SD, Esch JV, Feringa BL, Schryver FCD (2002) *Chem Commun*, p 1894

113. Dmitriev A, Spillmann H, Lin N, Barth JV, Kern K (2003) *Angew Chem Int Ed* 41:2670
114. Spillmann H, Dmitriev A, Lin N, Messina P, Barth JV, Kern K (2003) *J Am Chem Soc* 125:10725
115. Stepanow S, Lingenfelder M, Dmitriev A, Spillmann H, Delvigne E, Lin N, Deng X, Cai C, Barth JV, Kern K (2004) *Nat Mater* 3:229
116. Safarowsky C, Merz L, Rang A, Broekmann P, Hermann BA, Schalley CA (2004) *Angew Chem Int Ed* 43:1291
117. De Feyter S, Abdel-Mottaleb MMS, Schuurmans N, Verkuijl B, Esch Jv, Feringa BL, De Schryver FC (2004) *Chem Eur J* 10:1124
118. Ruben M, Rojo J, Romero-Salguero FJ, Uppadine LH, Lehn J-M (2004) *Angew Chem Int Ed* 43:3644
119. Alam MS, Strömsdörfer S, Dremov S, Müller P, Kortus J, Ruben M, Lehn J-M (2005) *Angew Chem Int Ed* 44:7896
120. Clair S, Pons S, Brune H, Kern K, Barth JV (2005) *Angew Chem Int Ed* 44:7294
121. Clair S, Pons S, Fabris S, Baroni S, Brune H, Kern K, Barth JV (2006) *J Phys Chem B* 110:5627
122. Stepanow S, Lin N, Payer D, Schlickum U, Klappenberger F, Zoppellaro G, Ruben M, Brune H, Barth JV, Kern K (2007) *Angew Chem Int Ed* 46:710
123. Barth JV (2007) *Annu Rev Phys Chem* 58:375
124. Schlickum U, Decker R, Klappenberger F, Zoppellaro G, Klyatskaya S, Ruben M, Silanes I, Arnau A, Kern K, Brune H, Barth JV (2007) *Nano Lett* 7:3813
125. Zhao A, Li Q, Chen L, Xiang H, Wang W, Pan S, Wang B, Xiao X, Yang J, Hou JG, Zhu Q (2005) *Science* 309:1542
126. Iancu V, Deshpande A, Hla S-W (2006) *Nano Lett* 6:820
127. Wende H, Bernien M, Sorg C, Ponpandian N, Kurde J, Miguel J, Piantek M, Xu X, Eckhold P, Kuch W, Baberschke K, Panchmatia PM, Sanyal B, Oppenheimer RM, Eriksson O (2007) *Nat Mater* 6:516
128. Stepanow S, Lin N, Barth JV (2008) *J Phys Cond Matter* 20:184002
129. Dmitriev A, Lin N, Weckesser J, Barth JV, Kern K (2002) *J Phys Chem B* 106:6907
130. Stepanow S, Strunskus T, Lingenfelder M, Dmitriev A, Spillmann H, Lin N, Barth JV, Wöll C, Kern K (2004) *J Phys Chem B* 108:19392
131. Cañas-Ventura ME, Klappenberger F, Clair S, Pons S, Brune H, Kern K, Strunskus T, Wöll C, Fasel R, Barth JV (2006) *J Chem Phys* 125:184710
132. Donhauser ZJ, Mantooh BA, Kelly KE, Bumm LA, Monnell JD, Stapleton JJ Jr, Rawlett AM, Allara DL, Tour JM, Weiss PS (2001) *Science* 292:2303
133. Castonguay M, Roy J-R, Rochefort A, McBreen PH (2000) *J Am Chem Soc* 122:518
134. Yokoyama T, Kamikado T, Yokoyama S, Mashiko S (2004) *J Chem Phys* 121:11993
135. Dmitriev A, Seitsonen AP, Spillmann H, Lin N, Strunskus T, Wöll C, Barth JV, Kern K (2006) *ChemPhysChem* 7:2197
136. Klappenberger F, Cañas-Ventura ME, Clair S, Pons S, Schlickum U, Kern K, Brune H, Qiu Z-R, Ruben M, Strunskus T, Wöll C, Fasel R, Comisso A, Vita AD, Barth JV (2007) *ChemPhysChem* 8:1782
137. Tomba G, Lingenfelder M, Costantini G, Kern K, Klappenberger F, Barth JV, Colombi Ciacchi L, De Vita A (2007) *J Phys Chem A* 111:12740
138. Auwärter W, Klappenberger F, Weber-Bargioni A, Schiffrin A, Strunskus T, Wöll C, Pennec Y, Schiffrin A, Riemann A, Barth JV (2007) *J Am Chem Soc* 129:11279
139. Romaner L, Heimel G, Brédas J-L, Gerlach A, Schreiber F, Johnson RL, Zegenhagen J, Duhm S, Koch N, Zojer E (2007) *Phys Rev Lett* 99:256801

140. Weber-Bargioni A, Auwärter W, Klappenberger F, Reichert J, Lefrançois S, Strunskus T, Wöll C, Schiffrin A, Pennec Y, Barth JV (2008) *ChemPhysChem* 9:89
141. Barth JV (2000) *Surf Sci Rep* 40:75
142. Brune H (1998) *Surf Sci Rep* 31:121
143. Barth JV (2006) In: Grütter P, Hofer W, Rosei F (eds) *Properties of single molecules on crystal surfaces*. World Scientific, Singapore
144. Nielsen LP, Besenbacher F, Stensgaard I, Lægsgaard E, Engdahl C, Stoltze P, Jacobsen KW, Nørskov JK (1993) *Phys Rev Lett* 71:754
145. Chambliss DD, Johnson KE (1994) *Phys Rev B* 50:5012
146. Barth JV, Behm RJ, Ertl G (1995) *Surf Sci* 341:62
147. Fischer B, Barth JV, Fricke A, Nedelmann L, Kern K (1997) *Surf Sci* 389:366
148. Besenbacher F, Chorkendorff I, Clausen BS, Hammer B, Molenbroek AM, Nørskov JK, Stensgaard I (1998) *Science* 279:1913
149. Ruben M (2005) *Angew Chem Int Ed* 44:1594
150. Ruben M, Lehn J-M, Müller P (2006) *Chem Soc Rev* 35:1056
151. Safarowsky C, Rang A, Schalley CA, Wandelt K, Broekmann P (2005) *Electrochim Acta* 50:4257
152. Gong JR, Wan LJ, Yuan QH, Bai CL, Jude H, Stang PJ (2005) *Proc Natl Acad Sci USA* 102:971
153. Nagy G, Mayer D, Wandlowski T (2002) *Phys Chem Commun* 5:112
154. Tao NJ (2006) *Nat Nanotechnol* 1:173
155. Wang D, Wan L-J (2007) *J Phys Chem C* 111:16109
156. Auwärter W, Weber-Bargioni A, Brink S, Riemann A, Schiffrin A, Ruben M, Barth JV (2007) *ChemPhysChem* 8:250
157. Shubina TE, Marbach H, Flechtner K, Kretschmann A, Jux N, Buchner F, Steinrück H-P, Clark T, Gottfried JM (2007) *J Am Chem Soc* 129:9476
158. Weber-Bargioni A, Reichert J, Seitsonen AP, Auwärter W, Schiffrin A, Barth JV (2008) *J Phys Chem C* 112:3453
159. Lu X, Hipps KW, Wang XD, Mazur U (1996) *J Am Chem Soc* 118:7190
160. Drain CM (2002) *Proc Natl Acad Sci USA* 99:5178
161. Milic TN, Chi N, Yablon DG, Flynn GW, Batteas JD, Drain CM (2002) *Angew Chem Int Ed* 41:2117
162. Hipps KW, Scudiero L, Barlow DE, Cooke MP (2002) *J Am Chem Soc* 124:2126
163. Bonifazi D, Spillmann H, Kiebele A, Wild Md, Seiler P, Cheng F, Güntherodt H-J, Jung T, Diederich F (2004) *Angew Chem Int Ed* 43:4759
164. Suto K, Yoshimoto S, Itaya K (2006) *Langmuir* 22:10766
165. Leung K, Rempe SB, Schultz PA, Sproviero EM, Batista VS, Chandross ME, Medforth CJ (2006) *J Am Chem Soc* 128:3659
166. Vaughan OPH, Williams FJ, Bampos N, Lambert RM (2006) *Angew Chem Int Ed* 45:3779
167. Auwärter W, Weber-Bargioni A, Schiffrin A, Riemann A, Gröning O, Fasel R, Barth JV (2006) *J Chem Phys* 124:194708
168. Auwärter W, Schiffrin A, Riemann A, Weber-Bargioni A, Pennec Y, Barth JV (2008) *Int J Nanotechnol* 5:1171
169. Lukasczyk T, Flechtner K, Merte LR, Jux N, Maier F, Gottfried JM, Steinrück H-P (2007) *J Phys Chem C* 111:3090
170. Lensen MC, Elemans JAAW, van Dingenen SJT, Gerritsen JW, Speller S, Rowan AE, Nolte RJM (2007) *Chem Eur J* 13:7948
171. Flechtner K, Kretschmann A, Bradshaw LR, Walz M-M, Steinrück H-P, Gottfried JM (2007) *J Phys Chem C* 111:5821

172. Yoshimoto S, Itaya K (2007) *J Porph Phthaloc* 11:313
173. Grillo SE, Tang H, Coudret C, Gauthier S (2002) *Chem Phys Lett* 355:289
174. Gersen H, Schaub R, Xu W, Stensgaard I, Laegsgaard E, Linderoth TR, Besenbacher F, Nazeeruddin MK, Grätzel M (2006) *Appl Phys Lett* 89:264102
175. Xu W, Dong M, Vázquez-Campos S, Gersen H, Lægsgaard E, Stensgaard I, Crego-Calama M, Reinhoudt DN, Linderoth TR, Besenbacher F (2007) *J Am Chem Soc* 129:10625
176. Tanaka H, Kawai T (1997) *J Vac Sci Technol B* 15:602
177. Yamada T, Suzuki H, Hidenori S, Mashiko S (2004) *J Natl Inst Inf Commun Technol* 51:111
178. Suzuki H, Yamada T, Kamikado T, Okuno Y, Mashiko S (2005) *J Phys Chem B* 109:13296
179. Okabayashi Y, Kanai K, Ouchi Y, Seki K (2006) *Rev Sci Instrum* 77:033905
180. Rader HJ, Rouhanipour A, Talarico AM, Palermo V, Samori P, Müllen K (2006) *Nat Mater* 5:276
181. Swarbrick JC, Ben Taylor J, O'Shea JN (2006) *Appl Surf Sci* 252:5622
182. Payer D, Rauschenbach S, Malinowski N, Konuma M, Virojanadara C, Starke U, Dietrich-Buchecker C, Collin J-P, Sauvage J-P, Lin N, Kern K (2007) *J Am Chem Soc* 129:15662
183. Guo S, Kandel SA (2008) *J Chem Phys* 128:014702
184. Shoji O, Tanaka H, Kawai T, Kobuke Y (2005) *J Am Chem Soc* 127:8598
185. Repp J, Meyer G, Paavilainen S, Olsson FE, Persson M (2006) *Science* 312:1196
186. Weber-Bargioni A (2007) PhD thesis, UBC Vancouver
187. Breitruck A, Hoster HE, Meier C, Ziener U, Behm RJ (2007) *Surf Sci* 601:4200
188. Lin N, Langner A, Tait SL, Rajadurai C, Ruben M, Kern K (2007) *Chem Commun*, p 4860
189. Matena M, Riehm T, Stöhr M, Jung TA, Gade LH (2008) *Angew Chem Int Ed* 47:2414
190. Frederick BG, Leibsle FM, Haq S, Richardson NV (2000) *Surf Rev Lett* 409:512
191. Perry CC, Haq S, Frederick BG, Richardson NV (1998) *Surf Sci* 409:512
192. Chen Q, Perry CC, Frederick BG, Murray PW, Haq S, Richardson NV (2000) *Surf Sci* 446:63
193. Giessen M (2001) *Prog Surf Sci* 68:1
194. Pascual JI, Barth JV, Ceballos G, Trimarchi G, De Vita A, Kern K, Rust H-P (2004) *J Chem Phys* 120:11367
195. Lin N, Payer D, Dmitriev A, Strunskus T, Wöll C, Barth JV, Kern K (2005) *Angew Chem Int Ed* 44:1488
196. Payer D, Comisso A, Dmitriev A, Strunskus T, Lin N, Wöll C, DeVita A, Barth JV, Kern K (2007) *Chem Eur J* 13:3900
197. Lingenfelder M, Spillmann H, Dmitriev A, Stepanow S, Lin N, Barth JV, Kern K (2004) *Chem Eur J* 10:1913
198. Stepanow S, Lin N, Vidal F, Landa A, Ruben M, Barth JV, Kern K (2005) *Nano Lett* 5:901
199. Vidal F, Delvigne E, Stepanow S, Lin N, Barth JV, Kern K (2005) *J Am Chem Soc* 127:10101
200. Meot-Ner M (2005) *Chem Rev* 105:213
201. Dmitriev A, Spillmann H, Lingenfelder M, Lin N, Barth JV, Kern K (2004) *Langmuir* 41:4799
202. Tait SL, Wang Y, Lin N, Costantini G, Baraldi A, Esch F, Petaccia L, Lizzit S, Kern K (2008) *J Am Chem Soc* 130:2108

203. Classen T, Fratesi G, Costantini G, Fabris S, Stadler FL, Kim C, Gironcoli SD, Baroni S, Kern K (2005) *Angew Chem Int Ed* 44:6142
204. Tait SL, Langner A, Lin N, Stepanow S, Rajadurai C, Ruben M, Kern K (2007) *J Phys Chem C* 111:10982
205. Pennec Y, Auwärter W, Schiffrin A, Weber-Bargione A, Barth JV (2007) *Nat Nanotechnol* 2:99
206. Wegner D, Yamachika R, Wang Y, Brar VW, Bartlett BM, Long JR, Crommie MF (2008) *Nano Lett* 8:131
207. Stepanow S, Lin N, Barth JV, Kern K (2006) *J Phys Chem B* 110:23472
208. Zhang Y-F, Zhu N, Komeda T (2007) *J Phys Chem C* 111:16946
209. Lin N, Stepanow S, Vidal F, Kern K, Alam MS, Strömsdörfer S, Dremov V, Müller P, Landa A, Ruben M (2006) *Dalton Trans*, p 2794
210. Lin N, Stepanow S, Vidal F, Barth JV, Kern K (2005) *Chem Commun*, p 1681
211. Langner A, Tait SL, Lin N, Rajadurai C, Ruben M, Kern K (2007) *Proc Natl Acad Sci USA* 104:17927
212. Fehllhammer WP, Fritz M (1993) *Chem Rev* 93:1243
213. Przychodzen P, Korzeniak T, Podgajny R, Sieklucka B (2006) *Coord Chem Rev* 250:2234
214. Decker R (2008) PhD thesis, EPF Lausanne
215. Hooks DE, Fritz T, Ward MD (2001) *Adv Mater* 13:227
216. Clair S, Pons S, Seitsonen AP, Brune H, Kern K, Barth JV (2004) *J Phys Chem B* 108:19392
217. Barth JV, Brune H, Ertl G, Behm RJ (1990) *Phys Rev B* 42:9307
218. Mendez J, Caillard R, Otero G, Nicoara N, Martin-Gago J (2006) *Adv Mater* 18:2048
219. Grant AG, Jones TE, Baddeley CJ (2007) *J Phys Chem C* 111:10534
220. Zhang Y-F, Zhu N, Komeda T (2008) *Surf Sci* 602:614
221. Stepanow S, Lin N, Barth JV, Kern K (2006) *Chem Commun*, p 2153
222. Seitsonen AP, Lingensfelder M, Spillmann H, Dmitriev A, Stepanow S, Lin N, Kern K, Barth JV (2006) *J Am Chem Soc* 126:5634
223. Zotti LA, Teobaldi G, Hofer WA, Auwärter W, Weber-Bargioni A, Barth JV (2007) *Surf Sci* 601:2409
224. Peng G, Elp Jv, Jang H, Que L, Armstrong WH, Cramer SP (1995) *J Am Chem Soc* 117:2515
225. Gao L, Ji W, Hu YB, Cheng ZH, Deng ZT, Liu Q, Jiang N, Lin X, Guo W, Du SX, Hofer WA, Xie XC, Gao H-J (2007) *Phys Rev Lett* 99:106402
226. Dubois LH, Nuzzo RG (1992) *Annu Rev Phys Chem* 43:437
227. Ulman A (1996) *Chem Rev* 96:1533
228. Yang HC, Aoki K, Hong H-G, Sackett DD, Arendt MF, Yau S-L, Bell CM, Mallouk TE (1993) *J Am Chem Soc* 115:11855
229. Hatzor A, Moav T, Cohen H, Matlis S, Libman J, Vaskevich A, Shanzer A, Rubinstein I (1998) *J Am Chem Soc* 120:13469
230. Haga M-A, Kobayashi K, Terada K (2007) *Coord Chem Rev* 251:2688
231. Uosaki K, Kondo T, Zhang X-Q, Yanagida M (1997) *J Am Chem Soc* 119:8367
232. Lin C, Kagan CR (2003) *J Am Chem Soc* 125:336
233. Ashkenazy G, Cahen D, Cohen R, Shanzer A, Vilan A (2002) *Acc Chem Res* 35:121
234. Menozzi E, Pinalli R, Speets EA, Ravoo BJ, Dalcanale E, Reinhoudt DN (2004) *Chem Eur J* 10:2199
235. Biemmi E, Scherb C, Bein T (2007) *J Am Chem Soc* 127:8054
236. Shekhah O, Wang H, Kowarik S, Schreiber F, Paulus M, Tolan M, Sternemann C, Evers F, Zacher D, Fischer RA, Wöll C (2007) *J Am Chem Soc* 129:15118

237. Crespo-Biel O, Ravoo BJ, Reinhoudt DN, Huuskens J (2006) *J Mater Chem* 16:3997
238. Pirondini L, Stendardo AG, Geremia S, Campagnolo M, Samori P, Rabe JP, Fokkens R, Dalcanale E (2003) *Angew Chem Int Ed* 42:1384
239. Surin M, Samori P, Jouaiti A, Kyritsakan N, Housseini MW (2007) *Angew Chem Int Ed* 46:245
240. Figgemeier E, Merz L, Hermann BA, Zimmermann YC, Housecroft CE, Güntherodt H-J, Constable EC (2003) *J Phys Chem B* 107:1157
241. Díaz DJ, Storrier GD, Bernhard S, Takada K, Abruña HD (1999) *Langmuir* 15:7351
242. Díaz DJ, Bernhard S, Storrier GD, Abruña HD (2001) *J Phys Chem B* 105:8746
243. Räisänen MT, Mögele F, Feodorow S, Rieger B, Ziener U, Leskelä M, Repo T (2007) *Eur J Inorg Chem*, p 4028
244. Newkome GR, Wang P, Moorefield CN, Cho TJ, Mohapatra PP, Li S, Hwang S-H, Lukoyanova O, Echegoyen L, Palagallo JA, Iancu V, Hla S-W (2006) *Science* 312:1782
245. Jeong KS, Kim SY, Shin U-S, Kogej M, Hai NTM, Broekmann P, Jeong N, Kirchner B, Reiher M, Schalley CA (2005) *J Am Chem Soc* 127:17672
246. Yuan Q-H, Wan L-J, Jude H, Stang PJ (2005) *J Am Chem Soc* 127:16279
247. Li S-S, Yan H-J, Wan L-J, Yang H-B, Northrop BH, Stang PJ (2007) *J Am Chem Soc* 129:9268
248. Yuan Q-H, Wan L-J (2006) *Chem Eur J* 12:2808
249. Ziener U, Lehn J-M, Mourran A, Möller M (2002) *Chem Eur J* 8:951
250. Weeks L, Thompson LK, Shapter JG, Pope KJ, Xu Z (2003) *J Microsc* 212:102
251. Milway VA, Abedin SMT, Niel V, Kelly TL, Dawe LN, Dey SK, Thompson DW, Miller DO, Alam MS, Müller P, Thompson LK (2006) *Dalton Trans*, p 2835
252. Wang Z, Deng Q, Luan Y, Wu X, Wan L, Wang C, Lee GU, Yin S, Yang J, Bai C (2003) *J Phys Chem B* 107:13384
253. Borrás-Almenar JJ, Coronado E, Müller A, Pope MT (2004) *Polyoxometalate molecular science*. Kluwer, Dordrecht
254. Pope MT, Müller A (2001) *Polyoxometalate chemistry: from topology via self-assembly to applications*. Kluwer, Dordrecht
255. Mal SS, Kortz U (2005) *Angew Chem Int Ed* 44:3777
256. Alam MS, Dremov V, Müller P, Postnikov A, Mal SB, Hussain F, Korz U (2006) *Inorg Chem* 45:2866
257. Tominaga M, Suzuki K, Kawano M, Kusukawa T, Ozeki T, Sakamoto S, Yamaguchi K, Fujita M (2004) *Angew Chem Int Ed* 43:5621
258. Busi M, Laurenti M, Condorelli GG, Motta A, Favazza M, Fragalà IL, Montalti M, Prodi L, Dalcanale E (2007) *Chem Eur J* 13:6891
259. Liu Y, Zhao Y-L, Zhang H-Y, Song H-B (2003) *Angew Chem Int Ed* 42:3260
260. Mateo-Marti E, Welte L, Ama-Ochoa P, Sanz Miguel PJ, Gómez-Herrero J, Martín-Gago JA, Zamora F (2008) *Chem Commun*, p 945
261. Novokmet S, Alam MS, Dremov V, Heinemann FW, Müller P, Alsfasser R (2005) *Angew Chem Int Ed* 44:803
262. Olea D, González-Prieto R, Priego JL, Carmen Barral M, de Pablo PJ, Rosario Torres M, Gómez-Herrero J, Jiménez-Aparicio R, Zamora F (2007) *Chem Commun*, p 1591
263. Zhang HM, Zhao W, Xie Z-X, Long L-S, Mao B-W, Xu X, Zheng L-S (2007) *J Phys Chem C* 111:7570

Surfaces: Two-Dimensional Templates

Conrad Becker (✉) · Klaus Wandelt (✉)

Institut für Physikalische und Theoretische Chemie der Universität Bonn,
Wegelerstr. 12, 53115 Bonn, Germany
conrad.becker@uni-bonn.de, k.wandelt@uni-bonn.de

1	Introduction	46
1.1	Templates, Self-Assembly, and -Organization	47
1.1.1	Self-Organization	49
1.1.2	Self-Assembly	49
1.1.3	Template-Assisted Assembly	50
1.1.4	Template-Controlled Assembly	51
1.2	Elements that Constitute a 2D Template	52
2	Strategies for Template Generation	55
2.1	Reconstructions of Clean Surfaces	55
2.2	Vicinal Surfaces	57
2.3	Adsorbate-Induced Reconstructions	58
2.3.1	Epitaxial Metal Films	59
2.3.2	Epitaxial Inorganic Films and Layers	61
2.3.3	Epitaxial Organic Layers	66
3	Metal Surfaces as Templates	66
3.1	Reconstructed Metal Surfaces	67
3.2	Vicinal Surfaces	68
3.3	Epitaxial Metal Films	71
3.4	Inorganic Layers and Films	72
4	Oxide Surfaces as Templates	74
4.1	Epitaxial Alumina Films	74
4.2	Titania	76
4.3	Epitaxial Iron Oxide Films	77
5	Beyond Simple Templates	78
6	Summary	80
	References	80

Abstract Producing nanoscale structures on solid surfaces in a controlled way is a technological challenge that has an important impact on a variety of fields such as microelectronics, magnetic storage technology, and heterogeneous catalysis. Currently most processes are based on a top-down approach, which relies on an active patterning of a surface by, for example, lithography or imprinting. As the desired structures become smaller these top-down processes will reach the physical limit of their resolution. A bottom-up approach, which is based on a template-controlled growth of nanostructures

on a prestructured substrate, can provide access to structural dimensions of only a few nanometers. The challenge for the growth of such nanostructures on surfaces is to identify and design suitable surfaces, which act as templates due to their intrinsic physical and chemical properties. These 2-dimensional (2D) templates can then be utilized to produce nanostructures of metals, semiconductors, or organic compounds.

Keywords Growth · Nanostructure · Template

Abbreviations

1D	One-dimensional
2D	Two-dimensional
3D	Three-dimensional
AFM	Atomic force microscopy
BDA	4,4'-Biphenyl-dicarboxylic acid
CoPc	Cobalt phthalocyanine
CVD	Chemical vapor deposition
LEED	Low-energy electron diffraction
LT	Low temperature
ML	Monolayer
NN	1-Nitro-naphthalene
PTCDA	3,4,9,10-Perylenetetracarboxylic-dianhydride
PVD	Physical vapor deposition
QD	Quantum dot
RT	Room temperature
SPA-LEED	Spot profile analysis LEED
SPM	Scanning probe microscopy
STM	Scanning tunneling microscopy
TDA	4,1',4',1''-Terphenyl-1,4''-dicarboxylic acid
TPA	1,4-Benzene-dicarboxylic acid
UHV	Ultrahigh vacuum
XRD	X-ray diffraction

1

Introduction

In ancient times the molds for the production of bells were referred to as “templates”. These templates imposed their structure on the material, which was to be processed. In the same way other templates are used today to shape a workpiece. Not only in the shaping of materials but also in the formatting of information, e.g. in the software industry, templates play an important role.

Recently the fabrication of nanomaterials has become increasingly important because nanomaterials exhibit physical and chemical properties different from their bulk counterparts as a consequence of having at least one spatial dimension in the nanometer range such as ultrathin films (“nanosheets”), “nanowires”, and clusters (“nanodots”). One of the challenges in this context

is the availability of suitable nanostructures that can be used as templates in nanomaterials production.

Template-based structure formation aims at reproducing or creating a desired functionality, e.g. the above-mentioned bell has a certain sound.

In general two alternative approaches can be employed to prepare nanoscale surface templates: The so-called top-down approach, which relies on the active manipulation (“machining”) of the surface morphology by physical (e.g. lithography) or chemical (e.g. imprinting) processes on a meso- or nanoscopic scale or on the direct manipulation of entities on the atomic or molecular scale using, for example, the STM for the assembly of the desired structure step by step. While these approaches can be successfully applied in many cases they are also subject to certain restrictions because of their limited resolution (lithography, for a comprehensive review see [1]) or slowness (sequential manipulation). An alternative route is the self-organization of a system, which is driven by its intrinsic physical and chemical properties, the so-called bottom-up approach. Especially in the nanometer range the latter approach promises to yield superior results since it is not limited by the spatial resolution of a specific fabrication process or the slowness of an active structuring method. A necessary prerequisite in order to exploit these advantages, however, will be a full control of the processes, which lead to the spontaneous formation of nanostructures on surfaces. In order to achieve this goal the energy landscape or energetic conditions of the pattern formation on solid surfaces have to be known. On the atomic scale it is this spontaneous template-controlled route to the formation of nanostructures on surfaces, which will be described and discussed in the following. Of course, the field is intimately connected to the availability of local probes, which allow exploring the structures on surfaces on an atomic scale. Since the advent of the scanning tunneling [2] and the scanning force microscope [3] nanoscience has consequently made an important leap forward, which results in an ever-growing number of structures of solid surface known with atomic precision.

1.1

Templates, Self-Assembly, and -Organization

Before studying template-controlled processes in more detail one must establish the relation between the terms “templating”, self-organization, and self-assembly, which are often used in this context. In a recent review Busch described the action of a “chemical template” as follows: “In a templated process, molecular entities, or their components, actively organize complementary entities, resulting in selected results that would be highly improbable in the absence of the templating interaction. A second feature of template processes is the common, but not essential, use of molecular/atomic entities as anchors that facilitate the selected result but which, post reaction, can be removed, leaving the highly improbable structure as a stable entity” [4].

The key point of this conjecture is that the template organizes entities (building blocks) geometrically in such a way that the desired product is obtained. This is a marked difference to self-assembly, which will be explained in more detail below.

If we focus on the aspect of producing highly unlikely structures the role of solid surfaces in template-controlled processes can be easily rationalized. Consider a certain number of particles in a box with a diathermic wall in a heat bath. At sufficiently high temperature and low concentration the particles will be in the gas phase and randomly distributed (Fig. 1a). Here a vast number of configurations is possible and will be generated by the thermal motion of the particles. If the temperature of the heat bath surrounding the box is lowered sufficiently the particle will adhere to the wall of the box (Fig. 1b) and will eventually be immobilized. This will select a small number of configurations out of the vast number of initial configurations and thus reduce the entropy of the system. In the sense of Busch's definition a highly unlikely structure has been created by the adsorption (anchoring) of the particles on the wall of the box. Lowering the temperature even further will result in the formation of 3D structures on the walls of the container (Fig. 1c). In this example already most of the concepts needed to understand a surface template are contained: the generation of a highly unlikely structure and the kinetic (thermal) control of this structure. Likewise the adsorption of molecules on a solid surface reduces the number of configurations of the particles as compared to the corresponding gas phase. The interactions between the surface and the adsorbed particles as well as between the adsorbed particles point the route to the smaller configuration space, thereby creating "negentropy" – a term well-known in information theory. This 2D template effect is, however, only the first stage in the fabrication of a surface template since it determines only the orientation of the molecule relative to the surface. The second prerequisite for the template-controlled growth of nanostructures, which in general is not yet provided in

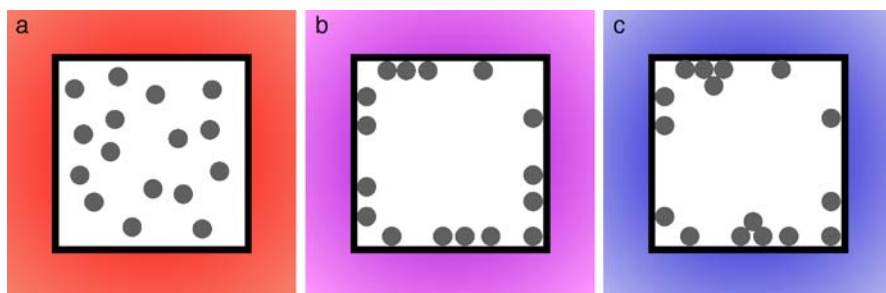


Fig. 1 Schematic presentation of particles in a hot (a), a cold (b), and a very cold (c) box. Lowering of the temperature will result in the formation of structures, which are confined to the wall

this approach, is the lateral distribution of the adsorbed particles. Here the atomic scale structure or more precisely “corrugation” of solid surfaces enters the scene.

In this context the role of self-assembly vs. -organization for the generation of a template has to be investigated. In order to do this we first have to explore the precise meaning of the two terms “self-assembly” and “self-organization”.

1.1.1

Self-Organization

A short comprehensive explanation of the concepts “self-organization” and “self-assembly” is given in [5]. Self-organization is a rather general concept, which applies not only to ordering phenomena in a geometrical or topological sense but also describes processes such as phase transformations, herd formation of animals, and the origin of life itself. It depends only on the intrinsic properties of a system such as interactions between the constituents of the system. Self-organization is a rather counterintuitive concept since it seems to contradict the 2nd law of thermodynamics, which predicts an increase of the entropy (disorder) of a system.

However, we must bear in mind that this applies to closed or isolated systems only since open systems can release entropy to their environment while reducing the entropy of the system itself. Therefore, self-organization is not restricted to the formation of equilibrium structures. The beauty of self-organization for the generation of surface templates is lent to the fact that “nature is doing the job”. The inherent physical and chemical interactions between all constituents of a self-organized system represent the information, which restricts the configuration space – thus, creating “negentropy”. The only challenge that the experimentalist faces is to conceive appropriate systems and to provide the right conditions, which will generate nanopatterns by self-organization. It has also the advantage that not only regular patterns may emerge from a self-organization process but also the formation of irregular patterns seems to be possible depending on the correct choice of the system. The latter is a big advantage over self-assembly, which is discussed below.

1.1.2

Self-Assembly

Self-assembly is a more limited phenomenon as compared to self-organization. Kuhn and Ulman [6] gave a rather elegant definition: “Self-assembly is a spontaneous process, guided by information content intrinsic to the *assembling units*, in which multiple levels of structural organization are built into a product.” In that sense it is similar to crystallization except that the complexity of the building blocks involved is greater in self-assembly and

length-scales beyond a single lattice constant can emerge in the product. The driving force is the minimization of the free energy of the system, e.g. the generation of an equilibrium structure. Since *intrinsic* forces play the decisive role for the ordering during adsorbate self-assembly these processes must be clearly distinguished from a template effect, which is imposed on the system by *extrinsic* interactions with the substrate.

As an example the formation of ordered molecular structures (molecular self-assembly) [7] should be mentioned. In these cases the ordering (assembly) occurs by the intrinsic properties of the adsorbates, which are, for example, weak intermolecular forces.

The formation of self-assembled monolayers (SAMs) on solid surfaces must be clearly distinguished from this case since a part of the spatial information required is provided by the surface. This case can be regarded as *directed self-assembly* of building blocks, which involves structure-directing additives, for example the solid surface. It is clearly distinct from *spontaneous self-assembly* and can rather be thought of being closely related to a template-assisted process. This may be rationalized by the pattern formation of a molecular layer on different surface orientations of the same material, which leads us to the concept of template-assisted assembly.

1.1.3

Template-Assisted Assembly

In contrast to self-assembly or self-organization, which rely on the intrinsic properties of a system, template-assisted assembly provides a way to externally control the formation of a structure. The template contains spatial information, which is explicitly imposed on the building blocks of a system. In a first step this can be a mild template effect, which only assists in the pattern formation. This effect is encountered, for example, in the structure formation of PTCDA on Ag(1 1 1) and Ag(1 1 0) [8]. In these cases the final structure of the overlayer is not only controlled by the mutual interaction of the PTCDA building blocks (self-assembly) but also assisted by the substrate. The different crystallographic orientation of the respective surfaces leads to the formation of either a herringbone pattern or a linear assembly on Ag(1 1 1) and Ag(1 1 0), respectively (Fig. 2). Similar results have been found for PTCDA on Cu(1 1 1) [9] and Cu(1 1 0) [10] as well as Au(1 1 1) and Au(100) [11].

It must, however, be realized that in these processes the template does not ultimately control the structure of the final assembly but that the mutual interactions of the entities deposited on the surface also play a decisive role. However, it guides us to the desired control of the growth on surfaces and may be useful for the production of templates as we will see later.

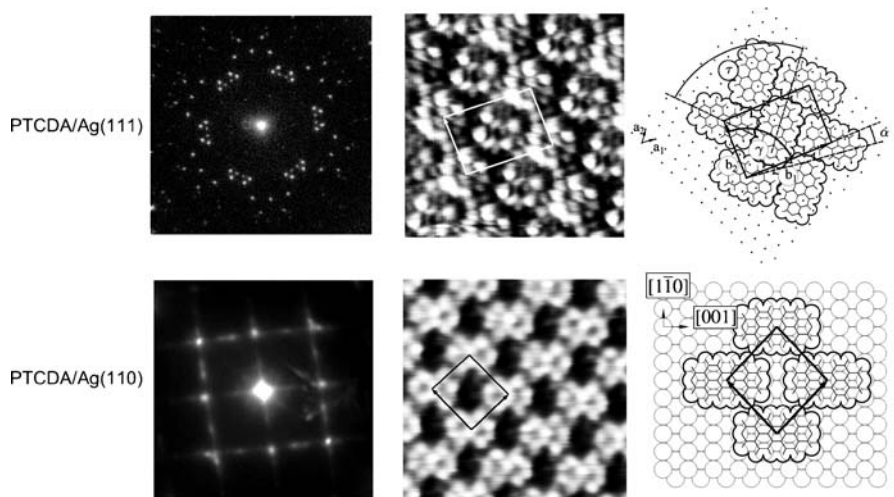


Fig. 2 LEED pattern, STM images, and schematic models of self-assembled PTCDA monolayers on Ag(111) (*top*) and Ag(110) (*bottom*). The layers show a different symmetry due to the different symmetry of the substrate. Scan sizes are $4.5 \times 4.5 \text{ nm}^2$ (*top*) and $4.4 \times 4.4 \text{ nm}^2$ (*bottom*) (from [8])

1.1.4

Template-Controlled Assembly

A key feature of template-controlled assembly is that the topology of the adsorbate is *entirely* determined by the template regardless of the actual nature of the entities that are to be arranged. In contrast to template-assisted assembly the mutual interactions of the deposited entities are in this case not important anymore or play only a minor role. Since, of course, the interaction of the template with the building blocks to be assembled is specific, a single template can still serve for the generation of different final structures (metals, semiconductors, organic layers). It is this property that is one of the big advantages of template-controlled assembly as opposed to template-assisted assembly or self-assembly and -organization.

From the above it is apparent that the distinction between self-assembly and self-organization is not always easy to make since the processes involved may be rather complex (for a review see [12]). However, the external control, which is exerted by a template and which may differ in relative strength, provides a clear distinction between template-controlled processes and self-ordering processes. A key factor on surfaces in this context will be the transition from adsorbate-adsorbate dominated interactions to substrate-adsorbate (template) dominated processes. This transition is displayed in Fig. 3. Apparently the transition is smooth so that template-assisted processes

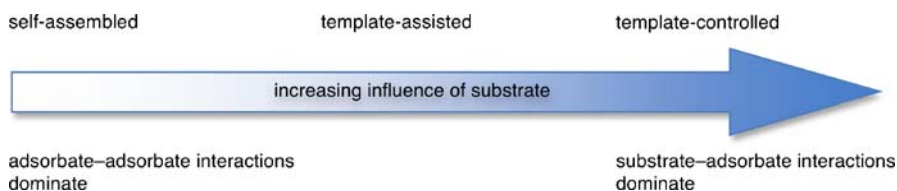


Fig. 3 Scheme showing the transition from self-assembly to template-control

are likely to occur rather frequently as exemplified by the case of so-called self-assembled monolayers (SAMs).

1.2

Elements that Constitute a 2D Template

Since for the classification of templates the topology is one of the key factors, surfaces can be referred to as 2-dimensional (2D) templates as they organize entities in two dimensions. However, solid surfaces are not perfectly flat but they exhibit a periodic modulation of specific surface properties such as electronic or geometric structure, and in some cases also chemical composition down to the atomic level. This suggests that the modulation of these properties may be used to control the spatial arrangement of entities on these surfaces in order to create desired but otherwise highly unlikely structures. This template route to growth on surfaces requires knowledge of the fundamental interactions on solid surfaces, which in the simplest case is the adsorption of a single atom or molecule on a specific surface site. This can be, for example, rationalized by looking at the adsorption of ethene on a single platinum atom in a matrix of copper atoms. At a temperature of 150 K an ethene molecule will adsorb only atop the platinum atom [13] and thus be restricted to such single platinum sites in a mixed copper platinum surface. Now only one further step is required in order to form a surface template – a defined lateral distribution of the platinum atoms in the copper matrix. This template indeed already exists in nature as the (1 1 1) surface of an ordered

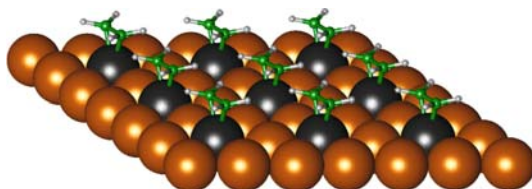


Fig. 4 DFT simulation of an ethene monolayer on $\text{Cu}_3\text{Pt}(111)$. Because of the stronger interaction of ethene with Pt compared to Cu the molecules are forced to Pt atop sites only

Cu_3Pt crystal, which exhibits a (2×2) ordering of single platinum atoms in the surface layer and ethene molecules will consequently adsorb atop the platinum atoms in an ordered (nanostructured) way [13] (Fig. 4).

From the above we can identify two key factors for template-controlled growth on surfaces: the presence of anchors (specific interaction sites) and the self-organized (e.g. ordered) distribution of these anchors on the surface. In order to illustrate this a LEGO® base plate may act as an example. The base plate shows, much like a solid surface, a regularly modulated interaction potential, which allows the bricks to take only certain positions and orientations (Fig. 5a). It does, however, not impose an ordered arrangement of the bricks. Thus, if we position at random 25 bricks on this base plate no ordered pattern will result. In that sense, even though the orientation of the bricks is fixed by the structure of the base plate in two dimensions, it does not lead to the formation of a controlled nanopattern. In other words: a mere periodic modulation of a specific surface property is not sufficient to make a template if it possesses the same unit cell size as the surface lattice. A true 2D template will, thus, require a modulation of a surface property, with a sufficiently larger unit cell compared to the crystallographic surface unit cell. In our example we can accomplish this by periodically blocking certain sites on the base plate by bricks without “knobs”. If we then again place 25 bricks on this structure a certain order of the overlayer is reached and the surface can be regarded as a template (Fig. 5b). However, a certain disorder is still present in the stripes thus created. If we then even go one step further by “functionalizing” the base plate in such a way that a periodic array of “adsorption sites” for the (2×2) -bricks is formed, a perfect model for a 2D template is created (Fig. 5c) as for instance realized by the (2×2) arrangement of the Pt atoms in the $\text{Cu}_3\text{Pt}(111)$ surface in Fig. 4. Moreover, the arrangement of the (2×2) -bricks in Fig. 5c itself can now act as a template.

In Fig. 6 the ordered 2×2 bricks are covered by larger entities, which by themselves would not be able to stick to the pre-structured surface due to their size. We will call this specific situation a 2nd generation template since it utilizes a structure, which was already generated in a template-controlled process.

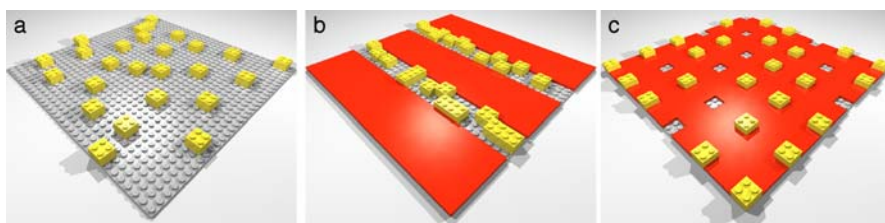


Fig. 5 a–c Lego® models illustrating the function of a 2D template. The models were created using MLCAD (<http://www.lm-software.com/mlcad/>) and rendered with POV-Ray (<http://www.povray.org/>)

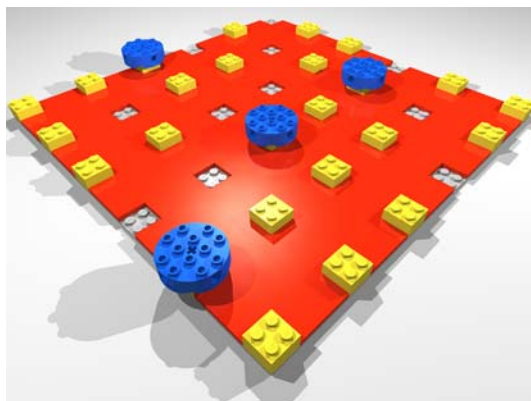


Fig. 6 Lego® model of a 2nd generation template. The model was created using MLCAD (<http://www.lm-software.com/mlcad/>) and rendered with POV-Ray (<http://www.povray.org/>)

In this simple model a crucial point is however missing, since the LEGO® bricks have no mutual interaction, which may influence their distribution on the base plate. Such mutual interactions are, however, common for adsorbed entities on surfaces and can influence their special arrangement as has been shown, for example, in the case of PTCDA on the Ag surfaces in Fig. 2. To avoid that the lateral interaction of the deposited entities plays the decisive role for the structure formation in a template-controlled process and in order to ensure that the growth is solely controlled by the template the active sites of the template have to be sufficiently far apart from each other or provide a much stronger interaction than the intermolecular interaction. In general this condition requires the active sites to be separated by at least a few atomic distances (≥ 1 nm).

From the above we could thus derive two conditions, which must be fulfilled by a surface in order to act as a 2D template:

- A site-specific interaction has to be present, which anchors the entities deposited onto the surface to this site.
- The entities must be able to reach these anchoring sites by diffusion, which may require a certain thermal activation.

Concerning the interactions that ultimately govern the action of a 2D template the classification is not facile. Since we may be dealing with surfaces of metals, semiconductors, insulators, or even organic materials a great variety of interaction mechanisms are found such as metallic, covalent, ionic, or van der Waals bonding. This is even complicated further by the fact that the entities, which are deposited onto the surface, may be either inorganic or organic. Ultimately this leads to a vast variety of interaction mechanisms, which can be used for template-controlled growth. However, this can also be

regarded as an advantage because it provides a practically unlimited number of conceivable ways for the generation of a template.

Finally, we should address the question of the influence of substrate temperature – thus kinetics – on the template-controlled growth on surfaces. It is quite obvious from the example of the particles in a box (Fig. 1) that temperature strongly influences the structures formed. On the one hand it has to be low enough to allow for the adsorption of the building blocks on the surface (Fig. 1b), on the other hand it has to be high enough to provide a sufficient mobility of the entities on the surface in order to avoid a mere hit-and-stick (random) adsorption (Fig. 1c). In that sense the structures formed on surfaces by a template-controlled process will be subject to strong kinetic effects and temperature control will be an important factor (see Sects. 3 and 4).

2

Strategies for Template Generation

As already mentioned in the introduction the top-down and bottom-up approaches will be suitable for the generation of surface templates and are successfully applied. Here we will focus on the generation of 2D templates by self-organization. This approach relies on the physical and chemical properties of the system and has therefore the advantage that nature does the job of pattern formation. The only task is to find suitable systems, which self-organize in a desired manner to a specific predefined pattern. This is of course a rather demanding task and will constitute the major obstacle for the fabrication of 2D templates via this route. We therefore will continue by describing the process of pattern formation by self-organization on solid surfaces in greater detail. We will restrict ourselves to the surfaces of metals and thin films on metal substrates since in particular pattern formation on semiconductors is a large field by itself, which would surely be beyond the frame of this communication. A comprehensive theoretical overview on the forces that govern pattern formation on solid surfaces can be found in [14].

2.1

Reconstructions of Clean Surfaces

Often the surface atoms of clean metal surfaces are not found exactly at the same in-plane positions as in equivalent bulk crystallographic planes. This phenomenon is in general due to the fact that the coordination number of the surface atoms is lower than in the bulk, which eventually leads to a rearrangement of the surface atoms to compensate for the missing bonds. The system will thus seek to minimize the surface energy [15], which leads to a rearrangement of the surface atoms. If the displacements are only vertical, leaving the symmetry of the surface unchanged from that of the equivalent

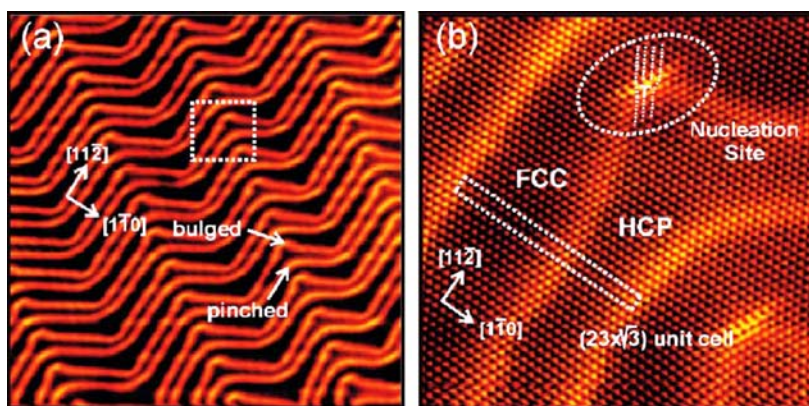


Fig. 7 STM images of the Au(111)-($\sqrt{3} \times 22$) reconstruction (from [22, 23])

crystal planes of the bulk, the process is called *relaxation*. However, if the displacements are parallel to the surface unit cell, it may differ in size and, sometimes, symmetry from the equivalent bulk crystallographic plane. In this case a *reconstruction* is present. One of the best-known reconstructions is that of the Au(111) surface. Its ($\sqrt{3} \times 22$) reconstruction has been characterized by a variety of methods such as LEED [16], He atom diffraction [17], STM [18, 19], and XRD [20, 21]. On this particular surface the number of surface atoms even exceeds the number of atoms in a {111} plane of the bulk by 4%, which leads to an increased electron density in the surface plane. The STM and diffraction measurements indicate that regions with a normal fcc-like stacking and hcp-like stacking alternate leading to the formation of a characteristic “herringbone” or “chevron” pattern on the surface, which is displayed in Fig. 7.

Recent DFT calculations indicated that the Au(111)-($\sqrt{3} \times 22$) reconstruction is exothermic by 0.43 eV per surface unit cell [24] and thus favorable for the relaxation of the surface stress found in the unreconstructed surface. Moreover, the different regions (fcc and hcp) have been found to differ significantly in the density of states [24, 25], which suggests that this long-range modulation of the electronic properties of the surface may render the reconstruction suitable for use as a template. The high thermal stability of this reconstructed surface is also in favor of its use as a template since it has been found that the reconstruction is stable up to temperatures of 865 K [21].

A reconstruction, which is similar in size to the above-mentioned herringbone reconstruction of the Au(111) surface is the Pt(100)-(5×20) (or Pt(100)-hex) and Pt(100)-hex-R0.7° reconstruction (Fig. 8) [26–31]. Similar reconstructions are present on the Ir(100) [26, 28, 32] and Au(100) surface [28, 33]. These systems share the peculiarity that the topmost layer is quasi-hexagonally reconstructed, which leads to an atom density that is about 20% higher than in the underlying {100} planes and about 8% higher than

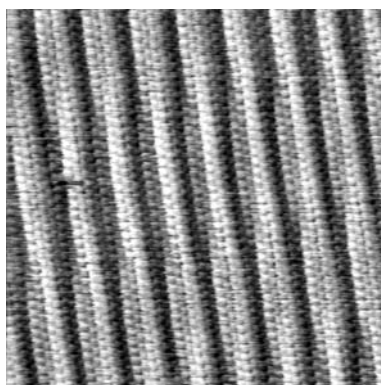


Fig. 8 STM image of the Pt(100)-hex reconstruction (from [30])

in the $\{111\}$ surface plane of the same metal [34]. A theoretical investigation of various fcc transition metal (100) surfaces indicated that for late transition metals such as Au, Ir, and Pt the tensile excess stress of the unreconstructed surface is the driving force for the reconstruction [35].

A common feature of the reconstructed (100) surfaces is that the reconstruction leads to a streaky appearance (Fig. 8), which suggests that they may constitute a template for the growth of one-dimensional nanostructures (“nanowires”).

Reconstructed clean metal surfaces may thus be interesting templates. However, their given structure does not provide the experimentalist with a control on the nature and physical dimensions of the nanostructure. This implies that these surfaces can be suitable candidates for the investigation of the basic properties of templates on an atomic scale but are less interesting in terms of applications. To overcome this limitation systems are needed for which the pattern formation by self-organization can to some extent be controlled by the experimentalist. This leads us to two promising systems: stepped metal surfaces and thin films on metal surfaces.

2.2

Vicinal Surfaces

Metal surfaces, which are generated by cutting a crystal parallel to a plane slightly off a low index plane, can also be used as templates. By such an approach vicinal surfaces are generated, which consist of terraces of a particular low index plane of variable width, depending on the angle of miscut, separated by monatomic steps. By doing so it is not evident that the resulting surface is thermodynamically stable. Consequently, vicinal surfaces tend to facet in order to minimize their energy. The challenge is thus to find vicinal surfaces, which are stable and provide step sites for the nu-

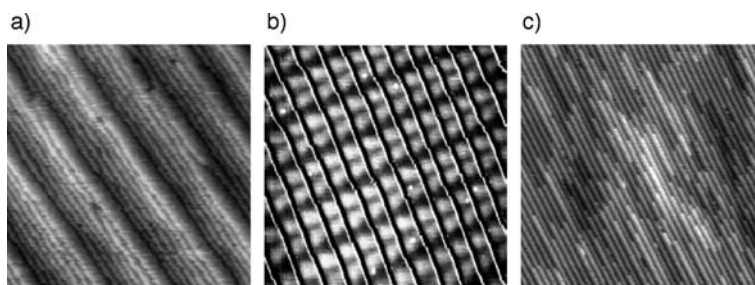


Fig. 9 STM images of different Au vicinal surfaces: **a** Au(4 3 3), **b** Au(7 8 8), and **c** Au(3 3 2) (from [36])

cleation of, for example, metal islands. Again the surfaces of Au play an important role in this domain. An overview of the preparation and stability of faceted vicinal Au surfaces can be found in [37]. In particular the Au(4 5 5) [38], Au(5 7 7), Au(4 3 3) (Fig. 9a), and Au(11 9 9) [39] surfaces (Fig. 9a) are subject to faceting. Whereas the former two show a hill and valley structure with a relatively long period above 100 nm the latter ones show faceting into Au(1 1 1) and Au(7 5 5) terraces with 7 nm and 11 nm periodicity, respectively. While these surfaces are faceted in their equilibrium state in order to release the stress induced by the miscut, other vicinal Au surfaces are not subject to faceting. Among these surfaces two different types can be distinguished: (a) stable vicinal surfaces, whose terraces are not reconstructed (Au(3 3 2) (Fig. 9c), and Au(7 5 5)), and (b) whose terraces are reconstructed (Au(7 8 8) (Fig. 9b) and Au(11 12 12)). The latter ones are characterized by the presence of remnants of the dicommensuration lines of the herringbone reconstruction as seen in Fig. 9b, which play – as on Au(1 1 1) – an important role for the growth of nanostructures as will be shown below [36, 40]. Even though Au surfaces seem to play an important role in the field of vicinal surfaces, which is certainly due to the high stability of these surfaces, other metals also show stable non-faceted vicinal surfaces.

2.3

Adsorbate-Induced Reconstructions

After having exploited the formation of regular nanoscale superstructures on clean metal surfaces we will now turn to systems in which the patterning is induced by the deposition of material on a clean metal surface. In many cases this will lead to a reconstruction of the system on the nanometer scale. This approach is particularly interesting because it provides – as opposed to the nanopatterns found on clean surfaces – a higher level of control of the nature and size of the formed nanostructure. We can distinguish three basic types of systems, which have to be considered: metal films, insulator films,

and layers of inorganic or organic adsorbates. These systems will be discussed below.

2.3.1 Epitaxial Metal Films

One of the most frequently observed phenomena in epitaxial growth is the formation of strain relief patterns. These are caused by the mismatch of the unit cell size of the substrate and the deposited film. In many cases the strain or stress, which is imposed on the thin film by the substrate lattice is relieved by reconstruction of the film. This reconstruction can but must not necessarily lead to a nanopatterned film. An interesting example is the growth of Ag on Pt(111) (see Fig. 10) [41]. It has been shown for this particular system that the first Ag layer grows pseudomorphically exhibiting an isotropic compressive strain of 4.3% whereas in higher layers this strain is relieved by the formation of a dislocation network [42–47]. In order to improve the long-

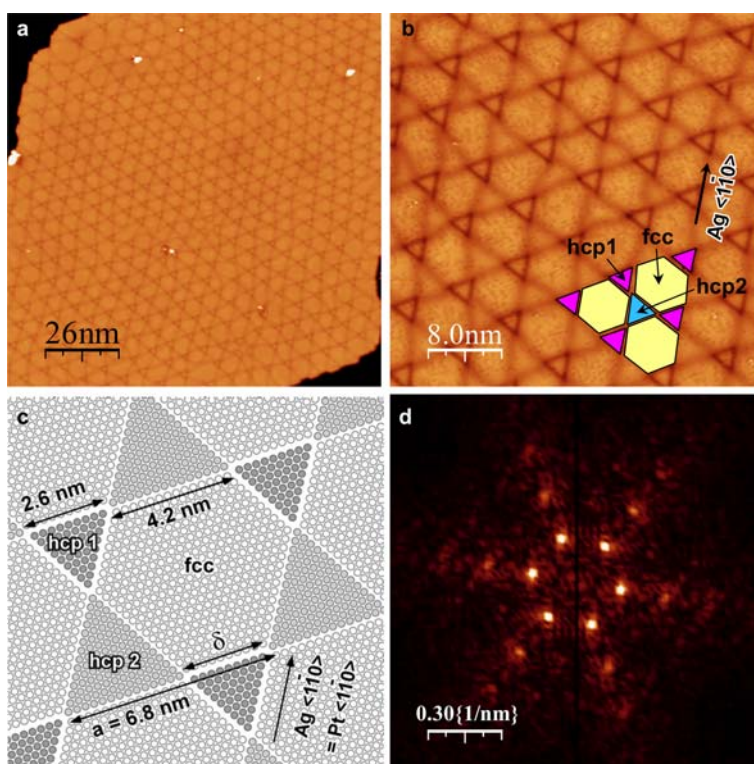


Fig. 10 STM images of a reconstructed 2 ML Ag film on Pt(111) (a, b) and the corresponding model (c) and FFT image (d) (from [41])

range order of the dislocation network a 2 ML thick Ag film on Pt(1 1 1) can be annealed at 530 °C. This film shows then a nicely ordered surface and, as in the case of the gold herringbone reconstruction, the pattern comprises areas of fcc and hcp stacking (Fig. 10) forming a hexagonal pattern with a lattice constant of 6.8 nm.

For Pd on Ni(1 1 1) a moiré pattern is found at a coverage of 2 ML [48], which is also present for Ag on Cu(1 1 1) in the monolayer regime at 150 K deposition temperature. In this case, however, a triangular pattern is found if the deposition is done at RT [49–51]. A similar case is present for a Au monolayer on Ni(1 1 1). At 170 K deposition temperature a rotated moiré pattern is found while annealing at 400 K or deposition at RT results in the formation of a triangular structure [52].

For different thicknesses of Cu on Ru(0001) [53] pronounced variations of the morphology have been observed. While the first monolayer is pseudomorphic, the second layer shows a unilaterally contracted “striped” phase, which resembles the herringbone reconstruction of the Au(1 1 1) surface. For 3 ML thickness a more complex triangular relaxation is found and finally for 4 ML coverage a fully relaxed quasi-hexagonal superstructure is formed. A similar evolution of the nanopatterns is found for Au, Ag, and their 2D alloys on Ru(0001) [54] as well as Ag on Re(0001) for which the 1st layer is pseudomorphic, the 2nd layer shows a uniaxial expansion, while for more layers a moiré pattern evolves [55]. Likewise for Ni on Ru(0001) [56] a large variation of the film morphology is found as a function of coverage.

Another type of reconstruction that is commonly found after film growth on Pt(1 1 1) is the so-called wagon-wheel pattern. This particular reconstruction is found for example with Cr/Pt(1 1 1) [57, 58] and Ce/Pt(1 1 1) [59, 60] and also for various oxide films (see below). Another example of temperature control of the pattern is found in the case of Ti on W(100) where a square nanomesh with a lattice constant of 4.5 nm can be produced by annealing at 1370 K [61].

The examples mentioned above nicely show how metal films can be used to produce nanopatterned surfaces. Compared to clean metal surfaces and vicinal surfaces a better control on the formation of the surface morphology is gained since a number of parameters such as the nature of the deposit, layer thickness, and temperature can be changed. Most importantly, of course, is the chemical nature of the substrate and the film material chosen, which controls important properties such as lattice parameter, surface and interface free energy, and possible alloy formation. Secondly the *deposition temperature* will change the kinetic energy (mobility) of the deposited atoms, which in turn results in a temperature-dependent morphology of the film. Such morphology changes may also be reached by post-annealing of the deposit to higher temperatures. Moreover, the thickness of the metal film plays a crucial role, since important morphology changes have been observed as a function of film thickness.

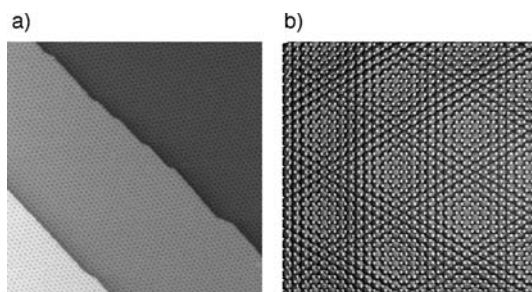


Fig. 11 **a** Large-scale STM image of a graphene layer on Ir(111) (Image size $125 \times 125 \text{ nm}^2$) and **b** ball model of the moiré pattern (from [62])

We will now refer to two systems, which rely on different physical effects or preparation procedures for the formation of nanopatterns. The first example is Ce/Ag(111) [63]. At temperatures of about 4 K the Ce atoms form a regular hexagonal lattice with a Ce–Ce atom distance of 3.2 nm on the Ag(111) surface, which is due to the long-range interaction of the Ce atoms mediated by the electron gas of the substrate. Because of the low temperature range this surface will definitely not present a growth template but the construction principle may be helpful in finding other surface structures with long-range order.

Far better candidates are carbon films, even though they are not metallic in a strict sense but they possess a high potential as growth templates. In the early 1990s Land et al. were able to show that the thermolysis of ethene on a Pt(111) surface leads to the formation of highly ordered hexagonal carbon monolayers, so-called graphene layers [64, 65]. These systems exhibit a superstructure in the nanometer range, which is due to the lattice mismatch between the Pt(111) substrate and the graphene layer (moiré pattern). Recently graphene layers have regained much attention and other systems were explored, for example graphene on Ir(111) [62] (Fig. 11) and Ru(0001) [66], which show a regular superstructure in the nanometer range.

Similar results may be expected if larger coronenes are deposited, which have a similar structure to graphene layers, e.g. hexaphenylbenzene, hexa-*peri*-hexabenzocoronene, and derivatives on Cu(111) [67].

2.3.2

Epitaxial Inorganic Films and Layers

Much like metal films also inorganic (insulating) layers show a variety of superstructures, which can be produced by self-organization. We will present here a number of examples, which illustrate the whole potential of using such layers for the generation of templates. In this context the experimentalist faces two major challenges. Firstly, the growth of an insulating layer is in gen-

eral more complex than the deposition of a metallic film. It involves at least a chemical reaction on the surface and may also require the parallel supply of more than one constituent of the layer. Secondly, high annealing temperatures are often required in order to establish the desired order, thus, calling for a substrate, which supports these temperatures. Furthermore, the layers should be accessible to a large number of experimental techniques and in particular STM. This implies that the layers must not be too thick in order to allow electron tunneling. Obviously these prerequisites will limit the number of available systems but nevertheless a number of promising candidates can be found in the literature.

Among the systems, which meet the requirements mentioned above, thin alumina films grown on a $\text{Ni}_3\text{Al}(1\ 1\ 1)$ surface play an important role. These films have been studied in depth during the past decade and show a variety of superstructures, which can be potentially used as templates. One of the big advantages of this system is that the films can be prepared by a simple high temperature oxidation of the $\text{Ni}_3\text{Al}(1\ 1\ 1)$ surface in vacuum [69]. Much like for other Ni–Al-based alloys such as $\text{NiAl}(1\ 1\ 0)$ this is due to a surface segregation of the Al at elevated temperature and the considerably higher heat of formation of Al_2O_3 compared to NiO [70, 71]. Early STM investigations showed the formation of a rather well-ordered superstructure at an oxidation temperature of 1000 K and the presence of a band gap indicating the formation of an alumina film [72]. This was later confirmed and the formation of a highly ordered alumina film was achieved after annealing the previously prepared film at 1050 K [73]. Additionally, a second well-ordered structure evolves on $\text{Ni}_3\text{Al}(1\ 1\ 1)$ after oxidation at 800 K. This structure has been ascribed to chemisorbed oxygen on Al on $\text{Ni}_3\text{Al}(1\ 1\ 1)$ and the resulting superstructure was interpreted as moiré pattern. The alumina film grown on $\text{Ni}_3\text{Al}(1\ 1\ 1)$ at 1000 K shows a few peculiarities, which are worth noting. Firstly, a strong dependence of the apparent topography on the applied STM bias voltage has been found, which resulted in a contrast reversal at bias voltages above 3.2 V [68]. The contrast reversal can be related to the electronic structure of the film showing a band gap, which extends up to a voltage of ~ 3.2 eV above E_F . At bias voltages around 2.4 V bright spots can be seen in the STM images of the film forming a highly ordered superstructure with a lattice constant of ~ 4.2 nm (Fig. 12), which has been referred to as “dot-structure”.

These bright spots are due to a reduced tunneling resistance at certain points of the films, which is caused by a localized electronic state in the band gap of the alumina film (Fig. 13). It has been shown that these spots are found at the coincidence points of the substrate and the film lattice, which are commensurate [74]. Recent AFM investigations also confirmed the presence of this superstructure and indicated that the alumina film consists of distorted hexagonal building blocks [75, 76]. High-resolution STM results, which are supported by DFT calculations, seem to suggest that at the coincidence points

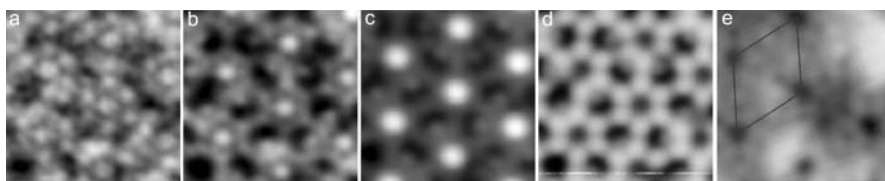


Fig. 12 Bias-dependent STM images of a thin alumina film on $\text{Ni}_3\text{Al}(1\ 1\ 1)$. The bias voltages are: **a** 0.5 V, **b** 1.5 V, **c** 2.0 V, **d** 3.2 V, and **e** 4.2 V. The contrast reversal above 3.2 V is clearly visible [68]

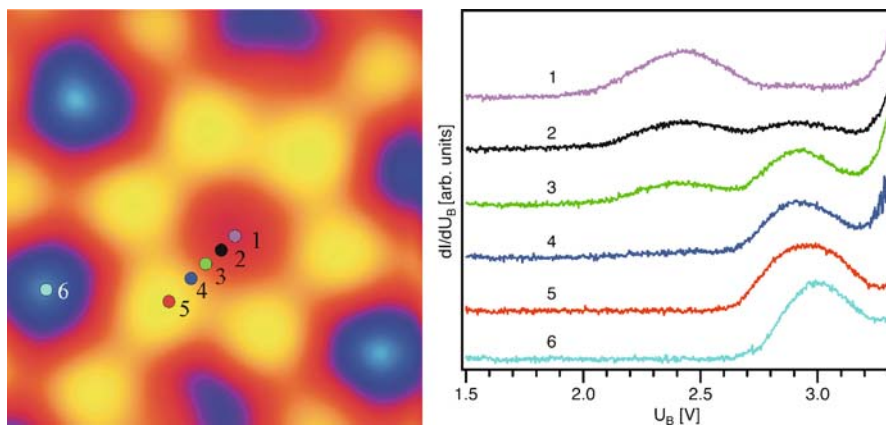


Fig. 13 STM of an alumina film on $\text{Ni}_3\text{Al}(1\ 1\ 1)$ (**a**) and **b** STS spectra taken at the points indicated in (**a**)

a hole in the film exists [77] but they are at variance with the AFM results, which do not show such holes so that the exact origin of the ordered array of bright spots on the alumina film on $\text{Ni}_3\text{Al}(1\ 1\ 1)$ is still under debate. However, the high structural quality of this film makes it an excellent candidate for template-controlled growth processes.

A similar approach as in the case of the alumina film on $\text{Ni}_3\text{Al}(1\ 1\ 1)$ can be used in other cases to produce well-ordered superstructures. In this context the Cu–O striped phase [78, 80] presents an interesting case. The adsorption of oxygen on the bare $\text{Cu}(1\ 1\ 0)$ surface above 450 K leads to a self-organization of the $\text{Cu}(1\ 1\ 0)-(2 \times 1)\text{O}$ reconstructed islands in a regular stripe pattern (Fig. 14a). The distances between the stripes is governed by a long-range repulsive interaction between the islands and the width of the stripes can be controlled by the oxygen coverage. This leads to the formation of a surface, which resembles a vicinal surface since flat terraces of metal are separated by a discontinuity. Much like in this example the nitrogen adsorption on the $\text{Cu}(100)$ surface leads to a regular lattice of nitrogen islands leaving only small stripes of bare Cu in-between [79, 81, 82] (Fig. 14b).

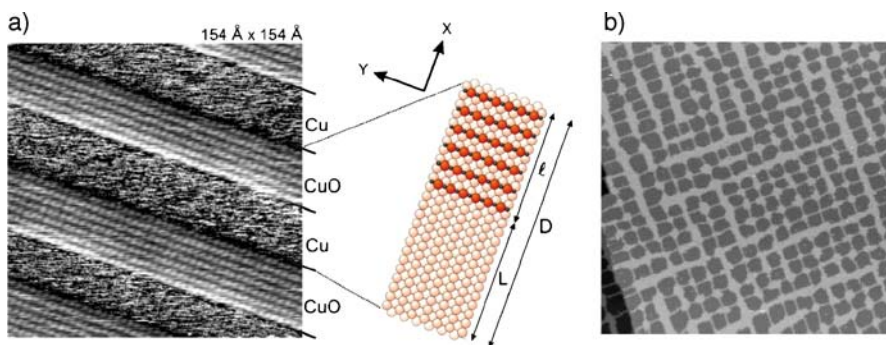


Fig. 14 STM images of nanopattern (**a**) generated by oxygen adsorption on Cu(110) (with corresponding structure model) [78] and **b** nitrogen adsorption on Cu(100) [79]

But also coadsorption of O and N on Cu(100) leads to a similar nanopattern [83]. Similar to the preceding cases the oxidation of Rh(111) leads to the formation of a Rh_2O_3 layer that shows a moiré pattern with a unit cell size of ~ 2.4 nm [84]. Finally, hydrogen adsorption on Ir(100) leads to the formation of a so-called (5×1) -H reconstruction, which consists of Ir nanowires, and may be exploited as a template [32].

While the preparation of the nanostructured films mentioned above relies on simple temperature-controlled adsorption and reaction mechanisms, a more sophisticated approach has to be applied for the systems described next.

The following systems will in general require an additional step in the preparation since none of the constituents of the final film are present in the substrate. Nicely ordered nanopatterns have been found for FeO on Pt(111) [85–88]. Again a moiré pattern with a unit cell size of ~ 2.6 nm evolves as a consequence of the lattice mismatch between Pt(111) and the FeO overlayer. Recent results, which include the theoretical investigation of a variety of possible FeO(111) layer structures, showed a contrast reversal in the STM images at certain bias voltages [89] much like the one found for alumina films on $\text{Ni}_3\text{Al}(111)$ and this observation was attributed to high symmetry positions of the Fe in the FeO(111) layer. The preparation of thicker Fe oxide layers leads to the formation of some Fe_3O_4 islands [90]. An even more complex structure evolves after oxidation of Fe films on Ru(0001) at elevated temperature [91]. For small film thickness – much as on Pt(111) – well-ordered FeO(111) films are found, which display a moiré pattern of 2.16 nm periodicity. If the thickness of the films is increased to four monolayers a new distorted-hexagonal superstructure evolves, which consists of ordered $\text{Fe}_3\text{O}_4(111)$ domains.

A rich set of different structures can also be obtained for ultra-thin TiO_x films on Pt(111), which are prepared by reactive evaporation of Ti in oxygen [92]. It has been shown that the structures that evolve depend on

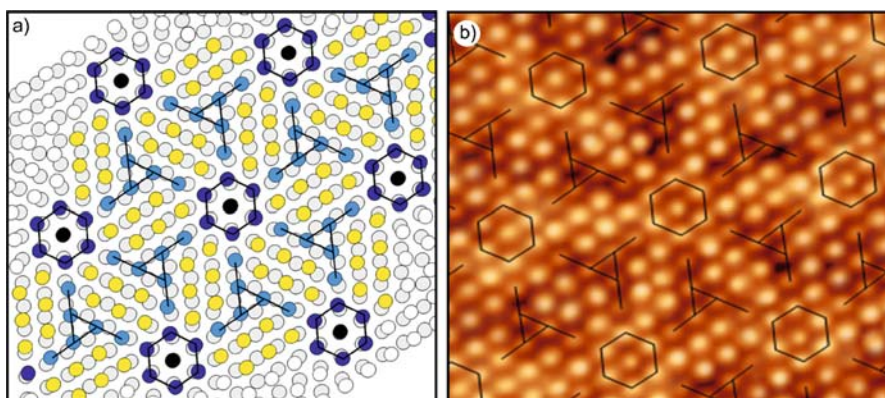


Fig. 15 **a** Schematic drawing of the moiré-like coincidence between the Pt(1 1 1) lattice and the w' -TiO_x superlattice and **b** corresponding atomically resolved STM image (from [93])

the growth conditions resulting in either a so-called *kagome-like* (k -TiO_x), *zigzag-like* (z -, z' -TiO_x), or *wagon-wheel-like* (w -, w' -TiO_x) appearance in STM [92, 93] (see Fig. 15). These phases are nonstoichiometric as opposed to the rectangular TiO₂ phase, which is obtained under different growth conditions [94]. The formation of a wagon-wheel phase is a commonly encountered phenomenon not only for TiO_x on Pt(1 1 1) but also for the following systems: TiO_x on Ru(0001) [95], VO_x on Pd(1 1 1) [96], VO_x on Rh(1 1 1) [97, 98], and iron oxide on Pt(1 1 1) [90, 99].

The richness of superstructures found especially for the oxide films mentioned above makes them interesting candidates for the engineering of nanopatterned surfaces. When compared to nanopatterns found on bare

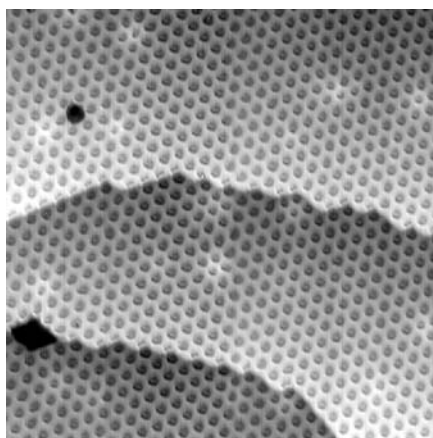


Fig. 16 STM image of the BN nanomesh on Rh(1 1 1) (from [100])

metal surfaces and metal films they provide a much higher degree of control on the patterning process, which is one of the key points in nanopatterning by self-organization.

Another promising approach for the generation of surface templates is the growth of boron nitride (BN) films. It was shown that on Ni(1 1 1) hexagonal BN films (h-BN) could be grown by thermal decomposition of $(\text{BN})_3\text{H}_6$ (borazine) at 1050 K [101, 102]. These films display a superstructure of 2.5 nm lattice constant, which has a very high structural quality being defect-free on a large scale. Later the formation of a so-called boron nitride nanomesh was found on Rh(1 1 1) [100] (Fig. 16). In this case the large lattice mismatch between the h-BN lattice and the Rh(1 1 1) substrate leads to a superstructure with a lattice constant of 3.2 nm. The structure is honeycomb-like and this suggests that the array of pits may be used as growth template. These results have triggered a number of follow-up studies and similar results were obtained for boron nitride on Ru(0001) [103], Pt(1 1 1) [101, 104, 105], Cu(1 1 1) [106], Pd(1 1 1) [101, 107], and Pd(1 1 0) [108] as well as Ni(1 1 0) [109] and Ni(100) [110].

2.3.3

Epitaxial Organic Layers

Apart from the nanopattern, which can be derived by the deposition of atoms and the formation of inorganic films, a virtually unlimited number of structures can be generated by the adsorption and self-organization of large organic molecules on surfaces. It is far beyond the scope of this communication to explore the whole universe of these structures but a few cases, which have a direct application as templates, shall be covered below (see for example Fig. 24). In the Introduction the formation of ordered layers of PTCDA on metal surfaces was mentioned as an example of the template-assisted assembly of molecular layers, however, these layers have not been used as templates so far.

3

Metal Surfaces as Templates

From the above it is evident that metal surfaces may be utilized as templates if certain conditions are met. If we consider reconstructed surfaces the reconstruction has to be stable during further deposition of material. The same holds for nanopatterns formed by deposition of thin films. Likewise vicinal surfaces may facet during the deposition of further material. This section will therefore be dedicated to the use of metal surfaces as growth templates. We use the classification of the systems that was established in Sect. 2 and begin with reconstructed metal surfaces.

3.1 Reconstructed Metal Surfaces

Among the reconstructed metal surfaces the Au(1 1 1)-($\sqrt{3} \times 22$) reconstruction (“herringbone” or “chevron” reconstruction) plays the most important role for template-controlled growth. Already in 1991 Voigtländer et al. were able to show that the elbows of this reconstruction phase are preferred nucleation sites for the growth of cobalt islands [36, 113–115] (Fig. 17a). This observation gave rise to a considerable number of follow-up investigations, which showed that also other metals are subject to a template-controlled growth on this particular surface. Among the systems, which show a template-controlled growth on the elbows of the “herringbone” reconstruction, we find Fe [116, 117], Ni [118, 119], Pd [120], Rh [121, 122], Mo [123], and to a lesser extent Mn [124]. Initially the template-controlled growth on the herringbone structure was believed to be due to a limited adatom mobility in the vicinity of the elbows, thus to be kinetically controlled. However, other metals such as Cu, Ag, Au [119], Ce [125], Al [126], and K [127] did not show a template-controlled growth on the herringbone structure. The latter two even lift the reconstruction through the formation of an alloy layer. It was proposed that two physical parameters govern the action of the template: the surface free energy and the heat of sublimation of the deposited metal, which both have to be higher than the corresponding values for Au [119]. In the case of Ni this leads to a substitution of adatoms in the substrate layer [128], which stabilizes the island formation. This view was however challenged later by a model, which again is based on limited diffusion in the fcc regions of the reconstructed surface leading to an enhanced formation of the critical nuclei for island growth [129]. Even though a number of theoretical investigations have been focused on this issue it still remains under debate [130–135]. But

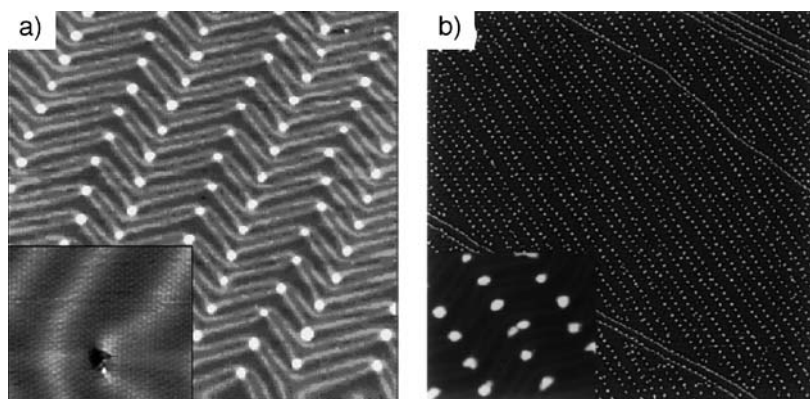


Fig. 17 STM images of nanostructures of Co (a) [111] and MoS₂ (b) [112] grown using a template-controlled process on Au(1 1 1)-($\sqrt{3} \times 22$)

not only metal islands could be produced by this approach on the Au(1 1 1)-($\sqrt{3} \times 22$) surface, but also semiconducting MoS₂ clusters were grown on this template [112] indicating the general character of the Au(1 1 1) surface as a growth template (Fig. 15b). An even more advanced growth mode was found for Au on Co islands on Au(1 1 1) [136]. Here the Co islands act as a 2nd generation template guiding the growth of the deposited Au such that they are attached to the existing Co islands.

Recently, the preparation of molecular overlayers came into focus of the work on Au(1 1 1). In this case of course the temperature will play a decisive role since the mobility of molecules, as compared to metal atoms, may be quite high even at RT. An interesting example of this fact is C₆₀ on Au(1 1 1), which shows preferential trapping at the elbows of the herringbone at 30 K. At slightly higher temperature (~ 80 K) the molecules are found on the terraces. Finally, at RT the C₆₀ molecules decorate the top of the step edges forming a 1D chain, which can be considered as a template effect of the steps [137]. A different behavior is found with 9-aminoanthracene molecules deposited on Au(1 1 1). In this case the molecules align in pairs along the dicommensuration lines (DL) of the herringbone structure [138]. The template-assisted ordering along the DLs is also found for 1-nitro-naphthalene (NN) molecules at low coverage and additionally also a preference for adsorption near the elbows is found for certain conditions [139, 140].

3.2

Vicinal Surfaces

When considering template-assisted or -controlled growth on vicinal surfaces, the first thing that comes to mind is the important role of the steps. Indeed on the lower edge of the steps the coordination number of adsorbed atoms is higher than on the terraces and thus the interaction energy should in principal be higher as well. Thus the specific interaction, which signifies a template site, is in principal provided by the step sites on vicinal surfaces. It should then suffice to control the migration (diffusion) of deposited entities (atoms, molecules) such that they can reach a step. Ultimately this means that we have to control the kinetics of the deposition process by adjusting the temperature and the deposition rate. For an in-depth review of the relevant processes the reader is referred to [141], where also the elementary steps occurring during growth on vicinal surfaces are explained in great detail.

Using this approach, which had already been proposed by Himpsel et al. in 1994 [142], mainly 1D nanostructures (lines, wires) along the step edges of vicinal surfaces can be produced and a number of examples can be found in the literature. Among these we find Cu on Mo(1 1 0) [143, 144] as well as Ni [145], Co [146], Cu [147], and Ag [147, 148] on Pt(9 9 7). These systems show – depending on the deposition temperature – a more or less pronounced 1D growth along the steps. Similar results were obtained for

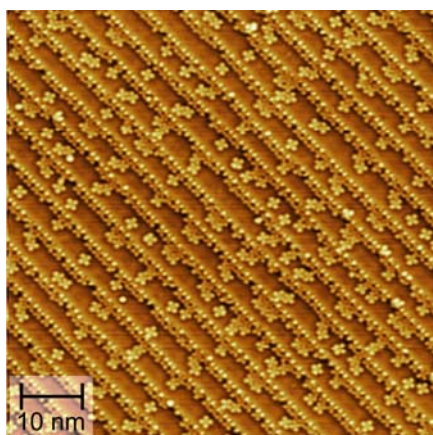


Fig. 18 STM image of CoPc growth on Au(7 8 8) (from [152])

Fe on vicinal Cu(1 1 1) where 1D magnetic domains (stripes) could be prepared [149], Ni on vicinal Rh(1 1 1) [150], and Fe on vicinal W(1 1 0) [151]. A summary, which is showing the most important details of these systems, is given in Table 1.

The 1D growth along steps is, however, not limited to metal overlayers. Recently also cobalt phthalocyanine (CoPc) has been found to nucleate along the steps of the vicinal Au(7 8 8) surface [152] (Fig. 18). This particular surface shows also remains of the herringbone structure of Au(1 1 1) and indeed a weak tendency for preferential adsorption of the CoPc on the fcc domains on the terraces has also been found.

The preferential adsorption of CoPc on the fcc domains of the Au(7 8 8) surface already shows that on a vicinal surface not only 1D structures can be produced but that 2D structures may also be accessible. In order to accomplish this a control of the kinetics of the nucleation process is needed, and can indeed be verified for a number of Au(1 1 1) vicinal surfaces. As always for nucleation processes the critical cluster density is an important figure, which is directly related to the diffusion length of the deposited entities, and thus the temperature, but in the case of a template-controlled growth also to the number of favorable nucleation sites imposed by the template. In the case of Co growth on Au(7 8 8) this has been studied in depth and it turned out that the growth of the Co islands is indeed template controlled in the temperature range from 60 to 300 K [153]. As can be seen in Fig. 19 in this temperature range the number of Co islands corresponds exactly to the number of preferred nucleation sites whereas at lower temperature the number of islands increases rapidly and at higher temperature fewer but larger Co islands are found. In this specific example two main parameters have been identified to be responsible for the template-controlled growth: the activation energy of

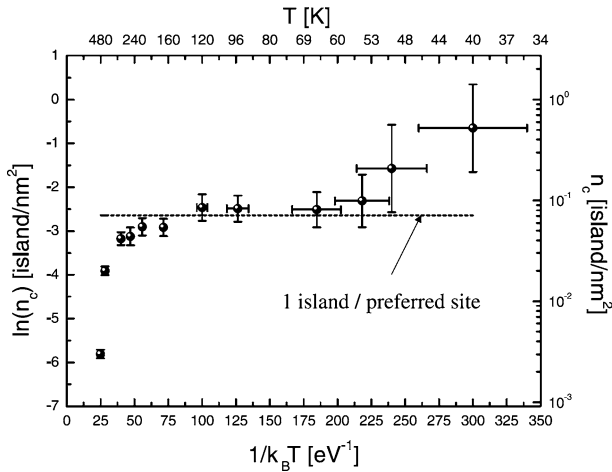


Fig. 19 Arrhenius plot of the critical Co cluster density as a function of deposition temperature. The *dotted line* indicates the density of the preferred nucleation sites on the Au(7 8 8) template (from [153])

diffusion E_{diff} and the trapping energy E_t , which has to be spent to leave the preferred site. Consequently the deviations from the template-controlled growth are due to a limited diffusion length at low temperature and an insufficient trapping energy at high temperatures. It is the interplay of these two parameters, which leads to the template-controlled growth on the Au(7 8 8) surface. Of course, E_t is what we called specific interaction above and which is one of the criteria for a surface being a template. The kinetic Monte Carlo (KMC) simulations presented in [153] are however not restricted to growth on vicinal surfaces but nicely explain also the growth on other surface templates. Using vicinal Au(1 1 1) surfaces as a template even a higher order of the structures can be reached compared to the Au(1 1 1) surface.

In particular not only metals such as Co, which have been subject to a template-controlled growth on Au(1 1 1), but also Ag, which did not show such a growth on Au(1 1 1), can be grown in a nicely ordered fashion on a vicinal Au(1 1 1) surface (Fig. 20a). In fact, a great variety of metals has been shown to exhibit template-controlled growth on vicinal Au(1 1 1) surfaces. Among these we find besides Co [154, 157–165], which is due to its magnetic properties by far the most exploited, Fe [161, 166], Ni [161], Mn [124], and Ag [155, 167] (for a review see [36]). Again the template-controlled growth of 2D nanostructures on vicinal surfaces is not limited to metallic systems. While already the adsorption of CoPc on Au(7 8 8) gave some indication of a possible 2D order, the growth of C_{60} on vicinal Au(1 1 1) surfaces leads to rather promising results in terms of 2D ordering. On the Au(11 12 12) a nicely ordered overlayer of C_{60} chains with lengths of four to five molecules has

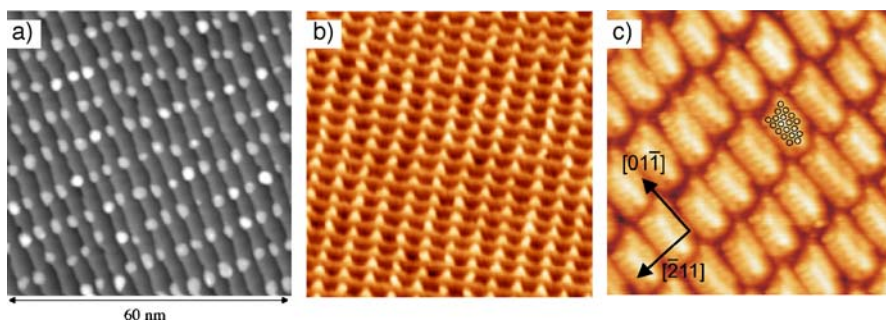


Fig. 20 STM images showing template-controlled nanostructures on vicinal Au surfaces. **a** Co on Au(7 8 8) [158], **b** Ag on Au(7 8 8) [155], and **c** C₆₀ on Au(7 8 8) [156]

been found after RT deposition [168]. A similar result was obtained for C₆₀ on Au(788) but in this case the formation of nearly rectangular C₆₀ islands was observed [156] (Fig. 20c). Again the length of the islands is four to five molecules imposed by the separation of the dicommensuration lines, which is of course identical on Au(7 8 8) and for example Au(11 12 12).

Vicinal Au surfaces seem to have a great potential as 2D templates not only for metal growth but also for the fabrication of ordered molecular assemblies.

3.3

Epitaxial Metal Films

After having exploited the use of reconstructed metal surfaces and vicinal surfaces as templates we will now turn to metal films. Since it has been shown that the nanopatterns of the above mentioned surfaces are in many cases excellent templates for overlayer growth the same can be expected for nanostructured metal films. Indeed a number of such systems have been investigated in terms of their potential use as templates. As the first example we refer to the homoepitaxial growth of Ag on the reconstructed 2 ML thick Ag film on Pt(1 1 1) (see Fig. 10). Already in 1995 Brune et al. were able to show that further Ag deposition at ~ 100 K on this specific surface leads to the ordered growth of Ag islands [169, 170]. Later it was reasoned that the ordering occurs due to the confined nucleation of adatoms within the superstructure cells of the periodic surface dislocation network [171]. The same effect is also present for the deposition of mass select Ag₇ clusters [172] and Fe film growth on 2 ML Cu on Pt(1 1 1) [170].

Even though it has been claimed that this approach will open an interesting route towards the formation of nanostructures on surfaces it has been exploited to a much lesser extent than, for example, the reconstructed Au(1 1 1)-($\sqrt{3} \times 22$) surface and the vicinal gold surfaces. Recently a new system has been proven to act as a growth template, which consists of a graphene

monolayer on Ir(1 1 1) (see Fig. 11). On this surface the deposition of Ir leads to the formation of ordered Ir islands [173]. One of the advantages of this approach is that the surroundings of the clusters consist of relatively inert graphene. Thus, new applications may be envisioned, which require inert surfaces and which are in general not provided by metal-supported systems. We will come back to this in the section on template-controlled growth on oxide surfaces.

3.4

Inorganic Layers and Films

A particular case in the context of metal surfaces is that of the nanostructured N/Cu(100) surface. In this case the nitrogen islands passivate part of the surface so that deposited metals will only adhere to the remaining bare copper patches. By this route a number of metallic nanostructures have been successfully grown. A good example is the growth of Au on N/Cu(100) where a nicely ordered square-based array of Au nanoparticles has been found [79] (Fig. 21a). Later studies on the same system showed again the detailed kinetics of the template-controlled growth process indicating that the temperature range, in which the template is active, extends only from ~ 210 K to ~ 290 K [174] (Fig. 21b). This example once more proves the importance of kinetic control of the growth process, which is a common feature of the examples cited so far. Furthermore, the N/Cu(100) system has also been successfully employed as a template for the growth of Ag [175, 176], Fe [177], and Co [176, 178–180].

An overview of the systems discussed in Sect. 3 is given in Table 1.

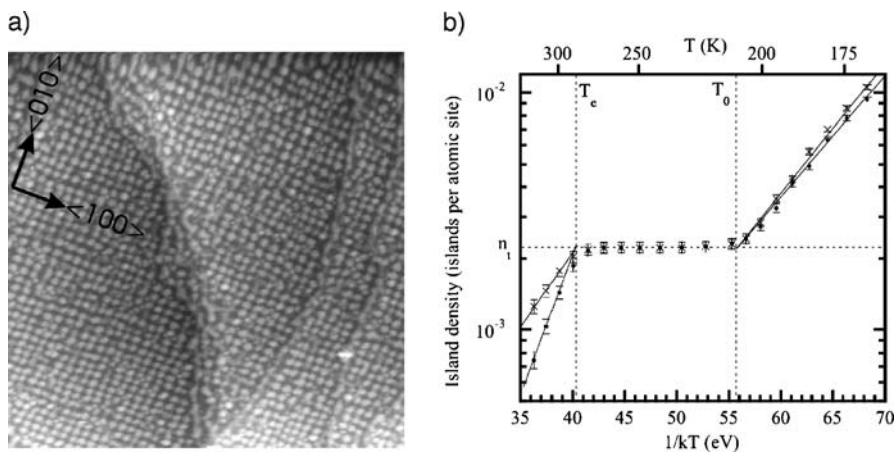


Fig. 21 **a** Gold nanodots grown on the N/Cu(100) template [79]. **b** Evolution of the island density with growth temperature for this system [174]

Table 1 Overview of template-controlled growth on metallic substrates

Substrate	Superstructure type	Deposit	Structure size (nm)	Structure type	Order
Au(1 1 1) [111, 115]	($\sqrt{3} \times 22$) reconstr.	Co	7.1×1.7	Islands	High
Au(1 1 1) [112]	($\sqrt{3} \times 22$) reconstr.	MoS ₂	7.1×1.7	Islands	High
Au(1 1 1) [116, 117]	($\sqrt{3} \times 22$) reconstr.	Fe	7.1×1.7	Islands	High
Au(1 1 1) [118, 119]	($\sqrt{3} \times 22$) reconstr.	Ni	7.1×1.7	Islands	High
Au(1 1 1) [120]	($\sqrt{3} \times 22$) reconstr.	Pd	7.1×1.7	Islands	High
Au(1 1 1) [121, 122]	($\sqrt{3} \times 22$) reconstr.	Rh	7.1×1.7	Islands	Medium
Au(1 1 1) [123]	($\sqrt{3} \times 22$) reconstr.	Mo	7.1×1.7	Islands	High
Au(1 1 1) [124]	($\sqrt{3} \times 22$) reconstr.	Mn	7.1×1.7	Islands	Medium
Au(1 1 1) [137]	($\sqrt{3} \times 22$) reconstr.	C ₆₀	7.1×1.7	2D single molecules ($T = 30$ K)	Medium
Au(1 1 1) [140]	($\sqrt{3} \times 22$) reconstr.	NN	7.1×1.7	2D single molecules ($T = 65$ K)	High
Mo(1 1 0) [144]	Vicinal	Cu	Irregular	1D stripes	
W(1 1 0) [151]	Vicinal	Fe	Irregular	1D stripes	
Pt(9 9 7) [145]	Vicinal	Ni	2	1D alloy	
Pt(9 9 7) [146]	Vicinal	Co	2	1D stripes	
Pt(9 9 7) [147]	Vicinal	Ag	2	1D stripes	
Pt(9 9 7) [147]	Vicinal	Cu	2	1D stripes	
Cu(1 1 1) [149]	Vicinal	Fe	Irregular	1D stripes	
Rh(1 1 1) [150]	Vicinal	Ni	Irregular	1D stripes	
Au(7 8 8) [152]	Vicinal + reconstr.	CoPc	3.8×7.2	1D stripes	
Au(7 8 8) [153, 154]	Vicinal + reconstr.	Co	3.8×7.2	2D Islands	
Au(7 8 8) [155, 167]	Vicinal + reconstr.	Ag	3.8×7.2	2D Islands	
Au(7 8 8) [156]	Vicinal + reconstr.	C ₆₀	3.8×7.2	2D Islands	
Au(7 8 8) [124]	Vicinal + reconstr.	Mn	3.8×7.2	1D stripes	
Au(7 8 8) [161]	Vicinal + reconstr.	Fe	3.8×7.2	1D alloy	
Au(7 8 8) [161]	Vicinal + reconstr.	Ni	3.8×7.2	1D alloy	
Au(11 12 12) [168]	Vicinal + reconstr.	C ₆₀	5.8×7.2	2D short chains	
Pt(1 1 1) [170, 175]	2 ML Ag film	Ag	6.8×6.8	Islands	Medium
Pt(1 1 1) [170]	2 ML Cu film	Fe	4.6×4.6	Islands	Medium
Ir(1 1 1) [173]	Graphene ML	Ir	2.5×2.5	Islands	High
Cu(1 0 0) [79]	Reconstr. N layer	Au	5×5	Islands	Medium
Cu(1 0 0) [175]	Reconstr. N layer	Ag	5×5	Islands	Low
Cu(1 0 0) [177]	Reconstr. N layer	Fe	5×5	Islands	Low
Cu(1 0 0) [178, 180]	Reconstr. N layer	Co	5×5	Islands	Medium

4 Oxide Surfaces as Templates

In this section the use of oxide surfaces as templates will be discussed. These surfaces are particularly interesting because of their potential use in industrial applications in which insulating or inert substrates are required. In this context one has to refer to nanocatalysts or electronic devices, which nowadays rely on an active patterning of the surface. Oxidic templates can be used for the fabrication of well-ordered model systems in these fields. In fact the search for more powerful catalysts is often hampered by the fact that the complexity of the real world catalyst does not allow an in-depth investigation. Ordered nanostructured model catalysts prepared in a template-controlled process can provide a pathway to systems of lower complexity, which opens a route to the investigation of basic steps in heterogeneous catalysis.

While metal surfaces and films apparently possess a great potential as templates, the field of oxidic templates has by far not been exploited to such an extent. However, a number of cases exist, which show the potential of the template approach for the generation of nanopatterns on insulating (oxide) surfaces. We will include here also nanopatterned bulk materials, which we did not explicitly treat in the section on pattern formation by self-organization above.

4.1 Epitaxial Alumina Films

Metal-supported alumina films are widely used for model catalysts since their properties are comparable to those of bulk alumina and their structural as well as the chemical characterization is – compared to bulk alumina – facilitated by the presence of the conducting substrate [71, 181]. The quest for a reduced complexity in such systems – in order to study the details of catalytic reactions on a molecular scale – calls for well-ordered supported metal particles on oxide films. This can be accomplished by making use of template-controlled growth processes. Here promising candidates are the thin alumina films grown on $\text{Ni}_3\text{Al}(1\ 1\ 1)$, which have a superstructure in the nanometer range (see Sect. 2.3). Early studies on the growth of Ag and Mn on $\text{Al}_2\text{O}_3/\text{Ni}_3\text{Al}(1\ 1\ 1)$ suggested that there is at least at low coverage a template-controlled growth of the metal particles during deposition at RT [182]. However, at higher coverage the template did not seem to be active any more due to kinetic effects. Further investigations using Cu and V as deposits proved the presence of a template-controlled growth – now also at higher coverage [183, 184]. In the case of Cu good results were obtained at RT, whereas for V higher substrate temperatures had to be applied in order to increase the mobility of the deposited V atoms, and the best results were obtained

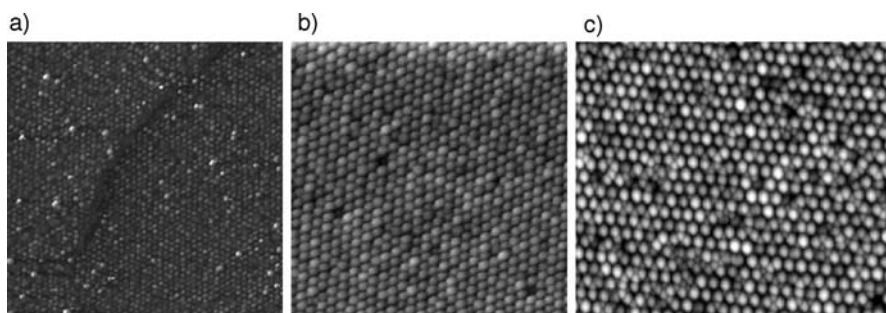


Fig. 22 STM images of ordered metal cluster arrays grown on $\text{Al}_2\text{O}_3/\text{Ni}_3\text{Al}(111)$. **a** Vanadium clusters grown at 550 K [184], **b** Pd clusters grown at RT [186], and **c** Fe clusters grown on the secondary Pd/ $\text{Al}_2\text{O}_3/\text{Ni}_3\text{Al}(111)$ template [77]

for a substrate temperature of 550 K (Fig. 22a) [184]. A striking difference between the growth of V and most other metals on the $\text{Al}_2\text{O}_3/\text{Ni}_3\text{Al}(111)$ surface was that the lattice constant of the ordered cluster array was 2.4 nm and not 4.2 nm as expected from the unit cell size of the alumina layer (see Sect. 2.3). Consequently a higher number density of clusters could be reached in this case [184]. We will come back to this point below. The growth of Au showed a behavior similar to Ag with a preferential nucleation on the template sites at low coverage and the formation of larger agglomerates at higher coverage. The growth of Fe on $\text{Al}_2\text{O}_3/\text{Ni}_3\text{Al}(111)$ was also investigated at different temperatures and showed a weak template effect of the alumina film showing the same lattice constant as V [185]. The best results in terms of a template-controlled assembly were obtained for Pd on $\text{Al}_2\text{O}_3/\text{Ni}_3\text{Al}(111)$, which shows an extremely strong preference for nucleation and growth on the template sites [186]. By this means an almost perfect layer of Pd clusters on $\text{Al}_2\text{O}_3/\text{Ni}_3\text{Al}(111)$ could be prepared (Fig. 22b).

The extremely good order that was reached in the case of Pd growth on the alumina film suggested that these clusters could serve as a 2nd generation template for the further deposition of other metals. Indeed this approach was proven to provide good results in the case of Au [187] and Fe [77] (Fig. 22c). Indeed, the presence of the Pd nuclei effectively controls the nucleation of these two metals.

The question about the physical origin of the template effect of the alumina film is not easy to answer, moreover since not only a unique site seems to function as template but rather two different sites are active depending on the deposited metal. Indeed the strong preference of Pd for nucleation on the so-called “dot structure” of the alumina film was attributed to the presence of a localized electronic state in the band gap of the oxide at this particular position [68, 186]. This view was lately however challenged by high-resolution STM investigations, which suggest the presence of a hole in the oxide film at that very position. It was claimed that Pd – as opposed to other metals –

preferentially occupies this hole, thereby acting as nucleus for the further cluster growth of the second metal at that position [77]. Since such holes were not visible in atomically resolved AFM images [75] the exact mechanism still remains under debate. In fact the action of the templating sites of alumina films on $\text{Ni}_3\text{Al}(1\ 1\ 1)$ resemble very closely the domain boundaries found on structurally similar alumina films grown on $\text{NiAl}(1\ 1\ 1)$ ([71] and references therein), which also act as nucleation centers for RT growth of a variety of metals.

The high-resolution STM images in [77] provide however an important clue on the nature of the preferred nucleation sites on $\text{Al}_3\text{O}_2/\text{Ni}_3\text{Al}(1\ 1\ 1)$. This surface is characterized by two high symmetry sites, which have a separation of 2.4 nm and 4.2 nm and correspond to the structures known as “network” and “dot” structure, respectively. Since all metals studied so far initially prefer to nucleate either on sites of the dot structure (Cu, Ag, Au, and Pd) or on sites of the network structure (Mn, Fe, V) it can be at least reasoned that the preferred nucleation sites are the high symmetry sites of the alumina film. Again the growth on the alumina template is kinetically controlled. It has been shown in the case of Pd that RT is a very favorable temperature and already at 400 K the island density starts to decrease [186].

Of course other alumina films have been used for the preparation of model catalysts and some of them as in the case of Co on $\theta\text{-Al}_2\text{O}_3/\text{CoAl}(100)$ [188] and Cr on $\text{Al}_2\text{O}_3/\text{NiAl}(001)$ [189] show a certain template effect, but the resulting layers are in general not as nicely ordered as on $\text{Al}_3\text{O}_2/\text{Ni}_3\text{Al}(1\ 1\ 1)$.

4.2

Titania

Titania (TiO_2) is also commonly used for the preparation of model catalysts and unlike alumina even the bulk material shows some conductivity, which is due to defects. Therefore, bulk TiO_2 is accessible to most experimental surface science techniques and has been studied extensively, also including the template-controlled growth of metals. Basically two nanopatterns on TiO_2 surfaces have been identified, which are due to self-organization processes: the so-called cross-linked structure of $\text{TiO}_2(1\ 1\ 0)$ [190, 191], and the network-like $(7\sqrt{2} \times 7\sqrt{2})R45^\circ$ reconstruction of $\text{TiO}_2(001)$ [192]. These two structures exhibit patterns that render them good candidates for template-controlled growth. However, only the former has been used in this context. It shows the template-controlled growth of Pd clusters, which are preferentially aligned along the rows of the cross-linked structure [193–195]. For this system a strong dependence of the order of the nanostructure on the deposition temperature is found. Also highly dispersed arrays of Au particles have been prepared on the $\text{TiO}_2(1\ 1\ 0)$ cross-linked surface, which could not be prepared on the $\text{TiO}_2(1\ 1\ 0)-(1 \times 1)$ surface, and it was suggested that this effect was due to suppression of Au diffusion on the cross-linked surface [196].

Recently well-ordered TiO_2 films on $\text{Pt}(1\ 1\ 1)$ have attracted some attention and have been exploited as growth templates. The z' - TiO_x (zigzag-like) phase has been shown to act as a template for the nanostructured growth of Au islands at RT [197], in marked contrast to the so-called w' - TiO_x (wagon-wheel-like) phase, which is nanostructured but does not act as a template.

4.3

Epitaxial Iron Oxide Films

Much like Al_2O_3 and TiO_2 also iron oxide films and bulk iron oxide single crystals can serve as growth templates. Regular patterns of Fe islands have been prepared on a 100 nm thick Fe_3O_4 film supported on $\text{MgO}(1\ 1\ 1)$, and on a $\text{Fe}_3\text{O}_4(1\ 1\ 1)$ single crystal ordered arrays of Cr and Fe clusters were obtained, respectively [198]. In this case the templating mechanism of the surface may be similar to the one found for $\text{Al}_2\text{O}_3/\text{Ni}_3\text{Al}(1\ 1\ 1)$ since bias-dependent STM images of the $\text{Fe}_3\text{O}_4(1\ 1\ 1)$ surface show the same type of contrast reversal.

Furthermore, the moiré pattern found for FeO thin films on $\text{Pt}(1\ 1\ 1)$ has been used as a template for the growth of nanopatterned Fe layers [198]. This effect is believed to be due to the strain relief in the oxide layer resulting in domains with fcc and hcp stacking. Thus, the same mechanism as found for similarly reconstructed metal surfaces should be responsible for the template-controlled growth on metal film templates. Table 2 summarizes the results obtained for the template-controlled growth on the surfaces discussed in Sect. 4.

Table 2 Overview of template-controlled growth on metallic substrates

Substrate	Superstructure type	Deposit	Structure size (nm)	Structure type	Order
$\text{Ni}_3\text{Al}(1\ 1\ 1)$ [186]	Al_2O_3 film	Pd	4.2×4.2	Islands	High
$\text{Ni}_3\text{Al}(1\ 1\ 1)$ [184]	Al_2O_3 film	V	2.4×2.4	Islands	High
$\text{Ni}_3\text{Al}(1\ 1\ 1)$ [183]	Al_2O_3 film	Cu	4.2×4.2	Islands	Medium
$\text{Ni}_3\text{Al}(1\ 1\ 1)$ [185]	Al_2O_3 film	Fe	2.4×2.4	Islands	Low
$\text{Ni}_3\text{Al}(1\ 1\ 1)$ [187]	Pd on Al_2O_3 film	Au	4.2×4.2	Islands	High
$\text{Ni}_3\text{Al}(1\ 1\ 1)$ [77]	Pd on Al_2O_3 film	Fe	4.2×4.2	Islands	High
$\text{CoAl}(1\ 0\ 0)$ [188]	θ - Al_2O_3 film	Co	irregular	Islands	Low
$\text{TiO}_2(1\ 1\ 0)$ [193]	(1×2) reconstr.	Pd	$\sim 3 \times 3$	Islands	Medium
$\text{TiO}_2(1\ 1\ 0)$ [196]	(1×2) reconstr.	Au	Irregular	Islands	Low
$\text{Pt}(1\ 1\ 1)$ [197]	z' - TiO_x	Au	$\sim 2.3 \times 2.3$	Islands	Medium
$\text{MgO}(1\ 1\ 1)$ [198]	Fe_3O_4 film	Fe	4.2×4.2	Islands	Medium
$\text{Fe}_3\text{O}_4(1\ 1\ 1)$ [198]	Reconstr.	Cr	4.2×4.2	Islands	Medium

5 Beyond Simple Templates

Let us now explore the potential use of template-controlled growth for the fabrication of nanostructures in a more advanced fashion leaving the domain of simple growth by kinetically controlled processes, which has already been exploited for instance by the examples of bimetallic clusters on $\text{Al}_2\text{O}_3/\text{Ni}_3\text{Al}(1\ 1\ 1)$ in Sect. 4. In this case the Pd clusters on the surface were used as a second-generation template in order to control the nucleation of Au and Fe on top of the initial Pd clusters. This is so to speak a first step towards hierarchical assembly, which will ultimately lead to a control of building processes in the third dimension based on a 2D template. This can be visualized by again referring to the LEGO® model introduced in Fig. 5. If we use the surface realized by template-controlled growth shown in Fig. 5c as a 2nd generation template we are able to control the growth of the next layer if the interaction is specific. Furthermore, we are able to organize entities, which by themselves would not order on the original template since this may not possess the appropriate sites. Such a situation is depicted in Fig. 6. The round LEGO® bricks do not stick to the original template site but will stick to the (2×2) -bricks placed on the original template. This is a general assembly procedure, which under favorable circumstances can be pursued in the following generations given that the interaction is always specific. In this context organic chemistry promises to provide the building blocks for such assemblies by combining structure and functionality. This approach will eventually lead to an engineering of nanostructured molecular layers controlled by shape and functionalization of the used molecules. A good example of such a process is given in [199] by 2D metal–organic networks on $\text{Cu}(100)$. In this case three linker molecules (TPA, BDA, and TDA) of different size are co-deposited with Fe and form cavity networks of varying size and structure.

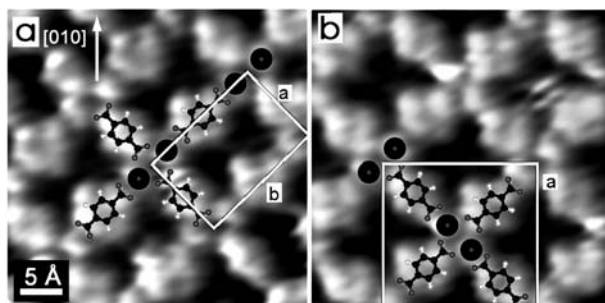


Fig. 23 STM topographs of the Fe-TPA networks: **a** α -phase and **b** β -phase. Tentative models and the unit cells of the Fe-Fe arrays are superimposed on the STM topographs (from [199])

An example of such a network is given in Fig. 23. Here the formation of the structure results from the interplay of the carboxylate groups of the molecules and the Fe centers, the positions of the latter being in turn affected by the interaction with the Cu(100) substrate. It is thus a template-assisted process in which the final structure is to some extent controlled by the symmetry of the primary substrate. These so-called metal–organic coordination networks (MOCNs) can also be tailored to yield other structures with different symmetry and it has been shown that a threefold symmetry of a Fe(biphenolate) network is found on the Ag(1 1 1) and the Cu(100) surface, i.e. regardless of the symmetry of the substrate [200]. Further on the MOCN layers can be used as hosts for the deposition of C_{60} guest molecules – thus acting as templates.

This method is, however, by far not limited to MOCNs. In Fig. 24 the formation of a porous network of porphyrin-based molecules on Ag(1 1 1) is shown. In fact the joint action of the hexagonal substrate and the intermolecular interaction leads to a self-organization process that provides the desired nanoscopic superstructure with a lattice constant of 3.3 nm. This surface can now be utilized for the template-controlled deposition of C_{60} molecules, which will reside as guests in the pores of the templating layer [201]. Similar results have also been obtained on Ag(100) [202]. This again proves the feasibility of a hierarchical template-controlled assembly of molecules on solid surfaces. For the same systems again a mobility of the C_{60} molecules, which results in the hopping of the C_{60} between adjacent pores, has been found, underlining the importance of temperature – and thus kinetics – for template-controlled processes on surfaces. It is the latter point, which also constitutes one of the major drawbacks of this concept. Molecular architectures often rely on weak interactions that show only a limited stability with respect to temperature, rendering them not suitable for real world application. It will thus be one of the important future challenges to tailor molecular interactions such that they are on the one hand strong enough to form stable structures but on the other hand are only so strong that a kinetic control of the organi-

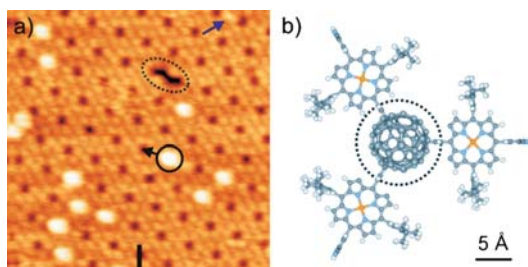


Fig. 24 **a** STM image showing C_{60} guests in the pits of a template created from a porphyrin derivative on Ag(1 1 1) and **b** proposed molecular model of a C_{60} molecule hosted inside a supramolecular porphyrin-based pore (from [201])

zation process is feasible. For further information on templating by molecular layers the reader is referred to [203].

The biggest drawback of this approach in the context of the systems discussed here is that not many organic molecules are apt for utilization under ultrahigh vacuum (UHV) conditions. Therefore, other approaches may be necessary to exploit the full potential of the method, for example preparation from solution (see e.g. [204]).

6

Summary

In the previous sections the fascinating world of template-controlled 2D nanostructures has been explored. A basic feature of the work presented here is that a bottom-up approach for the generation of the 2D templates is used, which relies on self-organization. Following this strategy a great variety of nanostructures can be produced by a route, which requires no time-consuming intervention of the experimentalist. The conditions that a nanostructured surface has to meet in order to serve as a 2D template in this approach is that the interaction between the active sites of the template and the deposited entities has to be specific. The template-controlled growth can then be steered by the kinetics of the deposition process. A large number of examples have been cited that prove the viability of this approach.

Recent advances in the growth of organic molecular layers suggest that beyond this rather simple kinetically controlled approach a molecular assembly due to directed forces between the deposited entities, which rather creates equilibrium structures, is feasible. This will open the way to an even bigger number of potential surface templates.

References

1. Lin BJ (1996) *CR Phys* 7:858
2. Binnig G, Rohrer H, Gerber CH, Weibel E (1982) *Phys Rev Lett* 50:120
3. Binnig G, Quate CF, Gerber CH (1986) *Phys Rev Lett* 56:930
4. Busch DH (2005) *Top Curr Chem* 249:1
5. John K, Bär M (2005) *Phys Rev Lett* 95:198101
6. Kuhn H, Ulman A (1995) *Supramolecular assemblies: vision and strategy*. In: Ulman A (ed) *Thin Films*, Vol. 20. Academic Press, NY, p 1
7. Whitesides GM, Boncheva M (2002) *Proc Natl Acad Sci USA* 90:4769
8. Zou Y, Kilian L, Scholl A, Schmidt T, Fink R, Umbach E (2006) *Surf Sci* 600:1240
9. Wagner T, Bannani A, Bobisch C, Karacuban H, Möller R (2007) *J Phys Condens Matter* 19:056009
10. Gabriel M, Stöhr M, Möller R (2002) *Appl Phys A* 74:303
11. Mannsfeld S, Toerker M, Schmitz-Hübsch T, Sellam F, Fritz T, Leo K (2001) *Org Electron* 2:121

12. Sendova-Franks AB, Franks NR (1999) *Phil Trans R Soc London* 354:1395
13. Becker C, Wandelt K (2007) *Topics Catal* 46:151
14. Suo Z, Lu W (2000) *J Nanopart Res* 2:333
15. Bach C, Giesen M, Ibach H, Einstein T (1997) *Phys Rev Lett* 78:4225
16. Van Hove MA, Koestner RJ, Stair PC, Bibérian JP, Kesmodel LL, Bartos I, Somorjai GA (1981) *Surf Sci* 103:189
17. Harten U, Lahee AM, Toennies JP, Wöll CH (1985) *Phys Rev Lett* 54:2619
18. Wöll C, Chiang S, Wilson RJ, Lippel PH (1989) *Phys Rev B* 39:7988
19. Barth JV, Brune H, Ertl G and Behm RJ (1990) *Phys Rev B* 42:9307
20. Huang KG, Gibbs D, Zehner DM, Sandy AR, Mochrie SGJ (1990) *Phys Rev Lett* 65:3313
21. Sandy AR, Machrie SGJ, Zehner DM, Huang KG, Gibbs D (1991) *Phys Rev B* 43:4667
22. Lauritsen JV, Besenbacher F (2006) *Adv Catal* 50:97
23. Morgenstern K, Kibsgaard J, Lauritsen JV, Lægsgaard E, Besenbacher F (2007) *Surf Sci* 601:1967
24. Wan Y, Hush NS, Reimers JR (2007) *Phys Rev B* 75:233416
25. Bürgi L, Brune H, Kern K (2002) *Phys Rev Lett* 89:176801
26. Heilmann P, Heinz K, Müller K (1979) *Surf Sci* 83:487
27. Bickel N, Heinz K (1985) *Surf Sci* 163:435
28. Van Hove MA, Koestner RJ, Stair PC, Bibérian JP, Kesmodel LL, Bartos I, Somorjai GA (1981) *Surf Sci* 103:189
29. Borg A, Hilmen AM, Bergene E (1994) *Surf Sci* 306:10
30. Nohlen M, Schäfer B, Wandelt K (2004) *J Phys Chem B* 108:14663
31. Sinsarp A, Yamada Y, Sasaki M, Yamamoto S (2004) *Appl Surf Sci* 237:587
32. Heinz K, Hammer L, Klein A, Schmidt A (2004) *Appl Surf Sci* 237:519
33. Fedak DG, Gjorstein NA (1967) *Surf Sci* 8:77
34. Abernathy DL, Mochrie SGJ, Zehner DM, Grübel G, Gibbs D (1992) *Phys Rev B* 45:9272
35. Fiorentini V, Methfessel M, Scheffler M (1993) *Phys Rev Lett* 71:1051
36. Rousset S, Repain V, Baudot G, Garreau Y, Lecoeur J (2003) *J Phys Condens Matter* 15:S3363
37. Rousset S, Pourmir F, Berroir JM, Klein J, Lecoeur J, Hecquet P, Salanon B (1999) *Surf Sci* 422:33
38. Rousset S, Berroir JM, Repain V, Garreau Y, Etgens VH, Lecoeur J, Pinchaux R (1999) *Surf Sci* 443:265
39. Pourmir F, Rousset S, Gauthier S, Sotto M, Klein J, Lecoeur J, Bellier JP (1995) *Surf Sci* 324:L337
40. Repain V, Berroir JM, Rousset S, Lecoeur J (1999) *Europhys Lett* 47:435
41. Ait-Mansour K, Ruffieux P, Xiao W, Gröning P, Fasel R, Gröning O (2006) *Phys Rev B* 74:195418
42. Brune H, Röder H, Boragno C, Kern K (1994) *Phys Rev B* 49:2997
43. Röder H, Bromann K, Brune H, Kern K (1997) *Surf Sci* 376:13
44. Bromann K, Brune H, Giovannini M, Kern K (1997) *Surf Sci* 388:L1107
45. Brune H, Giovannini M, Bromann K, Kern K (1998) *Nature* 394:451
46. Brune H (1998) *Surf Sci Rep* 31:121
47. Gestermann S, Nohlen M, Schmidt M, Wandelt K (1997) *Surf Rev Lett* 6:1179
48. Terada S, Yokoyama T, Saito N, Okamoto Y, Ohta T (1999) *Surf Sci* 433:657
49. Meunier I, Trégliat G, Legrand B, Tétot R, Aufray B, Gay JM (2000) *Appl Surf Sci* 162:219

50. Bendouan A, Cercellier H, Fagot-Revurat Y, Kierren B, Yu Yurov V, Malterre D (2003) *Appl Surf Sci* 212:33
51. Bendouan A, Cercellier H, Fagot-Revurat Y, Kierren B, Yu Yurov V, Malterre D (2003) *Phys Rev B* 67:165412
52. Jacobsen J, Pleth Nielsen L, Besenbacher F, Stensgaard I, Lægsgaard E, Rasmussen T, Jacobsen KW, Norskov JK (1995) *Phys Rev Lett* 75:489
53. Günther C, Vrijmoeth J, Hwang RQ, Behm RJ (1995) *Phys Rev Lett* 74:754
54. Ling WL, Hamilton JC, Thürmer K, Thayer GE, de la Figuera J, Hwang RQ, Carter CB, Bartelt NC, McCarty KF (2006) *Surf Sci* 600:1735
55. Parschau M, Schlatterbeck D, Christmann K (1997) *Surf Sci* 376:133
56. Meyer JA, Schmid P, Behm RJ (1995) *Phys Rev Lett* 74:3864
57. Zhang L, van Ek J, Diebold U (1998) *Phys Rev B* 57:R4285
58. Zhang L, van Ek J, Diebold U (1999) *Phys Rev B* 59:5837
59. Baddeley CJ, Stephenson AW, Hardacre C, Tikhov M, Lambert RM (1997) *Phys Rev B* 56:12589
60. Berner U, Schierbaum K (2002) *Phys Rev B* 65:235404
61. Trembulowicz A, Ciszewski A (2007) *Nanotechnology* 18:345503
62. Coraux J, N'Diaye AT, Busse C, Michely T (2008) *Nano Lett* 8:565
63. Silly F, Pivetta M, Ternes M, Patthey F, Pelz JP, Schneider WD (2004) *Phys Rev Lett* 92:016101
64. Land TA, Michely T, Behm RJ, Hemminger JC, Comsa G (1992) *Surf Sci* 264:261
65. Land TA, Michely T, Behm RJ, Hemminger JC, Comsa G (1991) *Appl Phys A* 53:414
66. Marchini S, Gunther S, Wintterlin J (2007) *Phys Rev B* 76:075429
67. Gross L, Moresco F, Ruffieux P, Gourdon A, Joachim C, Rieder KH (2005) *Phys Rev B* 71:165428
68. Maroutian T, Degen S, Becker C, Wandelt K, Berndt R (2003) *Phys Rev B* 68:155414
69. Becker C, Kandler J, Raaf H, Linke R, Pelster T, Dräger M, Tanemura M, Wandelt K (1998) *J Vac Sci Technol A* 16:1000
70. Jaeger RM, Kuhlenbeck H, Freund HJ, Wuttig M, Hoffmann W, Franchy R, Ibach H (1991) *Surf Sci* 259:235
71. Bäumer M, Freund HJ (1999) *Prog Surf Sci* 61:127
72. Rosenhahn A, Schneider J, Becker C, Wandelt K (1999) *Appl Surf Sci* 142:169
73. Rosenhahn A, Schneider J, Becker C, Wandelt K (2000) *J Vac Sci Technol A* 18:1923
74. Degen S, Krupski A, Kralj M, Langner A, Becker C, Sokolowski M, Wandelt K (2005) *Surf Sci* 576:L57
75. Hamm G, Barth C, Becker C, Wandelt K, Henry CR (2006) *Phys Rev Lett* 97:126106
76. Gritschneider S, Becker C, Wandelt K, Reichling M (2007) *J Am Chem Soc* 129:4925
77. Schmid M, Kresse G, Buchsbaum A, Napetschnig E, Gritschneider S, Reichling M, Varga P (2007) *Phys Rev Lett* 99:196104
78. Zeppenfeld P, Diercks V, David R, Picaud F, Ramseyer C, Girardet C (2002) *Phys Rev B* 66:085414
79. Ellmer H, Repain V, Sotto M, Rousset S (2002) *Surf Sci* 511:183
80. Kern K, Niehus H, Schatz A, Zeppenfeld P, Goerge J, Comsa G (1991) *Phys Rev Lett* 67:855
81. Leibsle FM, Dhesi SS, Barrett SD, Robinson AW (1994) *Surf Sci* 317:309
82. Ellmer H, Repain V, Rousset, Croset B, Sotto M, Zeppenfeld P (2001) *Surf Sci* 476:95
83. Yagyu K, Nakatsuji K, Yoshimoto Y, Tsuneyuki S, Komori F (2007) *Surf Sci* 601:4837
84. Gustafson J, Mikkelsen A, Borg M, Lundgren E, Kohler L, Kresse G, Schmid M, Varga P, Yuhara J, Torreles X, Quiros C, Andersen JN (2004) *Phys Rev Lett* 92:126102
85. Vurens GH, Salmeron M, Somorjai GA (1998) *Surf Sci* 201:129

86. Galloway HC, Sautet P, Salmeron M (1996) *Phys Rev B* 54:R11145
87. Kim YJ, Westphal C, Ynzunza RX, Galloway HC, Salmeron MB, Van Hove MA, Fadley CS (1997) *Phys Rev B* 55:R13448
88. Ritter M, Ranke W, Weiss W (1998) *Phys Rev B* 57:7240
89. Giordano L, Pacchioni G, Goniakowski J (2007) *Phys Rev B* 76:07416
90. Kim YJ, Westphal C, Ynzunza RX, Wang Z, Galloway HC, Salmeron M, Van Hove MA, Fadley CS (1998) *Surf Sci* 416:68
91. Ketteler G, Ranke W (2002) *Phys Rev B* 66:033405
92. Sedona F, Rizzi GA, Agnoli S, Llabré, Xamena FX, Papageorgiou A, Ostermann D, Sambì M, Finetti P, Schierbaum K, Granozzi G (2005) *J Phys Chem B* 109:24411
93. Sedona F, Agnoli S, Granozzi G (2006) *J Phys Chem B* 110:15359
94. Sedona P, Finetti F, Rizzi GA, Mick U, Sutara F, Svec M, Matolin V, Schierbaum K, Granozzi G (2007) *J Phys Chem C* 111:869
95. Männig A, Zhao Z, Rosenthal D, Christmann K, Hoster H, Rauscher H, Behm RJ (2005) *Surf Sci* 576:29
96. Surnev S, Vitali L, Ramsey MG, Netzer FP, Kresse G, Hafner J (2000) *Phys Rev B* 61:13945
97. Schoiswohl J, Sock M, Eck S, Surnev S, Ramsey MG, Netzer FP, Kresse G (2004) *Phys Rev B* 69:155403
98. Schoiswohl J, Kresse G, Surnev S, Sock M, Ramsey MG, Netzer FP (2004) *Phys Rev Lett* 92:206103
99. Ranke W, Ritter M, Weiss W (1999) *Phys Rev B* 60:1527
100. Corso M, Auwärter W, Muntwiller M, Tamai A, Greber T, Osterwalder J (2004) *Science* 303:217
101. Nagashima A, Tejima N, Gamou Y, Kawai T, Oshima C (1995) *Phys Rev Lett* 75:3918
102. Auwärter W, Kreuz TJ, Greber T, Osterwalder J (1999) *Surf Sci* 429:229
103. Goriachko A, He Y, Knapp M, Over H, Corso M, Brugger T, Berner S, Osterwalder J, Greber T (2007) *Langmuir* 23:2928
104. Paffett MT, Simonson RJ, Papin P, Paine RT (1990) *Surf Sci* 232:286
105. Müller F, Stöwe K, Sachdev H (2005) *Chem Mater* 17:3464
106. Preobrajenski AB, Vinogradov AS, Mårtensson N (2005) *Surf Sci* 582:21
107. Morscher M, Corso M, Greber T, Osterwalder J (2006) *Surf Sci* 600:3280
108. Corso M, Greber T, Osterwalder J (2005) *Surf Sci* 577:L78
109. Greber T, Brandenberger L, Corso M, Tamai A, Osterwalder J (2006) *e-J Surf Sci Nanotechol* 4:410
110. Desrosiers RM, Greve DW, Gellman AJ (1997) *Surf Sci* 382:35
111. Rousset S, Croset B, Girard Y, Prévot G, Repain V, Rohart S (2005) *CR Phys* 6:33
112. Helveg S, Lauritsen JV, Lægsgaard E, Stensgaard I, Nørskov JK, Clausen BS, Topsøe H, Besenbacher F (2000) *Phys Rev Lett* 84:951
113. Voigtländer B, Meyer G, Amer N (1991) *Phys Rev B* 44:10354
114. Tölkes C, Zeppenfeld P, Krzyzowski MA, David R, Comsa G (1997) *Surf Sci* 394:170
115. Fruchart O, Renaud G, Barbier A, Noblet M, Ulrich O, Deville JP, Scheurer F, Mane-Mane J, Repain V, Baudot G, Rousset S (2003) *Europhys Lett* 63:275
116. Voigtländer B, Meyer G, Amer N (1991) *Surf Sci* 255:L529
117. Bulou, Scheuer F, Ohresser P, Barbier A, Stanescu S, Quirós C (2004) *Phys Rev B* 69:155413
118. Chambliss D, Wilson R, Chiang S (1991) *Phys Rev Lett* 66:1721
119. Meyer J, Baikie I, Kopatzki E, Behm R (1996) *Surf Sci* 365:L647
120. Stephenson A, Baddeley C, Tikhov M, Lambert R (1998) *Surf Sci* 398:172
121. Altman E, Colton R (1994) *Surf Sci* 304:L400

122. Chado I, Scheurer F, Bucher JP (2001) *Phys Rev B* 64:094410
123. Biener MM, Biener J, Schalek R, Friend CM (2005) *Surf Sci* 594:221
124. Shiraki S, Fujisawa H, Nantoh M, Kawai M (2004) *Surf Sci* 552:243
125. Ma S, Zhao X, Rodriguez JA, Hrbek J (2007) *J Phys Chem C* 111:3685
126. Fischer B, Barth JV, Fricke A, Nedelmann L, Kern K (1997) *Surf Sci* 389:366
127. Barth JV, Schuster R, Behm RJ, Ertl G (1996) *Surf Sci* 348:280
128. Cullen WG, First PN (1999) *Surf Sci* 420:53
129. Boulot H, Goyhenex C (2002) *Phys Rev B* 65:045407
130. Padovani S, Scheurer F, Bucher J (1999) *Europhys Lett* 45:327
131. Padovani S, Chado I, Scheurer F, Bucher J (1999) *Phys Rev B* 59:11887
132. Chado I, Padovani S, Scheurer F, Bucher JP (2000) *Appl Surf Sci* 164:42
133. Goyhenex C, Bulou H, Deville JP, Trégila G (2002) *Appl Surf Sci* 188:134
134. Chado I, Goyhenex C, Bulou H, Bucher JP (2004) *Appl Surf Sci* 226:178
135. Chado I, Goyhenex C, Bulou H, Bucher JP (2004) *Phys Rev B* 69:085413
136. Wollschläger J, Amer NM (1992) *Surf Sci* 277:1
137. Fujita D, Yakabe T, Nejoh H, Sato T, Iwatsuki M (1996) *Surf Sci* 366:93
138. Lauffer P, Graupner R, Jung A, Hirsch A, Ley L (2007) *Surf Sci* 601:5533
139. Böhringer M, Morgenstern K, Schneider WD, Berndt R (1999) *J Phys Condens Matter* 11:9871
140. Böhringer M, Morgenstern K, Schneider WD, Berndt R (1999) *Phys Rev Lett* 83:324
141. Kuhnke K, Kern K (2003) *J Phys Condens Matter* 15:S3311
142. Himpfel FJ, Mo YW, Jung T, Ortega JE, Mankey GJ, Willis RF (1994) *Superlatt Microstruct* 15:237
143. Jung T, Mo YW, Himpfel FJ (1995) *Phys Rev Lett* 74:1641
144. Jung T, Schlittler R, Gimzewski JK, Himpfel FJ (1995) *Appl Phys A* 61:467
145. Gambardella P, Kern K (2001) *Surf Sci* 475:L229
146. Gambardella P, Blanc M, Bürgi L, Kuhnke K, Kern K (2000) *Surf Sci* 449:93
147. Gambardella P, Blanc M, Brune H, Kuhnke K, Kern K (2000) *Phys Rev B* 61:2254
148. Marisco M, Blanc M, Kuhnke K, Kern K (1997) *Phys Rev Lett* 78:94
149. Shen J, Skomski R, Kalua M, Jenniches H, Sunda Manoharan S, Krischner J (1997) *Phys Rev B* 56:2340
150. Schoiswohl J, Mitteldorfer F, Surnev S, Ramsey MG, Andersen JN, Netzer F (2006) *Surf Sci* 600:L274
151. Hauschild J, Elmers HJ, Gradmann U (1998) *Phys Rev B* 57:R677
152. Kröger J, Jensen H, Néel N, Berndt R (2007) *Surf Sci* 601:4180
153. Rohart S, Baudot G, Repain V, Girard Y, Rousset S, Bulou H, Goyhenex C, Provaille L (2004) *Surf Sci* 559:47
154. Weiss N, Cren T, Epple M, Rusponi S, Baudot G, Rohart S, Tejada A, Repain V, Rousset S, Ohresser P, Scheurer F, Benock P, Brune H (2005) *Phys Rev Lett* 95:157204
155. Didiot C, Fagot-Revurat Y, Pons S, Kierren B, Malterre D (2007) *Surf Sci* 601:4029
156. Néel N, Kröger J, Berndt R (2006) *Adv Mater* 18:174
157. Repain V, Berroir J, Rousset S, Lecoeur J (2000) *Surf Sci* 447:L152
158. Repain V, Baudot G, Ellmer H, Rousset S (2002) *Europhys Lett* 58:730
159. Baudot G, Rohart S, Repain V, Ellmer H, Girard Y, Rousset S (2003) *Appl Surf Sci* 121:360
160. Baudot G, Girard Y, Repain V, Rohart S, Rousset S, Kreckelbergh S, Coati A, Garreau Y (2004) *Surf Sci* 557:171
161. Shiraki S, Fujisawa H, Nantoh M, Kawai M (2004) *Appl Surf Sci* 237:284
162. Witkowski N, Borensztein Y, Baudot G, Repain V, Girard Y, Rousset S (2004) *Phys Rev B* 70:085408
163. Rohart S, Baudot G, Repain V, Girard Y, Rousset S (2005) *J Cryst Growth* 275:e203

164. Repain V, Rohart S, Girard Y, Tejada A, Rousset S (2006) *J Phys Condens Matter* 18:S17
165. Rohart S, Girard Y, Nahas Y, Repain V, Rodary A, Rousset S (2008) *Surf Sci* 602:28
166. Shiraki S, Fujisawa H, Nantoh M, Kawai M (2005) *J Phys Soc Jpn* 74:2033
167. Didiot C, Pons S, Kierren B, Fagot-Revurat Y, Malterre D (2006) *Surf Sci* 600:3917
168. Wende W, Ruffieux P, Ait-Mansur K, Gröning O, Palotas K, Hofer WA, Gröning P, Fasel R (2006) *J Phys Chem B* 110:21394
169. Brune H, Bromann K, Röder H, Kern K, Jacobsen J, Stoltze P, Jacobsen K, Nørskov J (1995) 52:R14380
170. Brune H, Giovanni M, Bromann K, Kern K (1998) *Nature* 394:451
171. Bromann K, Giovannini M, Brune H, Kern K (1999) *Eur Phys J D* 9:25
172. Jödicke H, Schaub R, Monot R, Butte J, Harbich W (2001) *Surf Sci* 475:109
173. N'Diaye AT, Bleikamp S, Feibelmann PJ, Michely T (2006) *Phys Rev Lett* 97:215501
174. Prévot G, Guesmi H, Croset B (2007) *Surf Sci* 601:2017
175. Silva S, Leibsle F (1999) *Surf Sci* 440:L835
176. Leibsle F (2002) *Surf Sci* 514:33
177. Parker T, Wilson L, Condon N, Leibsle F (1997) *Phys Rev B* 56:6458
178. Silva S, Jenkins S, York S, Leibsle F (2000) *Appl Phys Lett* 76:1128
179. Mukai K, Matsumoto Y, Tanaka K, Komori F (2000) *Surf Sci* 450:44
180. Komori F, Lee K, Nakatsuji K, Iimori T, Cai Y (2001) *Phys Rev B* 63:214420
181. Freund HJ, Ernst N, Risse T, Hamann H, Rupprechter G (2001) *Phys Stat Sol A* 187:257
182. Becker C, von Bergmann K, Rosenhahn A, Wandelt K (2001) *Surf Sci* 486:L443
183. Wiltner A, Rosenhahn A, Becker C, Pervan P, Milun M, Kralj M, Wandelt K (2001) *Thin Solid Films* 400:71
184. Becker C, Rosenhahn A, Wiltner A, von Bergmann K, Schneider J, Pervan P, Milun M, Kralj M, Wandelt K (2002) *New J Phys* 4:75
185. Lehnert A, Krupski A, Degen S, Franke K, Decker R, Rusponi S, Kralj M, Becker C, Brune H, Wandelt K (2006) *Surf Sci* 600:1804
186. Degen S, Becker C, Wandelt K (2004) *J Chem Soc Faraday Discuss* 125:343
187. Hamm G, Becker C, Henry CR (2006) *Nanotechnology* 17:1943
188. Rose V, Podursky V, David R, Franchy R (2007) *Surf Sci* 601:786
189. Méndez J, Niehus H (1999) *Appl Surf Sci* 142:152
190. Bennett RA, Stone P, Price NJ, Bowker M (2002) *Phys Rev Lett* 82:3831
191. Bowker M (2006) *Curr Opin Solid State Mater Sci* 10:153
192. Nörenberg H, Dinelli F, Brigs GAD (1999) *Surf Sci* 436:L635
193. Bennett RA, Newton MA, Smith RD, Evans J, Bowker M (2002) *Mater Sci Technol* 18:710
194. Bennett RA, Tarr DM, Mulheran PA (2003) *J Phys Condens Matter* 15:S3139
195. Bowker M (2007) *Phys Chem Chem Phys* 9:3514
196. Maeda Y, Fuitani T, Tsubota S, Haruta M (2004) *Surf Sci* 562:1
197. Sedona F, Agnoli S, Fanetti M, Kholomanov I, Cavaliere E, Gavioli L, Granozzi G (2007) *J Phys Chem C* 111:8024
198. Berdunov N, Mariotto G, Balakrishnan K, Murphy S, Shvets IV (2006) *Surf Sci* 600:L287
199. Stepanow S, Lin N, Barth JV, Kern K (2006) *J Phys Chem B* 110:23472
200. Stepanow S, Lin N, Payer D, Schlickum U, Klappenberger F, Zoppellaro G, Ruben M, Brune H, Barth JV, Kern K (2007) *Angew Chem* 119:724
201. Spillmann H, Kiebele A, Stöhr M, Jung TA, Bonifazi D, Cheng F, Diederich F (2006) *Adv Mater* 18:275

-
202. Bonifazi D, Kiebele A, Stöhr M, Cheng F, Diederich F, Spillmann H (2007) *Adv Funct Mater* 17:1051
 203. Wang C, Bai CL (2006) Template effects of molecular assemblies studied by scanning tunneling microscopy (STM). In: Bhushan B, Fuchs H (eds) *Applied Scanning Probe Methods IV*. Springer, Berlin Heidelberg, p 159
 204. Safarowsky C, Rang A, Schalley CA, Wandelt K, Broekmann P (2005) *Electrochim Acta* 50:4257

Two-Dimensional Crystal Engineering at the Liquid–Solid Interface

Shuhei Furukawa^{1,2} · Steven De Feyter¹ (✉)

¹Division of Molecular and Nano Materials, Department of Chemistry,
and INPAC – Institute for Nanoscale Physics and Chemistry,
Katholieke Universiteit Leuven, Celestijnenlaan 200F, 3001 Leuven, Belgium
Steven.DeFeyter@chem.kuleuven.be

²Present address:

ERATO Kitagawa Integrated Pores Project, Japan Science and Technology Agency (JST),
Kyoto Research Park Bldg 3, Shimogyo-ku, 600-8815 Kyoto, Japan

1	Introduction	88
1.1	Two-Dimensional Crystals	88
1.2	Crystal Engineering Concept	89
1.3	From 3D to 2D Crystal Systems	89
1.4	Self-Assembling Processes Leading to 2D Crystals	90
1.5	Network Topology	91
2	Conformational Control of Molecules	92
3	Directional Forces in Control	93
3.1	Hydrogen Bonding	93
3.2	Metal–Ligand Coordination	96
4	One-Dimensional and Two-Dimensional Patterns	98
4.1	1D	98
4.2	2D	101
5	Multicomponent	105
6	2D Porous Structures	112
6.1	2D Pores: Connected by Hydrogen Bonds	113
6.2	2D Pores: Connected by Alkyl Chains	116
7	The Effect of the Solvent	121
8	The Effect of the Substrate	122
9	From Monolayers to Multilayers	124
10	Functionality and Reactivity in 2D	125
10.1	From Molecular Electronics	125
10.2	... to Polymerization and Reactivity	126
11	Conclusions and Perspectives	129
	References	130

Abstract Three-dimensional crystal engineering is a well-known concept. The invention of the scanning tunneling microscope opened the door to explore this engineering concept in two dimensions with submolecular resolution. The tools of supramolecular chemistry are also at play on surfaces but the large variety of interactions—molecule–molecule, molecule–substrate, molecule–solvent, solvent–substrate—are a challenge for the design of appropriate molecules which self-assemble at the liquid–solid interface into the targeted pattern. Herein, we review the efforts to reach the ultimate goal, two-dimensional crystal engineering at the liquid–solid interface, including the formation of two-dimensional porous networks and multicomponent systems. Two-dimensional crystal engineering is more than an academic effort: it finds applications in fields ranging from molecular electronics to reactivity on surfaces.

Keywords Crystal · Engineering · Scanning tunneling microscopy · Supramolecular chemistry

Abbreviations

2D	Two-dimensional
2DSD	Two-dimensional structural database
3D	Three-dimensional
DBA	Dehydrobenzo[12]annulenes
HBC	Hexabenzocoronene
HOPG	Highly oriented pyrolytic graphite
ISA	Isophthalic acid
MM	Molecular mechanics
PA	Phthalic acid
PAH	Polycyclic aromatic hydrocarbon
SAM	Self-assembled monolayer
STM	Scanning tunneling microscope
TTA	Terephthalic acid
TTF	Tetrathiofulvalene
UV	Ultraviolet
UHV	Ultra-high vacuum

1

Introduction

1.1

Two-Dimensional Crystals

Control of the lateral assembly and spatial arrangement of molecules on surfaces is the subject of intensive research, because it potentially allows these surfaces to become functional, e.g. conductive, catalytically active, porous, chiral, etc. To create two-dimensional (2D) patterns on atomically flat surfaces, there are mainly two approaches. The first one is the spontaneous formation of chemisorbed self-assembled monolayers (SAMs), where the molecules are immobilized on substrates by chemisorption, e.g. thi-

ols on gold. The molecules are almost oriented vertically and the strong molecule-substrate interaction allows for isolating and investigating individual molecules embedded in a matrix. In contrast to chemisorption, the second approach, physisorption, is a weaker type of interaction, rendering the molecules more mobile, a prerequisite to form dense and surface-confined ordered—crystalline— phases. Here, we review the formation of 2D highly crystalline phases at the liquid–solid interface, induced by physisorption.

1.2

Crystal Engineering Concept

Remarkable progress has been made in the area of molecular organic or organic–inorganic hybrid crystal materials with infinite network systems. One of the promising routes to create such molecular-based materials is self-assembly, where selective and directional non-covalent interactions such as hydrogen bonds and coordination bonds between molecules dominate the topologies of molecular architectures. This synthetic strategy is known as *crystal-engineering* or crystal network prediction in the field of three-dimensional (3D) crystal systems [1–5].

The entire network structure is divided into several components, so-called molecular building-blocks or tectons, which consist of core parts and interaction parts. The geometrical shape of the core part controls the direction of the interaction. The interaction parts are substituents such as carboxylic acid groups for hydrogen bonds and carboxylates for coordination bonds, which control the interaction strength and affect the equilibrium of the crystallization process. By choosing appropriate molecular building blocks, we can construct the desired molecular networks and frameworks.

1.3

From 3D to 2D Crystal Systems

Thanks to the success of single-crystal X-ray crystallography an enormous amount of information on molecular networks in 3D crystals is available and this database supports the application of 3D crystals as solid-state materials. 2D crystals are also expected to be important for several types of applications, for instance in the field of molecular electronics where the electronic devices most likely will need to be supported by a substrate. However, at surfaces, this *crystal engineering* concept has not been fully exploited yet (Fig. 1). Scanning probe techniques, the tools which allow the investigation of molecular order on surfaces with submolecular resolution, are a relatively new family of techniques and the field of 2D crystal engineering started roughly only about 15 years ago. The current research still focuses on understanding the processes which control the outcome of the self-assembly process, and applications are rare. The invention of the scan-

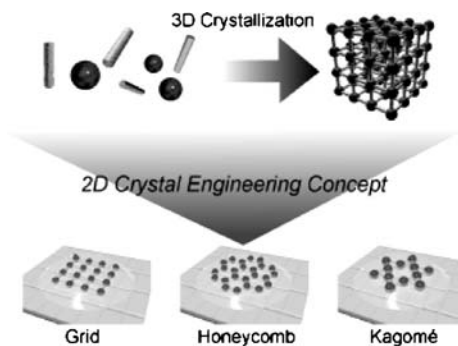


Fig. 1 2D crystal engineering concept

ning tunneling microscope (STM) [6] in the early 1980s opened new ways to investigate surface phenomena on a truly atomic scale thanks to the localized nature of the probing. In STM, a metallic tip is brought very close to a conductive substrate and by applying a voltage between both conductive media, a tunneling current may result. The exponential distance dependence of the tunneling current provides excellent means to control the distance between the probe and the surface, and molecules and molecular assemblies can be visualized with almost atomic resolution. While single-crystal X-ray crystallography typically delivers an averaged structure of an entire 3D single-crystal, STM allows investigating 2D crystals in real space, revealing structural aspects, including defects, impossible to observe by averaging techniques.

1.4

Self-Assembling Processes Leading to 2D Crystals

Typically 3D crystals grow from a solution containing the molecular building blocks. Collisions of these molecular components induce the nucleation of crystals, followed by a growth process on their crystal surfaces. The interaction strength between the building-blocks plays an important role in controlling the kinetic aspects of the crystallization process. The formation of 2D crystals, and their visualization, typically occurs in two different environments: either under ultra-high vacuum (UHV) condition or in solution, thus, at liquid–solid interfaces.

In UHV, molecules are deposited by molecular beam epitaxy, and the mobility of the molecules is restricted to the surface plane, which allows molecules to rotate and translate and to find each other in order to form the thermodynamically most stable structure at a given temperature. Therefore, by tuning the annealing temperature, the network structure can be controlled.

The liquid–solid interface supports the growth of 2D crystals on surfaces too. The liquid phase acts as a reservoir of dissolved species which can diffuse towards the substrate, adsorb, diffuse laterally and desorb. These dynamic processes favor the repair of defects. Under equilibrium conditions, relatively large domains of well-ordered patterns are formed. Large domains grow at the expense of small domains via a process which is called Ostwald ripening. Furthermore, the solvent plays a significant role in the network formation. The choice of solvent affects the mobility of molecules, especially, the adsorption–desorption dynamics via the solvation energy and possibly also via solvent viscosity.

Molecule–substrate interactions affect the outcome of the self-assembly process too; a too strong interaction slows down the molecular mobility and impedes the formation of 2D crystals. Too weak interactions hamper the surface-confined formation of 2D crystals too. In the case of physisorption, the molecule–substrate interactions are of the van der Waals type. The strength of this interaction can be tuned by the molecular composition and by the choice of the substrate. These substrates are typically atomically flat metal or semimetal crystals. The symmetry matching of the molecules with the substrate affects the molecular network topologies. Hence, for a successful rational fabrication of network structures on surfaces, a deep understanding of such molecule–substrate interactions is essential.

1.5

Network Topology

In this contribution, we focus on the formation of monolayer networks at the liquid–solid interface and the parameters controlling the molecular ordering, highlighting the role of intermolecular interactions, the solvent and the substrate (Fig. 2). Reducing the dimensionality of the crystal system from 3D to 2D simplifies the design of the network topologies to 1D and 2D networks. We discuss the formation of multicomponent networks and pay a lot of at-

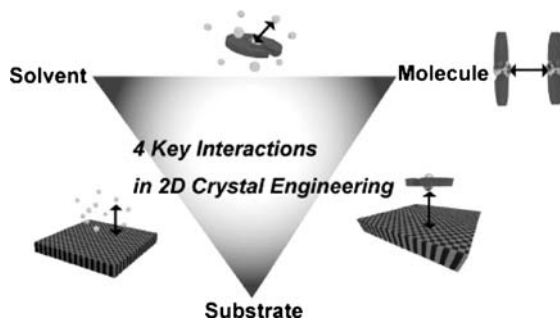


Fig. 2 Self-assembly at the liquid–solid interface: the interactions involved

tention to a new class of 2D crystals, the 2D nanoporous systems. Finally, we end by illustrating the potential of these surface-confined 2D crystals in the area of molecular electronics and chemical reactivity. Instead of giving an exhaustive overview of all studies reported at the liquid–solid interface, we prefer to limit ourselves to a number of examples which clearly illustrate the power and limitations of crystal engineering at the liquid–solid interface.

2

Conformational Control of Molecules

Engineering refers to control, control of the structure-properties of the building blocks and control of the engineered architecture. At the molecular level, an important aspect of engineering is control of the molecular conformation. Upon adsorption of a molecule from solution onto the substrate, there is a substantial decrease in the conformational degrees of freedom. The challenge is to design the molecular building block so that upon adsorption on the surface, its preferred 2D conformation matches the conditions set for successful 2D crystallization (long-range order): important aspects are “shape complementarity”—leading to a dense defect-free 2D molecular network—and “functionality complementarity”—leading to optimal intermolecular interactions which complement the “shape complementarity”. Foldamers are an interesting class of molecules to investigate this aspect. A 2D turn mimic should obey the requirements that (1) the entire structure is flat, (2) the alkyl groups are spaced by approximately 5.0 Å, that is the optimal distance for H-bonding between hydrogen bonding functional groups in those alkyl chains, and (3) the H-bonding groups should be kept in registry, with respect to position as well as orientation. Such a 2D turn element was designed for oligo-amide sequences [7]. The catechol moiety (Fig. 3) is flat and bifunctional; the ortho-substitution pattern endows the structure with the necessary geometry for making turns. A systematic conformational search identified the conformation most likely to fold in a plane involving the formation of an intramolecular hydrogen bond. The length of the spacers between the catechol and amide moieties is the crucial parameter in the folding process. As forecasted by the calculations, derivatives obeying the rule $n = m + 1$ or $n = m + 3$ give folded structures upon adsorption at the liquid–solid interface. However, in general no long-range ordering is observed and only in the case where the amide groups are positioned asymmetrically with respect to the length of the alkyl chains ($m = 3$, $n = 6$), 2D crystals of perfectly folded molecules are formed. The latter aspect is very important, introducing asymmetry allows enthalpy to overrule entropy: limit the orientational choice of the molecules by favoring one in terms of enthalpy interactions.

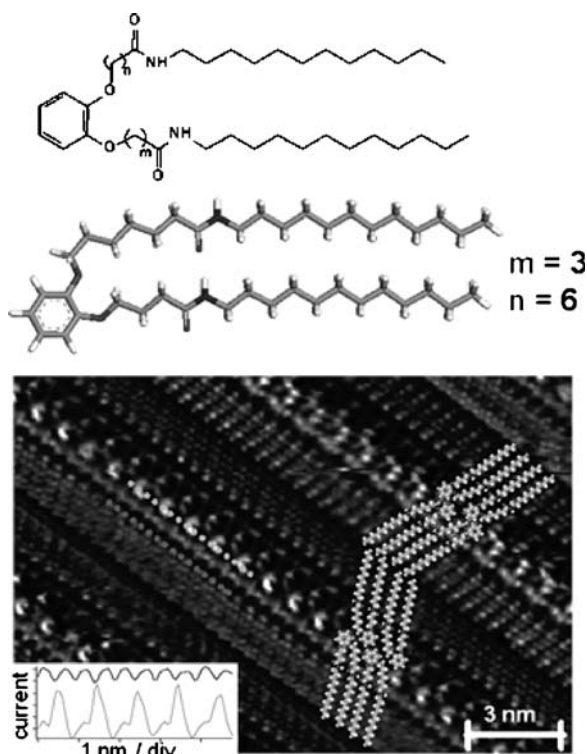


Fig. 3 *Top*: molecular models of the foldamers. *Bottom*: constant-height STM image of a monolayer of the foldamer ($m = 3$, $n = 6$) at the 1-octanol-graphite interface. *Insets*: line profiles and a tentative model of packing. (Reproduced with permission from [7])

3 Directional Forces in Control

Hydrogen bonding and metal–ligand-based interactions are the favored interactions to direct the self-assembly of molecules on a surface because these are a relatively strong and directional type of interaction. In other words, they are ideal from an “engineering” point of view. First, we will introduce the concept of hydrogen bonding in directing the molecular order on surfaces. Second, metal–ligand interactions as promising modes of interactions to steer molecular self-assembly on surfaces will be discussed.

3.1 Hydrogen Bonding

Some of the simplest compounds are the phthalic acid derivatives (Fig. 4). They consist of a phenyl group and two or more carboxylic acid groups.

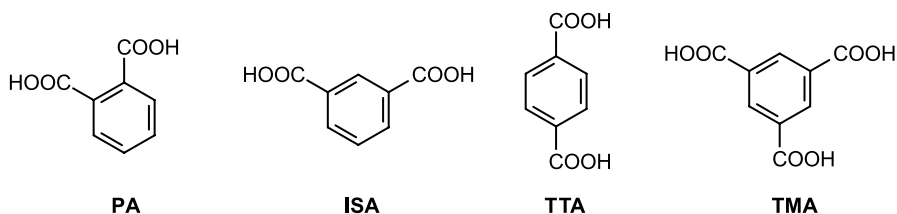


Fig. 4 Chemical structures of benzene carboxylic acid derivatives

On the basis of the relative position of the carboxylic acid groups they are called phthalic acid (PA) (1,2-benzenedicarboxylic acid), isophthalic acid (ISA) (1,3-benzenedicarboxylic acid) and terephthalic acid (TTA) (1,4-benzenedicarboxylic acid). If both carboxylic acid groups are in the 1,2-position (phthalic acid), no monolayer formation was observed at the liquid–solid interface. This is attributed to the fact that the carboxylic acid groups are not co-planar and therefore the molecule is not flat. More importantly, it is conceptually not possible for phthalic acid to form extended rows based upon hydrogen bond interactions between the carboxylic acid groups. In the case of TTA and ISA, densely packed structures are formed. The outcome of the self-assembly is dominated by the hydrogen-bonding interactions between the molecules [8]. In addition, van der Waals interactions between the phenyl groups stabilize the patterns. As expected, TTA self-assembles into linear chains with the molecules linked by hydrogen bonds between adjacent carboxylic acid groups (Fig. 5 *Left*). ISA self-assembles in zigzag rows, again dominated by the hydrogen-bonding interactions between the carboxylic acid groups (Fig. 5 *Right*). Trimesic acid (TMA) (1,3,5-benzenetricarboxylic acid) forms 2D porous structures, an aspect which will be discussed in detail in Sect. 6.

Very often, alkylated molecules are used for self-assembly purposes. This is because of the very good match between the structural parameters of the

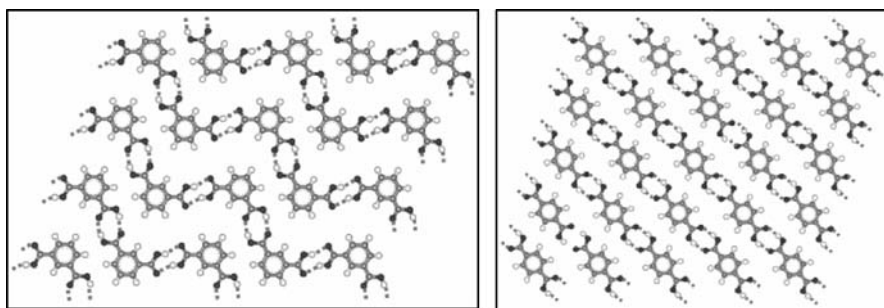


Fig. 5 *Left*: 2D crystal packing of ISA. *Right*: 2D crystal packing of TA. (Reproduced with permission from [8])

alkyl chains (the distance between next neighbor methylene groups measures 2.51 Å) and the distance between adjacent hexagons in the graphite lattice (2.46 Å). The correspondence between the zigzag alternation of methylene groups and the distance between the honeycomb centers of the graphite leads to a stabilization energy of about 64 meV per methylene group [9, 10]. On the one hand this is a blessing. The van der Waals interactions between the alkyl chains and graphite lead to relatively strong but reversible interaction energies, stabilizing the adsorption of the molecules [11]. Alkylated molecules are physisorbed on graphite and typically, molecules can translate over the surface or desorb/readsorb. This mobility is crucial in order to achieve a highly regular packing within the time scale of the experiment (typically several hours). On the other hand, alkylation often complicates the outcome of the self-assembly process as the final result can deviate from the anticipated pattern based on directional non-covalent interactions. Despite the fact that the molecule-substrate interactions are relatively weak, intermolecular interactions between alkyl chains compete with intermolecular hydrogen bonding (or other directional) interactions. This effect/competition is the more important the longer the alkyl chains. Furthermore, the alkyl chains are typically directed along one of the main symmetry axes of graphite, and again, this tendency is more pronounced for the longer alkyl chains. Let us first discuss an example where alkyl chain-alkyl chain and alkyl chain-substrate interactions support the intrinsic outcome of the self-assembly pattern directed by hydrogen-bonding. An alkylated terephthalic acid derivative (2,5-bis(dodecyloxy)terephthalic acid) (TTA1) self-assembles in a 2D crystal at the liquid-solid interface (Fig. 6C,D) [12]. All terephthalic acid groups (the bright features) are perfectly in line and the alkyl chains between rows of terephthalic acid groups are separated by interdigitated alkyl chains which run almost perpendicular to these terephthalic acid rows (but parallel to one of the main symmetry axes of graphite). The distance between terephthalic acid groups along a row is 0.960 ± 0.008 nm, which matches very well the distance between terephthalic acid molecules in 3D crystals (0.955 nm) and the interaction between the terephthalic acid groups matches the one for alkyl-free TTAs. The distance between the alkyl chains is about 0.48 nm. In contrast to alkylated terephthalic acid molecules, isophthalic acid derivatives with a linear alkyl chain in the 5-position, such as ISA1 self-assemble into a 2D crystal which is quite different from the one formed by isophthalic acid itself (Fig. 6A) [13]. The ISA groups are arranged in a double row adopting a distorted “zig/zag” pattern. The alkyl chains are fully extended, interdigitated, closely packed, and almost perpendicular to the lamella axis. The intermolecular distance between ISA moieties along a row measures only 9.4 ± 0.2 . This is in contrast with the situation in 3D crystals of the same type of molecule, where the distance between ISA groups is 15.7 Å [14]. Despite the directional nature of hydrogen bonding, optimal hydrogen bonding between ISA groups based upon the classical carboxylic acid dimer is not

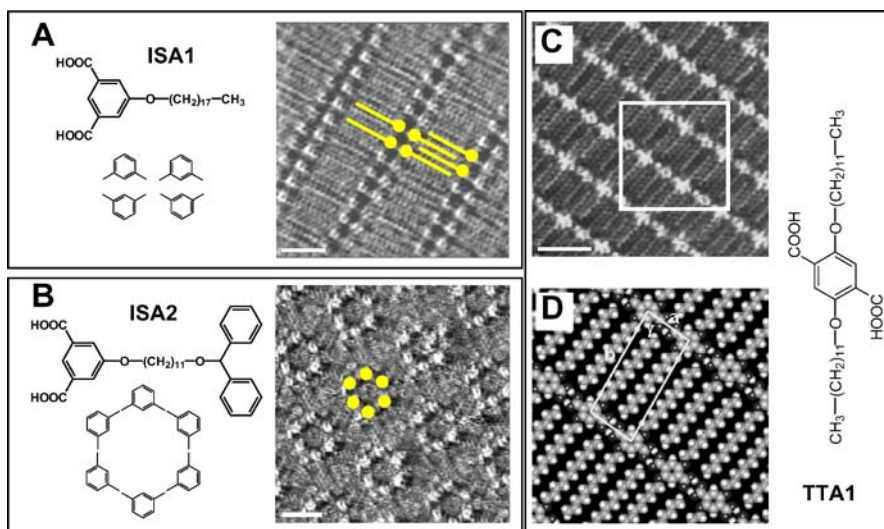


Fig. 6 Chemical structures, representative STM image and schematic motif/model of **A** ISA1 physisorbed at the 1-phenyloctane-graphite interface, **B** ISA2 at the 1-octanol-graphite interface, and **C, D** TTA1 at the 1-phenyloctane-graphite interface. The *scale bar* in the STM images represents 2 nm. (Reproduced with permission from [12] and [13])

formed. The interaction between the interdigitating alkyl chains and the alkyl chain–substrate interaction plays a crucial role in directing the ordering of these alkylated isophthalic acid molecules. In contrast, a new motif is formed when bulky benzhydryl groups are introduced at the end of a long alkyl chain (ISA2). This molecule exclusively shows the formation of rosette structures, containing six molecules (Fig. 6B). The rosettes are by themselves organized in a hexagonal arrangement. The bright features are attributed to the location of the aromatic ISA groups and close inspection indeed shows that every ring is composed of six bright spots, indicating stabilization by hydrogen bonding. The interior of these rosettes might be filled with mobile solvent molecules. So, changing the nature of the alkyl chain may affect the hydrogen bonding motif formed. As we will see later, the formation of a rosette-type pattern is typical for TMA.

3.2

Metal–Ligand Coordination

The self-assembly of metal–ligand-based architectures at surfaces is a promising and versatile method for the fabrication of 2D metal-ion arrays. Most of those experiments have been carried out under UHV conditions showing the remarkable potential of this approach [15]. Under ambient conditions, only in a few occasions metal–ligand polymers [16] or 2D grids [17–19] are formed.

Most examples deal with the self-assembly of alkylated ligands which upon complexation to dimers or tetramers, organize in 2D networks [20]. As an example we highlight the bottom-up fabrication of 1D coordination networks that form 1D and 2D arrays on graphite under ambient conditions. In order to realize 1D networks, a noncentric **tecton** or building block bearing two coordination poles was designed. A combination of tectons which expose one monodendate and one tridentate coordination pole with metal centers offering four free coordination sites that occupy the corners of a square match the requirement for the formation of directional 1D coordination networks (Fig. 7A). For the metal center, either octahedral dicationic metals associated with two coordinating anions occupying the apical positions or square-planer metal centers could be used. Indeed, the combination of the neutral **tecton** with CoCl_2 led to the formation of 1D coordination networks on graphite

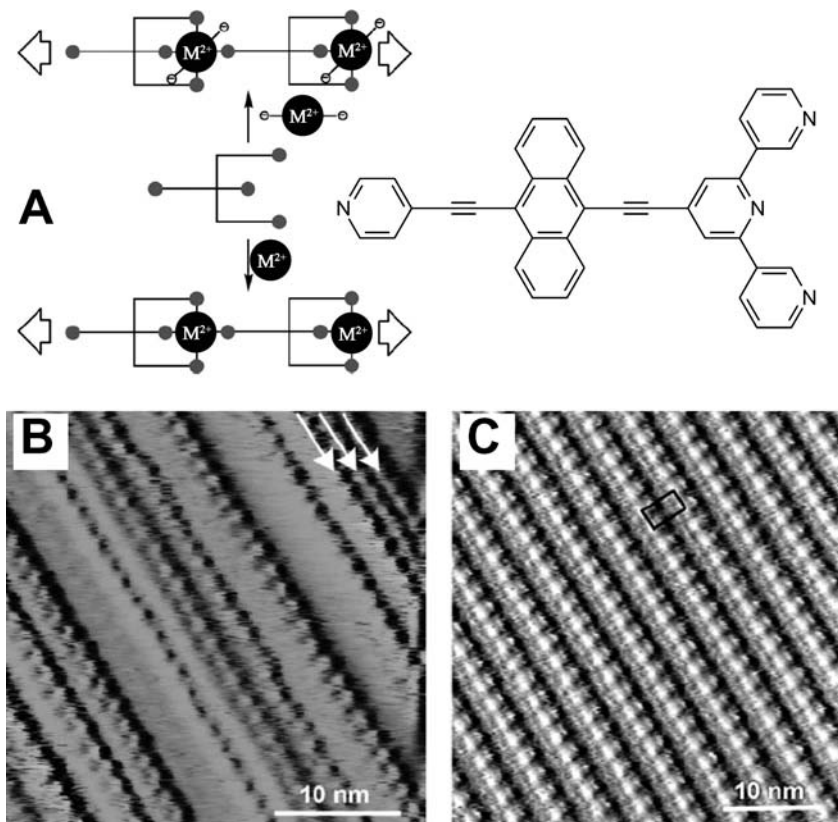


Fig. 7 A Schematic representation of the principle of 1D network formation based on metal-ligand coordination and chemical structure of **tecton**. B, C STM images of the network generated upon combining the tecton with B CoCl_2 and C Pd^{II} . (Reproduced with permission from [16])

(Fig. 7B). Perfectly straight nanostructures with a length up to 400 nm were obtained. Given the high electron densities of Co^{II} metal centers, the bright spots along the rows, separated by 1.7 nm, were attributed to the Co ions complexed with the **tecton**. Note that the orientation of adjacent rows is not correlated. In the case of Pd^{II} , regular 2D lattices were formed (Fig. 7C), a feature which will be discussed in Sect. 4.2.

4

One-Dimensional and Two-Dimensional Patterns

2D crystal engineering assumes the formation of regular and defect-free patterns ... in 2D. There are many examples though at the liquid–solid interface where the order is mainly along one direction only, therefore 1D. We will discuss some aspects of how to control order in 1D and how to make sure that 1D repetition is the major outcome of the self-assembly. Overall ordering in 2D might be achieved simultaneously but is not necessarily the prime target, in terms of an anticipated application (e.g. the formation of conjugated (conductive) supramolecular chains). By listing some of the aspects which favor 1D growth, simultaneously we also deal with those aspects of the self-assembly which favors regular pattern formation in 2D.

4.1

1D

The typical way to stimulate and favor 1D growth is the design of molecules which contain strong directional groups in the “center” of the molecules and only weak non-directional groups at their extremes.

Quinacridone is a text-book example of a molecule which carries all information to self-assemble into 1D stacks via hydrogen bonding (Fig. 8). On its long sides, it carries carbonyl and amine functions. These strong intermolecular hydrogen-bonding interactions render this molecule typically insoluble. Quinacridone is an organic semiconductor and a commercial product of the pigment industry. Recently, a new approach was described for the preparation of surface-supported supramolecular structures of this dye [21]. Most of the molecular systems discussed herein self-assemble at the liquid–solid interface. It is a major challenge though to induce the self-assembly of insoluble species on a substrate, not using high-tech approaches such as vacuum sublimation (organic molecular beam epitaxy). A technique was introduced where nanocrystals of the respective compound are brought into direct contact with the substrate. The concept is simple: when the binding energy of the molecule to the substrate exceeds the binding energy of the molecules in the nanoparticle, single molecules will detach from the nanoparticle, and adsorb on the substrate surface. In combination with thermally activated diffusion, highly

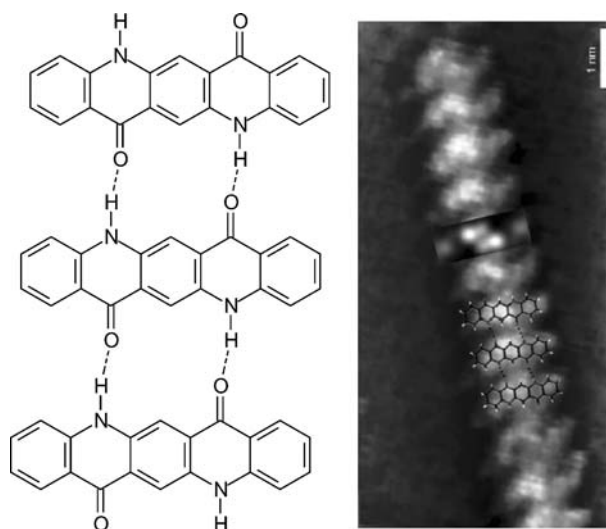


Fig. 8 *Left*: chemical structure of quinacridone and supramolecular chains. *Right*: STM image of quinacridone supramolecular wires on graphite. (Reproduced with permission from [21])

ordered supramolecular chains can form. The growth is definitively 1D controlled. Gaps of various sizes between the 1D structures give rise to structures which are more complex than a truly periodic pattern in 2D.

In contrast to quinacridones, porphyrins and phthalocyanines, decorated with carboxylic acid groups, spontaneously self-assemble into 2D patterns due to their symmetry [22].

A related system which forms 1D structures based upon metal–ligand coordination has already been introduced in Sect. 3.2. On the one hand, the combination of **tecton** and CoCl_2 gave rise to pure 1D metal–ligand polymers. There was no extension of order into 2D. On the other hand, complexation of the same tecton with Pd^{II} displays the parallel packing of 1D networks that leads to the generation of a 2D nanoscale array. What is the difference between both systems? In both cases, the high shape persistence of the 1D nanostructures is determined by the directionality of the coordination bonds formed between the metal center and **tecton** and the rigidity of the latter. It is suggested that the parallel stacking of the 1D structures of Co is due to the graphite substrate lattice where step edges dictate the relative orientation of the networks assembled at the surface. Because of the nonplanarity of the octahedral assembling node, the ligand backbones cannot be fully planar on the graphite substrate, and it is suggested that the 1D networks are stabilized by interactions with the step edges of graphite rather than by side-to-side packing interactions between the 1D rows. In the case of Pd^{II} a charged square-planar assembling node is formed by the palladium center and one terpyridine and one pyridine

unit belonging to consecutive tectons. In contrast to CoCl_2 , the orientation of the 1D networks are laterally correlated suggesting a cooperative process that takes place during the generation of 1D networks on graphite. Moreover, the unit cell area suggests the coadsorption of BF_4^- counterions in the monolayer. The lateral correlation may also be attributed to the planar disposition of the assembling node, and thus the 1D networks favoring π -stacks interactions between the polycationic 1D networks and the surface.

Both the hydrogen-bonding and metal–ligand coordination example show that 1D directionality leads to 1D periodicity which is not necessarily extended into 2D regular networks. As hydrogen bonding is the most popular type of interaction at the liquid–solid interface, we will continue to use this type of interaction to demonstrate “engineering” principles at the liquid–solid interface.

Substances are often alkylated in order to enhance their solubility but also to assist the molecules into assembling in ordered structures at the liquid–solid interface. In addition to the alkylation of quinacridones [23], this approach has also been used for the formation of 1D stacks of alkylated oligothiophenes and tetrathiofulvalene (TTF) derivatives. In contrast to quinacridones, oligothiophenes and TTF do not carry functional groups which lead to directional intermolecular interactions. Moreover, in case of the quinacridones, the molecules are lying with their conjugated part parallel to the substrate. In view of the objective to form supramolecular stacks of molecules which are potentially efficient charge carriers, it is crucial to have these semiconductor type molecules oriented such that their conjugated planes overlap, at least in part. These π -electron rich units stack flat on the graphite surface in the absence of strong intermolecular interactions. It turned out that the introduction of amide or urea groups in the alkyl chain side groups is very effective to generate hydrogen-bonded chains and to modify the molecular orientation and create one-dimensional assemblies. For instance, in the case of the oligothiophene derivatives [24], within a lamella each molecule is stabilized by eight hydrogen bonds, which determines the intermolecular distance of 0.46 nm. Also in the case of the alkylated TTF derivative (Fig. 9), the STM images of physisorbed layers show equally spaced continuous lines of high tunneling current, indicative of the formation of supramolecular fibers at the surface [25]. The repeat distance between TTF units within a fiber was found to be approximately 0.44 ± 0.03 nm, in good accord with an X-ray structure of a related molecule with one amide group. The planes of the TTF moieties are not parallel to the highly oriented pyrolytic graphite (HOPG) surface, but are tilted up with stacking between them at a high angle to the plane. Molecular modeling of several columnar stacks with molecular mechanics (MM) shows that among the stable structures found, those in which both π – π interactions and hydrogen bonding are both operative give rise to straight, regular stacks with the TTF units parallel to each other. To address the issue of the molecule–molecule versus molecule–substrate interactions, two different types of stacks on the

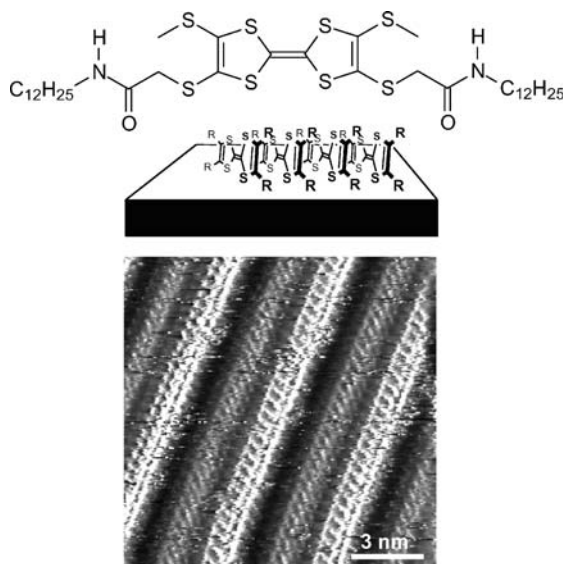


Fig. 9 *Top*: chemical structure of the TTF derivative. *Middle*: cartoon of the TTF stacking. *Bottom*: STM image of the TTF derivative at the HOPG–octanoic acid interface. (Reproduced with permission from [25])

graphite surface were modeled, examining their behavior in time at room temperature with molecular dynamics. A stack of the unsubstituted TTF's, i.e. without amide groups, breaks up and the molecules are spread on the surface, adsorbed flat because of the strong interaction of the TTF with the π -system of graphite. In contrast, amide-substituted TTF stacks are stable: the planes of TTF units remain perpendicular to the surface and parallel to each other and the hydrogen-bonding pattern between the amide groups is preserved. This shows that hydrogen bonding is required to maintain the TTF units in a 1D π -stacking configuration.

The lateral interaction between the 1D rows is definitely much weaker than along the 1D rows. Does it mean that these patterns of alkylated molecules are not periodic in 2D? Not necessarily, some of these 1D systems will assemble into highly ordered 2D structures, while others will not. For instance, in the case of alkylated bis-ureaderivatives (with or without oligothiophenes), the molecular orientation in adjacent rows, defined by the orientation of the carbonyl groups, is not correlated [26].

4.2 2D

Are the alkylated terephthalic acid derivatives discussed in Sect. 3.1 a good example of 1D driven crystallization? Actually, they are not. The central

terephthalic acid groups are indeed centered in the molecules and perfect rows based upon hydrogen-bonding are formed. It is obvious from Fig. 6C–D though that this molecule forms a perfect 2D crystal. The reason is that alkyl chains of adjacent rows are interdigitated. The distance between two TTA moieties (0.96 nm) is too large for stabilizing van der Waals interactions between alkyl chains of adjacent molecules of the same row. Only if the alkyl chains were tilted by 60° from the row normal, the interchain distance would be appropriate. This is not observed experimentally though. The alkyl chains run almost perpendicular to the TTA rows and alkyl chains of adjacent rows are interdigitated. The interchain distance is then only 0.48 nm and that leads to a stable structure.

A related example is the effect of metal complexation of an alkylated bipyridine derivative on graphite (Fig. 10) [27, 28]. This symmetric bipyri-

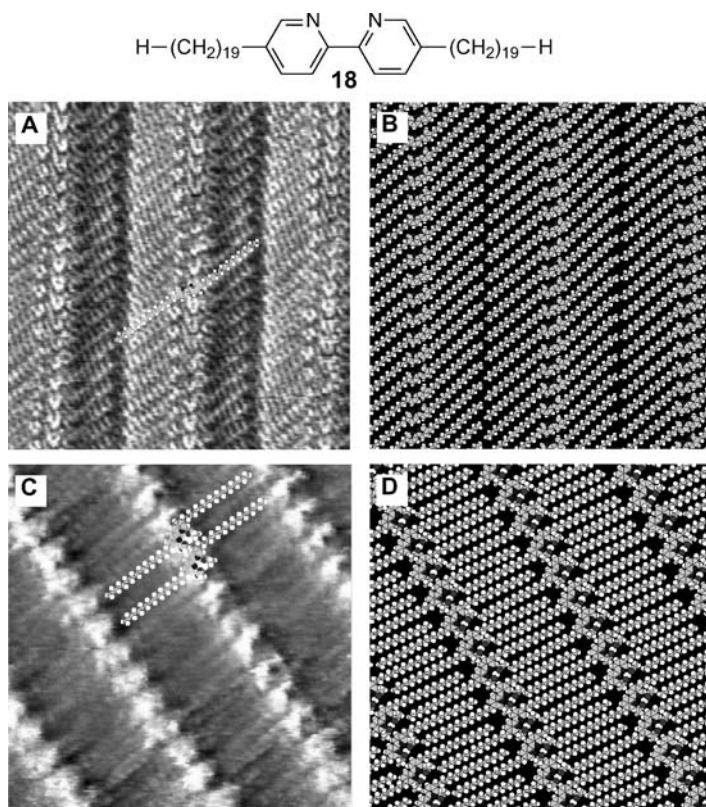


Fig. 10 **A** STM image showing a monolayer of the bipyridine derivative physisorbed at the 1-phenyloctane-graphite interface. Image size: $9.1 \times 9.1 \text{ nm}^2$. **B** Molecular model. **C** STM image showing a monolayer of the bipyridine derivative physisorbed at the 1-phenyloctane-graphite interface after addition of $\text{Pd}(\text{OAc})_2$ solution. Image size: $10.2 \times 10.2 \text{ nm}^2$. **D** Molecular model. (Reproduced with permission from [27])

dine derivative assembles in 1D rows at the liquid–solid interface. The intermolecular distance between two adjacent bipyridine rows is 0.69 nm. That is a fairly large distance and indeed, the alkyl chains do not run perpendicular to the bipyridine row. They form an angle of about 50° which leads to an interchain distance of about 0.45 nm. Upon complexation of the bipyridine moieties with palladium acetate, the distance between two adjacent bipyridine groups increases to 0.94 nm. Similar to the alkylated terephthalic acid derivatives, the alkyl chains run now perpendicular to the rows and those of adjacent rows are interdigitated.

The group of Matzger recently focused on a number of engineering principles and observed for instance that multiple inequivalent molecules are possible in 2D packing [29]. This means that the asymmetric unit contains more than one inequivalent molecule. For instance, 1,3-dinonadecanoylbenzene self-assembles into rows which extend in 2D. A peculiar observation is that adjacent rows are not equivalent (Fig. 11): the dense row contains twice as many molecules as the neighboring rows. One unit cell contains six molecules.

The principle of multiple inequivalent molecules is a well-known phenomenon in 3D crystals and has been confirmed as a general principle by Matzger et al. in 2D crystallization studies of related 1,3-disubstituted benzene derivatives [30]. In total eight different phases were observed at the liquid–solid interface with different degrees of complexity, with varying space groups, number of molecules in the asymmetric unit and conformations. A number of these molecules showed polymorphism. Polymorphism is actually observed quite regularly for 2D crystals at the liquid–solid interface. The determination of most motifs is based on a competition between close packing and distortion of the equilibrium geometry of the individual molecules accommodating electrostatic interactions. For so-called conformational pseudopolymorphism–polymorphism induced by different conforma-

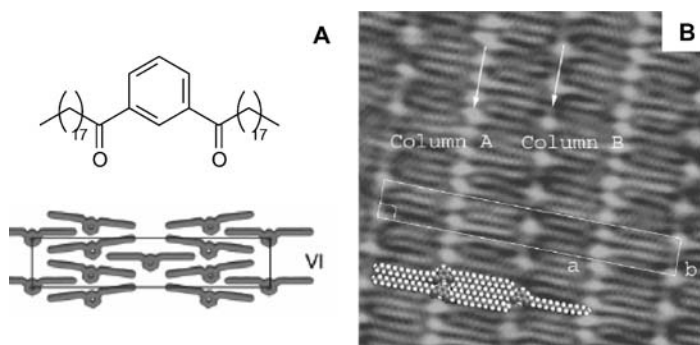


Fig. 11 **A** Chemical model of 1,3-dinonadecanoylbenzene and model of the molecular ordering. **B** STM ($15 \times 15 \text{ nm}^2$) image at the 1-phenyloctane-graphite interface. (Reproduced with permission from [29] and [30])

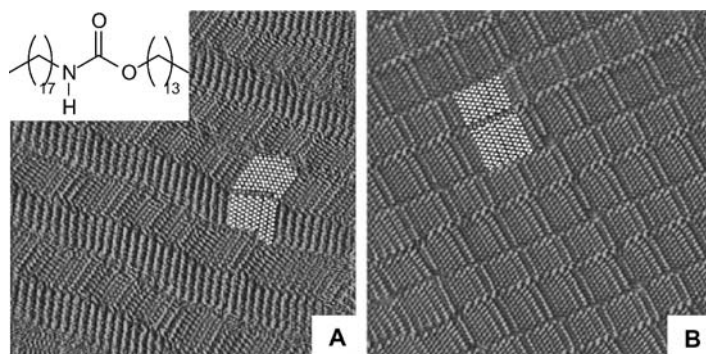


Fig. 12 STM images ($20 \times 10 \text{ nm}^2$) of **carbamate** obtained at the 1-phenyloctane-graphite interface. **A** Bent domain. **B** Linear domain. (Reproduced with permission from [31])

tions of the molecule—it was observed that the order of stability was affected by the length of the alkyl groups [31]. Basically, the **carbamate** (Fig. 12) can adapt a linear or folded conformation as far as the orientation of the alkyl chains is concerned. The bent form enables an optimal hydrogen-bonding geometry at the cost of decreased alkyl chain interaction, whereas the linear form maximizes van de Waals interactions between the alkyl chains while reducing the hydrogen bonding. In addition, in the linear form both alkyl chains can align along one of the main symmetry axes of graphite. Therefore, the alkyl chain length determines which conformation is adopted, with the linear one being favored for carbamates having longer alkyl chains (Fig. 12). Initially both pseudopolymorphs were observed but in function of time, the “bent” polymorph evolved in to the “linear” polymorph [32], via a process which is called Ostwald ripening. For instance, during the first 30 minutes of a measuring session, both polymorphs were observed but in time, “linear” domains grow at the expense of “bent” domains. The “linear” domains are the thermodynamic more stable ones.

Matzger et al. have done a tremendous effort in evaluating the data of all known systems which self-assemble in 2D patterns at the liquid–solid interface so far [33]. More specifically, they have compiled those data in what they call a two-dimensional structural database (2DSD). This compilation is a 2D analogue of the 3D crystal structure databases. They described the 2DSD as “*providing the unified view of interfacial self-assembly essential for investigation of 2D crystallization and comparison with bulk crystals to uncover the basic similarities underlying all forms of self-assembly and the differences due to the presence of an interface*”. 876 monolayers are included in this database. For each entry in the 2DSD, a structural description that matched the STM image was developed including the plane group, the number of molecules in the asymmetric unit, and the symmetry element on which the molecules resides.

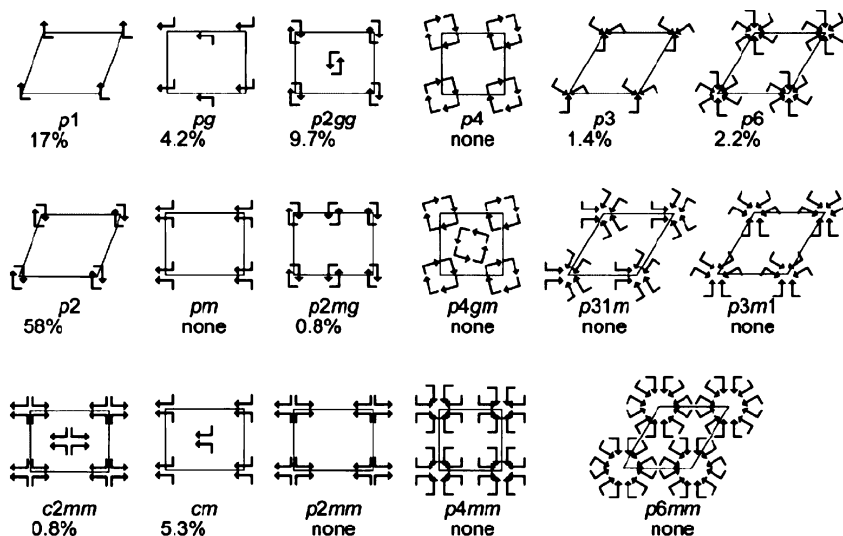


Fig. 13 Schematic representation of the 17 plane groups used to describe monolayer symmetry for entries in the 2DSD, and their abundances. (Reproduced with permission from [33])

Figure 13 is a schematic representation of the 17 plane groups used to describe monolayer symmetry. What strikes is the preference of a few plane group symmetries out of numerous possibilities and it resembles the space group preference apparent in the crystal structures of organic and metallo-organic compounds. In 3D, 5 of the 230 space groups describe more than 75% of all crystal structures. These space groups have in common that they allow the densest packing and maximize intermolecular interactions. In 2D, the plane groups $p1$, $p2$, pg , and $p2gg$ are predicted to enable objects of any shape to contact the largest number of neighboring objects. And indeed, these space groups are favored. Together $p2$ (58%), $p1$ (17%) and $p2gg$ (10%) represent 85% of these structures. Therefore, it is safe to conclude that the monolayer structures are in general influenced by the tendency toward minimization of empty space.

5 Multicomponent

So far, we have reviewed a number of self-assembling aspects of monocomponent systems in one and two dimensions. It is a challenge to extend the insights gained in these studies to direct the ordering in multicomponent systems. The study of multicomponent networks is an active domain of research and could be the subject of a dedicated review itself. Here, only a few recent

key examples will be introduced aiming at giving some insight in principles ruling multicomponent 2D crystal formation. In this section, we will limit ourselves to the discussion of multicomponent systems [34, 35] which do not arise from the adsorption of guest species in macrocycles or other 2D porous systems (see Sect. 6).

Given that the fabrication of highly ordered monocomponent supramolecular structures by design at surfaces is not always trivial, the controlled formation of multicomponent assemblies with a well-defined ordering creates an even bigger challenge. Many binary mixtures investigated so far show phase separation on the nanometer scale or the formation of randomly mixed monolayers [36–38]. So, what is needed to successfully create this type of multicomponent crystals? There are different approaches. One of the earliest examples reported involved the self-assembly of 5-alkoxy-isophthalic acid derivatives and pyrazine derivatives. The latter ones acted as hydrogen-bond acceptors, and were co-adsorbed in a well-defined fashion between rows of isophthalic acid groups [14]. In a very similar approach, alcohol solvent molecules turned out to co-adsorb in between adjacent isophthalic acid rows [39]. It is important to note at this stage that the solvent is indeed not just a spectator. It can be actively involved in directing the self-assembly process, an aspect which will be covered in some detail in Sect. 7.

Rosei et al. took also advantage of the hydrogen-bonding interaction between carboxylic acid groups and alcohol groups to form well-defined co-crystals of trimesic acid and linear alcohols [40–42]. While TMA typically forms a honeycomb (also called chicken wire) or flower-type 2D porous pattern at the liquid–solid interface (see Sects. 6.1 and 7), in the presence of linear alcohols a new pattern appeared: a mixed monolayer of TMA dimer tapes separated by a tape of perpendicular linear alcohol chains. Interestingly, by changing the length of the alkyl chain, the distance between TMA tapes was modulated (Fig. 14). All alcohols with an odd number of carbon atoms produced a nearly perpendicular orientation of alcohol chain axis with respect to the TMA tape. A small tilt was observed for the alcohols with an even number of alcohol molecules. This difference was interpreted in terms of the dense alkyl-chain packing: for even-numbered alcohols, efficient packing requires adjacent alkyl chains to shift by one carbon atom along the chain axis, resulting in a tilt.

In another study the complex formation of two distinctly different but related systems which are designed to form trimers based upon hydrogen bonding were compared [43]. The central unit of the anticipated trimer is a merocyanine dye (**MER**) or a substituted perylene bisimide derivative (**PB**). Both dyes have two sets of hydrogen bonding sites, i.e. $-\text{CO}-\text{NH}-\text{CO}-$ (imide), where NH is a hydrogen bond donor (D) and CO a hydrogen bond acceptor (A), giving rise to a A–D–A sequence. Most importantly, the relative orientation of the hydrogen bonding units differs in both molecules: in **PB** both A–D–A sets are parallel but facing opposite directions, while in **MER**

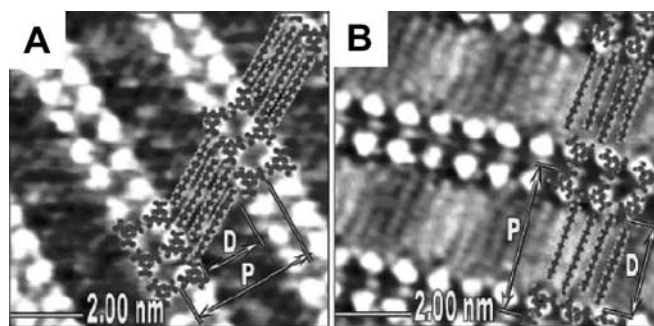


Fig. 14 STM images of a monolayer obtained by mixing TMA with **A** 1-hexadecanol ($C_{16}H_{33}OH$) and **B** 1-heptadecanol ($C_{17}H_{35}OH$) at the heptanoic acid-graphite interface. (Reproduced with permission from [40])

these sets are at an angle of $\sim 120^\circ$. For the formation of well-defined hetero-complexes, an alkylated diamino triazine derivative (**DAT**) having a D–A–D hydrogen-bonding set, i.e. $NH - N - NH$, is selected to form complementary hydrogen bonding with the A–D–A sequence. This type of interaction should favor hetero-complex formation as recently found in solution. It is anticipated that the interaction between **DAT** and **MER** will give rise to a termolecular complex having a *triangle configuration*. Also **DAT** and **PB** are expected to form a termolecular complex, though now in a *linear fashion*. This difference may also strongly affect their long-range ordering. As anticipated upon mixing the two components, termolecular complexes are formed at the liquid–solid interface which is a clear indication that hydrogen bonding is indeed involved (Fig. 15).

However, there are important differences between both systems. A **DAT**/**MER** mixture leads to the formation of true 2D crystals: hetero-complexes are exclusively formed and they organize in large domains. In contrast, **DAT**:**PI**:**DAT** complexes are formed only locally, they assemble in rows, they do not cover complete domains, and they coexist with non-complexed **DAT**-dimers within the same domain. Moreover, also the conditions to achieve hetero-complex formation and 2D ordering are different. For the **DAT**/**MER** system, the solution contains the compounds in a 2 : 1 ratio, anticipating and leading to termolecular (2 : 1) complex formation. Adding the compounds in sequence did not give rise to formation of monolayers of the complex: only domains with the pure compounds were observed. In order to successfully form **DAT**:**PBR**:**DAT** complexes at the liquid–solid interface, it was necessary to add a large excess of **PB**, typically in a 1 : 9 ratio. Both **DAT** and **MER** show a higher affinity for graphite than **PB** as expressed by the fact that both **DAT** and **MER** self-assemble on the surface into ordered monolayers with laterally immobilized molecules, while it was not possible to visualize **PB** under analogous experimental conditions. The very high excess of **PB** required to induce

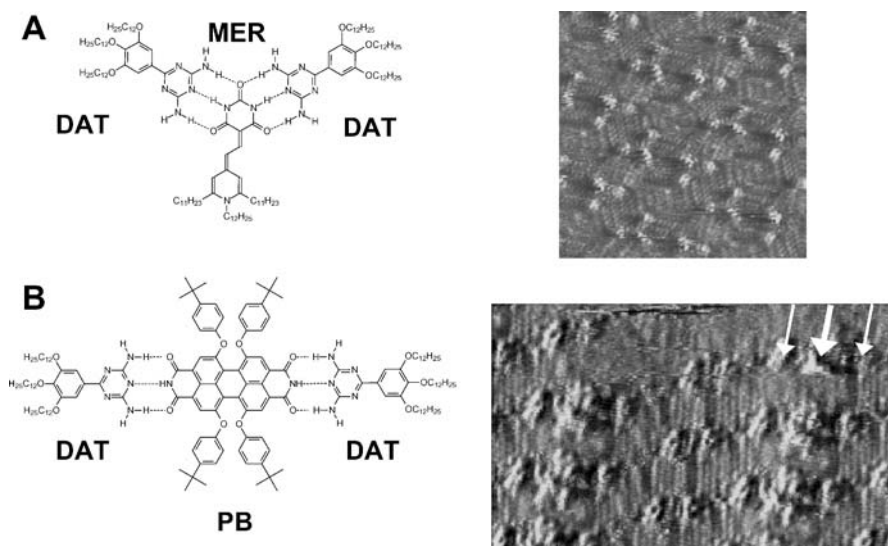


Fig. 15 **A** Scheme of the anticipated termolecular complexes DAT:MER:DAT and corresponding STM image (11.5 × 11.5 nm²). **B** Scheme of the anticipated termolecular complexes DAT:MER:DAT and corresponding STM image (12.3 × 7.5 nm²). (Reproduced with permission from [43])

heterocomplex adsorption, in combination with the fact that **PB** co-adsorbs with **DAT** only gradually in time, leads to the conclusion that the formation of a **DAT**-layer is at least kinetically favored compared to **PB** and heterocomplex adsorption.

The data presented suggest some guidelines for the successful preparation of heterocomplexes based upon hydrogen bonding at the liquid–solid interface and the creation of two-dimensional networks. Heterocomplex formation on surfaces will be favored if in addition to non-covalent interactions between the different partners which exceed the intermolecular interactions between molecules of the same kind, the tendency of adsorption of the heterocomplexes is higher or comparable to the pure components. If so, heterocomplexes formed in solution may successfully adsorb on the substrate and grow to 2D crystals. In the case that heterocomplexes have a lower affinity for adsorption on the substrate than (one of) the pure components, the expected higher affinity of (one of) the pure compounds for the substrate will favor the adsorption of the pure compound(s) and destabilize the heterocomplexes formed in solution. Therefore, heterocomplex formation on the substrate should be disfavored. However, in case the heterocomplex formation does not disturb significantly the 2D ordering of the dominant species (i.e. **DAT** for the **DAT/PB** system), heterocomplex formation might still be observed. Upon successful heterocomplex formation on the substrate, the formation of 2D crystalline domains will be favored if the structure of the

heterocomplexes is not compatible with the ordering of (one of) the pure components.

There is a revival in the study of nucleic acid bases and mixtures thereof at the liquid-solid interface. Besenbacher et al. investigated in detail the self-assembly of pure and mixed assemblies of adenine and thymine [44]. The unique aspect of the current approach is the intimate relation between experiment and molecular modeling revealing unprecedented insight in the self-assembly properties of nucleic acids. The motivation behind the detailed study of these multicomponent systems is the potential of DNA nucleobases to complex proteins and other biological systems.

All the previous examples are based on hydrogen-bonding (donor-acceptor) interactions between the interacting components. However, hydrogen bonding or other directional noncovalent interactions are not a prerequisite to form for instance patterns with alternating rows of molecules. Some alkylated-substituted phthalocyanines adsorb in between rows of 1-iodooctadecane, though the origin of this effect is not well-understood as the interaction between the molecules is of the van der Waals type [45].

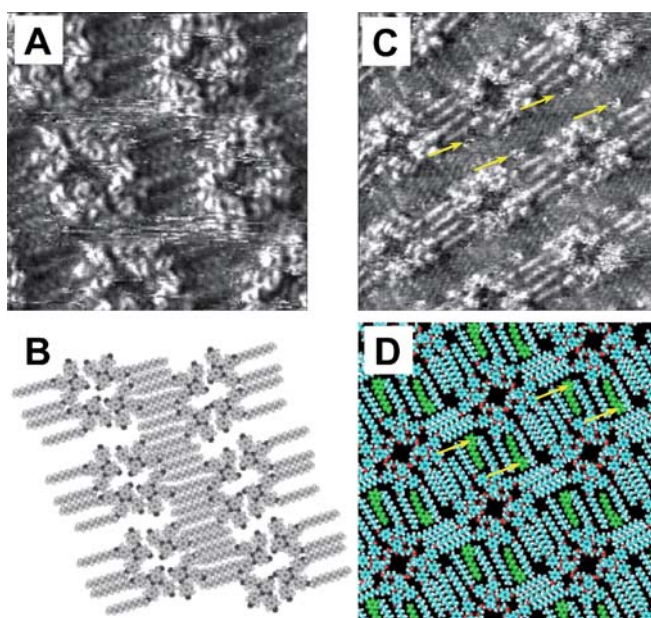


Fig. 16 **A** STM-image ($8.4\text{ nm}\times 8.4\text{ nm}$) of monodendron physisorbed at the 1-octanol-graphite interface. **B** Tentative molecular model. The alkyl chains along the unit cell vector a , and the hydroxyl group containing alkyl parts within the tetramers have been omitted. **C** STM-image ($12.8\text{ nm}\times 12.8\text{ nm}$) of **monodendron** physisorbed at the 1-phenyloctane-graphite interface. The location of the co-adsorbed 1-phenyloctane solvent molecules is indicated by *arrows*. **D** Tentative molecular model. The 1-phenyloctane molecules are indicated by *arrows*. (Reproduced with permission from [47])

Another example is the solvent dependent self-assembly of a **monodendron** at the liquid–solid interface (Fig. 16) [46, 47]. At the 1-octanol-graphite interface, tetramers are formed which appear distorted, and from row to row, the tetramers are tilted with respect to each other. The distance between the tetramers along the vector a measures 3.80 ± 0.06 nm. The alkyl chains between the tetramers along this direction are most likely directed to the solution. At the 1-phenyloctane-graphite interface, also tetramers are formed. The alkyl chains are interdigitated and separated by approximately 0.46 nm and can be divided into two sub-sets, depending on their contrast. Those two subsets are oriented perpendicular to each other. From every monodendron, two alkyl chains are oriented almost perpendicular to the unit cell vector a , and those alkyl chains are oriented along one of the main symmetry axes of graphite. The third alkyl chain which appears with a higher contrast in the images is oriented along the unit cell vector a . Between two tetramers are four of the latter type of alkyl chains. As a result, the distance

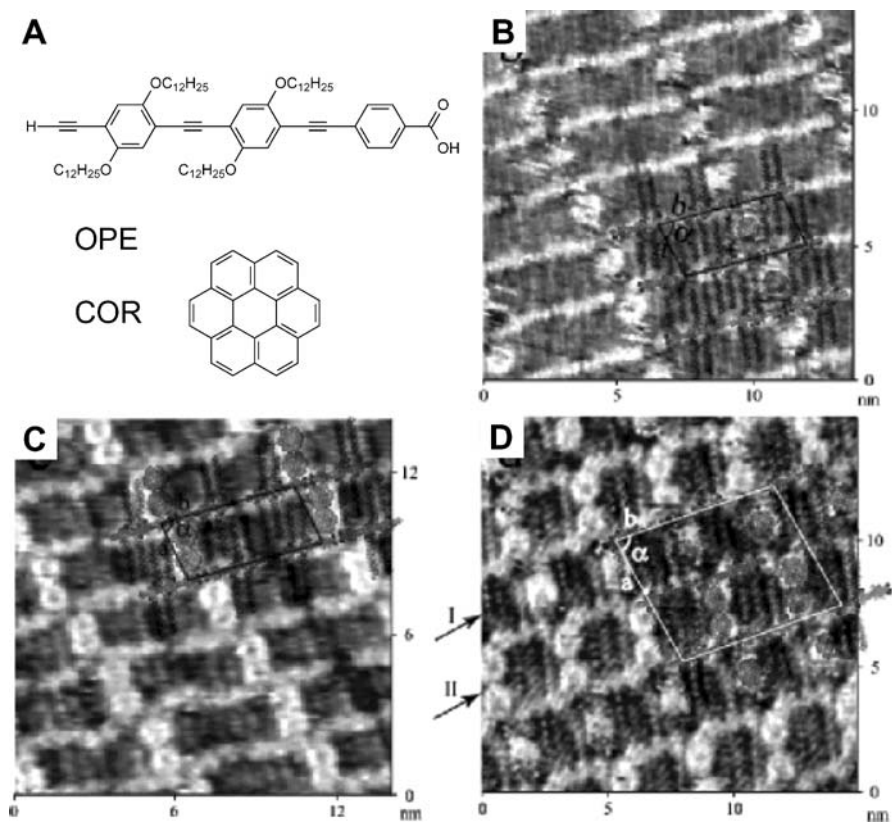


Fig. 17 A Chemical structures of OPE en COR. B–D STM images of different host–guest 2D crystals. (Reproduced with permission of [48])

anthracene rows separated by even length side chains adsorb via opposite enantiotopic faces and form monolayers with pg plane group symmetry (e.g. **Ant4**). If the anthracene rows are separated by odd length side chains, they adsorb via the same enantiotopic faces and the monolayers exhibit $p2$ plane group symmetry (e.g. **Ant3**) (Fig. 18). However, this principle can be overruled if the side chains contain oxygen atoms, e.g. for **Ant1** and **Ant2** which both form monolayers with a $p2$ plane group symmetry. The placement and orientation of the ether dipoles determine the monolayer morphology and overrules the odd–even effect. Dipolar control has been exploited to form co-crystals of **Ant1** and **Ant2**. Indeed, experimentally it is observed that a mixture of both compounds gives rise to a monolayer structure with a pg plane group symmetry. “Dipolar control” considerations strongly suggest that both molecules adsorb in alternating rows (Fig. 18).

6

2D Porous Structures

A relatively new but very exciting development in self-assembly studies at the liquid–solid interface is the formation of 2D surface-confined porous patterns, i.e. supramolecular networks with empty space. There are compounds which intrinsically contain a cavity such as macrocycles. Upon 2D self-assembly, a regular lattice of these macrocycles (and therefore also the cavities) can be formed, which subsequently can be addressed by guest molecules [50]. The self-assembly principles are similar to the other compounds discussed in this review and these systems will not be treated in detail here. One example though of this class of porous molecules is the cyclohexiopyrene structure **CT** (Fig. 19) [51]. This alkylated macrocycle self-assembles into rows which extend in two dimensions and the cavities could be identified clearly. Upon addition of C_{60} , surprisingly, these guest molecules were observed to adsorb on the rim rather than in the cavity in agreement with the n - and p -character of both compounds. The host–guest complexation is in this case driven by the donor–acceptor interaction which is more important than the guest–graphite interaction.

In this review, we focus on relatively low molecular weight species which form the corners/edges of supramolecular 2D porous systems. The host porous networks are typically sustained via hydrogen bonds, metal–ligand coordination or even van der Waals interactions. Again, such 2D porous networks offer the possibility to immobilize functional units as guest molecules in a repetitive and spatially ordered arrangement. The proper choice of the host template layer does not only allow adjusting the intermolecular distance between the guest molecules but also their relative orientation.

In order to form open porous structures rigid building blocks capable of forming intermolecular hydrogen bonds or metal coordination bonds are

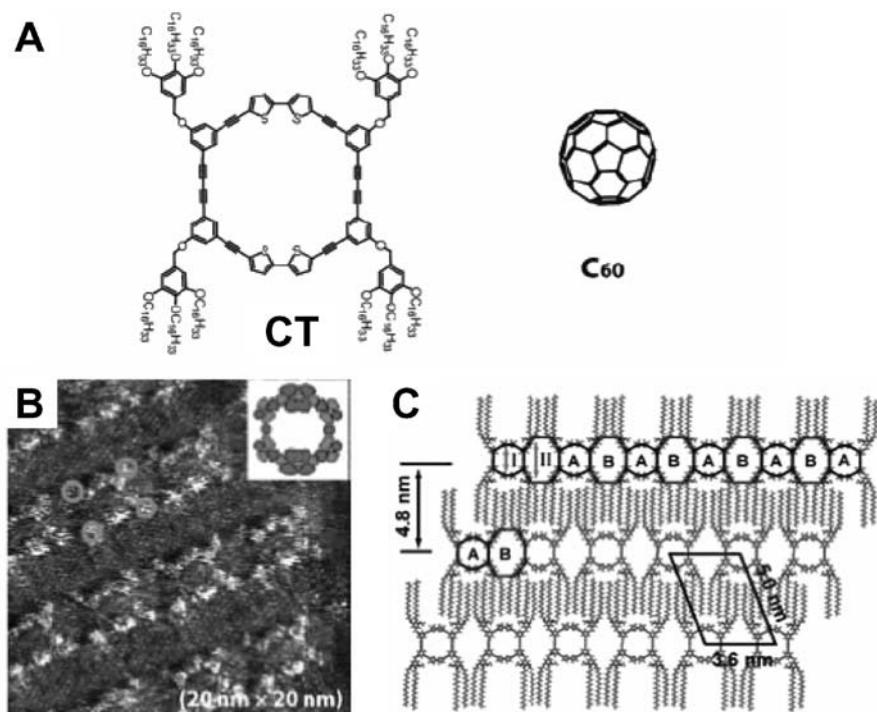


Fig. 19 **A** Chemical structure of CT and C₆₀. **B** STM image of a CT monolayer on graphite. **C** Tentative molecular model of the monolayer structure. (Reproduced with permission from [51])

ideal. Porous networks based on the latter type of interactions have not been demonstrated yet at the liquid–solid interface, to the best of our knowledge, but are popular under UHV conditions. Typically, the porous molecular patterns based on hydrogen-bonding interactions are rigid. But even when relatively strong intermolecular interactions are involved to stabilize the porous networks, other factors play a role too in their formation and stability such as the solvent (see Sect. 7). First, we will present some examples of “hydrogen”-bond stabilized systems. Second, we discuss the opportunities offered by porous networks which are stabilized by van der Waals interactions at the liquid–solid interface.

6.1

2D Pores: Connected by Hydrogen Bonds

TMA (Fig. 4) is the prototype example of a molecule which fulfills the requirements to lead to nanoporous network formation. TMA has a phenyl group with three carboxylic acid groups in the 1, 3 and 5 position. Therefore,

the molecule has a threefold symmetry. Carboxylic acid groups are very efficient in forming hydrogen bonds, especially via carboxylic acid–carboxylic acid dimer formation. Considering these structural and functional characteristics, the formation of a honeycomb structure is anticipated. Indeed, such TMA porous networks were observed at the interface between 1-heptanoic acid and graphite (Fig. 20) [52]. A very attractive property of these self-assembled porous networks is their ability to host guest molecules. It was possible to coadsorb C_{60} within cavities of the open TMA structure from the liquid phase, and lateral manipulation of the molecular guest by the STM tip was demonstrated at room temperature. Because of the increased tip–sample interaction as a result of lower tunneling resistance, a transfer of a C_{60} molecule from one cavity of the host structure to an adjacent one was achieved [53]. Not only C_{60} , but also coronene could be hosted in the porous network formed by the TMA molecules (Fig. 20) [54].

One of the targets in the formation of 2D porous nanostructures is to define and control the size of the cavities. The obvious approach is to extend the distance between the carboxylic acid groups and the center of the molecule, for instance by a phenyl group. 1,3,5-Benzenetribenzoic acid (BTB) is a rigid molecule and self-assembles also at the liquid–solid interface into honeycomb-type networks (Fig. 21A) [55]. The circular cavities have a diameter of about 2.8 nm. In case of TMA, the cavity diameter is about 1 nm only.

Instead of using phenyl groups to extend the distance between the central phenyl group and the carboxylic acid groups at the periphery, other rigid linkers are possible too [56]. Wang et al. used fluorene (FL) (Fig. 21B) [57]. As anticipated this molecule self-assembles at the liquid–solid interface into a honeycomb-type network too, with a cavity diameter of 3 nm. Interestingly, when only one or two of the fluorene moieties were terminated by carboxylic acid groups, no honeycomb-type networks were formed, stressing the importance of hydrogen bonding in stabilizing the porous pattern. One might

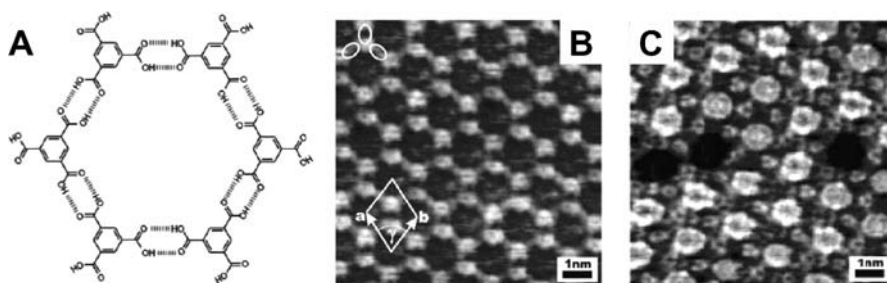


Fig. 20 **A** Hydrogen bonding scheme of a TMA honeycomb network. STM images recorded at the heptanoic acid–graphite interface of a TMA honeycomb network in **B** absence and **C** presence of COR molecules. Empty pores are black. (Reproduced with permission from [54])

actually wonder about the stability of these networks as the general tendency of molecules at the liquid–solid interface is to arrange into a dense packing. However, even if no guest molecules are added, the pores can not be empty and they must be “filled” by solvent molecules. These solvent molecules are most probably too mobile to be visualized.

It might actually become difficult to extend this principle to larger systems, because larger systems are synthetically not accessible or because of solubility problems. In order to extend the size of the cavity, Lackinger et al. introduced an appealing concept. They realized the formation of honeycomb-type networks via a multicomponent approach [58]. They selected two molecules with a three-fold symmetry: trimesic acid and 1,3,5-tris(4-pyridyl)-2,4,6-triazine (TPT) (Fig. 21C). TPT consists of a triazine ring in the center with three symmetrically disposed pyridyl rings and it is a planar molecule. Coadsorption of TPT as a proton acceptor together with TMA as proton donor leads to stable adsorption of TPT through $N \cdots H - OH$ bonds forming a honeycomb network with a 1 : 1 ratio of TPT and TMA. To avoid the formation of TMA

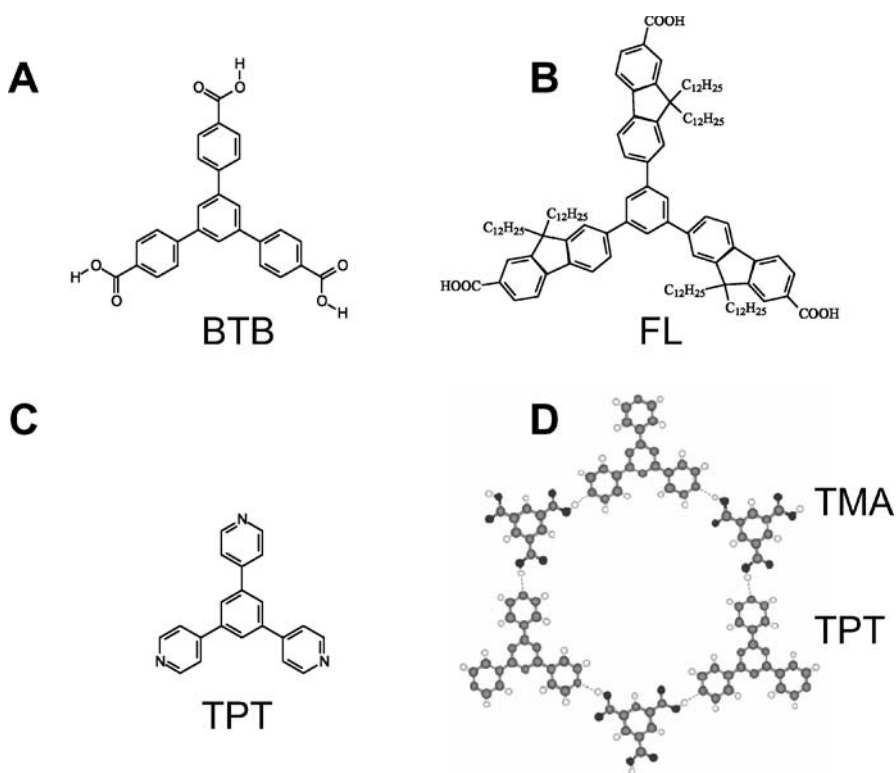


Fig. 21 Chemical structures of **A** BTB **B** FL and **C** TPT. **D** Molecular model of TMA-TPT honeycomb. (Reproduced with permission of [58])

domains, without coadsorption of the TPT molecules, the TPT molecules were added in excess. The resulting honeycomb network (Fig. 21D) is also attractive from another point of view: due to the nature of the hydrogen bonding between TMA and TPT, involving only the OH of the carboxylic acid groups, the carbonyl groups which point to the interior of the cavity could be used to stabilize the adsorption of guest molecules via hydrogen bonding.

6.2

2D Pores: Connected by Alkyl Chains

These hydrogen-bonded networks are rigid. Matrix rigidity favors guest selectivity, which is often desired. However, in those cases where the function of the 2D porous matrix is to host a variety of guest molecules such rigid 2D networks are of limited use. A flexible host network that undergoes slight structural changes to accommodate guest molecules of different size or “aggregation” number would, however, in addition to being open to host a larger set of different guest molecules, provide a reasonable high guest selectivity similar to bioenzymes, such as metalloproteins, which recognize their target substrates by an induced fit mechanism. Furthermore, it is not straightforward to fine tune the pore size by using rigid molecular building blocks as the increment in size is often large, e.g. when using phenyl or other aromatic spacers. Alkylated systems seem therefore appropriate building blocks as the length of the alkoxy chains can be changed by increments of 1.25 Å (one methylene unit).

Recently the formation of nanoporous networks stabilized via van der Waals interactions (via alkyl chain interdigitation) was reported [59]. Efficient building blocks are alkylated or alkoxyated dehydrobenzo[12]annulenes (DBA). The DBA derivatives contain a π -conjugated core, which is rhombic for DBA1 and triangular for DBA2, substituted with alkyl chains (Fig. 22). The alkyl chains ($C_{10}H_{21}$) on the rim of the DBA cores spread out radially: they play a significant role in the physisorption as well as in the topological control of the network by chain–chain interdigitation and directional correlation with the symmetry axes of HOPG. A typical STM image of a monolayer of DBA1 physisorbed on HOPG from TCB shows a Kagomé lattice pattern in which the bright feature located on each lattice point can be recognized as a DBA core (Fig. 22). This network is interpreted as a hexagonal packing pattern with corner-sharing as indicated with thick lines in Fig. 22 (left). On the other hand, compound DBA2 forms a honeycomb network as shown in Fig. 22 (right). This network can be considered as a side-sharing hexagonal packing. A Kagomé network and a honeycomb network consist of four-connected nodes and three-connected nodes at specific angles, respectively. For alkylated systems with a rhombic or triangular core, the core shape itself is not the only responsible element in defining the

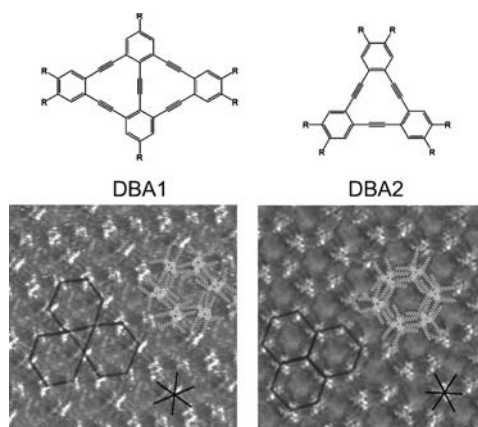


Fig. 22 Molecular models and corresponding STM images of Kagomé network (DBA1) (20.0 nm×20.0 nm) and Honeycomb network (DBA2) (18.7 nm×18.7 nm) recorded at the 1,2,4-trichlorobenzene-graphite interface. (Reproduced with permission from [62])

formation of respectively a Kagomé or honeycomb-type network. Thanks to the fact that the alkyl chains run nearly perpendicular to the sides of the core, in combination with their interdigitation, each core is translated obeying the symmetry aspects of the respective networks. The direction of the alkyl chains is determined by two factors: the position of alkylation, and their preferential orientation along the three C_3 axes of HOPG. Indeed, the graphite symmetry perfectly matches with the symmetry elements of the respective networks; the C_3 symmetry points are located on the center of the triangle lattice in the Kagomé network and on the lattice point in the honeycomb network. A related honeycomb-type forming network was reported for an alkylated system with a 2,4,6-tristyrylpyridine core [60]. In contrast, alkylated phthalocyanines were reported to form square host lattices [61].

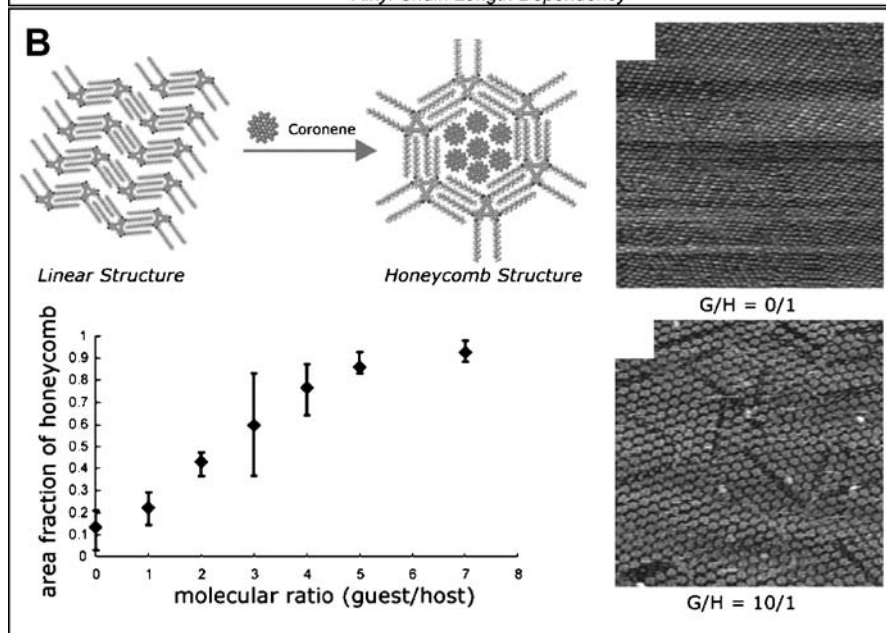
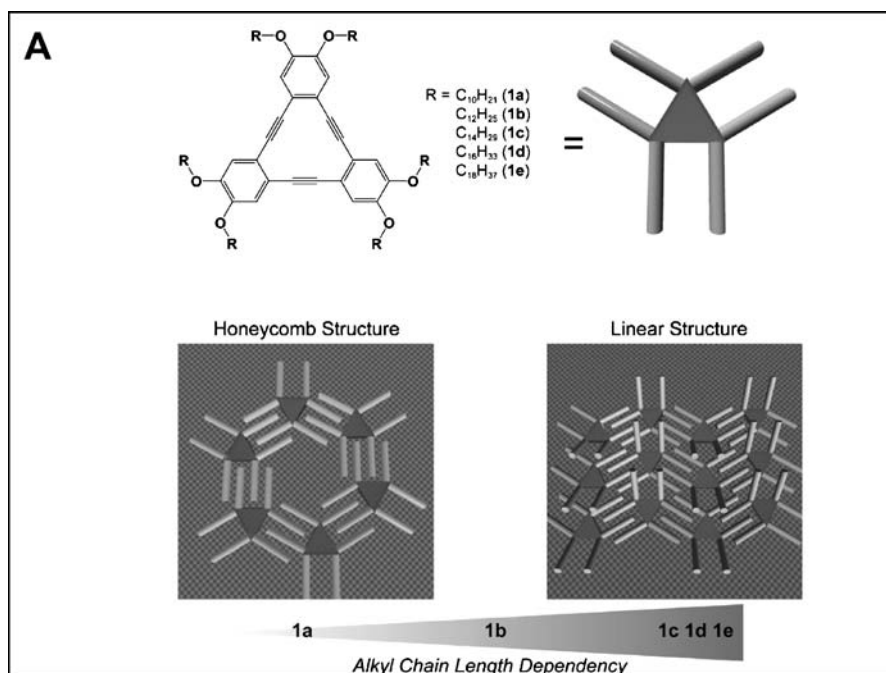
As discussed above, the advantage of alkylated systems is that the size of the cavities in the network can be adjusted by changing the length of the alkyl substituents. In principle, for the DBA derivatives with the triangular core, the pore size could be tuned from 2.9 nm (DBA-OC10) to 5.4 nm (DBA-OC20). Modeling shows that the total contribution of the void space to the overall network would increase though from 42% for DBA-OC12 to 56% for DBA-OC20. Experimentally, it was observed that DBAs with long alkoxy substituents (larger than $OC_{12}H_{23}$) tend to form close-packed linear structures rather than nanoporous honeycomb-type structures (Fig. 23A) [62]. Theoretical considerations show that the porous honeycomb motif is favored at the level of a single molecule, taking into account the balance of the van der Waals interactions with the substrate and between interdigitating alkoxy chains and the desolvation of the alkoxy chains. However, considering the

Fig. 23 **A** Chemical structure of a DBA derivative with alkoxy chains and cartoon demonstrating the transition from a porous honeycomb structure to a dense packing upon elongation of the alkyl chains. **B** Guest-induced transition from a dense network to a honeycomb network. The graph shows the honeycomb coverage as a function of the guest (g) to host (h) ratio. STM images ($96\text{ nm} \times 96\text{ nm}$) recorded at the 1,2,4-trichlorobenzene-graphite interface for different guest to host (g/h) ratios. (Reproduced with permission from [66])

total energy gain of the system taking into account the surface density of adsorbed molecules, a close packing is more favorable. Recently, it was observed that the formation of a honeycomb- or linear-type network not only depends on the length of the alkyl chain but also on the concentration of the DBAs in solution [63]. Upon decreasing the concentration, the honeycomb pattern becomes favored and for DBA-OC20, a honeycomb pattern can be observed with a pore size of 5.4 nm.

Porous networks stabilized by van der Waals interactions are suited to host guest molecules too. Schull et al. have reported the adsorption of coronene, hexabenzocoronene and other aromatic species with similar or smaller size in 1.3 nm diameter honeycomb cavities [64, 65]. Independent of their shape, the guest molecules appeared as featureless bright spots with a diameter of about 1.3 nm, which was attributed to fast guest-molecule translational and rotational diffusion inside the host cavity during the acquisition time. Guest molecules with a size exceeding the cavity diameter were not observed to adsorb. In a beautiful set of experiments, the temperature dependent dynamics of the different guest molecules was probed. The host matrices were incompletely filled by guest molecules (using substoichiometric concentrations) and the motion of the guest molecules, expressed by the average residence times, was followed. For each of the guest molecules, the experimental data obey an Arrhenius dependence with a pre-exponential factor of the order of 5×10^{14} Hz, which is attributed to the hindered molecular diffusion process in a given 2D matrix. The guest molecules can move in and out of the cavities but this long-range diffusion was observed to depend on the molecular weight, symmetry, or perimeter length as revealed by the difference in the activation energies determined from the Arrhenius fits.

Despite the fact that non-porous patterns are preferred for those building blocks with long alkyl chains (at least at “high” concentration), it was shown that the addition of a large excess of guest molecules (i.e. coronene) could induce a structural transformation from linear to nanoporous honeycomb surface confined DBA monolayers (Fig. 23B). The success of this approach was limited though to DBAs with alkoxy chain lengths up to OC₁₄H₂₉, so that the diameter of the (filled) cavity was still limited (3.9 nm) (Fig. 23) [66]. The guest molecules, or the guest assemblies, cancel the energetic cost for the formation of “cavities”. By using even larger nanographene-type guest



molecules, it was possible to extend this principle to DBA-OC20, which hosts six nanographenes as guest [67].

The flexibility of 2D porous networks has been demonstrated for hydrogen-bonded 2D networks of 1,3,5-tris(10-carboxydecyloxy)benzene (TCDB) on graphite (Fig. 24) [68, 69]. These systems combine the hydrogen-bonding abilities of the molecules described in Sect. 6.1 with the flexibility of the other alkyl chain containing building blocks in this section. These molecules resemble trimesic acid, except for the fact that decyloxy groups link the central phenyl groups with the carboxylic acid function. Tetragonal cavities are aligned in well-ordered columns as a result of dimer formation. Cu-phthalocyanine (CUP), coronene (COR) monomers and dimers could be hosted in the cavities, and even a supramolecular rectangle (2.1×1.2 nm) [70]. A remarkable aspect of the host-guest chemistry is that one of the unit cell parameters is changed dramatically upon complexation and dependent also on the guest type. The host network is flexible and adjusts its shape in response to the guest adsorption. However, there are limits to the flexibility: guest molecules which exceed the dimension of the cavity (2.4×1.2 nm), such as supramolecular squares (2.2×2.2 nm) are not adsorbed. In case of vanadyl phthalocyanines as guest, thermal annealing converted the dimer-entrapped architecture to a monomer-entrapped one [71].

It is safe to say that 2D porous networks are “hot” and we believe this will continue to be an active research line in the coming years.

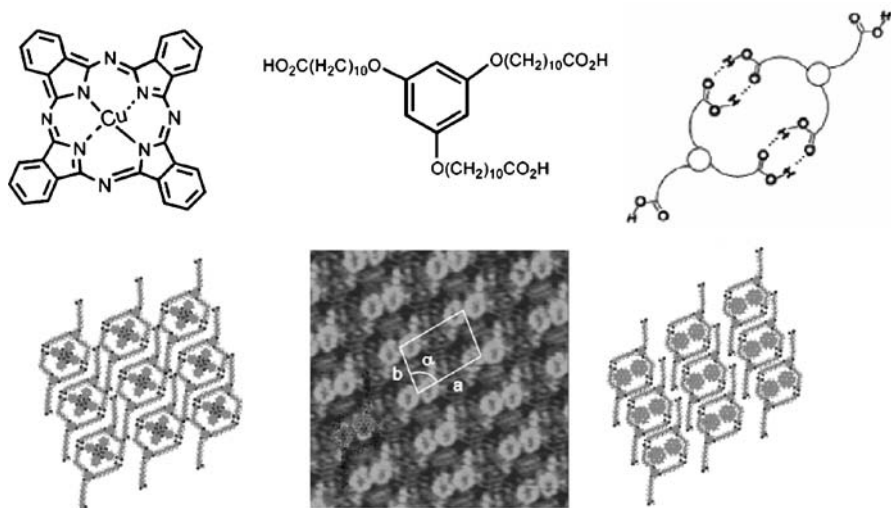


Fig. 24 *Top:* from left to right: chemical structure of CUP; TCDB; drawing of a TCDB dimer. *Bottom:* from left to right: model of the TCDB/CUP host-guest architecture; STM image ($11.8 \text{ nm} \times 11.8 \text{ nm}$) of the TDCB/COR host-guest architecture deposited from toluene on graphite; model of the TDCB/COR host-guest architecture. (Reproduced with permission from [68])

7

The Effect of the Solvent

In addition to molecule–molecule and molecule–substrate interactions, also the solvent plays an important role. This is actually an aspect which to a large extent has been neglected. Insight in the role of solvents is still in its infancy. The choice of solvents is mainly motivated by practical considerations: solubility of the molecules, low vapor pressure, chemical inertness, and low affinity for self-adsorption. However, it is our belief that the choice of solvent will become more and more important to direct the self-assembly of molecules at the liquid–solid interface. From time to time, it is reported that in a given solvent pattern x is formed and in another solvent pattern y , without going into the details of the effect of the solvent. Recently, a number of studies appeared with a clear focus on the effect of solvent on the self-assembly process. Basically, two different phenomena are observed.

The most dramatic effect of the solvent is that it co-adsorbs with solute molecules on the substrate forming a regular multicomponent 2D crystal (see Sect. 5). In most cases though, solvent co-adsorption was not anticipated and was observed by serendipity. However, its effect could be rationalized in most cases in a straightforward way.

In a number of studies though, the solvent effect is dramatic too but is not that well understood. Take for example the porous honeycomb networks formed by trimesic acid. This is actually only one of the different polymorphs which is observed. The other most important polymorph is the flower motif where in addition to carboxylic acid dimers also carboxylic acid trimers are observed (Fig. 25) [52]. So, these polymorphs differ in their molecular packing density and hydrogen-bonding schemes. Using a homologous series of alkanolic acids as solvents, ranging from butyric to nanoic, selective assembly of either the “flower” or “honeycomb” forms was achieved on graphite. Two different mechanisms were proposed: (1) stabilization of a specific basic precursor seed in the solution by a particular solvent or (2) solvent coadsorption and/or stabilization of the polymorph structures on the surface itself. Another aspect not taken into consideration could be the effect of TMA concentration, as it is observed that the less dense packing (honeycomb) is formed in the long-chain solvents where the solubility of TMA is low. Similar effects were observed for 1,3,5-benzenetribenzoic acid too [55]. By comparing the self-assembly in a series of solvents, it was observed that honeycomb pattern formation, with ideal nonpolar carboxylic acid dimerization, was favored in those solvents with the lowest dielectric constant. In addition, solubility and viscosity aspects were considered. These were also taken into account to evaluate polymorphism and solvent-dependent monolayer formation for alkylated DBA derivatives [59]. It is fair to say that although some solvent-dependent aspects have been revealed, more systematic studies, supported by molecular modeling, will be invaluable in getting more insight in the power-

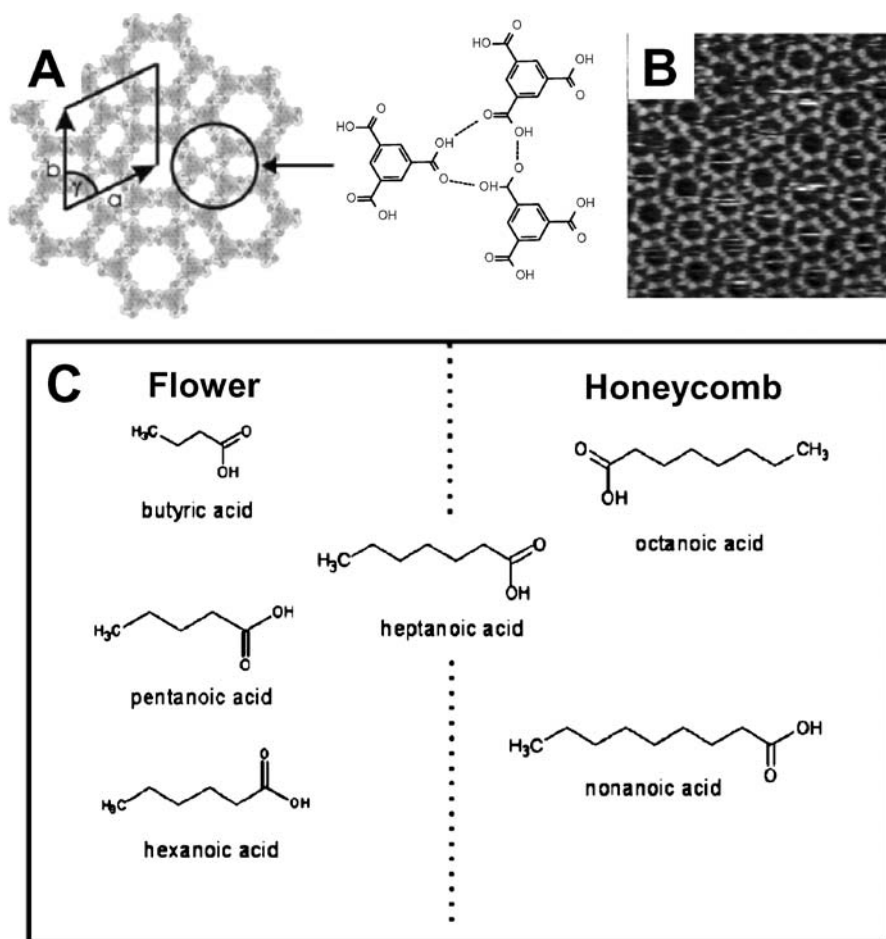


Fig. 25 **A** Model of the TMA “flower” motif and hydrogen-bonding scheme. **B** STM image (15 nm × 15 nm) of the TMA “flower” motif, observed at the pentanoic acid–graphite interface. **C** Relation between the observed TMA structure and the solvent. (Reproduced with permission from [52])

ful, but currently fuzzy role, which the solvent plays in directing/stabilizing monolayer formation at the liquid–solid interface.

8 The Effect of the Substrate

The studies reported above have all been carried out at the interface with HOPG. This substrate is clearly the favored substrate of experimentalists because it is easy to clean and to use. The many reports in the literature dealing

with self-assembly on this substrate clearly prove that this substrate fulfils the expectations. However, it is fair to say that one should broaden the scope of substrates used: Au(111) and MoS₂ are substrates which are also perfect from an experimental point of view to use at the liquid–solid interface. Such studies have been carried out more than a decade ago to investigate the substrate-dependent pattern formation of liquid-crystalline materials, clearly revealing its effect. More recently the effect of the substrate on the self-assembly of linear alkanes and alcohols was investigated in detail, revealing that also on Au(111) alkanes and alkanols [72] form highly ordered assemblies. On graphite, alkanes order in rows and the angle between the molecular row and the molecular axis is always 90° in both odd and even alkane 2D crystals. On Au(111), there is a clear odd–even effect. For odd alkanes this angle is 90° while for even alkanes, this angle is 60°, at least for chain lengths < 17 [73, 74]. This has been attributed to the incommensurability of the lattice of the alkanes with the Au(111) substrate: the length of the C–C–C zigzag (0.254 nm) of alkanes is close to the atomic spacing of graphite (distance between adjacent hexagons in the graphite lattice is 0.246 nm) while in case of Au(111), the nearest neighbor atomic distance is already 0.288 nm. Recently, some more intriguing subtle aspects of the ordering of alkanes on gold were reported including the fact that the 90° arrangement prevails for $n > 37$. It was concluded that the gold–alkane interaction is a little weaker than the graphite–alkane interaction, but still stronger than the MoS₂–alkane interaction where only tilted lamellae are detected [75].

Not only the difference in lattice values might effect the packing of the alkyl chains, and of molecular species in general [76]. The self-assembly of free-base meso-tetradodecylporphyrins (MTDP) on Au(111) is clearly different from the structure on graphite (Fig. 26). On the former substrate, the density of the porphyrin is higher and high-resolution images indicate that physisorption of these alkylated molecules on Au(111) distort the porphyrin

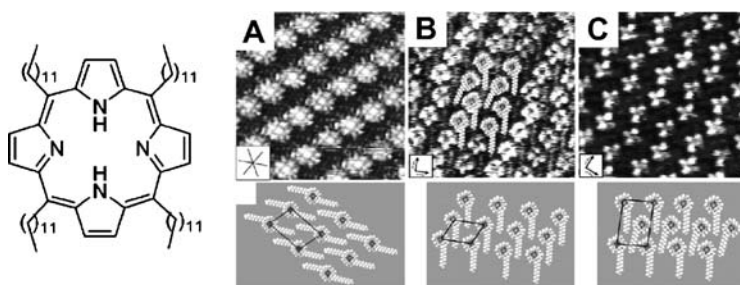


Fig. 26 Chemical structure of MTDP **A** STM image (8.1 nm×8.1 nm) and model of a monolayer at the *n*-tetradecane-graphite interface. **B, C** STM images and models of two polymorphs at the *n*-tetradecane-Au(111) interface (**B**: 9.5 nm×9.5 nm, **C**: 8.4 nm×8.4 nm). (Reproduced with permission from [77])

macrocycle out of planarity, probably caused by the coordination of the lone pairs of the nitrogen atoms of the porphyrin macrocycle [77]. Obtaining more insight into the role of the substrate will finally lead to a more effective 2D crystal engineering on surfaces.

9 From Monolayers to Multilayers

So far, we only considered the formation of monolayers. However, monolayers could prove to be ideal platforms to direct the templated growth into the third dimension: from 2D crystal engineering to templated growth in 3D. Ex-

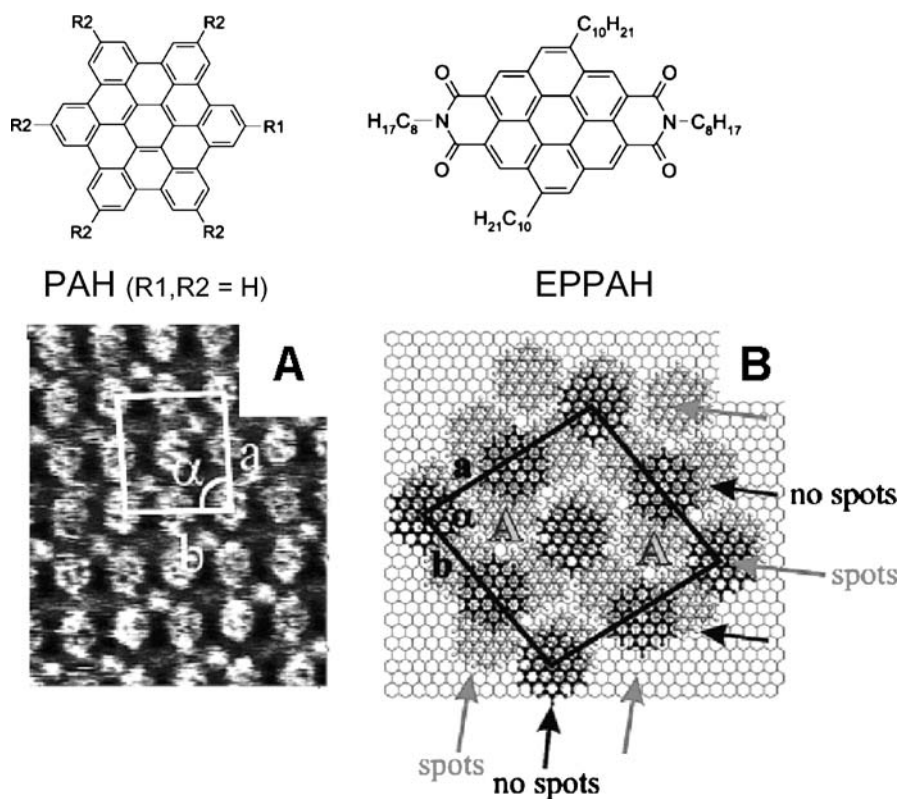


Fig. 27 **A** STM image ($11 \times 13 \text{ nm}^2$) at the liquid–graphite interface of a mixture of PAH and EPPAH. It is an image of a second epitaxial layer with a donor acceptor stoichiometry of 2 : 1 on top of a first epitaxial layer of PAH. The *large features* are PAH, the *smaller and brighter features* are EPPAH. EPPAH packs only every second row probably because of its preferential adsorption on the electron donor disk of PAH, which is exposed in the underlying first PAH layer (see model **B**). (Reproduced with permission from [81])

amples include the multilayer formation of alkylated TTF chains on top of the TTF layer underneath [78], or the adsorption of phthalocyanines [79] and hexabenzocoronenes [80] on alkane-type template layers. Rabe, Samori and Müllen et al. have extended the concept of controlled heteromolecular assembly in a direction perpendicular to the substrate.

Films prepared by co-deposition of a polycyclic aromatic hydrocarbon (PAH) and an electron-poor PAH (EPPAH) (Fig. 27) exhibit an oblique arrangement reflecting the formation of epitaxial composite layers of the electron donors and acceptors [81]. Interestingly, on top of a layer of donor molecules, within the same layer between two physisorbed donor molecules, acceptor molecules are co-adsorbed in a well-defined arrangement. When the acceptor co-crystallizes, the second PAH layer is stabilized (Fig. 27). These studies were extended to covalently linked electron donor–acceptor systems [82, 83].

10 Functionality and Reactivity in 2D

Why 2D crystal engineering? An important aspect is gaining insight into the factors that control the ordering of molecules at a liquid–solid interface [84]. However, this is not the final goal. Building on these insights, the molecular 2D crystals can be exploited as functional template layers with interesting applications in for instance the field of molecular electronics and surface-confined reactions.

10.1 From Molecular Electronics ...

Covalent linking of the HBC and the anthraquinone parts avoids the phase separation of the donor and acceptor parts in different areas. A very nice further development is the integration of this hexabenzocoronene–anthraquinone system (PAH-ANT) with 9,10-dimethoxyanthracene (DMA) [85]. DMA is an electron donor which is known to form a charge-transfer complex with anthraquinone. Upon mixing DMA with the compound discussed above, two types of self-assembled structures were observed (Fig. 28). A first one was indistinguishable from the patterns formed by the HBC–anthraquinone molecule. The second one, though—the one with the larger unit cell—showed six additional bright spots per unit cell (Fig. 28) which were attributed to charge-transfer complexes between anthraquinone and DMA. Interestingly, upon recording current (I)–voltage (V) curves on top of the HBC units, two distinctly different sets were obtained depending on whether or not charge-transfer complexes between anthraquinone and DMA were formed. In fact, a prototypical single-molecule field-effect transistor with nanometer-

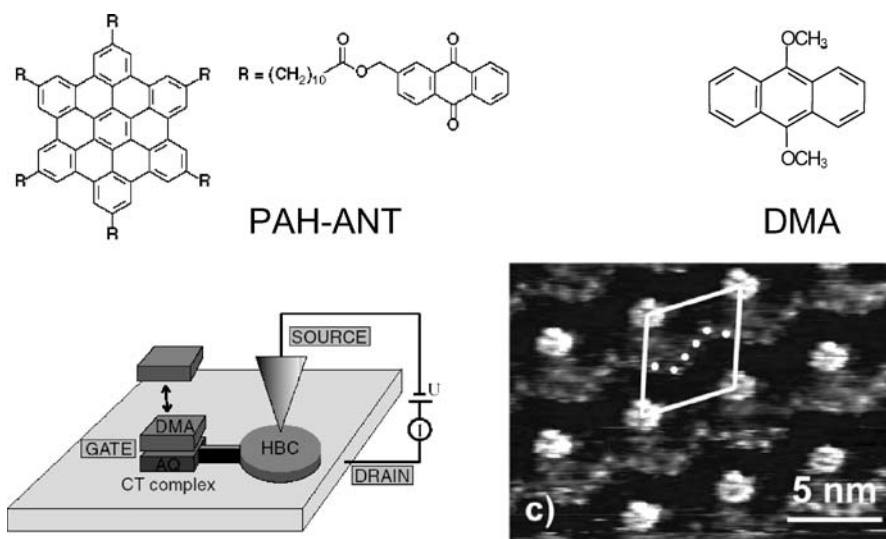


Fig. 28 *Top*: chemical structure of the hexabenzocoronene (HBC) derivative with six anthraquinone groups (PAH-ANT) and 9,10-dimethoxyanthracene (DMA). *Bottom*: schematic of the prototypical single-molecule field-effect transistor. High resolution STM image of a monolayer formed from a mixed solution of the HBC-anthraquinone molecule and DMA. The DMA molecules, indicated by *small white dots*, are adsorbed on top of the anthraquinone molecules and form a charge-transfer complex. (Reproduced with permission from [85])

sized gates was realized: the source and the drain are the graphite and tip electrodes, the channel is the aromatic hexabenzocoronene and the gate is a charge transfer complex, formed between anthraquinone, the acceptor, covalently linked to the “channel” and DMA, the donor, provided from solution.

10.2

... to Polymerization and Reactivity

The liquid–solid interface is an ideal environment to carry out reactions. In a first example, we highlight the preorganization of monomers as a prerequisite for reactivity on a surface: 2D crystal engineering in aid of chemical reactions. In a second example, the adsorbed molecular species catalyze an industrially relevant reaction and with the help of STM, important aspects of this reaction are revealed in real time and space.

A number of surface-confined reactions require a highly ordered prearrangement of the reactive species. The topochemical polymerization of diacetylenes is such a text book example. A critical aspect is the ordering of the diacetylene monomers, both with respect to the distance and the orientation. On the basis of the 3D crystal structures of numerous diacetylene monomers

and polymerized diacetylenes, maximal reactivity is expected when the stacking distance between two adjacent diacetylene moieties and the angle between the stacking axis and the diacetylene unit are $\sim 5 \text{ \AA}$ and $\sim 45^\circ$ [86], respectively. Therefore, it is absolutely necessary to design the diacetylene monomers so that upon self-assembly on surfaces these conditions are fulfilled too. Such light-driven and even STM-tip induced polymerization reactions are possible at the liquid-solid interface [87, 88]. These polymerization reactions were targeted, both for an isophthalic acid derivative containing one diacetylene unit, and a terephthalic acid derivative (TTA-DIA), containing two diacetylene chains. The latter compound (Fig. 29) has been designed and synthesized for the purpose of forming 2D linked nanostructures [89]. Evidently, the location of the diacetylene function in the alkyl chain is critical. As isophthalic acid and terephthalic acid derivatives don't assemble in simple rows, but form a pattern in which the alkyl chains of adjacent rows are interdigitated (see Fig. 6), it was crucial to have the diacetylene functions in the center of the alkyl chain. The formation of such an interdigitated pattern has no particular advantage, except in view of the targeted 2D polymer formation. Because of the presence of two diacetylene units and the network formation by interdigitation of the alkyl chains, TTA-DIA is a potential candidate for the creation of 2D polymers. The bright lines in Fig. 29A indicate the random formation of three polymerized diacetylene rows caused by UV irradiation. After the UV-stimulated polymerization, a pulse (height: -3.2 V , width: 500 ns) was applied in the middle of the image, indicated by the white arrow. A newly created polymerized diacetylene backbone is indicated in Fig. 29B. The tip induced polydiacetylene chain is located next to a UV-light-induced polymer chain. The tip-induced polydiacetylene chain in Fig. 29B propagates in both directions with respect to the location of the pulse. Figure 29C shows the schematic model of 2D connected 1D nanostructures of polydiacetylene. Clearly, adjacent rows of polydiacetylene chains are chemically connected, and form a 2D nanostructure.

Recently, an oxidation catalysis has been demonstrated and in real space and time visualized at the liquid-solid interface [90]. This breakthrough study revealed beautifully how single molecule techniques can be used to probe reactivity catalyzed by surface-confined metal porphyrins on Au (Fig. 30). Metal porphyrins occur in nature and they are involved in light harvesting in plants and oxygen binding haem. Furthermore, manganese porphyrins are used to catalyze the chemical transformation of alkenes into epoxides. An important step in this catalyzed reaction is the activation of an external oxidant, by binding its oxygen atom to the metal center. Here, Elemans et al. started from the hypothesis that also molecular oxygen could be used as oxidant, where the gold substrate activates the catalyst to react with molecular oxygen. Prior to the catalysis experiments the manganese porphyrins (**Mn1**) were physisorbed at the interface between gold and *n*-tetradecane. The alkylated porphyrins are highly ordered, though the alkyl

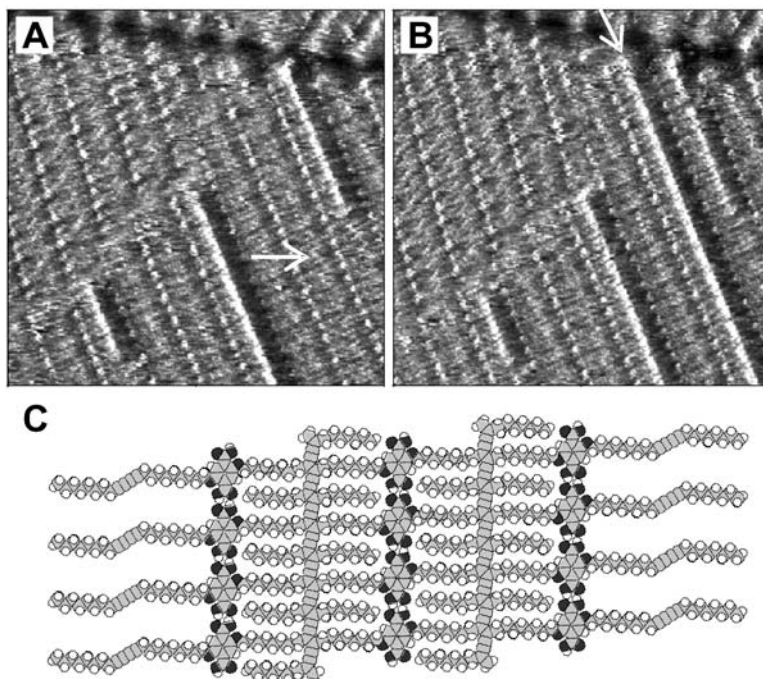
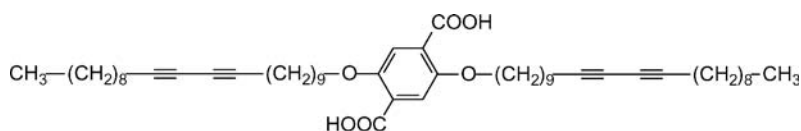


Fig. 29 **A** STM image (27.1 nm×27.1 nm) of a monolayer of TTA-DIA after 30 minutes of UV light irradiation. A pulse (height: -3.2 V, width: 500 ns) was applied at the position indicated with a *white arrow*. **B** STM image (27.1 nm×27.1 nm) of the monolayer of TTA-DIA at the same area after application of a single pulse. The *white arrow* in the image indicates the polydiacetylene backbone created by pulsing. **C** Molecular model of a 2D nanostructure formed by the covalent connection of adjacent parallel polydiacetylene chains. (Reproduced with permission from [89])

chains were not visualized. Upon exposure of the monolayer to molecular oxygen, some of the **Mn1** molecules appeared with a greater height, and the abundance of these features scaled with the oxygen content in solution. Surprisingly, these high-level features attributed to oxygen-bound molecules are not distributed randomly. There is a significant preference for pairs of adjacent porphyrins at the cost of monomeric species. Each oxygen molecule probably dissociates upon its reaction with the metal center and two identical mono-oxygen-coordinated species are formed. Such an oxidized surface could in principle act as a heterogeneous catalyst for epoxidation reactions.

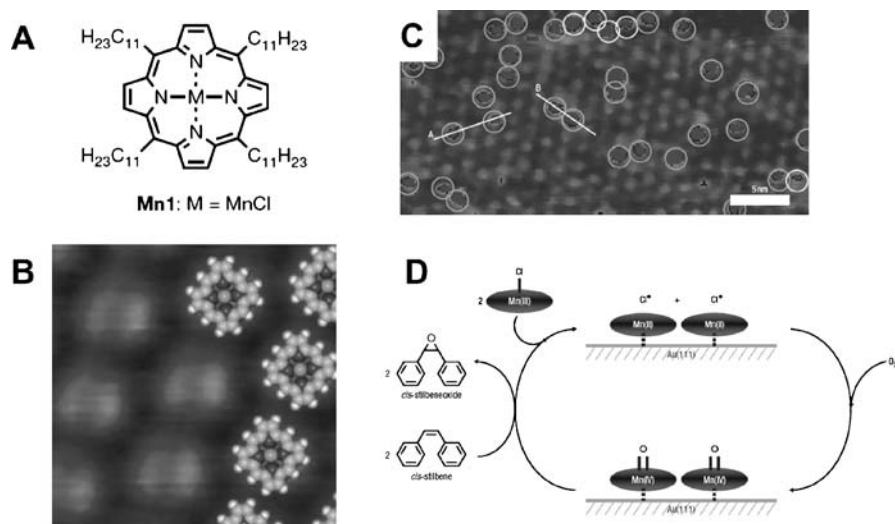


Fig. 30 **A** Molecular structure of **Mn1**. **B** STM image of **Mn1** recorded at the *n*-tetradecane-Au(111) interface. **C** STM image of a monolayer of **Mn1** at the *n*-tetradecane-Au(111) interface after exposure to O_2 . The population of the “bright spots” is about 8%. **D** Proposed catalytic cycle of the epoxidation reaction carried out at the liquid–solid interface. (Reproduced with permission from [90])

The catalytic epoxidation of *cis*-stilbene was followed in real time and real space. A sudden drop of the number of oxidized **Mn1** porphyrins was observed upon addition of stilbene. The catalytic reaction was confirmed by evaluation of the amount of epoxides formed in time.

11 Conclusions and Perspectives

For more than a decade, the liquid–solid interface has proven to be an attractive medium to aid molecular systems to self-assemble into patterns on an atomically flat surface. The outcome of various simultaneously acting interactions such as those between molecules, between molecules and substrates, between molecules and the solvent and the substrate and the solvent is often the formation of surface-confined highly regular networks. Similar to “traditional” supramolecular chemistry in solution, also on surfaces the typical noncovalent interactions are successfully exploited to direct the molecular ordering, going from 1D systems to perfect 2D monocomponent and multicomponent crystals. To what extent though are the results reported in literature the result of “engineering”. On the basis of our own experience, we have to admit that many “successful” systems did not always give rise to the anticipated results, but luckily enough revealed often more interesting and

important aspects of self-assembly at the liquid–solid interface. Engineering is not easy. It requires a set of rules which allows predicting the outcome of the self-assembly process with a high degree of reliability. When faced with the question how a given molecule is going to adsorb on a well-known surface, the answer is often vague and most often the “I-don’t-know” approach is the most honest one. Only for the most simple systems, we can predict more or less in a reliable way the outcome of the self-assembly. Moreover, many systems are polymorphous. Furthermore, the role of the solvent is still mysterious.

However, it is our belief that the concept of 2D crystal engineering at the liquid–solid interface will continue to inspire many researchers. Reactivity, molecular electronics and exploitation of template effects, both for porous and nonporous 2D crystals, will remain active research areas the coming years.

References

1. Braga D, Brammer L, Champness NR (2005) *CrystEngComm* 7:1
2. Brammer L (2004) *Chem Soc Rev* 33:476
3. Evans OR, Lin WB (2002) *Acc Chem Res* 35:511
4. Moulton B, Zaworotko MJ (2001) *Chem Rev* 101:1629
5. Melendez RE, Hamilton AD (1998) *Top Curr Chem* 198:97
6. Binnig G, Rohrer H, Gerber C, Weibel E (1982) *Phys Rev Lett* 49:57
7. Schuurmans N, Uji-i H, Mamdouh W, De Schryver FC, Feringa BL, van Ech J, De Feyter S (2004) *J Am Chem Soc* 126:13884
8. Lackinger M, Griessl S, Markert T, Jamitzky F, Heckl WM (2004) *J Phys Chem B* 108:13652
9. Cyr DM, Ventakaraman B, Flynn GW (1996) *Chem Mater* 8:1600
10. Gellman AJ, Paserba KR (2002) *J Phys Chem B* 106:13231
11. Yin S, Wang C, Cui X, Xu B, Bai CL (2001) *Surf Interf Anal* 32:248
12. De Feyter S, Gesquière A, Abdel-Mottaleb MM, Grim PCM, De Schryver FC, Meiners C, Sieffert M, Valiyaveetil S, Müllen K (2000) *Acc Chem Res* 33:520
13. De Feyter S, Gesquière A, Klapper M, Müllen K, De Schryver FC (2003) *Nano Lett* 3:1485
14. Eichhorst-Gerner K, Stabel A, Moessner G, Declercq D, Valiyaveetil S, Enkelmann V, Müllen K, Rabe JP (2006) *Angew Chem Int Ed Engl* 35:1492
15. Stepanow S, Lingenfelder M, Dmitriev A, Spillmann H, Delvigne E, Lin X, Deng XB, Ca CZ, Barth JV, Kern K (2004) *Nat Mater* 3:229
16. Surin M, Samori P, Jouaiti A, Kyritsakas N, Hosseini MW (2007) *Angew Chem Int Ed* 46:245
17. Alam MS, Strömsdörfer S, Dremov V, Müller P, Kortus J, Ruben M, Lehn JM (2005) *Angew Chem Int Ed* 44:7896
18. Semenov A, Spatz JP, Möller M, Lehn JM, Sell B, Schubert D, Weidl CH, Schubert US (1999) *Angew Chem Int Ed* 111:2701
19. Mourran A, Ziener U, Möller M, Breuning E, Ohkita M, Lehn JM (2005) *Eur J Inorg Chem* 2641
20. Zell P, Mögele F, Ziener U, Rieger B (2006) *Chem Eur J* 12:3847

21. Trixler F, Markert T, Lackinger M, Jamitzky F, Heckl WM (2007) *Chem Eur J* 13:7785
22. Lei SB, Wang C, Yin SX, Wang HN, Xi F, Liu HW, Xu B, Wan LJ, Bai C (2001) *J Phys Chem B* 105:10838
23. De Feyter S, Gesquière A, De Schryver FC, Keller U, Müllen K (2002) *Chem Mater* 14:989
24. Gesquière A, De Feyter S, De Schryver FC, Schoonbeek F, van Esch J, Kellogg RM, Feringa BL (2001) *Nano Lett* 1:201
25. Puigmartí-Luis J, Minoia A, Uji-i H, Rovira C, Cornil J, De Feyter S, Lazzaroni R, Amabilino DB (2006) *J Am Chem Soc* 128:12602
26. De Feyter S, Grim K, van Esch J, Kellogg RM, Feringa BL, De Schryver FC (1998) *J Phys Chem B* 102:8981
27. Abdel-Mottaleb MMS, Schuurmans N, De Feyter S, van Esch J, Feringa BL, De Schryver FC (2002) *Chem Commun*, p 1894
28. De Feyter S, Abdel-Mottaleb MMS, Schuurmans N, Verkuijl B, van Esch J, Feringa BL, De Schryver FC (2004) *Chem Eur J* 10:1124
29. Kim K, Matzger AJ (2002) *J Am Chem Soc* 124:8772
30. Plass KE, Kim K, Matzger AJ (2004) *J Am Chem Soc* 126:9042
31. Kim K, Plass KE, Matzger AJ (2005) *Langmuir* 21:647
32. Kim K, Plass KE, Matzger AJ (2003) *Langmuir* 19:7149
33. Plass KE, Grzesiak AL, Matzger AJ (2007) *Acc Chem Res* 40:287
34. Yang Y, Wang C (2007) *Int J Nanotechnol* 4:4
35. Surin M, Samori P (2007) *Small* 3:190
36. Venkataraman B, Breen JJ, Flynn GW (1995) *J Phys Chem* 99:6608
37. Padowitz DF, Sada DM, Kemer EL, Dougan ML, Xue WA (2002) *J Phys Chem B* 106:593
38. De Feyter S, Larsson M, Schuurmans N, Verkuijl B, Zorinants G, Gesquière A, Abdel-Mottaleb MM, van Esch J, Feringa BL, van Stam J, De Schryver FC (2003) *Chem Eur J* 9:198
39. Vanoppen P, Grim PCM, Rücker M, De Feyter S, Moessner G, Valiyaveetil S, Müllen K, De Schryver FC (1996) *J Phys Chem* 100:19636
40. Nath KG, Ivasenko O, Miwa JA, Dang H, Wuest JD (2006) *J Am Chem Soc* 128:4212
41. Nath KG, Ivasenko O, MacLeod JM, Miwa JA, Wuest JD, Nanci A, Perepichka DF, Rosei F (2007) *J Phys Chem C* 111:16996
42. MacLeod JM, Ivasenko O, Perepichka DF, Rosei F (2007) *Nanotechnology* 18:1
43. De Feyter S, Miura A, Yao S, Chen Z, Wuerthner F, Jonkheijm P, Schenning APHJ, Meijer EW, De Schryver FC (2005) *Nano Lett* 5:77
44. Mamdouh W, Dong M, Xu S, Rauls E, Besenbacher F (2006) *J Am Chem Soc* 128:13305
45. Lei SB, Yin SX, Wang C, Wan LJ, Bai CL (2007) *Chem Mater* 14:2837
46. Mamdouh W, Uji-i H, Dulcey AE, Percec V, De Feyter S, De Schryver FC (2004) *Langmuir* 20:7678
47. Mamdouh W, Uji-i H, Ladislav JS, Dulcey AE, Percec V, De Schryver FC, De Feyter S (2006) *J Am Chem Soc* 128:317
48. Gong JR, Yan HJ, Yuan QH, Xu LP, Bo ZS, Wan LJ (2006) *J Am Chem Soc* 128:317
49. Wei Y, Tong W, Wise C, Wei X, Armbrust K, Zimmt M (2006) *J Am Chem Soc* 128:13362
50. Mena-Osteritz E, Bäuerle P (2006) *Adv Mater* 18:447
51. Pan GB, Cheng XH, Höger S, Freyland W (2006) *J Am Chem Soc* 128:4218
52. Lackinger M, Griessl S, Heckl WM, Hietschold M, Flynn GW (2005) *Langmuir* 21:4984

53. Griessel SJH, Lackinger M, Jamitzky F, Markert T, Hietschold M, Heckl WM (2004) *J Phys Chem B* 108:11556
54. Griessel SJH, Lackinger M, Jamitzky F, Markert T, Hietschold M, Heckl WM (2004) *Langmuir* 20:9403
55. Kampschulte L, Lackinger M, Maier AK, Kishore RSK, Griessel S, Schmittel M, Heckl WM (2006) *J Phys Chem B* 110:10829
56. Zhou H, Dang H, Yi JH, Nanci A, Rochefort A, Wuest JD (2007) *J Am Chem Soc* 129:13774
57. Ma Z, Wang YY, Wang P, Huang W, Li YB, Lei SB, Yang YL, Fan XL, Wang C (2007) *ACSNano* 1:160
58. Kampschulte L, Griessel S, Heckl WM, Lackinger M (2005) *J Phys Chem B* 109:14074
59. Tahara K, Furukawa S, Uji-I H, Uchino T, Ichikawa T, Zhang J, Mamdouh W, Sonoda M, De Schryver FC, De Feyter S, Tobe Y (2006) *J Am Chem Soc* 128:16613
60. Bléger D, Kreher D, Mathevet F, Attias AJ, Schull G, Huard A, Douillard L, Fiorini-Debuisschert C, Charra F (2007) *Angew Chem Int Ed* 46:7404
61. Liu Y, Lei SB, Yin S, Xu S, Zheng Q, Zeng Q, Wang C, Wan L, Bai CL (2002) *J Phys Chem B* 106:12569
62. Furukawa S, Uji-I H, Tahara K, Ichikawa T, Sonoda M, De Schryver FC, Tobe Y, De Feyter S (2006) *J Am Chem Soc* 128:3502
63. Lei S, Tahara K, De Schryver FC, Van der Auweraer M, Tobe Y, De Feyter S (2008) *Angew Chem Int Ed* 47:2964
64. Schull G, Douillard L, Fiorini-Debuisschert C, Charra F (2007) *Nano Lett* 6:1360
65. Schull G, Douillard L, Fiorini-Debuisschert C, Charra F, Mathevet F, Kreher D, Attias AJ (2006) *Adv Mater* 18:2954
66. Furukawa S, Tahara K, De Schryver FC, Van der Auweraer M, Tobe Y, De Feyter S (2007) *Angew Chem Int Ed* 46:2831
67. Lei S, Tahara K, Feng X, Furukawa S, De Schryver F, Müllen K, Tobe Y, De Feyter S (2008) *J Am Chem Soc*, in press
68. Lu J, Lei SB, Zeng Q, Kang S, Wang C, Wan LJ, Bai CL (2007) *J Phys Chem B* 108:5161
69. Kong XH, Deng K, Yang YL, Zeng QD, Wang C (2007) *J Phys Chem C* 111:17382
70. Li SS, Yan HJ, Wan LJ, Yang HB, Northrop BH, Stang PJ (2007) *J Am Chem Soc* 129:9268
71. Kong XH, Deng K, Yang YL, Zeng QD, Wang C (2007) *J Phys Chem C* 111:9235
72. Zhang HM, Yan JW, Xie ZX, Mao BW, Xu X (2006) *Chem Eur J* 12:4006
73. Uosaki K, Yamada R (1999) *J Am Chem Soc* 121:4090
74. Yamada R, Uosaki K (2000) *J Phys Chem B* 104:6021
75. Zhang HM, Xie ZX, Mao BW, Xin X (2004) *Chem Eur J* 10:1415
76. Katsonis N, Marchenko A, Fichou D (2003) *J Am Chem Soc* 125:13682
77. Katsonis N, Vicario J, Kudernac T, Visser J, Pollard MM, Feringa BL (2006) *J Am Chem Soc* 128:15537
78. Lei SB, Puimarti-Luis J, Minoia A, Van der Auweraer M, Lazzaroni R, Amabilino DB, De Feyter S (2008) *Chem Commun* 6:703
79. Lei SB, Wang C, Wan LJ, Bai CL (2004) *J Phys Chem B* 118:1173
80. Piot L, Marchenko A, Wu J, Müllen K, Fichou D (2005) *J Am Chem Soc* 127:16245
81. Samori P, Severin N, Simpson CD, Müllen K, Rabe JP (2002) *J Am Chem Soc* 124:9457
82. Samori P, Yin X, Tchegotareva N, Wang Z, Pakula T, Jäckel F, Watson MD, Venturini A, Müllen K, Rabe JP (2004) *J Am Chem Soc* 126:3567
83. Jäckel F, Wang Z, Watson MD, Müllen K, Rabe JP (2004) *Chem Phys Lett* 387:372

84. Hermann BA, Scherer JL, Housecroft CE, Constable EC (2006) *Adv Func Mater* 16:221
85. Jäckel F, Watson MD, Müllen K, Rabe JP (2004) *Phys Rev Lett* 92:188303
86. Enkelmann V (1984) *Adv Polym Sci* 63:91
87. Grim PCM, De Feyter S, Gesquière A, Vanoppen P, Rucker M, Valiyaveetil S, Moessner G, Müllen K, De Schryver FC (1997) *Angew Chem Int Ed Eng* 36:2601
88. Okawa Y, Aono M (2001) *Nature* 409:683
89. Miura A, De Feyter S, Abdel-Mottaleb MMS, Gesquière A, Grim PCM, Moessner G, Sieffert M, Klapper M, Müllen K, De Schryver FC (2003) *Langmuir* 19:6474
90. Hulsken B, Van Hameren R, Gerritsen JW, Khoury T, Thordarson P, Crossley MJ, Rowan AE, Nolte RJM, Elemans JAAW, Speller S (2007) *Nat Nanotechnol* 2:285

Porous Networks Through Colloidal Templates

Qin Li¹ · Markus Retsch¹ · Jianjun Wang¹ · Wolfgang Knoll¹ ·
Ulrich Jonas^{1,2} (✉)

¹Max Planck Institute for Polymer Research,
Ackermannweg 10, 55128 Mainz, Germany

²FORTH/IESL, Voutes Str., P.O. Box 1527, 71110 Heraklion, Crete, Greece
jonas@mpip-mainz.mpg.de or ujonas@iesl.forth.gr

1	Introduction	136
2	Fabrication of Colloidal Films and Crystals	139
2.1	Colloidal Material Selection	139
2.2	Particle Film Formation Strategies	140
2.3	Porous Replica Formation	143
2.4	Template Removal	144
3	Metal Based Networks	145
3.1	Materials	145
3.2	Nanoparticle Codeposition	146
3.3	Nanoparticle Infiltration	146
3.4	Metal Precursor Infiltration and Transformation	147
3.5	Electroless Metal Deposition	147
3.6	Electrochemical Metal Deposition	148
4	Semiconductor and Carbon Based Networks	149
4.1	Materials	149
4.2	Opal Infiltration with Semiconductor Nanoparticles	150
4.3	Salt Infiltration and Chemical Conversion	151
4.4	Alkoxide Infiltration and Hydrolysis	151
4.5	Oxide Reduction	152
4.6	Melt Infiltration	152
4.7	Chemical Vapor Deposition	152
4.8	Electrochemical Deposition	153
5	Metal Oxide Based Networks	154
5.1	Materials	154
5.2	Alkoxide Infiltration and Hydrolysis	154
5.3	Salt Infiltration and Chemical Conversion	155
5.4	Opal Infiltration with Metal Oxide Nanoparticles	155
6	Polymer Based Networks	155
6.1	Materials	155
6.2	In Situ Polymerization and Crosslinking	156
6.3	Electropolymerization	157
6.4	Application Examples	159

7	Hierarchical Porous Networks	160
7.1	Structural Considerations	160
7.2	Block Copolymer Templating	161
7.3	Multiple-Size Colloid Templating	162
7.4	Surfactant Templating	163
7.5	Ionic Liquid Templating	163
7.6	Porous Particles	165
7.7	Wall Functionalization	165
7.8	Large-Scale Structure Hierarchies	166
7.8.1	External Confinement	166
7.8.2	Confined Local Deposition	167
7.8.3	Patterning of a Homogeneous Colloidal Crystal	167
8	Functional Networks	168
8.1	For Sensing Platforms	168
8.2	For Optoelectronics	171
8.3	For Control of Surface Properties	172
	References	173

Abstract Porous networks represent a class of materials with interconnected voids with specific properties concerning adsorption, mass and heat transport, and spatial confinement, which lead to a wide range of applications ranging from oil recovery and water purification to tissue engineering. Porous networks with well-defined, highly ordered structure and periodicities around the wavelength of light can furthermore show very sophisticated optical properties. Such networks can be fabricated from a very large range of materials by infiltration of a sacrificial colloidal crystal template and subsequent removal of the template. The preparation procedures reported in the literature are discussed in this review and the resulting porous networks are presented with respect to the underlying material class. Furthermore, methods for hierarchical superstructure formation and functionalization of the network walls are discussed.

Keywords Colloidal crystal · Hierarchical structure · Inverse opal · Porous networks · Replica · Template

1

Introduction

A *porous material* consists of at least two immiscible phases of which one is usually a continuous solid material, the matrix, which surrounds the second phase of finely dispersed voids, the pores, containing a liquid, gas, or vacuum. If the void phase is discontinuous and comprises individually separated cavities filled with gas (bubbles), the material represents a foam structure. On the other hand, if both phases form two interpenetrating continua with the matrix as well as the pores being continuous, the material represents a sponge structure or a so-called *porous network*. Such porous networks with interconnected voids are the focus of this article as they may have funda-

mental properties advantageous in adsorption, mass and heat transport, and spatial confinement, which result in a myriad of practical applications ranging from oil recovery and water purification to tissue engineering. Moreover, when the porous networks possess a well-defined, highly ordered structure with periodicities around the wavelength of light, they may exhibit exquisite optical properties [1–3]. The statement from the accomplished architect, Robert le Ricolais: “the art of structure is where to put the holes”, is often borrowed as the matching analogy to the designs of functional porous materials [4, 5], where the key parameters requiring precise control are the pore dimensions, their spatial arrangement, connectivity, and the chemical functionalization. Depending on the pore dimensions and according to the IUPAC definition [6, 7], they are referred to as *macropores* if the width exceeds about 50 nm, and *micropores* with widths below ca. 2 nm. In the intermediate size range they are called *mesopores*. Such materials belong to the class of *colloidal systems*, which show, at least in one dimension, discontinuities in the order of about 1 nm to 1 μm and may include such diverse systems as colloidal dispersions and continuous porous networks. Of particular interest is the fact that the former can be used as a template to produce the latter, which is discussed in detail here. *Colloidal dispersions* form the basis for the templating material and cover an extremely broad range of systems, in which the kinetic units being dispersed throughout a liquid are of a size ranging from nanometers to micrometers. They have long been recognized as an important class of materials [8, 9], and the ever-growing demands on the faster, better performances in devices yet smaller in size and cheaper in cost have spurred a vital development in colloidal science and technology [10–12].

In order to create a controlled porous network structure, generally two approaches can be classified, namely the “top-down” and “bottom-up” approaches. Typically, the former is favored by nano-physicists and involves focused molecular, ion, or electron beam etching, which becomes considerably cumbersome in 3D porous structure formation, in particular for large-scale production purposes. The latter approach is often favored in chemical and biological systems by synthesizing materials from individual atoms and molecules [13]. In the bottom-up approach, a sacrificial template with the desired architecture is firstly synthesized with the target material filled in the interstices. The following removal of the template results in an inverse structure, the porous network. Although the underlying mechanisms in template preparation could be complex, the bottom-up approach offers a superior flexibility, reproducibility, parallelism, and efficiency in structure formation [13], which is also of interest for large-scale production in an industrial environment.

In this respect, colloidal particles are ideal candidates serving as templates for the formation of amorphous and highly ordered porous networks, particularly for macroporous networks, owing also to the maturing synthesis routes of various colloidal particles with controlled size, geometry, and composition [14–18]. Due to their small sizes and the forces exerted upon

them through the dispersion media [19–22], colloidal particles have the ability to self-assemble into ordered, crystalline structures under certain experimental conditions and for well-defined particle size distributions, e.g., mono [23], binary [24], and ternary dispersions [25]. The most common type of colloidal crystals formed by self-assembly of monodisperse particles has a face-centered cubic (fcc) lattice symmetry with the highest crystalline packing density of 74% volume filling. In this packing geometry one sphere is in direct contact with 12 surrounding spheres; correspondingly, the resulting replica network has a free volume of 74% with a large internal surface-to-volume ratio. The contact points between the templating particles lead to orifices between the spherical voids (removed particles) in the resulting replica and consequently ensures an open, fully continuous 3D network. The spherical void dimension directly relates to the templating particle diameter (considering potential shrinkage due to the replica solidification process and particle template removal), while the connecting orifice area between voids depends on various parameters, such as the templating particle type, the colloidal template pretreatment (like annealing), and the replica material and preparation method. For disordered particle templates formed from polydisperse colloids, the same logic essentially holds true, that continuous networks result from pores between contacting particles; only the long-range order is missing in that case [26].

Based on the resulting colloidal crystal ensembles, porous networks can be formed in two principal ways, which are schematically represented in Fig. 1:

1. Infiltration with a second material (the matrix, e.g., an ultraviolet (UV) or thermally curable prepolymer [27, 28], an ordinary organic precursor with initiators [29], a sol-gel precursor [30, 31], or a dispersion of nanoparticles (1–50 nm) [32–34]) into the interstices of the colloidal template, followed by solidification and the removal of colloidal template via dissolution, pyrolysis, or chemical etching.

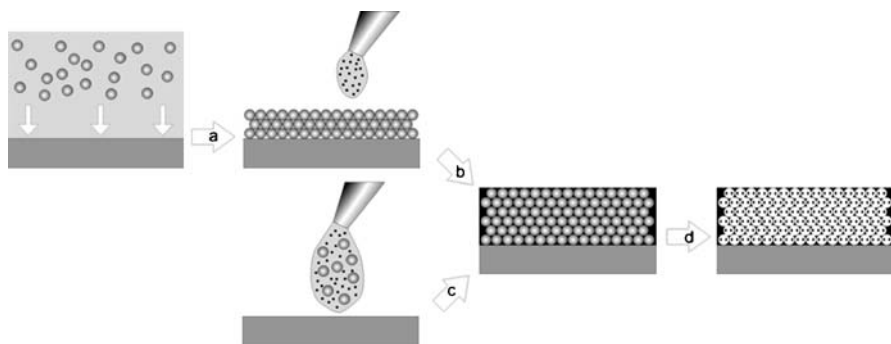


Fig. 1 Scheme of preparation routes to macroporous networks by colloidal crystal templating

2. Codeposition of the colloidal template together with the matrix material, typically in the form of nanoparticles, while the colloidal particles form a highly ordered structure, which can be further processed to remove the sacrificial particle template [25, 35].

In this contribution, we intend to provide a comprehensive account of the state of the art in colloidal template formation, template inversion/replication, and the various types of porous networks attributed to their chemical compositions, and of their applications in an assortment of frontier areas in materials science. As such, the article provides a summary and extension of valuable reviews published previously [10, 36–41].

2

Fabrication of Colloidal Films and Crystals

2.1

Colloidal Material Selection

The first step toward the successful formation of porous networks requires a rational design of the colloidal film template. Using such colloidal templates inherently requires (1) the preparation of the network matrix within the interstitial sites of the template, and (2) the removal of the templating material. Thus, the colloidal material has to be selected in a way that (a) is compatible with the matrix preparation process, and (b) allows its removal without damaging the matrix framework. For this purpose, differences in solubility or thermal stability between the template and the matrix are often exploited, with combinations of organic/polymeric (good solubility in organic solvents, low thermal stability) and inorganic (very selective solubility, high thermal stability) materials being very common.

The most widespread system is the combination of polystyrene (PS) or poly(methyl methacrylate) (PMMA) latex as template with silica for the matrix material. In this case the polymer can be dissolved in many organic solvents, such as toluene and tetrahydrofuran (THF). PS and PMMA also show complete thermal degradation at reasonably low temperatures (below 450 °C), while the silica matrix easily withstands organic solvent and thermal treatment during template removal. Colloidal particles made of silica, PS, and PMMA are readily available in a broad range of sizes and can easily be handled in water as suspending liquid, which is of particular safety and environmental concern in industrial applications. Furthermore, they are cheap and mostly monodisperse in size, which permits particle crystallization into highly ordered structures. All these properties have made it easy to adjust the desired pore size in the resulting porous network. As shown in the example above, the combination of inorganic (e.g., silica) and organic

(polymer) materials exploits their opposing physical properties, which are necessary to selectively remove the template without affecting the network matrix. Many polymeric template materials can be removed by either selective dissolution in organic solvents, like THF, or by combustion. Vice versa, a silica template can be dissolved in hydrofluoric acid without affecting many common polymeric materials.

Even though the usage of polymeric or silica particles represents the easiest way of templating porous networks, a variety of other techniques and particles in the colloidal regime have evolved. For example, liquid emulsion droplets as templates were used by Imhof and Pine [42]. According to the authors, the advantage of liquid droplet templates relies on the fact that they are flexible and can adjust their shape, allowing higher packing densities than achievable for hard spheres. Secondly, the flexible droplets would adjust for volume shrinkage during solidification and drying of the matrix. Thirdly, the liquid template can be removed under very mild conditions (by evaporation or dissolution). In this method the authors first produced an emulsion of monodispersed oil droplets in formamide, then this emulsion was added to a metal alkoxide solution in formamide, which was finally hydrolyzed and converted to a gel by the addition of ammonia. The density of the porous network could be adjusted by centrifugation of the emulsion, which assembles the emulsion droplets in a hexagonally packed manner. Accessibility of the pores and the internal surface area was determined by nitrogen sorption measurements.

Another technique utilizing liquid droplets is breath figure templating, which was reported by Francois et al. [43–45]. Under the influence of a moist air flow, water droplets condense on the surface of a polymer solution. They form a hexagonal array and sink into the polymer solution, thereby serving as template. After complete evaporation of the solvent and water droplets, a polymer film remains with hexagonally arranged pores.

Biological materials can possess intriguing structural features, which can barely be mimicked by laboratory methods. In order to take advantage of these structural features, biological material such as bacterial threads [46] or echinoid skeletal plates [47] were also employed as templates.

Conceptually, any form of discrete colloidal objects could be used as a template structure, including gas bubbles, liquid droplets, and solid particles. In this review we will focus on porous networks that are produced from solid, mainly monodisperse, colloidal particles.

2.2

Particle Film Formation Strategies

The size of the colloidal particles ultimately determines the size of the resulting pores, and the geometry of the pore arrangement is essentially determined by the packing symmetry of the templating particles. Monodisperse

particles can be arranged in highly ordered, long-range structures, which in most cases are constituted of an fcc lattice. A variety of techniques have been established to pack colloidal particles into fcc crystals, with a selection of the most common ones presented in Fig. 2.

The simplest technique is sedimentation, where under the influence of gravity monodisperse particles slowly settle down and arrange into a hexagonal pattern. Drying of the supernatant solution yields the dry colloidal crystal. This method is time consuming and strongly dependent on the diameter and density of the constituting spheres [48, 49]. Settling of the colloidal particles can be greatly accelerated by applying an enhanced gravitational field in a centrifuge [50, 51].

Another technique is to assemble the particles under the influence of a liquid flow field, as achieved by filtering the dispersion. A membrane with pore sizes smaller than the particle diameter is used while continuously drawing the dispersion through a funnel, and the colloidal particles are retained at the membrane surface and accumulate [30, 52]. Simultaneous application of an oscillating shear field during the filtration process improves the quality of particle ordering [53].

Since colloidal particles such as PS latex and silica nanoparticles are stabilized by electrostatic repulsion, their charged state can also be exploited for the assembly process. Either a constant (dc) or alternating (ac) electric field is applied perpendicular to the receiving substrate, above which the dispersion is confined. By adjusting the direction of the electric field the particle assembly can either be accelerated under the simultaneously acting gravitational field or it can be slowed down. It was further shown that single monolayer formation is possible by the controlled application of an ac field, which results in the continuous formation and dissolution of a close-packed particle

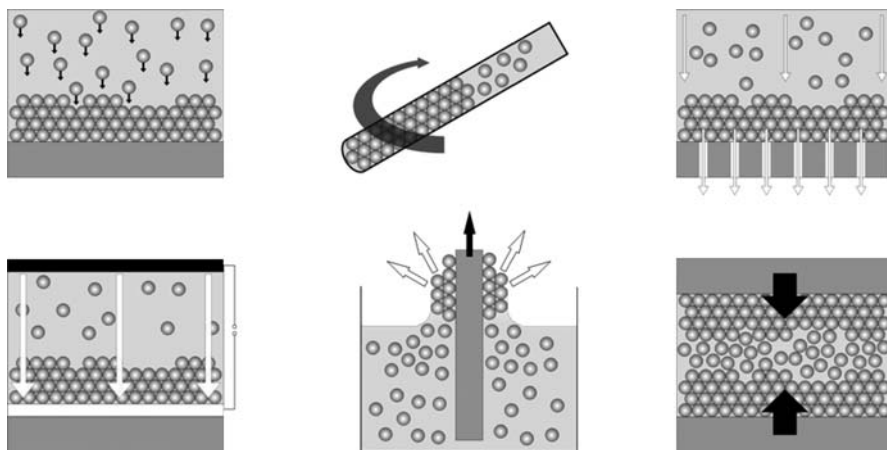


Fig. 2 Schematic representation of various methods for colloidal crystal formation

layer [54]. Additionally, the influence of a simultaneously acting hydrodynamic flow field was investigated, showing that the domains of crystalline order grow with increasing flow rate [55].

Another widespread technique is to assemble the particles under convective flow. In contrast to the filtration method, the liquid flow is generated in this approach by the evaporation of the dispersion medium. In order to avoid uncontrolled aggregation at the drying front, namely the “coffee ring” effect [56], the particles are not assembled on a horizontal substrate but on a tilted or vertically standing specimen. The onset of crystallization occurs along the meniscus line (the contact line between the liquid, the substrate, and the air), while enhanced medium evaporation at this line leads to a solvent flux, which drags the particles from the suspension bulk toward this crystallization edge [57]. As the evaporation continues, the contact line slowly migrates down the substrate and assembly of the particles takes place in a homogeneous film. The thickness of the resulting crystal is determined by the particle concentration in the suspension and increases along the substrate as the concentration increases continuously with evaporation. The rate of evaporation, which is controllable by the environmental humidity and temperature, governs the quality and domain size of the crystal [58]. Simultaneous lifting of the substrate, as outlined by Dimitrov and Nagayama [59], or continuous removal of the dispersion allows a further degree of control, with the thickness of the colloidal crystal being uniform over the entire substrate and depending on the speed of substrate lifting or dispersion lowering, respectively.

The application of widespread standard polymer processing techniques to the formation of colloidal crystals was introduced by Ruhl et al. [60]. They demonstrated the fabrication of a large colloidal crystal film, which comprises core-shell latex particles. Upon coagulation the soft shell of the particles causes the formation of a rubbery mass, which can be uniaxially compressed. The radial horizontal flow during the compression induces crystallization of the particles from the surface of the plates inward. The soft shell constitutes the matrix in which the hard spheres are embedded. This technique is promising for efficient application to other polymer processing methods like extrusion or injection molding.

In many cases it is necessary to synthesize porous materials in a well-defined preordered shape or within confined geometries, which introduces a pathway to fabricate hierarchically ordered porous materials. The techniques mentioned above have been shown to be capable of producing structured and well-ordered templates [61] within capillaries [50], thin plates [62], micromolds [63], or photoresist patterns [64, 65]. Spatial adjustment of the surface functionality on the substrate and its wetting properties can yield patterned colloidal films [66, 67]. Finally, confining the particle dispersion itself by printing techniques produces micropatterned arrays [68]. This was also shown to work without the necessity of preceding surface patterning steps [69].

2.3

Porous Replica Formation

Conceptually, besides the assembly of the templating particles, the second logical step is to fill the free voids with the material of which the final porous specimen should consist. Three fundamental cases should be distinguished: (1) nonreactive or (2) reactive infiltration, and (3) codeposition. Most common are cases 1 and 2, where the infiltration is usually done by applying a solution of the desired material to the template crystal. The last case 3 is significantly different from the other two, as filling of the free voids occurs simultaneously during template crystal formation.

Nonreactive infiltration has been shown by the use of particles smaller than the channels of the free voids, such as CdSe quantum dots [34], silica or titania particles [70], and gold as metallic nanoparticles [33]. After evaporation of the dispersion liquid, the porous network can be obtained without any further chemical modification of the infiltrated particles. However, calcination often helps to increase the strength of the network by sintering the nanoparticles together, but often at the expense of network shrinkage and fracturing. Other examples of nonreactive infiltration are filling of the free voids with molten metal [71, 72] or by precipitation of inorganic salts [73].

A lot of research has also been devoted to the infiltration of macroporous templates by reactive components. Porous polymeric material was synthesized by either infiltration of a monomer–initiator mixture with subsequent polymerization [29], or by infiltration of a prepolymer solution, which can be UV-cured afterwards [27]. A quite common route to fabricate metal oxide networks is to infiltrate the precursor structure with its corresponding sol-gel solution, which eventually hydrolyzes and solidifies in the desired porous shape. This technique has been shown for a great variety of materials (compare Table 2 in [10], Table 1 in [37], and Table 1 in [38]), such as silica [52], titania [30, 50], zirconia [30] or alumina [30], just to mention a few. Another pathway to metal oxide structures was introduced by Park et al., who precipitated acetate salt solutions of the desired material in the free voids. After addition of oxalic acid the porous metal oxide was formed during the combustion of the latex template [73].

Various electrochemical approaches have been used to infiltrate colloidal templates with a great variety of metals, semiconductors, and conducting polymers. Both electroless deposition by chemical reduction and electrodeposition under the influence of an electric current were demonstrated. In the former case, the voids of the colloidal material have to be first infiltrated by an appropriate nucleating crystal. Growing from these nucleation sites, the remaining space was filled with materials such as gold, silver, nickel, copper, or platinum [74]. Under these conditions, metal deposition occurs simultaneously throughout the whole template, which may bear the danger of blocking

narrow channels and preventing further salt transport for complete filling of the interstitial voids. Electrodeposition allows the formation of porous semiconductor materials like CdSe and CdS [75] or conducting polyaniline matrices [76]. Due to the gradual and complete filling of the voids starting from the electrode surface, the filling factor is usually very high, which in turn leads to a lower shrinkage of the porous network during template removal.

A solvent-free method was introduced by chemical vapor deposition (CVD) of isoprene in a nitrogen atmosphere at 800 °C. This method yielded, after dissolution of the templating silica colloids, a conducting inverse carbon opal [77]. A semiconductor replica made of silicon could also be produced by CVD [78].

Codeposition, which represents the concurrent processes of colloidal crystal template formation and simultaneous filling of the interstitial sites with the desired framework material, is usually achieved by the deposition of a mixture of the templating colloids with the matrix material precursor (for example, a sol-gel precursor or nanoparticles). For this purpose, a dispersion of large particles, which will constitute the template, is mixed with nanoparticles of the framework material, which have to be small enough to easily fit into the interstitial space without interfering with crystal formation. By this method porous silica [25, 32, 35] and titania [32] were fabricated.

In general, the successful formation of inverse opals greatly depends on the degree and quality of the void filling procedure. Therefore, some requirements have to be met and some compromises have to be made. Firstly, the infiltrating liquid has to be compatible with the solubility and surface properties of the constituting spheres. Otherwise the liquid may dissolve or swell the template, or it will not properly wet the nanochannels and nanocavities, leaving them unfilled. Especially when using polymer solutions for the infiltration process, optimization of the experimental conditions may be tedious, since the maximum polymer concentration at the lowest possible viscosity is required to ensure full void filling in a reasonable time frame. Too low concentrations might lead to thin, fragile networks, while too concentrated samples might not replicate all voids. Possible improvements to difficult sample infiltration processes are, for instance, repeated infiltration and drying cycles using a more dilute sample, or application of a vacuum during the template filling process to prevent entrapment of air bubbles.

2.4

Template Removal

The last step in the process of porous network preparation requires template removal. This is normally achieved by particle dissolution or combustion. In the case of polymer particle templates, both methods of dissolution in organic solvents (like toluene or THF) or pyrolysis (often at temperatures

> 350 °C) are available. The pyrolysis temperature has to be adjusted with regard to the polymer template as well as the network material. In the case of inorganic particles this step is often accompanied by sintering of the nanoparticles, leading to a stronger porous network matrix. On the other hand, inorganic silica particle templates cannot be pyrolyzed and are usually removed by etching with hydrofluoric acid.

A fundamental prerequisite for complete removal of the templating material is a continuous, fully interconnected network, since template material entrapped in closed pores will not be accessible by the solvent and chemicals, or it will destroy the network lattice during their combustion by the enormous volume expansion of the volatile pyrolysis products.

Depending on the volume filling factor of the matrix material, substantial shrinkage of the porous network accompanied by crack formation may occur for low filling fractions during template removal. Furthermore, annealing the replica material at elevated temperatures may lead to a transformation from one modification or crystal phase to another that is thermodynamically more stable at these temperatures, as shown for the thermal conversion of amorphous titania or its anatase phase to the rutile structure [79].

3

Metal Based Networks

3.1

Materials

Metals are an important class of materials with a vast range of technical applications that exist not only as pure elements, including the elements left from the diagonal through the periodic table of elements between beryllium (Be) and polonium (Po), but also in combinations of several metals as alloys and as intermetallic compounds. The striking properties, on which such applications rely, result from the fact that the conduction band and valence band energetically overlap. As a consequence, the valence electrons are free to move around the metal ion cores as the so-called electron gas, which gives rise to the metallic character. This metallic character manifests itself as good electrical and thermal conductivity, and by the absorbance and reflectance of electromagnetic radiation, in particular of visible light, which provides a metallic luster. In terms of mechanical properties, metals are usually ductile, elastic, and malleable, their melting points ranging from well below room temperature, like 234.32 K (−38.83 °C) for mercury (Hg, liquid at room temp.), up to 3695 K for tungsten (W).

Nanoporous metallic networks combine these very interesting properties with an intricate spatial architecture for applications in electronics, optics (particularly as photonic crystals), optoelectronics, catalysis, fuel cells, and

sensors, to name but a few. Such metal networks could be prepared by colloidal crystal templating; the utilized methods may be categorized into (a) codeposition of metal nanoparticles with the templating microspheres, and (b) posterior infiltration of metal or metal precursors into the preformed colloidal crystal templates. The latter category can be further divided into four subcategories:

1. Metal nanoparticle infiltration
2. Metal precursor infiltration and transformation
3. Electroless deposition
4. Electrochemical deposition

as discussed in the individual paragraphs below. The subsequent removal of the colloidal crystal template leads to the metallic inverse opals with nanoporous network structure.

3.2

Nanoparticle Codeposition

Direct infiltration of colloidal crystal templates with molten metals is difficult, due to the usually high melting temperatures and surface tension of the melt, and would require high pressures. This was shown for gallium and tellurium [71, 72], but the templating opal was not removed. A more practical approach is the codeposition of metal nanoparticles with the templating colloidal particles during colloid crystallization. The codeposition of a mixed suspension of gold nanoparticles and PS latex microspheres led to fcc packing of the polymer latex with the interstitial spaces filled by gold nanoparticles after evaporation of the solvent. Dissolution of the templating latex particles by toluene resulted in the metallic inverse opals [80, 81]. When such macroporous gold films were used as substrates for surface-enhanced Raman spectroscopy (SERS), the signal enhancement was an order of magnitude greater than that observed for gold nanoparticles randomly absorbed on glass substrates, which was explained by the ordering and monodispersity of the macropores [81].

3.3

Nanoparticle Infiltration

Similarly to the codeposition procedure above, the metal can also be delivered as nanoparticles to the colloidal crystal template, but in this case after preparation of the template. This was demonstrated for gold nanoparticles, which were filled into the interstitial sites of a polymer opal by filtering a gold nanoparticle suspension through the preassembled opal with a filter small enough to hold back the nanoparticles [33]. The templating opal was prepared before in very much the same way by filtration of a PS latex suspension.

The polymer template was removed in two different ways, by toluene extraction and by pyrolysis, which resulted in very different types of gold replicas. In the first case the nanoparticles retained their shape, which led to a hierarchical network structure with nanopores between the nanoparticles and macropores from the templating polymer spheres. When the latex was removed by calcination at 300 °C, the gold nanoparticles fused to a dense metal matrix with only macropores.

3.4

Metal Precursor Infiltration and Transformation

Instead of infiltration with neat metal nanoparticles, the interstitial voids of the template opal can also be filled with a metal precursor. The impregnation of the preformed colloidal crystals with the metal precursor, followed by transformation of the precursor to the neat metal and removal of the template, results in metallic inverse opals. For example, nickel oxalate was precipitated in a PS opal and converted into a NiO macroporous network by calcination of the metal salt and combustion of the polymer. In a subsequent step, the nickel oxide was reduced to neat Ni in a hydrogen atmosphere to yield a macroporous metal network [82]. It was further suggested by the authors that by the same technique other metal networks (e.g., Mg, Mn, Fe, Zn from their oxides and Ca, Sr, Ba etc. from their carbonates) should be accessible.

Tungsten inverse opals were synthesized by CVD of the volatile tungsten precursor $W(CO)_6$ inside the colloidal crystal with direct conversion into neat tungsten metal [83]. Another approach to tungsten replicas employs infiltration of the PMMA colloidal crystal template with the aqueous tungsten precursors, acylated peroxotungstic acid or ammonium metatungstate hydrate. Reduction in hydrogen at 800 °C removed the polymer template and formed a tungsten skeleton with periodic structure [84]. These open network structures made of tungsten are thought to have great potential for modified thermal emission [85].

3.5

Electroless Metal Deposition

Jiang et al. first demonstrated the preparation of macroporous metal films from colloidal crystals by electroless metal deposition [74, 86]. Colloidal silica was first functionalized with thiol groups by coating with 3-mercaptopropyltrimethoxysilane, then these silica colloids were crystallized onto a glass substrate. Immersion of the crystal templates into a gold nanoparticle suspension (~ 5 nm) resulted in the binding of the gold nanoparticles onto the colloid surfaces. Electroless deposition with existing standard recipes led to Ni, Cu, Au, Pt, and Ag inverse opals.

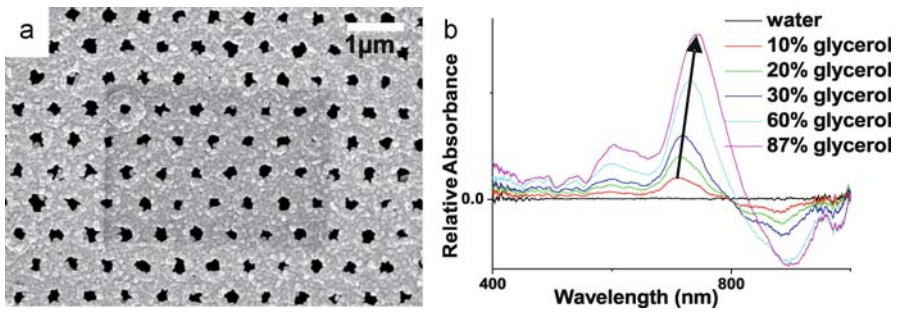


Fig. 3 **a** SEM image of a gold/silica composite opal; **b** absorption spectra showing a red shift of the plasmonic response with the increase of the refractive index of the surrounding medium [35]

Jonas and coworkers deposited gold nanoparticles on silane-functionalized silica inverse opals prepared by the codeposition procedure. The gold/silica hybrid inverse opals shown in Fig. 3a were then formed within the macroporous silica network by electroless deposition of HAuCl_4 with hydroxylamine hydrochloride [35].

A plasmonic response of the gold/silica composite inverse opals was observed (Fig. 3b), which showed a pronounced spectral change upon the variation of the surrounding dielectric medium by addition of glycerol to the water phase. This property suggests an application of the hierarchically structured replica in the field of optical sensors.

3.6

Electrochemical Metal Deposition

When the colloidal template is deposited onto a conducting electrode, electrochemical metal deposition within the interstitial voids can be achieved by immersing the opal into a metal salt solution in an electrochemical cell and running a current across the opal. By this technique, Au, Ag, W, Pt, Pd, Co, Ni, and Zn macroporous networks have been fabricated [87–90]. Grating samples with voids of varying depth could be easily formed by controlling the total charge passed through the electrochemical cell, as shown in Fig. 4A [91], where t is the film thickness and a is the radius of the templating latex particles. The SEM and AFM images showed that the local surfaces of the samples were smooth on the sub-10-nm scale. Due to the low surface roughness, the structural regularity, and the spherical segment void geometry, reflectivity measurements on these truncated spherical nanocavities revealed void plasmon modes localized inside the cavity and SPP propagating modes on the structure surface [91–93]. These results are shown in Fig. 4B and provide a deeper understanding of the nature of plasmon fields in metallic pore structures as a prerequisite for the development of plasmon applications [94–96].

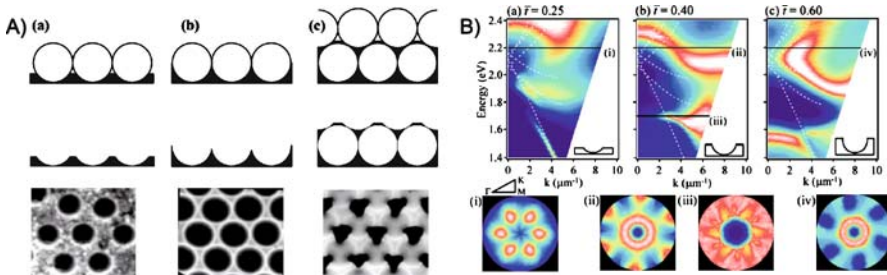


Fig. 4 **A** Schematic cross section of metal film growth and corresponding scanning electron micrographs (below) of the gold nanocavities fabricated with $a = 350$ nm latex spheres of thickness t for (a) $a/2$, (b) a , and (c) $2.1a$ [91]. **B** Measured energy dispersion of the reflectivity for TM polarized light as a function of the in-plane wave vector for increasing relative void depth, $\bar{t} = t/(2a)$ (a–c). Log color scale: white dotted lines show a zone-folded plasmon dispersion, sample orientations of $\phi = 30^\circ$ in all cases. (i–iv) k space cuts through dispersion relation at: (i) $(\bar{t}, E) = (0.25, 2.2 \text{ eV})$; (ii) $(\bar{t}, E) = (0.4, 2.2 \text{ eV})$; (iii) $(\bar{t}, E) = (0.4, 1.7 \text{ eV})$; (iv) $(\bar{t}, E) = (0.6, 2.2 \text{ eV})$, symmetry shown above (i). Light shade corresponds to absorption features [93]

4 Semiconductor and Carbon Based Networks

4.1 Materials

Semiconductors are materials that were originally defined by their conductivity lying between those of metals and insulators in the range of about 10^{-9} to $10^3 \Omega^{-1} \text{ cm}^{-1}$ at 300 K, which often increases with higher temperatures. A more general definition is based on the electronic band structure in these materials, particularly the bandgap of about 0.1–4 eV that separates the fully filled valence band from the empty conduction band at 0 K. For semiconductors to become conductive, electrons have to be raised from the valence to the conduction band, which is the basis of many interesting properties, like thermal conductivity, electron and hole transport, as well as their optical characteristics. Specifically, a high refractive index below the absorption edge, where semiconductors are transparent to electromagnetic radiation, is highly valuable, since inverse semiconductor opals with a high refractive index contrast between the matrix and the voids and are predicted to possess a complete photonic bandgap. With the appropriate structural and materials parameters (periodicity of several hundred nanometers and fcc lattice symmetry, about 80% porosity, refractive index contrast > 2.8), such a photonic bandgap would exist at optical wavelengths, where the propagation of electromagnetic radiation is prohibited by destructive interference of multiple Bragg reflections [97]. The conductivity, on the other hand, can be increased by doping the semiconductor with foreign atoms, which increases the charge

carrier density. This possibility enabled the usage of the semiconductors as active electronic elements, like transistors, light-emitting diodes, and integrated circuits. Ultimately, such nanostructured materials could be exploited in optoelectronic applications to simultaneously control the flow of electric current and light, as well as spontaneous emission.

Semiconducting materials include pure elements like carbon (as boron-doped diamond or semiconducting nanotubes), silicon, germanium, gray (crystalline) tin, selenium, tellurium, and boron, compound semiconductors like metal oxides (e.g., TiO_2 , ZnO) and other metal chalcogenides (like CdS , CdSe), salts (like CuCl), or other binary elemental compounds (like GaAs , InP), and semiconductor alloys (like $\text{Ga}_{1-y}\text{Al}_y\text{As}$), as well as ternary and quaternary compounds (e.g., CuGaSe_2). From many of these materials inverse opals have been prepared by various methods, as outlined below [39, 97]. As carbon exists in several semiconducting modifications (e.g., boron-doped “blue” diamond and carbon nanotubes) and since graphite (technically a semimetal) has a conductivity of about $10^3 \Omega^{-1} \text{cm}^{-1}$, which makes carbon inverse opals composed of graphitic carbon particularly interesting for electrode applications (e.g., batteries and fuel cells), they are also mentioned here under semiconductor materials [98]. Due to the fact that semiconductors span such a wide range of material classes, a categorization is attempted here by the fabrication processes rather than the specific material type.

4.2

Opal Infiltration with Semiconductor Nanoparticles

Probably the conceptually most straightforward approach to semiconductor porous networks consists of opal infiltration with nanoparticles of the semiconductor material, followed by sintering of the nanoparticles to obtain a stable matrix and finally removal of the template particles. In order to fully access the voids of the opal template, the matrix nanoparticles must be smaller than the narrowest channel between the tetrahedral and octahedral voids in the fcc lattice of the template opal, which means the nanoparticle should have a relative radius of less than 0.1547. For practical purposes a radius ten times smaller than this limiting value is usually employed. Infiltration of the opal host is achieved by concentrating a nanoparticle suspension in a volatile liquid over the template opal. After stabilization of the nanoparticle network by thermal treatment, which fuses the semiconductor particles to a stable matrix, the template particles are removed by dissolution. This was shown for CdSe nanocrystals in a silica opal [34]. The nanoparticles can also be cocrystallized with the template particles, as demonstrated with titania nanoparticles and PS template colloids, followed by matrix compacting through applied pressure and burning off the polymer template [99]. The advantage of the latter approach lies in the possibility to achieve very high filling ratios without being limited to particle diffusion through the interstitial sites

of the template opal, which also speeds up the preparation time from months for the infiltration process to days for the cocrystallization.

4.3

Salt Infiltration and Chemical Conversion

The network matrix material can also be introduced as a solution of a precursor salt and subsequently converted by a chemical reaction to the desired solid. The reagents for this conversion can also be applied as a solution or via the vapor phase. Furthermore, the chemical transformation can be simply induced by heating of the composite, which in the case of polymer latex templates can simultaneously be used to remove the templating opal by pyrolysis of the polymer into volatile products. Amongst a large variety of other metal oxides, an inverse ZnO opal network was prepared by repeatedly immersing a PS colloidal crystal into a solution of ZnO in acetic acid and drying. After treatment of the incubated opal with oxalic acid to precipitate the metal salt, calcination of the zinc oxalate and pyrolysis of the PS latex at 400 °C leads to the formation of the macroporous ZnO network [73]. In a similar process, termed chemical bath deposition (CBD), CdS networks with a high template filling fraction could be obtained by repeated treatment of the silica template opal with first CdSO_4 and then $\text{S} = \text{C}(\text{NH}_2)_2$ solutions in water [41]. Such inverse CdS opals may find optical applications due to the properties of optical gain and inhibition of spontaneous emission. The salt infiltration and conversion method was also applied to prepare inverse opal networks of polyaniline, an organic semiconductor polymer. For this purpose wet PS colloidal crystals were first infiltrated with aniline hydrochloride and then polymerization was induced within the interstitial voids by treatment with potassium peroxodisulfate. After formation of the polyaniline matrix the PS template particles were removed by dissolution with THF [100].

4.4

Alkoxide Infiltration and Hydrolysis

Closely related to the salt infiltration method discussed above is the utilization of metal alkoxide precursors in a sol-gel process to fill the interstitial sites in an opal template. The template is first infiltrated with an alkoxide (neat or as solution), then the hydrolysis and condensation reaction following the infiltration transforms the alkoxides into an extended network of the corresponding metal oxide. By this method TiO_2 networks besides other oxides were initially prepared with a strong focus on their optical properties as photonic crystals [30, 50]. For this purpose a high refractive index material is desired, which would be the rutile modification of titania with the highest refractive index. Nevertheless, the sol-gel procedure provides an amorphous or anatase modification with lower refractive index. By calcination of the anatase

phase at high temperatures above 700 °C it converts into the rutile modification, but the order of the network is lost. Other semiconductor metal oxide networks, like zirconia, were also prepared by the sol–gel method [79]. The advantage of the sol–gel infiltration lies in the efficient filling of the opal template, while the drawback is the strong volume shrinkage after calcination and removal of the polymer opal template. The large volume reduction on going from the metal alkoxide to the calcined oxide is due to loss of the alcohol substituent as well as sintering of the condensation product.

4.5

Oxide Reduction

A further extension of the preparation of oxide networks by the sol–gel method is the reduction of the oxide to the corresponding pure element, as demonstrated for germanium [101]. An inverse germanium dioxide opal is obtained via the sol–gel procedure with $\text{Ge}(\text{OCH}_3)_4$ and then reduced in an H_2 atmosphere at 550 °C. Due to the volume reduction during the process sequence, these procedures were repeated several times to obtain high filling fractions. For this purpose silica opals were used as templates, which are robust against calcination and reduction at higher temperatures, and which were removed in the final step by HF etching. The resulting Ge networks are interesting materials for optical applications in the infrared region, since Ge possesses a very high refractive index contrast of 4.

4.6

Melt Infiltration

Infiltration of opal templates directly by a melt of the matrix material is very appealing since it does not require further chemical transformation and yields very high filling ratios, but it is limited to low melting materials and usually high pressure to force the melt into the interstitial sites. The infiltration process was demonstrated for tellurium [71], which melts at 450 °C, but the template has not been removed in these early studies.

In a melt infiltration-related procedure glassy carbon networks were fabricated by filling the voids in a silica opal with a phenol resin, which was subsequently cured, the silica template removed by HF, and the polymer network carbonized by heating to 900–1000 °C in an argon atmosphere [77].

4.7

Chemical Vapor Deposition

In CVD a volatile reagent is supplied via the gas phase to the interior of the opal template, where it reacts and transforms into the solid matrix material. The particular feature of this method is the fact that the reagent is in the vapor

phase, allowing easy access to the very narrow and remote voids in the template opal. On the other hand, since the material is isotropically deposited in the voids, the risk of blocking the narrow channel and hindering subsequent deposition in larger voids behind the blockage may be an issue. Nevertheless, CVD has been successfully applied to prepare a variety of inverse opal structures with high filling fractions, including neat Si [78], neat Ge [102], and graphitic carbon and diamond inverse opals [77]. In the case of Si, silica sphere templates were infiltrated with disilane (Si_2H_6) gas at about 200 Torr and 250–350 °C. After decomposition of the precursor and growth of elemental Si, the infiltrated opal was annealed at 600 °C to allow Si diffusion in the voids and improve crystallinity. The silica template spheres were then removed by HF etching. For the inverse Ge opal, digermane (Ge_2H_6) gas was infiltrated into a silica opal at liquid nitrogen temperatures and 300–1000 Torr, after which the sample was heated to 200–350 °C for digermane decomposition. After annealing at 500 °C and subsequent template removal, an inverse microcrystalline Ge opal was obtained. The high refractive index contrast in the Ge ($n = 4$) and Si ($n = 3.5$) networks provide a full photonic bandgap in the inverse opal below their absorption edge (Ge larger than 1850 nm, Si larger than 1100 nm). The graphitic carbon inverse opal with a conductivity of 10 S/cm was prepared from a propylene gas and nitrogen mixture (molar ratio 1 : 3) at 1 atm for 6 h at 800 °C, while the diamond inverse opal of cubic diamond was obtained from a methane plus hydrogen plasma inside a silica opal, which was first infiltrated with 2–5-nm diamond seed particles.

4.8

Electrochemical Deposition

If the chemical transformation of soluble precursors into insoluble semiconductor materials can be performed electrochemically at constant current (galvanostatic) or constant potential (potentiostatic), the semiconductor network may be prepared inside an opal template by electrodeposition. For this purpose one side of the templating opal has to be modified with an electrode and immersed into an electrolyte solution of the precursor inside an electrochemical cell equipped with a counter electrode. When a voltage is applied across the electrodes, the reaction of the soluble precursor occurs at the electrode surface in the opal, leading to the growth of the insoluble semiconductor within the voids of the opal. By this directed growth from the electrode/opal interface toward the interface of the template with the surrounding solution, complete filling of the interstitial sites in the opal is theoretically possible. An appealing feature of the electrodeposition method is the control over various experimental parameters, such as current, voltage, and electrolyte composition, which in turn provides control over structural parameters in the resulting network, such as filling fraction, wall thickness, and connecting pore diameter. With this method CdS [103], CdSe [75],

and ZnO [104] networks were prepared as inorganic semiconductor matrix materials. Furthermore, the method is also very appropriate for the preparation of organic semiconducting polymers, like polyaniline, polypyrrole, and polybithiophene [105, 106]. Such conducting polymer networks may be particularly interesting as electrodes with high internal surface in batteries, capacitors, and sensors.

5

Metal Oxide Based Networks

5.1

Materials

Besides the common features of most metal oxides as chemically stable and mechanically robust materials, this class of compounds can also provide unique functions for ceramics, high refractive index and magnetic materials, catalysis, and biocompatibility. A wide range of porous metal oxide materials have been synthesized over the last decade. In general three distinct pathways have been undertaken: a sol-gel synthesis of the metal alkoxide; infiltration with an appropriate metal salt and subsequent conversion; or infiltration or codeposition with preformed metal oxide nanocrystals.

5.2

Alkoxide Infiltration and Hydrolysis

The most widespread pathway to porous metal oxides is given by the condensation of a metal alkoxide sol-gel solution in the interstices of a polymeric (PS or PMMA) colloidal crystal. After condensation of the metal alkoxide into a crosslinked metal oxide film, the constituent spheres can be removed via two different methods. They can either be dissolved in an organic solvent such as THF, which requires no heat but an interconnected network of the polymeric spheres, or the organic material is removed by combustion, which usually takes place at temperatures higher than 400 °C. The method of template removal has a severe influence on the resulting metal oxide film as it can change the crystal structure during calcination. This was demonstrated for the case of aluminum oxide [107, 108]. By condensation of aluminum *sec*-butoxide in the presence of a structure-directing agent such as amines, mesoporous AlOOH (boehmite) is obtained. The calcination of this material at 500 °C yields γ -Al₂O₃. The condensation of metal alkoxides was extended to other metal oxides such as SiO₂, ZrO₂, Al₂O₃·H₂O, Fe₂O₃, Sb₄O₆, and WO₃ [30]. Various other groups have also fabricated a range of porous metal oxide materials via this route [50, 109]. Quite commonly shrinkage of the initial voids of up to 30% has been reported.

5.3

Salt Infiltration and Chemical Conversion

A method that does not employ the use of the corresponding metal alkoxide was introduced by Yan et al. [73]. They infiltrated templates of PS spheres with acetic acid, ethanol, water, or a mixed solution of the corresponding metal acetate salt. After drying, this composite material was impregnated with a solution of oxalic acid. Finally, the PS spheres were removed by calcination, which simultaneously yielded the metal oxide framework. The advantage of this route is the reduced sensitivity to moisture and the better availability of metal salts as compared to metal alkoxides. Furthermore, not only are metal oxides accessible but also pure metal networks can be fabricated when the calcination step is conducted under a reducing atmosphere. In this way the fabrication of MgO, Cr₂O₃, Mn₂O₃, Fe₂O₃, Co₃O₄, NiO, ZnO, and metallic Ni porous networks were demonstrated, as mentioned in Sect. 3.

5.4

Polal Infiltration with Metal Oxide Nanoparticles

In another approach Subramanian et al. [32] infiltrated the polymeric opal template directly with ultrafine particles instead of employing metal alkoxides or salts. In this approach infiltration with a nanocrystalline material of known crystal phase is possible, and therefore materials with a predetermined crystal structure of the walls can be obtained even at mild processing conditions. For instance, TiO₂ frameworks with a rutile phase of the wall material could be obtained without the necessity to resort to sintering at high temperatures. Additionally, shrinkage, which commonly occurs in the case of condensation of metal alkoxides or conversion of metal salts, is largely reduced. Finally, this route opens a pathway to obtain porous metal oxide materials, which are barely accessible by wet chemistry approaches.

6

Polymer Based Networks

6.1

Materials

Polymers are an inexhaustible mine for materials scientists owing to the numerous properties that they can manifest, such as thermoplastics or thermosets, flexible or rigid, hydrophilic or hydrophobic, conductive or insulating, biodegradable or nonfouling etc. These properties can be specifically tailored by simply varying the chemical structure and combination of the repeating units, their overall number in a single polymer chain, determining the molecu-

lar weight, and by the sequence and tacticity (stereochemistry) of the repeating units. Moreover, polymers often have the advantages of less weight per volume and lower costs compared to most inorganic and metallic materials, which are vital in practical applications particularly as construction materials. Owing to this great versatility, polymers have also been used as matrix material for porous networks derived from colloidal templates. Such polymer replicas have been prepared either by (1) in situ formation of the polymer within the voids of colloidal template by radical [29] or electropolymerization of appropriate monomers [106], or (2) infiltration of the template with the preformed polymers [27, 110] followed by removal of the template particles. In the latter case, three modes of infiltration are in principle possible:

- (a) Infiltration of a polymer solution followed by solvent removal
- (b) Infiltration with a hot polymer melt and solidification at room temperature
- (c) Infiltration with liquid prepolymer followed by crosslinking

A specific advantage of polymers as replication matrix over other materials, particularly inorganic oxides formed by pyrolysis, is the minimal volume change during matrix solidification, which substantially reduces the problem of crack and defect formation in the porous network. In chemical and biosensing applications, the chemical properties of the polymer network are particularly important because the polymer can serve as the analyte-binding surface while simultaneously acting as the transducer that responds to the analyte binding. Here again, the great chemical variability of organic polymers is of substantial advantage for specific tailoring of such surface properties during replica formation, or even in a postmodification of the inner surface after network preparation.

6.2

In Situ Polymerization and Crosslinking

Park and Xia [27] reported on utilizing colloidal crystals as templates for the fabrication of polymer based macroporous networks in the form of polyurethane membranes, representing strategy (2c) above. In their initial experiment, a flow cell was first packed with PS spheres to form a colloidal crystal and then filled with a liquid precursor of polyurethane. After UV exposure to solidify the polyurethane by chemical crosslinking into an insoluble matrix, the polymer-polymer composite was washed with toluene to selectively dissolve the PS beads, which resulted in a three-dimensional porous structure with interconnected pores of defined pore sizes. The big pores originated from the templating PS particles, while the small orifices formed at the contact points between neighboring template particles. The authors specifically pointed out that in these membranes the pore structure was fully accessible from the top and the bottom surfaces, which is an important prerequisite for many applications based on a medium flowing through

the membrane. Jiang et al. [111] extended the methodology to a more general framework for polymer based macroporous networks by strategy (1) employing silica colloids as the templating material, which can be removed later by hydrofluoric acid (HF) etching. Therefore, any monomer that does not degrade silica and whose resulting polymer is not affected by HF can be used to infiltrate the silica colloidal crystals. PMMA, PS, epoxy [111], and conducting polymers, such as poly(2,5-dioctyloxy-*p*-phenylenevinylene) and poly(2-methoxy-5-dodecyloxy-*p*-phenylenevinylene) [112], were successfully demonstrated to be made into macroporous networks with the inherited periodicity exhibiting distinctive optical properties relevant for photonic crystals. The interconnecting pore size was found to be dominated by two factors: the viscosity of the monomer liquid, and the shrinkage of the replica polymer during the polymerization process. In essence, the less viscous is the monomer liquid and the less the material shrinks during polymerization, the smaller is the interconnecting pore [111].

6.3

Electropolymerization

Electropolymerization has provided another parameter in controlling the interconnecting pore size through the applied voltage, with high voltage favoring larger pores and vice versa, which was demonstrated as an effective strategy by Sumida et al. [106] who electropolymerized pyrrole in the interstices of a silica colloidal crystal. Moreover, the replica film thickness can be tuned by the duration of electropolymerization. Due to the high controllability of the geometric structure parameters in the replica and the stimuli-responsive property of the conducting polymer itself, an electropolymerization strategy was soon adopted for fabrications of functional polymer macroporous networks. In the series work carried out by Cassagneau and Caruso, semiconducting polymer inverse opals [113], affinity biosensing polymer inverse opals (readout signal based on stop-band shifts) [114], and potentiometric biosensing polymer inverse opals [115] were fabricated through electropolymerization of pyrrole and polythiophene, poly(thiophene-*co*-3-thiophenemethanol) copolymer, and creatinine deiminase-doped polypyrrole, respectively. Their choice of employing a PS colloidal crystal template followed by THF removal preserved the chemical integrity and biological activity of the replica material, which would not tolerate the HF etching in silica template removal.

In more recent work conducted by Tian et al. [76], aniline was electropolymerized in the interstitial voids of PS colloidal crystals via both cyclic voltammetry and galvanostatic methods. The voltage change against the process time was observed in galvanostatic electropolymerization, which was ascribed to variation of the electrochemical reaction area. Distinct changes in the slope of the relation between voltage versus time were demonstrated to provide a clear indication of the polyaniline (PANI) replica growth stage, as shown

in Fig. 5. Doping of poly(styrene sulfonate) (PSS) into the PANI network was found not only to enhance the mechanical strength of the porous structure, but also to sustain a redox activity at neutral pH, which is a very desirable feature for biosensing applications in terms of pH-dependent protein stability. The elec-

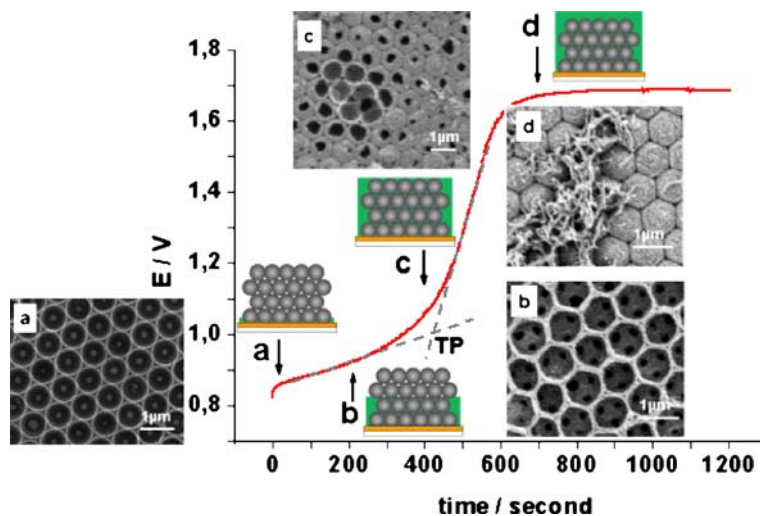


Fig. 5 Voltage changes during the galvanostatic electropolymerization of aniline to prepare PANI inverse opals. The *inset sketches* represent the stages of the formed PANI replica inside the PS template at the indicated points, with the SEM images showing the corresponding PANI inverse opals after stopping the polymerization at these points and subsequent PS template dissolution [76]

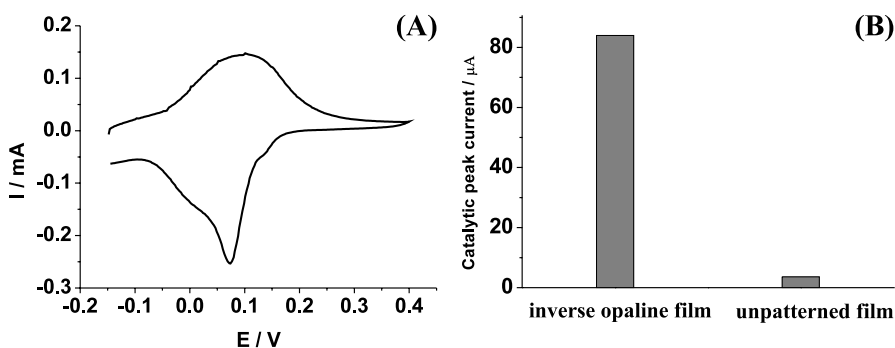


Fig. 6 **A** Cyclic voltammogram (CV) of PANI/PSS inverse opaline films in an effort to implement these structures in biosensors (measured in 0.1 M PBS buffer at pH 7.1). **B** Comparison of the electrocatalytic activity of a porous PANI/PSS inverse opaline film toward the oxidation of β -nicotinamide adenine dinucleotide (NADH) and that of the planar PANI/PSS film with the same film thickness (the NADH concentration was 10 mM, and the CV scan rate was 5 mV s^{-1}) [76]

trocatalytic capacity of the PANI/PSS inverse opal was found to be enhanced by an order of magnitude compared to a planar PANI/PSS film (Fig. 6).

6.4

Application Examples

Hydrogels exhibit reversible volume changes in response to a broad variety of environmental stimuli, such as temperature, pH, electric field, light intensity, pressure, enzymes, chemical species, and the presence of antigens [116, 117]. Their integrated function of simultaneous sensing and mechanical actuating is highly appealing for sensing applications, particularly for the optical stop-band readouts where lattice constant variation is a key parameter. Hydrogels have been successfully formed into macroporous networks as sensitive color indicators for pH [118], thermal and electrical changes [119], and humidity variations [120]. A salient advantage of this system is the facile diffusion and thus rapid response owing to interconnected pore structure and good mechanical stability of the concentrated hydrogel. Moreover, a large variety of functional groups can be incorporated to provide sensing motifs to different stimuli diffused in the hydrogel structure, such as metal ions [121] and glucose [122]. Typically, a pre-gel solution consisting of hydrogel monomers and crosslinking agents is first infiltrated into the interstitial space within the colloidal crystal. Crosslinking is then introduced by UV irradiation or thermal treatment depending on the crosslinking agents. Most of the hydrogel based inverse opal sensors operate in aqueous surroundings. However, the inverse opal hydrogel prepared by Barry and Wiltzius [120] makes use of polyacrylamide's natural hydrophilicity to induce dimensional change, and creates a novel humidity sensor which is workable in the dry state, albeit based on hydrogel.

As a consequence of the discussion above, macroporous polymer networks are particularly attractive in bio-related fields (biosensing, pharmaceutical and medical applications, etc.) as the polymer matrix encompasses a very broad range of advantageous properties (in terms of processing, functionalization, and biocompatibility). As one recent example, a mixture of double-stranded DNA and diazo resin molecules was successfully used for the matrix of a macroporous network formed in a colloidal crystal template [123]. The DNA was covalently attached to the diazo resin network and readily accessible to a dye applied from solution, which substantially altered the optical properties of the ordered network upon complexation with the DNA. As such it may be the basis for optical biosensing of DNA-related analytes. The sphere-templating strategy has further been borrowed in tissue engineering, where the design of a defined pore structure and connectivity is of crucial significance for the successful growth of cells [4]. In this case, biocompatible and degradable polymers must be employed, such as poly(HEMA) (HEMA: 2-hydroxyethyl methacrylate), which was transformed into a hierarchical 3D

structure by the combination of sphere templating with photolithographic irradiation to induce polymerization and crosslinking [124]. Since in these applications the template particle size usually ranges from tens of micrometers to 100 μm to accommodate cells with several micrometer dimensions, the example does not strictly belong to the colloidal regime, but as the concept follows the templating strategies discussed above, is thus mentioned here as an interesting extension.

7

Hierarchical Porous Networks

7.1

Structural Considerations

Besides the chemical composition, from which advanced functional materials inherit a substantial part of their properties, their spatial structure is also of fundamental importance, as it defines the interface of these materials with the surrounding medium. Due to the very different chemical bonding environment of surface atoms and molecules compared to their partners in the bulk, the materials properties can change severely with increasing surface-to-volume ratio. In particular, nanoporous networks exhibit a very large internal surface, which depends sensitively on the pore and channel geometry. By introducing a hierarchy of interconnected cavities at different length scales, the surface-to-volume ratio can be dramatically increased and the materials properties accordingly tailored. Furthermore, in such complex pore hierarchies the transport phenomena of penetrating liquid or gaseous media, as well as the diffusion of dispersed species, are fundamentally altered compared to a uniform pore architecture. As the pore dimensions are in the colloidal regime, fabrication of hierarchical network structures is usually achieved by bottom-up approaches, as discussed in further detail below.

In addition to specifically increasing the complexity of the pore architecture in the submicrometer range, such porous networks can also be structured three-dimensionally on much larger length scales than the pore size by microfabrication techniques in a top-down approach. This is of major importance for device fabrication and interfacing of the nanoscopic structures with the macroscopic world.

As outlined in the Introduction, porous materials can be classified into materials which consist of microporous (below 2 nm), mesoporous (2–50 nm), and macroporous (larger than 50 nm) channels and voids. Networks, which comprise various classes of pores with characteristically different dimensions, are termed “hierarchical” according to the discussion above. The controlled synthesis of hierarchically ordered porous materials is highly desirable and has attracted much attention during the last decade. The search for such syn-

thesis strategies is motivated by the superior materials properties, which are the basis for a large range of possible applications, like catalysis, sensing, selective filtering, chromatography, wave guides, and photonic crystals with a tunable bandgap. For the purpose of catalysis and sensing, an efficient mass transport can be provided by interconnected macropores that allow large molecules like proteins to efficiently diffuse to the reaction or detection sites, which are commonly located in the meso- and micropores of such hierarchical materials. Due to this pore hierarchy these materials possess a very large surface area and can thus expose maximal amounts of catalysts or receptors to the penetrating medium.

The practical synthesis of hierarchical networks can be achieved in various ways: quite commonly colloid particles are used for templating the macropores, while meso- and micropores can be introduced by phase separation of block copolymers or surfactants.

7.2

Block Copolymer Templating

A seminal example of hierarchical templating by a combination of top-down and bottom-up approaches was introduced by Yang et al. [63]. Using poly(dimethyl siloxane) (PDMS) stamp micromolding with PS latex templating and mesophase separation of a sol-gel block copolymer solution they produced ordered networks in 3D microstructures over three independently controllable length scales. The small mesopores with 10 nm diameter were produced by the well-known phase separation of block copolymers (here Pluronic F127) in a network matrix with 100-nm macropores, formed by infiltration of a colloidal crystal with 200-nm PS latex spheres, which itself was patterned in the micrometer range by shaping the colloidal crystal with a PDMS stamp. The organic material (PS latex and block copolymer) was removed by calcination at 450 °C in air. Figure 7 shows the ordering at the different length scales. The authors initially demonstrated the power of this templating procedure for niobia and silica materials. However, various other inorganic metal oxides can be structured by block copolymers, and a comprehensive study on metal oxides, such as TiO₂, ZrO₂, Al₂O₃, Nb₂O₅, WO₃, HfO₂, and SnO₂, and also mixed oxides like SiAlO_{3.5}, SiTiO₄, ZrTiO₄, Al₂TiO₅, and ZrW₂O₈, was reported [109]. With ethanol as solvent they found mesopores from 35 to 140 Å when using EO₂₀PO₇₀EO₂₀ as structure-directing block copolymer. The influence of the type of block copolymer (F127 or P123), the cosurfactant (*n*-pentanol or *n*-butanol), and the concentration of the cosurfactant on the resulting hierarchical material was investigated by Sen et al. [125]. The F127 copolymer produced ordered mesophases with a hole structure in the presence of *n*-butanol as cosurfactant, whereas a layered structure was produced in the presence of *n*-pentanol as cosurfactant. The P123 surfactant only produced a layered mesophase in the presence of

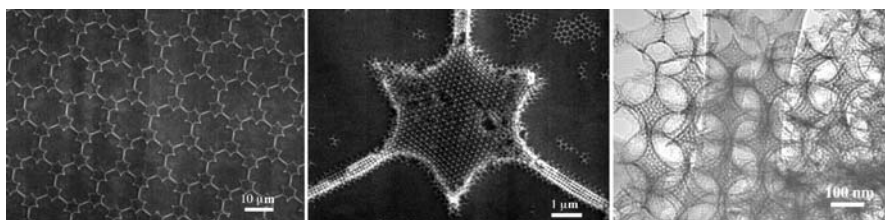


Fig. 7 SEM images (*left and middle*), at different magnifications, of hierarchically ordered mesoporous silica displaying organization over three discrete characteristic dimensions. Note the excellent ordering both in the triangular regions and in the connecting bridges. A lattice of the macroporous framework skeleton is visible in the *middle picture*. A TEM image of the same sample (*right*) shows that the framework of the macroporous skeleton is made up of ordered cubic mesoporous silica with an ordering length of 11 nm [63]

both cosurfactants. The walls of the mesopores were thick and contained disordered micropores. The preparation of hierarchical materials can also be extended to other framework materials such as carbon. Using a combination of macroporous templating by silica colloids and mesoporous scaffolding with F127 in the presence of resol as carbon source, Deng et al. [126] fabricated hierarchically ordered carbon. They found that the BET surface of such a material increases with increasing diameter of the silica spheres and the corresponding macropores.

7.3

Multiple-Size Colloid Templating

It has also been shown that a combination of interconnected macropores with distinct diameters can be fabricated in a single material. Wang et al. [25]

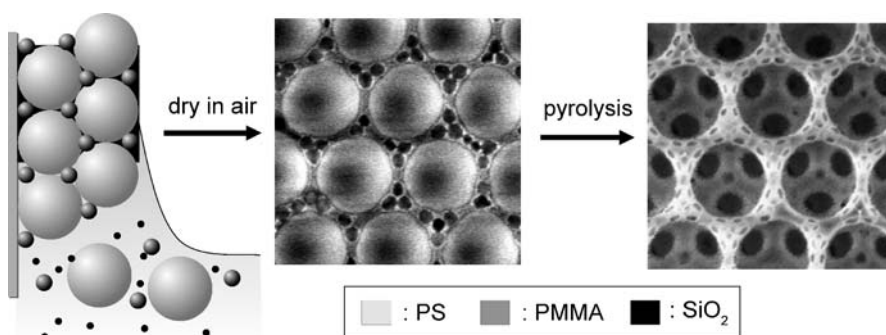


Fig. 8 *Left*: scheme of vertical lifting codeposition of trimodal colloidal particles. *Center*: trimodal colloidal crystal (tCC) consisting of large PS, intermediate PMMA, and small silica particles. *Right*: Top view of binary inverse opal (bIO) after PS and PMMA pyrolysis of the tCC in the center [25]

demonstrated the codeposition of PS particles (465 nm), PMMA particles (84 nm), and silica nanoparticles (6 nm), which resulted in macropores of two distinct sizes (460 and 80 nm) with interconnecting holes of 140 and 25 nm, as shown in Fig. 8. This vertical lifting codeposition method presents a very convenient preparation route to hierarchical structures, which only requires two fabrication steps (template particle and matrix codeposition, and template removal).

Luo et al. mention the possibility to infiltrate a binary PS crystal (130 and 210 nm) with a P123 block copolymer silica sol-gel solution, yielding mesoporous silica walls alongside two types of macropores [127].

7.4

Surfactant Templating

Besides block copolymers, surfactants are also well known to form various mesophases. Fujita et al. [128] employed octadecyltrimethylammonium chloride ($C_{18}TMACl$) to introduce meso- and macropores to a silica framework. The refractive index of the obtained material was determined to be very close to that of air (1.05) and significantly lower compared to analogous samples without mesopores (1.11). The surfactant tetrapropylammonium hydroxide (TPAOH) was used by Holland et al. [129] to synthesize silicalite in the free voids between templating PS latex spheres, resulting in a macro- and microporous material. They evidenced the presence and accessibility of the micropores by FT-IR, Hg porosimetry, and a type I N_2 adsorption/desorption isotherm. Hierarchical Pt networks were obtained by Yamauchi et al. [130] using a nonionic surfactant ($C_{16}EO_8$), which was capable of forming a lyotropic liquid crystalline (LLC) phase. Via a “solvent-evaporation-mediated direct physical casting (SEDPC)” method they were able to efficiently coinfiltrate the free space between the templating PS spheres with the LLC surfactant and a platinum salt solution. Pt metal was formed in the final process step by electrodeposition in the hierarchical template, which itself was removed by a solvent mixture to result in the porous Pt replica.

7.5

Ionic Liquid Templating

The concept of the dual templating method was further extended by Zhou et al. [131], who introduced amphiphilic ionic liquids (AILs) as structure-directing agents. The use of 1-hexadecyl-3-methylimidazolium chloride as AIL provides the following advantages. It structures the silica walls around the macropores of the inverse opal in a highly ordered, microporous lamellar fashion. The interlayer periodicity of the lamellae is about 2.7 nm, with ca. 1.3-nm-thick slit pores and 1.4-nm-thick walls, respectively. Additionally, due to the use of an ionic liquid instead of water during the silica condensation

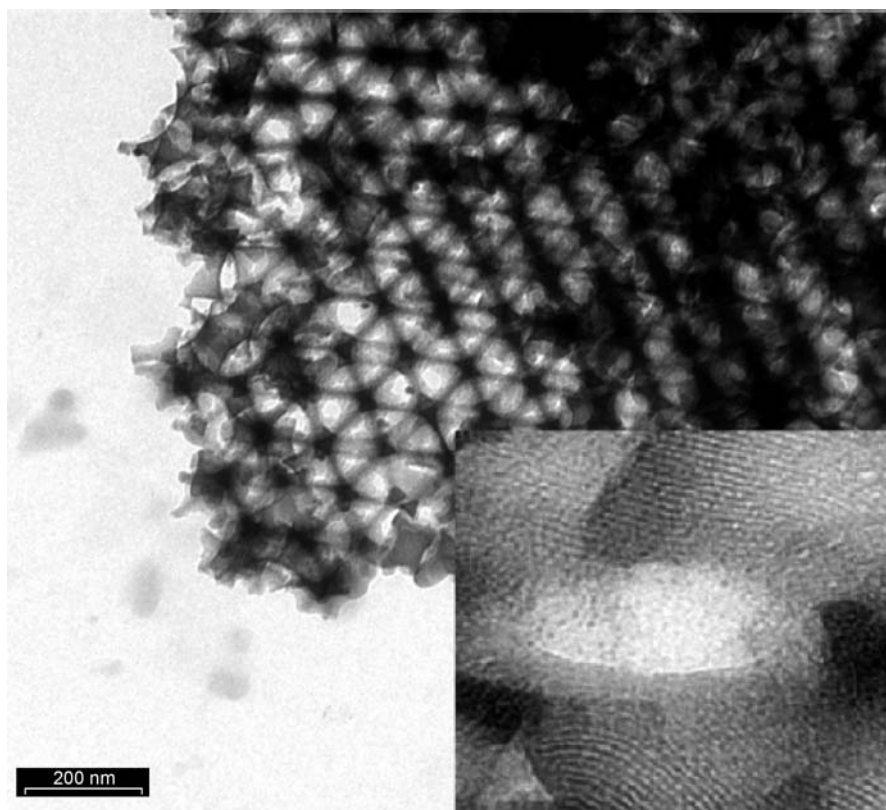


Fig. 9 TEM image of the tailored bimodal porous silica. The *inset* is the ten times magnified image. The *scale bar* is 200 nm [131]

process, no statistical solvent pores are generated, and thus the mechanical strength of the resulting network is greatly enhanced. Figure 9 shows the high order of the silica network on the macro- and microporous length scale, as obtained by the use of an AIL. The AIL process is not limited to silica materials, but was also applied to a great variety of various metal oxides, which is a broad field of research by itself [132].

Dual templating in a PS colloidal crystal by the combination of block copolymers (poly(ethylene-*co*-butylene)-*block*-poly(ethylene oxide), “KLE”) and ionic liquids (1-hexadecyl-3-methylimidazolium chloride, $C_{16}mimCl$) as meso- and microtemplating agents was demonstrated by Kuang et al., yielding a trimodal pore system [133]. The simultaneous use of these two structure-directing components in the interstitial sites of the particle crystal resulted in well-defined mesopores of the inverse opal walls, which were attributed to the KLE mesophase, and micropores, which could be assigned to the $C_{16}mimCl$.

7.6

Porous Particles

The materials which have been mentioned here so far are predominantly shaped in planar films of hierarchical order. However, the synthesis of hierarchically structured particles is also highly desirable, as they might be further processed and used for the preparation of composite porous materials. Wu et al. showed the synthesis of raspberry-like hollow silica spheres with a hierarchically structured, porous shell, using individual PS particles as sacrificial template [134]. In another intriguing approach by Li et al. [135], mesoporous cubes and near-spherical particles (Fig. 10) were formed by controlled disassembly of a hierarchically structured colloidal crystal, which itself was fabricated via PMMA latex and nonionic surfactant templating. The two different particle types concurrently generated by this method derive from the shape of the octahedral and tetrahedral voids, which are present in the template crystal with fcc lattice symmetry.

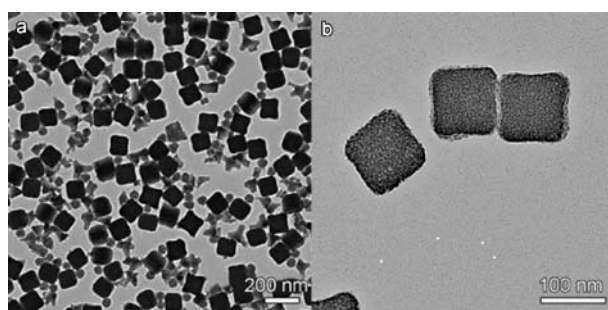


Fig. 10 **a** TEM image of the bimodally dispersed silica particles prepared through disassembly of 3DOM silica. A few replicas of the tetrahedral holes are visible among the smaller particles, although a larger fraction of these particles have transformed to more spherical shapes. **b** A higher-magnification view of the monodisperse silica nanocubes produced from the octahedral holes after centrifugation. A worm hole-like mesoporosity is clearly discernible [135]

7.7

Wall Functionalization

Functionalization of the walls (also discussed in Sect. 8) in a hierarchical material is the linchpin for potential applications in fields like separation and chromatography, electrochemical or pH sensing, and many more.

In general two functionalization approaches are available: either (1) direct functionalization of the macro- and mesopores during the hierarchical network formation; or (2) postfunctionalization of the porous material via the

appropriate surface chemistry, which is employed after network formation. The first case features a higher loading and a more homogeneous distribution of the corresponding functional moieties per volume element within the network material, while the latter case may provide a higher surface density of the functional groups solely in the wall region. Lebeau et al. demonstrated a one-pot synthesis of hierarchically ordered silica with dye-functionalized walls [136]. They used a PS latex crystal as the macroporous template and a sol-gel condensation of a triethoxysilane-functionalized dye in the presence of CTAB, which is the structure-directing template for mesopore formation. The organic dye remained active in the silica walls after the PS latex and surfactant were removed by solvent extraction. Tao et al. prepared silica walls functionalized with porphyrin and demonstrated the superior sensitivity of such hierarchically ordered materials for the detection of TNT molecules via fluorescence quenching [137].

7.8

Large-Scale Structure Hierarchies

As has already been outlined by Yang et al. [63], the implementation of a “top-down” process can introduce another level of hierarchy. Various techniques have been developed to structure colloidal crystals on a micrometer length scale. Patterning at these dimensions is crucial for the production of functional materials which might be of technical relevance. Furthermore, the functionality of a specific material can be greatly increased. Various methods that were employed for colloidal crystal patterning will be briefly reviewed here.

7.8.1

External Confinement

A patterned structure can be imposed on a colloidal crystal by geometric confinement of the space in which the crystal can grow. A straightforward case of that is the deposition of colloidal particles within a capillary [50]. The dimensions of the resulting material are simply given by the geometry of the capillary, after the accessible space has been completely filled with colloidal particles. The structure of such crystals can be fine-tuned by deposition of particles in a capillary which has an additional lateral pattern. This method was demonstrated for striplike patterns with a spacing of 100 μm by sandwiching a photoresist between two glass plates [64].

In another approach the micromolded pattern of a PDMS stamp was filled with colloidal particles [63]. The particle dispersion is drawn into the PDMS pattern by capillary forces, where the colloidal crystal forms upon evaporation. An example of a structure that is accessible by this technique is shown in Fig. 7 (left and middle).

Besides the geometrical confinement of the accessible space for a colloidal material, chemical interactions can also be exploited. Patterns that tailor the hydrophilicity or hydrophobicity of a substrate will be reproduced in the deposited material due to the difference in wetting capability. Similarly, electrostatic attraction and repulsion can be used. A prerequisite for this kind of patterning is the presence of a monolayer on the support, which renders the substrate surface properties, such as charge and wettability. Among various possibilities for the formation of patterned monolayers with organic moieties, microcontact printing and photodeprotection have been demonstrated. In the case of microcontact printing, a gold surface was first patterned with an anionic thiol by transfer with a PDMS stamp. In the second step either an alkyl thiol or cationic thiol was employed to fill the free spaces between the functionalized spots. Specific adsorption of colloidal particles to regions of the opposite charge was demonstrated [67]. When using a photosensitive monolayer, the pattern can be obtained by selective irradiation through a lithographic mask after monolayer formation. This method was demonstrated with the photoinduced deprotection of NVoc-protected silanes [66, 138].

7.8.2

Confined Local Deposition

Instead of patterning of the substrate on which the colloidal crystal is going to be formed, the colloidal dispersion itself can be applied onto a planar surface in a patterned way. Common ways to achieve this are inkjet or contact printing. The case of contact printing was demonstrated with a pin-tool plotter. A picoliter of colloidal dispersion was transferred to a titanium-coated glass substrate, to yield an array of up to 9600 single addressable colloidal crystals of spherical shape [68]. In order to ensure high reproducibility of the transferred structures, a patterned substrate was still necessary.

7.8.3

Patterning of a Homogeneous Colloidal Crystal

Structural hierarchy can also be obtained by direct modification of a single body crystal. In principle both a colloidal crystal or its inverse opal can be patterned after their homogeneous formation. Techniques to achieve this are electron-beam lithography or photopolymerization via a confocal microscope, for instance.

The latter case involves the infiltration of a colloidal crystal with a photopolymerizable monomer or a photoinitiator. Selective polymerization of the monomer in the focus of a confocal microscope via multiphoton polymerization renders a protected environment for the colloidal material. The unpolymerized monomer can be removed with the conservation of the engraved defect [139, 140].

Assembled particles can also be directly removed by electron-beam writing. This was demonstrated for PMMA particles. Stripes with a width of about 1, 3, and 5 particle diameters were written into a homogeneous colloidal crystal [141]. However, with this technique it might be difficult to introduce many structures into the bulk of the material over large regions. Another technique to introduce structures into inverse opals using the photoresist technology is discussed in Sect. 8.2.

8

Functional Networks

As illustrated in the previous sections, the choice of the matrix materials strongly determines the functionalities of the inverse networks. It is also evident that such a structurally intricate, porous architecture can be further enriched by subsequent surface functionalizations of the inner walls or by introducing additional structures a posteriori. The functionalization step is crucial in achieving the desired performance of the porous materials, particularly in applications such as chemo/biosensing, solar light harvesting, and optoelectronics, amongst others. The following discussions on the functional networks are based on their major applications reported so far.

8.1

For Sensing Platforms

The macroporous network derived from colloidal templates attracts particular interest from a chemo/biosensing perspective. This is due to its combinatorial advantage: in addition to the enormous surface area provided by the porous structure for immobilizing the target analytes, the ordered porous structure can also act as the transducer that converts the binding event into an optical signal, following Bragg's equation for the absorption maxima:

$$\lambda_{\max} = (8/3)^{1/2} D(\phi_{\text{NW}} n_{\text{NW}}^2 + \phi_{\text{TA}} n_{\text{TA}}^2 + \phi_{\text{MA}} n_{\text{MA}}^2 - \sin^2 \theta)^{1/2},$$

where D is the pore diameter, ϕ denotes the volume fraction, n is the refractive index, and θ is the angle between the incident light and the surface normal direction. The subscripts NW, TA, and MA stand for network, target analyte, and medium assay, respectively.

Thus, the only missing element is the specific recognition moieties, which must be introduced on the inner surfaces of the porous network to allow for the specific binding of the target analytes. The advantage of such a sensing platform also lies in the simplicity of its readout signal and instrumentation (colorimeter or standard spectrophotometer). Various strategies have been

implemented in introducing binding moieties onto the network surface depending on the chemical properties of the inverse opal.

Cassagneau and Caruso [114] have directly utilized the $-\text{CH}_2\text{OH}$ side chain of the polymer network formed by poly(thiophene-*co*-3-thiophenemethanol) copolymer. The $-\text{CH}_2\text{OH}$ group can covalently bind to biotin through an esterification reaction, while leaving the biotin active for the specific binding of avidin, as depicted in the schematic illustration of Fig. 11. It is evident that such an esterification reaction utilizing the functional groups belonging to the native porous structure provides a high functional density and robustness of the system.

However, most of the backbone materials of the porous structures do not possess native conjugative groups. Under such circumstances, they often resort to physisorption. Qian et al. [142] have used PS based inverse opals for detecting antibody analytes. For this purpose, they introduced a PBS solution of the proteins (staphylococcal protein A and goat anti-human IgG, both capturing human IgG) into the PS inverse opal. The following steps involved 1 h incubation at room temperature, overnight incubation at 4°C , and a bovine serum albumin (BSA) blocking of the surface with no previously bound proteins, as shown in Fig. 12. Their spectrophotometric measurement demonstrated the binding events of the immobilized proteins with the human IgG target.

Advanced strategies utilizing silanization prove to be a powerful method to immobilize the binding ligands on the pore surfaces. For that purpose, two modes have been reported: in mode I, 3-(aminopropyl)triethoxysilane (APTE) pretreated silica colloidal particles were used as the templating material forming the colloidal crystal, leaving positively charged amine groups at the outermost surface. Subsequent infiltration of a diluted gold nanoparticle (GNP) solution provided a thin layer of GNPs on the packed silica

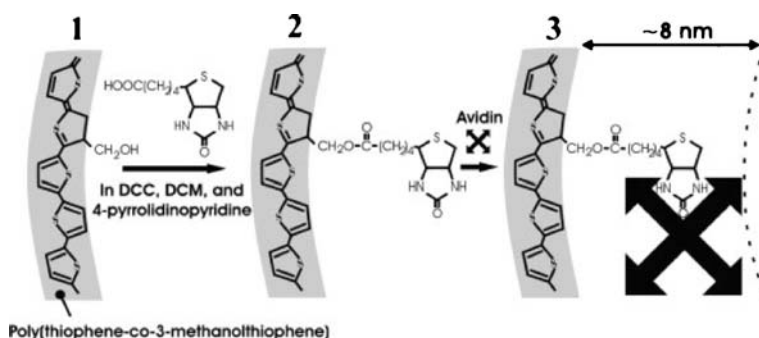


Fig. 11 1 Schematic representation of the esterification reaction involved in biotinylation of the surface in the poly(thiophene-*co*-3-thiophenemethanol) copolymer inverse opal. 2 The biotinylated copolymer surface is then primed for 3 biospecific binding with avidin [114]

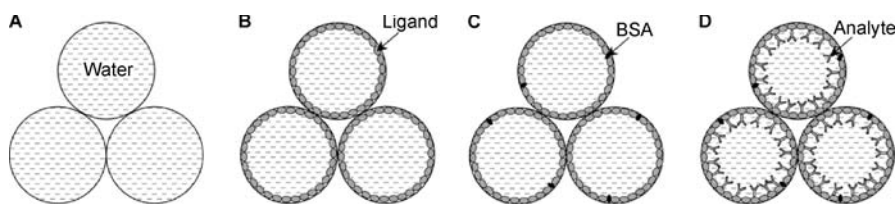


Fig. 12 **a** An aqueous solution is filled in the pores of an inverse polystyrene opal. **b** The ligand is immobilized on the pore surface. **c** The regions where no ligand was immobilized are blocked with BSA. **d** The target analyte binds on the pore surfaces [142]

particles, which was followed by infiltration with a toluene solution of PS. After evaporation of the toluene, the removal of the silica template resulted in a PS network with GNPs embedded on the inner replica surface [143]. Mode II presents a more straightforward approach: a silica inverse opal (applicable also to most metal oxide materials), formed by standard templating, was subjected to solution silanization with *N*-trimethoxysilylpropyl-*N,N,N*-trimethylammonium chloride (NR_4^+). The anchored silane provides functional moieties that can immobilize target molecules or nanoparticles. In this particular report [35], 20-nm GNPs were electrostatically adsorbed by the

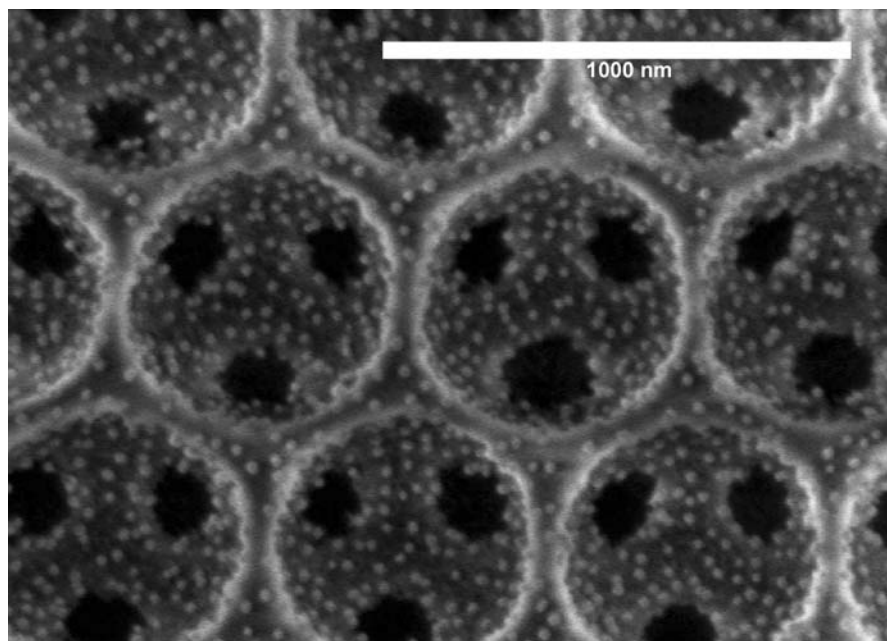


Fig. 13 SEM image of gold nanoparticles ($d = 20$ nm) deposited on the walls of a silica inverse opal. Scale bar: $1 \mu\text{m}$ [35]

positively charged silane with a uniform distribution of the GNPs on the pore surfaces (Fig. 13). These structures were further used for electroless gold deposition, as discussed in Sect. 3. Since the head groups of silanes can be flexibly modified by chemical synthesis, this functionalization strategy is very versatile. Tao et al. prepared silica walls functionalized with a silane carrying a porphyrin head group, and demonstrated the superior sensitivity of a hierarchically ordered material for the detection of TNT molecules via fluorescence quenching [137].

8.2 For Optoelectronics

Colloidal templating has enabled the fabrication of photonic crystals comprising high dielectric constant materials [37, 50]. Garcia-Santamaria et al. [144] found that by forming the inverse structure in a multilayered fashion using a CVD method, the resultant structure of alternating air, Si, Ge, and Si opened up two complete bandgaps. King et al. [145] infiltrated silica colloidal crystals with ZnS:Mn using atomic layer deposition (ALD), achieving thicknesses of 10 and 20 nm. The remaining interstitial space was filled with amorphous TiO₂, followed by a thermal treatment which converted the TiO₂ into the crystalline anatase phase. After dissolving the silica template, ALD was used to backfill the inverse opal with up to 10 nm of amorphous TiO₂, thus forming a three-layer luminescent inverse opal. This fabrication method allows independent control over the luminescence and refractive index, thus the photonic bandgap properties of the inverse opal can be specifically tailored.

By introducing defined point, line, and planar defects into such air-sphere crystals, light can be trapped or guided with minimum losses. The strategies to prepare related hierarchical structures with inverse opals is discussed in Sect. 7. Confocal microscopy was first used by Braun et al. for writing posterior structures and defects in inverse opals for the purpose of deriving waveguide and light trapping materials [139]. Yan et al. reported a simple method to embed micrometer-scale line defects in the interior of the macroporous structure [146]. Their strategy was based on sequential deposition of colloidal crystal films, as shown in Fig. 14. After forming the first multilayer colloidal crystal, a photoresist layer was spin-coated on top, followed by line structure patterning using conventional photolithography. The subsequent vertical deposition grew another multilayer of silica colloidal crystal between and on top of the photoresist structure. After infiltration of carbon and removal of the silica template, the embedded photoresist template was removed with acetone, yielding a carbon photonic crystal containing micrometer-scale line defects. Similar approaches were used to introduce planar defects [147, 157] and point defects [148].

The potential of inverse opals to manipulate light also attracted significant attention in laser and solar energy research. Dyes and quantum dots can

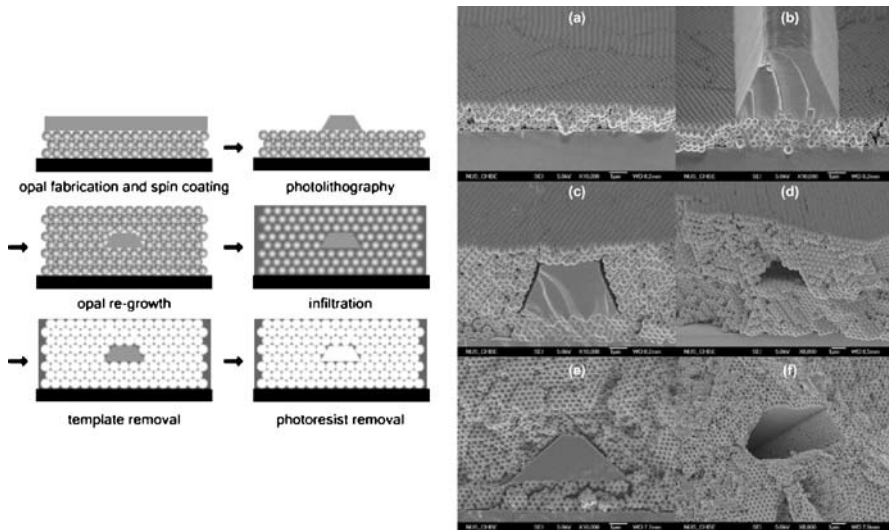


Fig. 14 **a** Schematic illustration of engineering air-core line defects within self-assembled inverse opals; **b** SEM images of the actual samples at various stages [146]

be adsorbed on the pore surfaces inside the inverse opals. It was found that by embedding light-emitting materials in a suitable inverse opal structure (with respect to lattice dimensions and refractive index), the light emission spectra [149, 150] and emission dynamics [151] were strongly modified. Moreover, the light harvesting efficiency is also enhanced by adsorbing sensitizer dyes on the inner surfaces of TiO_2 inverse opals due to the standing wave enhancement of the absorbance [152], which is particularly encouraging for the progress of solar energy harvesting. A recent study on this topic has adopted the chemical deposition method [153] to adsorb the CdSe quantum dots onto the inner surface of a TiO_2 inverse opal. Further treatments include dipping the electrode into NH_4F solution and then coating the electrode with ZnS. Both the chemisorption of CdSe and the subsequent surface passivation steps enhanced the inverse opal solar cell performance, resulting in a power conversion efficiency of 2.7% under solar illumination of $100 \text{ mW}/\text{cm}^2$ [154].

8.3 For Control of Surface Properties

Functionalization of the walls in porous materials is also the key for potential applications in the fields of separation, chromatography, catalysis, and coatings. Strategies for wall functionalization have also been discussed in Sect. 7.7. The consequences resulting from such a functionalization derive from two major features: firstly, modification of the wall composition directly influences the interfacial energy of the network with the surrounding

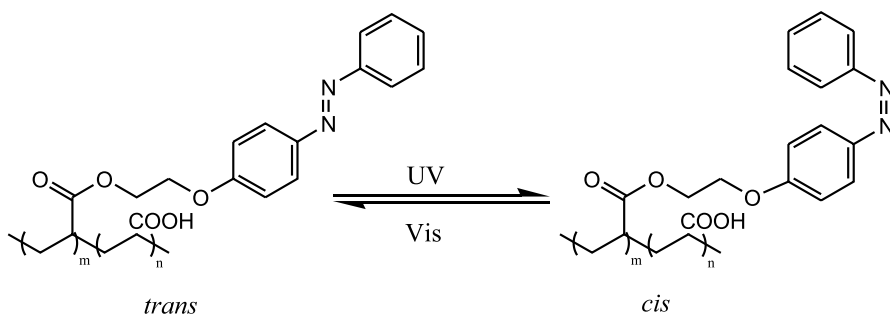


Fig. 15 Interconversion of *trans*- and *cis*-azobenzene derivatives upon UV and visible light irradiation. Adapted from [156]

medium, and hence controls wetting of the pores with this medium. Secondly, introduction of functional groups into the wall determines the specific interaction with molecules in the surrounding medium (important for separation and sensing) and allows further chemical modification of the wall, as described in Sect. 8.1. In the context of coatings, inverse opals have received interest in generating superhydrophobic and antireflective surfaces, due to their nanoscale roughness and high porosity, respectively. Gu et al. observed that when the silica inverse opal was modified by a fluoroalkylsilane, the contact angle increased to 155° compared to a 100° contact angle on a planar fluoroalkylsilane-modified silica surface [155]. In a recent study, a photoreversible azobenzene (shown in Fig. 15) monolayer was coated on the inverse opal surface via electrostatic layer-by-layer self-assembly [156]. The monolayer of azobenzene acted as a smart surface with photocontrollable properties. The contact angle could be reversibly switched between $140.8 \pm 3.0^\circ$ and $121.8 \pm 4.3^\circ$ under visible-light and UV-light irradiation, respectively.

Acknowledgements Q.L. is grateful for the financial support under the Marie Curie Incoming International Fellowship FP6-022360, M.R. acknowledges the financial support by the “Kekulé Mobility Fellowship” of the Stiftung Stipendien-Fonds des Verbandes der Chemischen Industrie e.V.

References

1. Joannopoulos JD, Villeneuve PR, Shanhui F (1997) Photonic crystals: putting a new twist on light. *Nature* 386:143
2. John S (1987) Strong localization of photons in certain disordered dielectric superlattices. *Phys Rev Lett* 58:2486
3. Yablonovitch E (1987) Inhibited spontaneous emission in solid-state physics and electronics. *Phys Rev Lett* 58:2059
4. Hollister SJ (2005) Porous scaffold design for tissue engineering. *Nat Mater* 4:518
5. Zhao XS, Su F, Yan Q, Guo W, Bao XY, Lv L, Zhou Z (2006) Templating methods for preparation of porous structures. *J Mater Chem* 16:626

6. IUPAC (2001) Definitions, terminology and symbols in colloid and surface chemistry, http://www.iupac.org/reports/2001/colloid_2001/index.html, last visited: 13.3.2008
7. Everett DH (1972) Definitions, terminology and symbols in colloid and surface chemistry. *Pure Appl Chem* 31:579
8. Hunter RJ (2001) Foundations of colloid science. Oxford University Press, New York
9. Russel WB, Saville DA, Schowalter WR (1989) Colloidal dispersions. Cambridge University Press, Cambridge
10. Xia Y, Gates B, Yin Y, Lu Y (2000) Monodispersed colloidal spheres: old materials with new applications. *Adv Mater* 12:693
11. Alivisatos AP (1996) Semiconductor clusters, nanocrystals, and quantum dots. *Science* 271:933
12. Ozin GA (1992) Nanochemistry: synthesis in diminishing dimensions. *Adv Mater* 4:612
13. Whitesides GM, Grzybowski B (2002) Self-assembly at all scales. *Science* 295:2418
14. Landfester K (2006) Synthesis of colloidal particles in miniemulsions. *Annu Rev Mater Res* 36:231
15. Matijevic E (1993) Preparation and properties of uniform size colloids. *Chem Mater* 5:412
16. Caruso F, Caruso RA, Moehwald H (1998) Nanoengineering of inorganic and hybrid hollow spheres by colloidal templating. *Science* 282:1111
17. LizMarzan LM, Giersig M, Mulvaney P (1996) Synthesis of nanosized gold-silica core-shell particles. *Langmuir* 12:4329
18. Glotzer SC, Solomon MJ (2007) Anisotropy of building blocks and their assembly into complex structures. *Nat Mater* 6:557
19. Derjaguin BV, Landau L (1941) Theory of the stability of strongly charged lyophobic sols and of the adhesion of strongly charged particles in solutions of electrolytes. *Acta Physicochim URSS* 14:633
20. Derjaguin B, Landau L (1993) Theory of the stability of strongly charged lyophobic sols and of the adhesion of strongly charged-particles in solutions of electrolytes. *Prog Surf Sci* 43:30
21. Verwey EJW, Overbeek JTG (1948) Theory of the stability of lyophobic colloids. Elsevier, Amsterdam
22. Denkov ND, Velev OD, Kralchevsky PA, Ivanov IB, Yoshimura H, Nagayama K (1992) Mechanism of formation of 2-dimensional crystals from latex particles on substrates. *Langmuir* 8:3183
23. Denkov ND, Velev OD, Kralchevsky PA, Ivanov IB, Yoshimura H, Nagayama K (1993) Two-dimensional crystallization. *Nature* 361:26
24. Kitaev V, Ozin GA (2003) Self-assembled surface patterns of binary colloidal crystals. *Adv Mater* 15:75
25. Wang J, Li Q, Knoll W, Jonas U (2006) Preparation of multilayered trimodal colloidal crystals and binary inverse opals. *J Am Chem Soc* 128:15606
26. Antonietti M, Berton B, Goltner C, Hentze HP (1998) Synthesis of mesoporous silica with large pores and bimodal pore size distribution by templating of polymer latices. *Adv Mater* 10:154
27. Park SH, Xia Y (1998) Fabrication of three-dimensional macroporous membranes with assemblies of microspheres as templates. *Chem Mater* 10:1745
28. Park SH, Xia Y (1998) Macroporous membranes with highly ordered and three-dimensionally interconnected spherical pores. *Adv Mater* 10:1045
29. Johnson SA, Ollivier PJ, Mallouk TE (1999) Ordered mesoporous polymers of tunable pore size from colloidal silica templates. *Science* 283:963

30. Holland BT, Blanford CF, Stein A (1998) Synthesis of macroporous minerals with highly ordered three-dimensional arrays of spheroidal voids. *Science* 281:538
31. Yin JS, Wang ZL (1999) Template-assisted self-assembly and cobalt doping of ordered mesoporous titania nanostructures. *Adv Mater* 11:469
32. Subramanian G, Manoharan VN, Thorne JD, Pine DJ (1999) Ordered macroporous materials by colloidal assembly: a possible route to photonic bandgap materials. *Adv Mater* 11:1261
33. Velev OD, Tessier PM, Lenhoff AM, Kaler EW (1999) A class of porous metallic nanostructures. *Nature* 401:548
34. Vlasov YA, Yao N, Norris DJ (1999) Synthesis of photonic crystals for optical wavelengths from semiconductor quantum dots. *Adv Mater* 11:165
35. Wang J, Ahl S, Li Q, Kreiter M, Neumann T, Burkert K, Knoll W, Jonas U (2008) Structural and optical characterization of 3D binary colloidal crystal and inverse opal films prepared by direct codeposition. *J Mater Chem* 18:981
36. Velev OD, Lenhoff AM (2000) Colloidal crystals as templates for porous materials. *Curr Opin Colloid Interface Sci* 5:56
37. Velev OD, Kaler EW (2000) Structured porous materials via colloidal crystal templating: from inorganic oxides to metals. *Adv Mater* 12:531
38. Hoa MLK, Lu M, Zhang Y (2006) Preparation of porous materials with ordered hole structure. *Adv Colloid Interface Sci* 121:9
39. Stein A (2001) Sphere templating methods for periodic porous solids. *Microporous Mesoporous Mater* 44–45:227
40. Stein A, Schrodner RC (2001) Colloidal crystal templating of three-dimensionally ordered macroporous solids: materials for photonics and beyond. *Curr Opin Solid State Mater Sci* 5:553
41. Meseguer F, Blanco A, Miguez H, Garcia-Santamaria F, Ibasate M, Lopez C (2002) Synthesis of inverse opals. *Colloids Surf A Physicochem Eng Asp* 202:281
42. Imhof A, Pine DJ (1997) Ordered macroporous materials by emulsion templating. *Nature* 389:948
43. Widawski G, Rawiso M, Francois B (1994) Self-organized honeycomb morphology of star-polymer polystyrene films. *Nature* 369:387
44. Pitois O, Francois B (1999) Crystallization of condensation droplets on a liquid surface. *Colloid Polym Sci* 277:574
45. Bunz UHF (2006) Breath figures as a dynamic templating method for polymers and nanomaterials. *Adv Mater* 18:973
46. Davis SA, Burkett SL, Mendelson NH, Mann S (1997) Bacterial templating of ordered macrostructures in silica and silica-surfactant mesophases. *Nature* 385:420
47. Meldrum FC, Seshadri R (2000) Porous gold structures through templating by echinoid skeletal plates. *Chem Commun* p 29
48. Mayoral R, Requena J, Moya JS, Lopez C, Cintas A, Miguez H, Meseguer F, Vazquez L, Holgado M, Blanco A (1997) 3D long-range ordering in an SiO₂ submicrometer-sphere sintered superstructure. *Adv Mater* 9:257
49. Davis KE, Russel WB, Glantschnig WJ (1991) Settling suspensions of colloidal silica: observations and X-ray measurements. *J Chem Soc Faraday Trans* 87:411
50. Wijnhoven JEGJ, Vos WL (1998) Preparation of photonic crystals made of air spheres in titania. *Science* 281:802
51. Vos WL, Megens M, Van Kats CM, Bosecke P (1997) X-ray diffraction of photonic colloidal single crystals. *Langmuir* 13:6004
52. Velev OD, Jede TA, Lobo RF, Lenhoff AM (1997) Porous silica via colloidal crystallization. *Nature* 389:447

53. Vickreva O, Kalinina O, Kumacheva E (2000) Colloid crystal growth under oscillatory shear. *Adv Mater* 12:110
54. Trau M, Seville DA, Aksay IA (1996) Field-induced layering of colloidal crystals. *Science* 272:706
55. Yoldi M, Gonzalez-Vinas W, Arcos MC, Sirera R (2006) Electrophoretic deposition of colloidal crystals assisted by hydrodynamic flows. *J Mater Sci* 41:2965
56. Deegan RD, Bakajin O, Dupont TF, Huber G, Nagel SR, Witten TA (1997) Capillary flow as the cause of ring stains from dried liquid drops. *Nature* 389:827
57. Denkov ND, Velev OD, Kralchevsky PA, Ivanov IB, Yoshimura H, Nagayama K (1992) Mechanism of formation of two-dimensional crystals from latex particles on substrates. *Langmuir* 8:3183
58. Cong H, Cao WX (2003) Colloidal crystallization induced by capillary force. *Langmuir* 19:8177
59. Dimitrov AS, Nagayama K (1996) Continuous convective assembling of fine particles into two-dimensional arrays on solid surfaces. *Langmuir* 12:1303
60. Ruhl T, Spahn P, Hellmann GP (2003) Artificial opals prepared by melt compression. *Polymer* 44:7625
61. del Campo A, Duwez A-S, Fustin C-A, Jonas U (2004) Assembly structures from colloids at patterned surfaces. In: Schwarz JA, Contescu C, Putyera K (eds) *Encyclopedia of nanoscience and nanotechnology*. Marcel Dekker, New York, p 725
62. Pieranski P, Strzelecki L, Pansu B (1983) Thin colloidal crystals. *Phys Rev Lett* 50:900
63. Yang P, Deng T, Zhao D, Feng P, Pine D, Chmelka BF, Whitesides GM, Stucky GD (1998) Hierarchically ordered oxides. *Science* 282:2244
64. Gates B, Yin Y, Xia Y (1999) Fabrication and characterization of porous membranes with highly ordered three-dimensional periodic structures. *Chem Mater* 11:2827
65. Golding RK, Lewis PC, Kumacheva E (2004) In situ study of colloid crystallization in constrained geometry. *Langmuir* 20:1414
66. Jonas U, del Campo A, Krüger C, Glasser G, Boos D (2002) Colloidal assemblies on patterned silane layers. *Proc Natl Acad Sci USA* 99:5034
67. Aizenberg J, Braun PV, Wiltzius P (2000) Patterned colloidal deposition controlled by electrostatic and capillary forces. *Phys Rev Lett* 84:2997
68. Burkert K, Neumann T, Wang JJ, Jonas U, Knoll W, Otteleben H (2007) Automated preparation method for colloidal crystal arrays of monodisperse and binary colloid mixtures by contact printing with a pintool plotter. *Langmuir* 23:3478
69. Park J, Moon J, Shin H, Wang D, Park M (2006) Direct-write fabrication of colloidal photonic crystal microarrays by ink-jet printing. *J Colloid Interface Sci* 298:713
70. Gu ZZ, Kubo S, Fujishima A, Sato O (2002) Infiltration of colloidal crystal with nanoparticles using capillary forces: a simple technique for the fabrication of films with an ordered porous structure. *Appl Phys A* 74:127
71. Bogomolov VN, Sorokin LM, Kurdyukov DA, Pavlova TM, Hutchison JL (1997) A comparative TEM study of the 3D lattice of tellurium nanoclusters fabricated by different techniques in an opal host. *Phys Solid State* 39:1869
72. Kozhevnikov VF, Diwekar M, Kamaev VP, Shi J, Vardeny ZV (2003) Fabrication and properties of gallium metallic photonic crystals. *Physica B* 338:159
73. Yan H, Blanford CF, Holland BT, Smyrl WH, Stein A (2000) General synthesis of periodic macroporous solids by templated salt precipitation and chemical conversion. *Chem Mater* 12:1134
74. Jiang P, Cizeron J, Bertone JF, Colvin VL (1999) Preparation of macroporous metal films from colloidal crystals. *J Am Chem Soc* 121:7957

75. Braun PV, Wiltzius P (1999) Electrochemically grown photonic crystals. *Nature* 402:603
76. Tian S, Wang J, Jonas U, Knoll W (2005) Inverse opals of polyaniline and its copolymers prepared by electrochemical techniques. *Chem Mater* 17:5726
77. Zakhidov AA, Baughman RH, Iqbal Z, Cui C, Khayrullin I, Dantas SO, Marti J, Ralchenko VG (1998) Carbon structures with three-dimensional periodicity at optical wavelengths. *Science* 282:897
78. Blanco A, Chomski E, Grabtchak S, Ibisate M, John S, Leonard SW, Lopez C, Meseguer F, Miguez H, Mondla JP, Ozin GA, Toader O, Van Driel HM (2000) Large-scale synthesis of a silicon photonic crystal with a complete three-dimensional bandgap near 1.5 micrometres. *Nature* 405:437
79. Holland BT, Blanford CF, Do T, Stein A (1999) Synthesis of highly ordered, three-dimensional, macroporous structures of amorphous or crystalline inorganic oxides, phosphates, and hybrid composites. *Chem Mater* 11:795
80. Tessier PM, Velev OD, Kalambur AT, Lenhoff AM, Rabolt JF, Kaler EW (2001) Structured metallic films for optical and spectroscopic applications via colloidal crystal templating. *Adv Mater* 13:396
81. Tessier PM, Velev OD, Kalambur AT, Rabolt JF, Lenhoff AM, Kaler EW (2000) Assembly of gold nanostructured films templated by colloidal crystals and use in surface-enhanced Raman spectroscopy. *J Am Chem Soc* 122:9554
82. Yan H, Blanford CF, Holland BT, Parent M, Smyrl WH, Stein A (1999) A chemical synthesis of periodic macroporous NiO and metallic Ni. *Adv Mater* 11:1003
83. Von Freymann G, John S, Schulz-Dobrick M, Vekris E, Tetreault N, Wong S, Kitaev V, Ozin GA (2004) Tungsten inverse opals: The influence of absorption on the photonic band structure in the visible spectral region. *Appl Phys Lett* 84:224
84. Denny NR, Han SE, Norris DJ, Stein A (2007) Effects of thermal processes on the structure of monolithic tungsten and tungsten alloy photonic crystals. *Chem Mater* 19:4563
85. Han SE, Stein A, Norris DJ (2007) Tailoring self-assembled metallic photonic crystals for modified thermal emission. *Phys Rev Lett* 99:053906
86. Kulinowski KM, Jiang P, Vaswani H, Colvin VL (2000) Porous metals from colloidal templates. *Adv Mater* 12:833
87. Bartlett PN, Baumberg JJ, Birkin PR, Ghanem MA, Netti MC (2002) Highly ordered macroporous gold and platinum films formed by electrochemical deposition through templates assembled from submicron diameter monodisperse polystyrene spheres. *Chem Mater* 14:2199
88. Bartlett PN, Baumberg JJ, Coyle S, Abdelsalam ME (2004) Optical properties of nanostructured metal films. *Faraday Discuss* 125:117
89. Baumberg JJ (2006) Breaking the mould: casting on the nanometre scale. *Nat Mater* 5:2
90. Netti MC, Coyle S, Baumberg JJ, Ghanem MA, Birkin PR, Bartlett PN, Whittaker DM (2001) Confined surface plasmons in gold photonic nanocavities. *Adv Mater* 13:1368
91. Coyle S, Netti MC, Baumberg JJ, Ghanem MA, Birkin PR, Bartlett PN, Whittaker DM (2001) Confined plasmons in metallic nanocavities. *Phys Rev Lett* 87:176801
92. Cole RM, Baumberg JJ, Garcia de Abajo FJ, Mahajan S, Abdelsalam M, Bartlett PN (2007) Understanding plasmons in nanoscale voids. *Nano Lett* 7:2094
93. Kelf TA, Sugawara Y, Baumberg JJ, Abdelsalam M, Bartlett PN (2005) Plasmonic band gaps and trapped plasmons on nanostructured metal surfaces. *Phys Rev Lett* 95:116802

94. Abdelsalam ME, Mahajan S, Bartlett PN, Baumberg JJ, Russell AE (2007) SERS at structured palladium and platinum surfaces. *J Am Chem Soc* 129:7399
95. Perney NMB, de Abajo FJG, Baumberg JJ, Tang A, Netti MC, Charlton MDB, Zoorob ME (2007) Tuning localized plasmon cavities for optimized surface-enhanced Raman scattering. *Phys Rev B* 76:035426
96. Sugawara Y, Kelf TA, Baumberg JJ, Abdelsalam ME, Bartlett PN (2006) Strong coupling between localized plasmons and organic excitons in metal nanovoids. *Phys Rev Lett* 97:266808
97. Norris DJ, Vlasov YA (2001) Chemical approaches to three-dimensional semiconductor photonic crystals. *Adv Mater* 13:371
98. Lee J, Kim J, Hyeon T (2006) Recent progress in the synthesis of porous carbon materials. *Adv Mater* 18:2073
99. Subramania G, Constant K, Biswas R, Sigalas MM, Ho KM (1999) Optical photonic crystals fabricated from colloidal systems. *Appl Phys Lett* 74:3933
100. Wang D, Caruso F (2001) Fabrication of polyaniline inverse opals via templating ordered colloidal assemblies. *Adv Mater* 13:350
101. Miguez H, Meseguer F, Lopez C, Holgado M, Andreassen G, Mifsud A, Fornes V (2000) Germanium FCC structure from a colloidal crystal template. *Langmuir* 16:4405
102. Miguez H, Chomski E, Garcia-Santamaria F, Ibisate M, John S, Lopez C, Meseguer F, Mondia JP, Ozin GA, Toader O, Van Driel HM (2001) Photonic bandgap engineering in germanium inverse opals by chemical vapor deposition. *Adv Mater* 13:1634
103. Braun PV, Wiltzius P (2001) Electrochemical fabrication of 3D microperiodic porous materials. *Adv Mater* 13:482
104. Sumida T, Wada Y, Kitamura T, Yanagida S (2001) Macroporous ZnO films electrochemically prepared by templating of opal films. *Chem Lett* 30:38
105. Bartlett PN, Birkin PR, Ghanem MA, Toh CS (2001) Electrochemical syntheses of highly ordered macroporous conducting polymers grown around self-assembled colloidal templates. *J Mater Chem* 11:849
106. Sumida T, Wada Y, Kitamura T, Yanagida S (2000) Electrochemical preparation of macroporous polypyrrole films with regular arrays of interconnected spherical voids. *Chem Commun* p 1613
107. Hicks RW, Pinnavaia TJ (2003) Nanoparticle assembly of mesoporous AlOOH (boehmite). *Chem Mater* 15:78
108. Ren TZ, Yuan ZY, Su BL (2004) Microwave-assisted preparation of hierarchical mesoporous–macroporous boehmite AlOOH and γ -Al₂O₃. *Langmuir* 20:1531
109. Yang PD, Zhao DY, Margolese DI, Chmelka BF, Stucky GD (1998) Generalized syntheses of large-pore mesoporous metal oxides with semicrystalline frameworks. *Nature* 396:152
110. Deutsch M, Vlasov YA, Norris DJ (2000) Conjugated-polymer photonic crystals. *Adv Mater* 12:1176
111. Jiang P, Hwang KS, Mittleman DM, Bertone JF, Colvin VL (1999) Template-directed preparation of macroporous polymers with oriented and crystalline arrays of voids. *J Am Chem Soc* 121:11630
112. Yoshino K, Tatsuhara S, Kawagishi Y, Ozaki M, Zakhidov AA, Vardeny ZV (1999) Amplified spontaneous emission and lasing in conducting polymers and fluorescent dyes in opals as photonic crystals. *Appl Phys Lett* 74:2590
113. Cassagneau T, Caruso F (2002) Semiconducting polymer inverse opals prepared by electropolymerization. *Adv Mater* 14:34
114. Cassagneau T, Caruso F (2002) Inverse opals for optical affinity biosensing. *Adv Mater* 14:1629

115. Cassagneau T, Caruso F (2002) Conjugated polymer inverse opals for potentiometric biosensing. *Adv Mater* 14:1837
116. Peppas NA, Hilt JZ, Khademhosseini A, Langer R (2006) Hydrogels in biology and medicine: from molecular principles to bionanotechnology. *Adv Mater* 18:1345
117. Qiu Y, Park K (2001) Environment-sensitive hydrogels for drug delivery. *Adv Drug Deliv Rev* 53:321
118. Lee YJ, Braun PV (2003) Tunable inverse opal hydrogel pH sensors. *Adv Mater* 15:563
119. Ueno K, Matsubara K, Watanabe M, Takeoka Y (2007) An electro- and thermochromic hydrogel as a full-color indicator. *Adv Mater* 19:2807
120. Barry RA, Wiltzius P (2006) Humidity-sensing inverse opal hydrogels. *Langmuir* 22:1369
121. Holtz JH, Asher SA (1997) Polymerized colloidal crystal hydrogel films as intelligent chemical sensing materials. *Nature* 389:829
122. Asher SA, Alexeev VL, Goponenko AV, Sharma AC, Lednev IK, Wilcox CS, Finegold DN (2003) Photonic crystal carbohydrate sensors: low ionic strength sugar sensing. *J Am Chem Soc* 125:3322
123. Yang L, Kang J, Guan Y, Wei F, Bai S, Zhang M, Zhang Z, Cao W (2006) 3D-ordered macroporous materials comprising DNA. *Langmuir* 22:11275
124. Bryant SJ, Cuy JL, Hauch KD, Ratner BD (2007) Photo-patterning of porous hydrogels for tissue engineering. *Biomaterials* 28:2978
125. Sen T, Tiddy GJT, Casci JL, Anderson MW (2004) Synthesis and characterization of hierarchically ordered porous silica materials. *Chem Mater* 16:2044
126. Deng Y, Liu C, Yu T, Liu F, Zhang F, Wan Y, Zhang L, Wang C, Tu B, Webley PA, Wang H, Zhao D (2007) Facile synthesis of hierarchically porous carbons from dual colloidal crystal/block copolymer template approach. *Chem Mater* 19:3271
127. Luo Q, Li L, Yang B, Zhao D (2000) Three-dimensional ordered macroporous structures with mesoporous silica walls. *Chem Lett* 29:378
128. Fujita S, Nakano H, Ishii M, Nakamura H, Inagaki S (2006) Preparation of hierarchical porous silica and its optical property. *Microporous Mesoporous Mater* 96:205
129. Holland BT, Abrams L, Stein A (1999) Dual templating of macroporous silicates with zeolitic microporous frameworks. *J Am Chem Soc* 121:4308
130. Yamauchi Y, Kuroda K (2006) Fabrication of a Pt film with a well-defined hierarchical pore system via solvent-evaporation-mediated direct physical casting. *Electrochem Commun* 8:1677
131. Zhou Y, Antonietti M (2003) A novel tailored bimodal porous silica with well-defined inverse opal microstructure and super-microporous lamellar nanostructure. *Chem Commun* p 2564
132. Taubert A, Li Z (2007) Inorganic materials from ionic liquids. *Dalton Trans* p 723
133. Kuang DB, Brezesinski T, Smarsly B (2004) Hierarchical porous silica materials with a trimodal pore system using surfactant templates. *J Am Chem Soc* 126:10534
134. Wu XF, Tian YJ, Cui YB, Wei LQ, Wang Q, Chen YF (2007) Raspberry-like silica hollow spheres: hierarchical structures by dual latex-surfactant templating route. *J Phys Chem C* 111:9704
135. Li F, Wang ZY, Stein A (2007) Shaping mesoporous silica nanoparticles by disassembly of hierarchically porous structures. *Angew Chem Int Ed* 46:1885
136. Lebeau B, Fowler CE, Mann S, Farcet C, Charleux B, Sanchez C (2000) Synthesis of hierarchically ordered dye-functionalised mesoporous silica with macroporous architecture by dual templating. *J Mater Chem* 10:2105
137. Tao SY, Shi ZY, Li GT, Li P (2006) Hierarchically structured nanocomposite films as highly sensitive chemosensory materials for TNT detection. *Chem Phys Chem* 7:1902

138. Del Campo A, Boos D, Spiess HW, Jonas U (2005) Surface modification with orthogonal photosensitive silanes for sequential chemical lithography and site-selective particle deposition. *Angew Chem Int Ed* 44:4707
139. Lee WM, Pruzinsky SA, Braun PV (2002) Multi-photon polymerization of waveguide structures within three-dimensional photonic crystals. *Adv Mater* 14:271
140. Taton TA, Norris DJ (2002) Device physics: defective promise in photonics. *Nature* 416:685
141. Muller M, Zentel R, Maka T, Romanov SG, Torres CMS (2000) Dye-containing polymer beads as photonic crystals. *Chem Mater* 12:2508
142. Qian WP, Gu ZZ, Fujishima A, Sato O (2002) Three-dimensionally ordered macroporous polymer materials: an approach for biosensor applications. *Langmuir* 18:4526
143. Ding SH, Qian WP, Tan Y, Wang Y (2006) In-situ incorporation of gold nanoparticles of desired sizes into three-dimensional macroporous matrixes. *Langmuir* 22:7105
144. Garcia-Santamaria F, Ibisate M, Rodriguez I, Meseguer F, Lopez C (2003) Photonic band engineering in opals by growth of Si/Ge multilayer shells. *Adv Mater* 15:788
145. King JS, Graugnard E, Summers CJ (2006) Photoluminescence modification by high-order photonic bands in TiO_2/ZnS : Mn multilayer inverse opals. *Appl Phys Lett* 88:081109
146. Yan QF, Zhou ZC, Zhao XS, Chua SJ (2005) Line defects embedded in three-dimensional photonic crystals. *Adv Mater* 17:1917
147. Tetreault N, Mihi A, Miguez H, Rodriguez I, Ozin GA, Meseguer F, Kitaev V (2004) Dielectric planar defects in colloidal photonic crystal films. *Adv Mater* 16:346
148. Yan QF, Chen A, Chua SJ, Zhao XS (2005) Incorporation of point defects into self-assembled three-dimensional colloidal crystals. *Adv Mater* 17:2849
149. Megens M, Wijnhoven J, Lagendijk A, Vos WL (1999) Fluorescence lifetimes and linewidths of dye in photonic crystals. *Phys Rev A* 59:4727
150. Schriemer HP, Van Driel HM, Koenderink AF, Vos WL (2001) Modified spontaneous emission spectra of laser dye in inverse opal photonic crystals. *Phys Rev A* 63:011801
151. Lodahl P, Van Driel AF, Nikolaev IS, Irman A, Overgaag K, Vanmaekelbergh D, Vos WL (2004) Controlling the dynamics of spontaneous emission from quantum dots by photonic crystals. *Nature* 430:654
152. Nishimura S, Abrams N, Lewis BA, Halaoui LI, Mallouk TE, Benkstein KD, van de Lagemaat J, Frank AJ (2003) Standing wave enhancement of red absorbance and photocurrent in dye-sensitized titanium dioxide photoelectrodes coupled to photonic crystals. *J Am Chem Soc* 125:6306
153. Gorer S, Hodes G (1994) Quantum size effects in the study of chemical solution deposition mechanisms of semiconductor films. *J Phys Chem* 98:5338
154. Diguna LJ, Shen Q, Kobayashi J, Toyoda T (2007) High efficiency of CdSe quantum-dot-sensitized TiO_2 inverse opal solar cells. *Appl Phys Lett* 91:023116
155. Gu ZZ, Uetsuka H, Takahashi K, Nakajima R, Onishi H, Fujishima A, Sato O (2003) Structural color and the lotus effect. *Angew Chem Int Ed* 42:894
156. Ge HL, Wang GJ, He YN, Wang XG, Song YL, Jiang L, Zhua DB (2006) Photoswitched wettability on inverse opal modified by a self-assembled azobenzene monolayer. *Chem Phys Chem* 7:575
157. Fleischhaker F, Arsenaault AC, Kitaev V, Peiris FC, Freymann GV, Manners I, Zentel R, Ozin GA (2005) Photochemically and thermally tunable planar defects in colloidal photonic crystals. *J Am Chem Soc* 127:9318

From Self-Assembly to Charge Transport with Single Molecules – An Electrochemical Approach

Bo Han^{1,3} · Zhihai Li¹ · Chen Li^{1,2} · Ilya Pobelov¹ · Guijin Su^{2,4} ·
Rocio Aguilar-Sanchez^{2,5} · Thomas Wandlowski^{1,2} (✉)

¹Institute of Chemistry and Biochemistry, University of Berne, Freiestrasse 3,
3012 Berne, Switzerland
thomas.wandlowski@dcb.unibe.ch

²Research Center Jülich, Institute of Bio- and Nanosystems 3, 52425 Jülich, Germany

³Present address:

SKF Engineering and Research Center, Kevinbaan 16, 3439 MT Nieuwegein, The Netherlands

⁴Present address:

Research Center for Eco-Environmental Sciences, State Key Laboratory of Environmental Chemistry and Ecotoxicology, Chinese Academy of Sciences, 18 Shuangqing Road, Haidian District, 100085 Beijing, P.R. China

⁵Present address:

Laboratorio de Electroquímica, Facultad de Ciencias Químicas, Universidad Autónoma de Puebla, 72570 Puebla, Mexico

1	Introduction	184
2	Characterization of Selected Substrate Surfaces	187
2.1	Au(111) in 0.05 M H ₂ SO ₄	188
2.2	Au(100) in 0.05 M H ₂ SO ₄	191
3	Molecular Self-Assembly Involving Directional Hydrogen Bonding	193
3.1	Introduction	193
3.2	TMA on Au(111) in 0.1 M H ₂ SO ₄	195
3.2.1	Overview Data	195
3.2.2	Structure Details of the Various TMA Adlayers on Au(111)-(1 × 1)	197
3.3	Self-Assembly of Other Aromatic Carboxylic Acids on Au(111)-(1 × 1)	212
4	Molecular “Self-Assembly” Involving Covalent Bond Formation	216
4.1	Introduction	216
4.2	Structure of BPn Adlayers on Au(111)-(1 × 1)	218
4.3	Selected Electrochemical Properties of BPn Adlayers on Au(111)-(1 × 1)	220
4.4	Electrical Properties of BPn Adlayers – An STS Study	226
5	Charge Transport in Single Au/Molecule/Au Junctions at Electrified Solid–Liquid Interfaces	231
5.1	Introduction	231
5.2	Charge Transport in Single Au/Alkanedithiol/Au Junctions – An STM Approach	233
5.3	Electrolyte Gating in (Single) Molecule Junctions Containing Redox-Active Viologen Derivatives	238

6	Concluding Comments	246
	References	247

Abstract Structure formation and self-assembly of physisorbed and chemisorbed organic monolayers will be described on electrified solid-liquid interfaces employing in-situ scanning tunneling microscopy (STM) and surface-enhanced infrared spectroscopy (SEIRAS) in combination with electrochemical techniques. We present first a case study on self-assembly by directional hydrogen bonding and its interplay with the electrode potential choosing aromatic carboxylic acids, with an emphasis on 1,3,5-benzenetricarboxylic acid (TMA). Structure and electrical characteristics of chemisorbed organic monolayers involving the formation of covalent bonds with the substrate surface will be discussed for a series of 4-methyl-4'-(*n*-mercaptoalkyl)biphenyls on Au(111) electrodes. In an attempt to explore single molecule properties, such as charge transport and redox-mediated tunneling, we subsequently introduce an STM-based technique to construct symmetric and asymmetric metal/(single) molecule/metal junctions. Employing α,ω -alkanedithiols and redox-active derivatives of viologens we demonstrate novel transport and single molecule electrochemical studies, which bear unique novel perspectives for fundamental as well as applied investigations.

Keywords Charge transport · Electrochemistry · Scanning tunneling microscopy (STM) · Scanning tunneling spectroscopy (STS) · Self assembly · Single molecules

Abbreviations

List of Symbols

<i>A</i>	Area [m ²]
Ag	Silver
Au	Gold
<i>a</i> _{Au}	Lattice vector
<i>b</i> _{Au}	Lattice vector
<i>c</i>	Molar concentration of species [M (mol l ⁻¹), mol m ⁻³]
<i>C</i>	Surface capacitance [F m ⁻²]
<i>e</i>	Electron (elementary) charge [1.62 × 10 ⁻¹⁹ C]
<i>E</i>	Electrode potential [V]
<i>E</i> ₀	Equilibrium potential of redox-pair [V]
<i>E</i> _{pzc}	Potential of zero charge (PZC) [V]
<i>E</i> _i , <i>E</i> _u , <i>E</i> _l	Initial, upper and lower potential in CV [V]
<i>E</i> _S , <i>E</i> _T	Sample and tip electrode potentials in EC STM [V]
<i>E</i> _{bias}	Bias voltage, <i>E</i> _{bias} = <i>E</i> _S - <i>E</i> _T [V]
<i>F</i>	Faraday constant [96 485 C mol ⁻¹]
FWHM	Full width at half maximum
<i>G</i>	Conductance [S]
<i>h</i>	Planck constant [6.626 × 10 ⁻³⁴ J s]
Hg	Mercury
<i>h</i> _{SAM}	SAM thickness
<i>i</i>	Current [A]
<i>i</i> _T	Tunneling current [A, nA, pA]
<i>j</i>	Current density [A m ⁻²]

k	Boltzmann's constant [1.38×10^{-23} J K ⁻¹]
k_i	Rate constant [variable]
l	Distance, length [m]
M	Molar mass [kg mol ⁻¹ , g mol ⁻¹]
Me	Metal
n	Integer number (various usage)
ox	Oxidized form of reactant
pK_a	ln (dissociation constant K_a)
q^M	Surface charge density [C m ⁻²]
red	Reduced form of reactant -
t	Time [s]
T	Temperature [K, °C]
z	Distance
α	Angle [°]
α_D, β_D	Decay constants
β_N	Decay constant per CH ₂ units
ξ, γ	Model parameters (Sect. 5.3)
e	Electron energy [J, eV]
ε_F	Fermi energy of solid body [J, eV]
ε	Dielectric constant
ε_0	Dielectric permittivity of vacuum [8.85×10^{-12} C ² N ⁻¹ m ⁻²]
Γ	Coverage/surface excess [mol m ⁻²]
ω_{eff}	Nuclear vibration frequency [s ⁻¹]
ρ	Density of the electronic levels (Sect. 5.3) [eV ⁻¹]
κ_d	Gouy-Chapman decay constant [m ⁻¹]
κ_{eff}	Effective decay constant
κ	Electronic transmission coefficient
λ	Gibbs energy of the environmental reorganization [J, eV]
η	Overpotential [V]
σ	Conductivity [S m ⁻¹]

List of Acronyms

1D	One-dimensional
2D	Two-dimensional
3D	Three-dimensional
nS	Alkanethiols CH ₃ (CH ₂) _{n-1} SH
6S	1-Hexanethiol CH ₃ (CH ₂) ₅ SH
8S	1-Octanethiol CH ₃ (CH ₂) ₇ SH
AFM	Atomic force microscopy
ATR	Attenuated total reflection
BA	Benzoic acid
BPn	4-Methyl-4'-(<i>n</i> -mercaptoalkyl)biphenyls; $n = 1-6$
CE	Counter electrode, also auxiliary electrode
CP AFM	Current probe atomic force microscopy
CV	Cyclic voltammetry, cyclic voltammogram
DFT	Density functional theory
DNA	Deoxyribonucleic acid
EC	Electrochemistry, electrochemical
EDL	Electrical double layer

ET	Electron transfer
FWHM	Full width at half maximum
HOMO	Highest occupied molecular orbital
HOPG	Highly oriented pyrolytic graphite
HS6V6	<i>N</i> -hexyl- <i>N'</i> -(6-thiohexyl)-4,4'-bipyridinium bromide
HS-6V6-SH	<i>N,N'</i> -bis(6-thiohexyl)-4,4'-bipyridinium bromide
IR	Infrared
IRAS	Infrared absorption spectroscopy
IA	Isophthalic acid
LEED	Low energy electron diffraction
LUMO	Lowest unoccupied molecular orbital
MCBJ	Mechanically controlled break-junction
MSE	Mercury-sulfate electrode
PZC	Potential of zero charge $E_q = 0$
QRE	Quasireference electrode
RHE	Real hydrogen electrode
RE	Reference electrode
SnS	Alkanedithiols $\text{HS}(\text{CH}_2)_n\text{SH}$
SAM	Self-assembled monolayer(s)
SCE	Saturated calomel electrode
SEIRAS	Surface enhanced infrared reflection absorption spectroscopy
SHE	Standard hydrogen electrode
SHG	Second harmonic generation
SPM	Scanning probe microscopy
STM	Scanning tunneling microscopy, microscope
STS	Scanning tunneling spectroscopy
TCPP	5,10,15,20-Tetrakis-(4-carboxylphenyl)-21H,23H-porphyrin
TMA	1,3,5-Trimethylbenzoic acid
TA	Terephthalic acid
THE	Trapped hydrogen electrode
UHV	Ultra-high vacuum with pressures lower than 10^{-7} Pa
V^{2+}	Viologen dication
$\text{V}^{+\cdot}$	Viologen radical-cation
V^0	Neutral form of viologen
WE	Working electrode

1

Introduction

Lehn describes *Supramolecular Chemistry* as the “chemistry of inter-molecular bonds, which involves recognition, transformation and translocation of information” [1] beyond the elementary structures of individual molecules. Rapidly expanding at the interdisciplinary frontiers of chemical science with physical and biological phenomena, supramolecular chemistry has opened up a broad range of activities to create and fabricate diverse nanoscale architectures via *recognition*, which implies the storage and read-out of molecular

information. Examples are complementary interaction sites, binding units, and molecular fragments within an individual molecular structure [1].

Derived from the concepts of supramolecular chemistry, “self-assembly” of chemical species is defined as “the spontaneous assembly of molecules into structured, stable and non-covalently bound aggregates” [2], or “the non-covalent interaction of two or more molecular subunits to form an aggregate whose novel structure and properties are determined by the nature and positioning of the components” [3]. Such spontaneous construction of supramolecular architectures from molecular constituents is usually achieved by selective and directional non-covalent interactions [4], which involve intermolecular electrostatic interactions (positive and negative charges, charge/dipole, dipole/dipole, π -stacking, and metal ion/ligand coordination, etc.), hydrogen-bonding or van der Waals interactions [1]. Figure 1 compares, as an example, different types of hydrogen-bonding relative to van der Waals and covalent interactions.

Various types of supramolecular self-assemblies have been revealed both in life sciences (e.g., double helix crosslinking of DNA, protein folding, formation of lipid bilayers), and in chemical systems (e.g., crystallization, formation of vesicles, adsorption on surfaces) [2]. Although the understanding of supramolecular self-assembly was initially developed from 3D crystal or solution

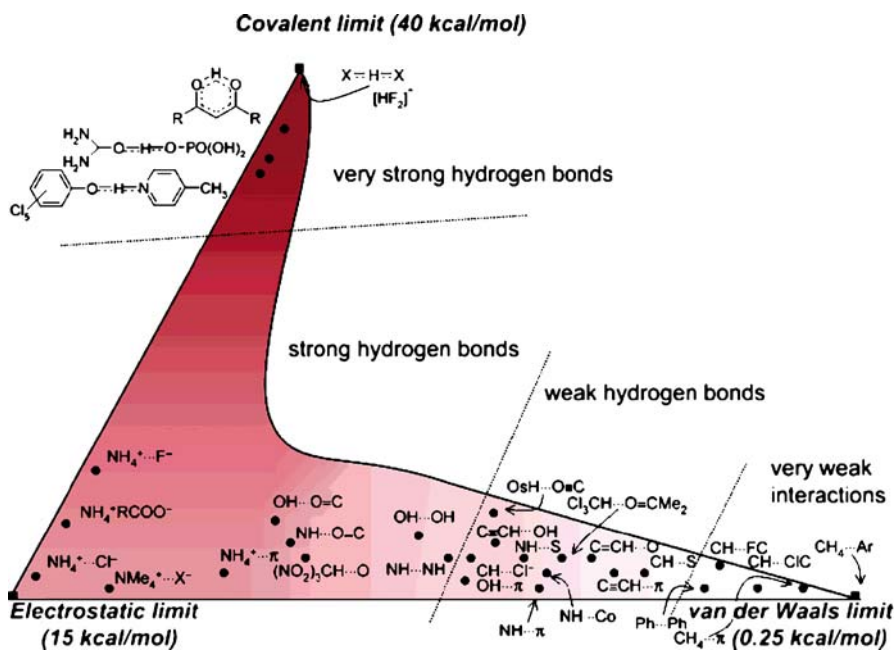


Fig. 1 Classification of different hydrogen-bonding interactions, with respect to the bond energy of electrostatic, van der Waals, and covalent interactions [5]

phases, most of the recent investigations focus on 2D self-assembly on surfaces or interfaces, whose formation and stability depend not only on intermolecular forces, but also on the interactions between individual molecular components and the solid substrate or support [6].

The two basic approaches for creating 2D nanoscale patterns and “devices” are the “top-down” and the “bottom-up” techniques (see Fig. 2). Compared to “top-down” methods, which are based on the reduction of feature sizes down to the sub-100 nm range, “bottom-up” methods aim to guide the assembly of molecular and/or atomic constituents into organized structures through ordering processes inherent in the manipulated system, such as the self-assembly of supramolecular building blocks. The bottom-up construction of molecular nanostructures has several unique advantages due to the nature of individual molecules [7, 8]: (i) molecules are essentially nanoscale objects (1 ~ 100 nm), which may play an important role as building blocks in future nanoelectronic devices (Moore’s law) [9]; (ii) high reproducibility due to self-assembly and recognition; (iii) dynamic stereochemistry offering possibilities of switching; (iv) versatile implementation of localized functions

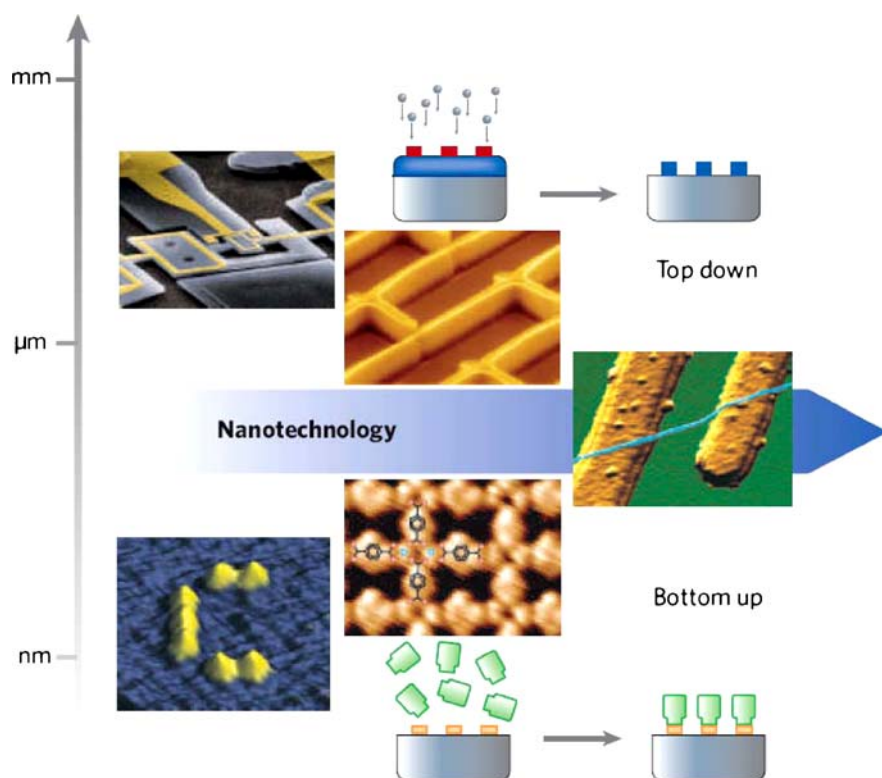


Fig. 2 “Top-down” and “bottom-up” approaches for controlling matter at the nanoscale [4]

with optical, electrical, magnetic, ion-binding, etc. properties, leading to applications in molecular optics, electronics, spintronics and ionics etc [1].

The parameters crucial for 2D supramolecular fabrication are the surface mobility of molecules, their lateral interactions and their coupling to the substrate atomic lattice, depending on the chemical nature of the system, the atomic environment, and the symmetry of a substrate [4]. These various effects provide unique opportunities for building desired nanostructures by adjusting the balance between lateral interactions and the molecule–substrate coupling.

In the following we shall discuss a few selected examples of our own work on structure formation and functionalization with organic adlayers and single molecules at *electrified* solid–liquid interfaces. Employing defined metal substrates and tailored molecules we address two aspects: (1) the monitoring of molecular recognition and self-organization at surfaces and interfaces and (ii) the local addressing of functionality with a specific focus on electron transport in metal–molecule–metal junctions. To reach these goals we employ concepts of supramolecular chemistry (the “bottom-up approach”). Typical structural motives are hydrogen bonding, electrostatic interactions, such as dipole and π – π stacking, as well as metal-ion/ligand coordination. We will distinguish between physisorbed, spontaneously assembled monolayers and chemisorbed monolayers involving the formation of chemical bonds between adsorbed molecules and the electrode surface. We like to emphasize the uniqueness of the *electrochemical approach*: The electrode acts as an additional coordination center. Furthermore, the electrode potential is a universal and very sensitive source to fabricate and to address molecular nanostructures.

We have organized the work herein as follows: In Sect. 2 we will discuss briefly two typical electrochemical substrates, Au(111) and Au(100) in 0.05 M H_2SO_4 , employing in-situ scanning tunneling microscopy (STM) and surface-enhanced infrared reflection/absorption spectroscopy (ATR-SEIRAS). Self-assembled physisorbed adlayers of various hydrogen-bonded carboxylic acids will be described in Sect. 3. Then we will focus on selected properties of chemisorbed “self-assembled” aromatic adlayers based on experiments with 4-methyl-4'-(*n*-mercaptoalkyl)biphenyls on Au(111) electrodes. Section 4 will give an introduction to electrochemical strategies for exploring charge transport in metal|single molecule|metal junctions. Examples will be discussed for alkanedithiols and redox-active derivatives of viologens. We will conclude with a brief outlook.

2

Characterization of Selected Substrate Surfaces

The macroscopic electrochemical experiments as well as the structural studies with molecular adlayers were performed on single crystal metal electrodes, such as Au(*hkl*), Ag(*hkl*) and Cu(*hkl*). To describe our experimen-

tal starting conditions as well as the methodology used we characterized the “clean” substrate surfaces comprehensively employing cyclic voltammetry, capacitance and impedance measurements, chronocoulometry, in-situ STM [7], FTIR [10] and surface X-ray scattering [11, 12]. As examples we will discuss selected results of two, in the experiments described below, most frequently used systems Au(111)/0.05 M H₂SO₄ and Au(100)/0.05 M H₂SO₄.

2.1

Au(111) in 0.05 M H₂SO₄

The “steady-state” and dynamic properties of the Au(111)/aqueous electrolyte interface were investigated experimentally with a variety of electrochemical and structure sensitive methods. Examples are impedance measurements [13], electroreflectance [14], LEED [14, 15] SHG [16], in-situ surface X-ray scattering [17] and STM [18–20] experiments. In the following paragraph we will only focus on some essential results of our in-situ STM and SEIRAS studies [21, 22].

Figure 3 illustrates the phase behavior of an Au(111)-electrode in sulfuric acid with a typical current vs. potential curve and STM-images of characteristic “steady-state” structures. The experiment started with a flame-annealed electrode after potential-controlled immersion at -0.20 V. The thermally induced Au(111)-($p \times \sqrt{3}$) reconstruction is preserved at negative charge densities [23]. As an example, Fig. 3A shows a large-scale in-situ STM-image of a freshly prepared Au(111)-electrode in 0.05 M H₂SO₄. The typical double row pattern of the reconstruction (6.3 nm periodicity, corrugation amplitude (0.20 ± 0.05) Å) due to the 4% compression of the top layer in one of the three [110]-directions is well developed. Entire sets of corrugation lines change their orientation in a zig-zag pattern by $\pm 120^\circ$ and thus form a periodic sequence of domain boundaries. This superperiodicity is known as “Chevron” or “herringbone”-structure. The reconstructed Au(111)-($p \times \sqrt{3}$) surface in an electrochemical environment has the very same structure as its counterpart in vacuum [24, 25].

Details of this uniaxially compressed structure are shown in Fig. 3B. The individual gold atoms are clearly resolved. Their positional arrangement changes periodically in the (110)-direction from face-centered cubic (*fcc*) through a transitional region of so-called “bridging sites” to hexagonal close-packed (*hcp*). The stripe-to-stripe separation within a double row amounts to (2.6 ± 0.3) nm (gold atoms in *hcp* and bridge sites), while the closest distance between adjacent stripes of two different double rows (gold atoms in *fcc* and “bridge sites”) was estimated to (3.7 ± 0.3) nm. Changing the electrode potential towards positive charge densities causes the lifting of reconstruction, and the extra amount of gold atoms from the ca. 4% more densely packed ($p \times \sqrt{3}$) structure forms monatomic high gold islands on the surface (Fig. 3C). Subsequently, the so-called “electrochemical annealing” takes place. Small islands

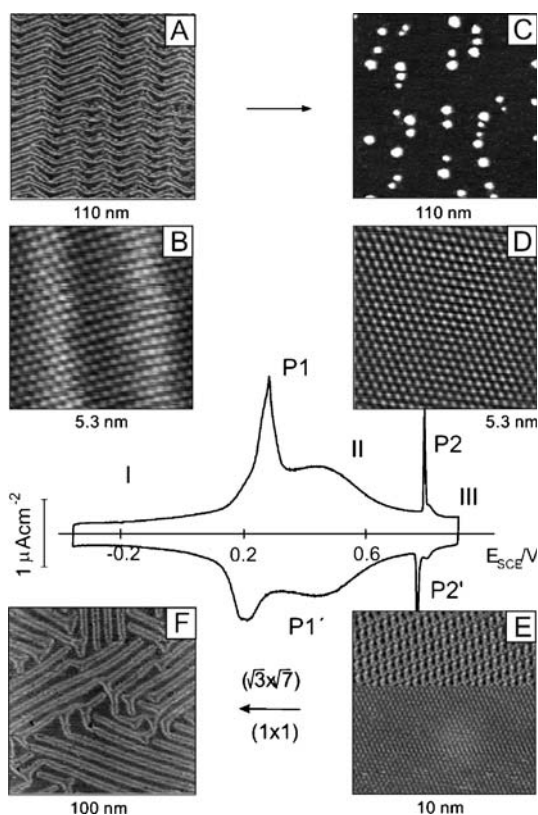


Fig. 3 Cyclic voltammogram for Au(111) in 0.05 M H_2SO_4 , scan rate 10 mV s^{-1} . In-situ STM-images represent the substrate surface structure at various stages of the potentiodynamic experiment: **A** large-scale image of a thermally reconstructed Au(111)-($p \times \sqrt{3}$) surface, $E = -0.20 \text{ V}$; **B** atomic resolution of **A**; **C** Au(111)-(1×1) surface with monatomic high gold islands after lifting the surface reconstruction, $E = 0.60 \text{ V}$; **D** atomic resolution of **C**; **E** disorder/order transition of the $(\sqrt{3} \times \sqrt{7})$ (hydrogen) sulfate overlayer; **F** potential-induced reconstructed Au(111)-($p \times \sqrt{3}$) surface at $E = -0.20 \text{ V}$

disintegrate, and larger ones grow either due to statistical fluctuations at rims (two-dimensional Ostwald ripening) and/or the merging of equal size islands [26].

The maximum P1 in the current vs. potential curve correlates with the substrate surface transition. The difference in zero charge potentials between the reconstructed ($p \times \sqrt{3}$) and the unreconstructed (1×1) gold surfaces gives rise to an additional current contribution due to double layer charging. Figure 1D shows the ideal terminated (1×1) surface with atomic resolution. Around 0.80 V a disorder/order transition takes place within the layer of adsorbed (hydrogen-)sulfate ions [27–30]. The formation/dissolution of the so-called $(\sqrt{3} \times \sqrt{7})$ overlayer correlates with the

current maxima P2/P2' in the voltammogram. Figure 3E illustrates the dissolution of this ($\sqrt{3} \times \sqrt{7}$) phase after application of a cathodic potential step. The atomic/ionic resolution of the (hydrogen-)sulfate structure (top) as well as of the gold lattice (bottom) allow us to derive that the main maxima of the overlayer are located at bridge positions of the underlying Au(111) lattice.

The phase transition between the reconstructed and the unreconstructed gold surface is reversible in aqueous electrolyte at room temperature. Stepping the potential towards negative charge densities, e.g. past the current maximum P1' in Fig. 3, causes the reconstruction to reappear within a short time. The reconstruction lines are now no longer aligned in only one direction or "super"-domain, as in the case of the initial (thermally induced) reconstruction, but they run in a rather irregular zig-zag pattern in all three main crystallographic directions of the underlying Au(111) substrate (Fig. 3F). The rims of the monatomic gold islands formed during the transition ($p \times \sqrt{3}$) \rightarrow (1×1) serve as nucleation centers in the reformation of the ($p \times \sqrt{3}$) phase.

The structure and orientation of water molecules on quasi single-crystalline Au(111-20 nm) thin film electrodes in contact with aqueous sulfuric acid solution were studied by surface-enhanced infrared reflection absorption spectroscopy employing an ATR configuration (ATR-SEIRAS) [22, 31]. The spectrum of interfacial water is strongly dependent on electrode potential, ionic strength and pH. Figure 4A shows a series of SEIRA spectra recorded within the potential range of an ideally polarizable Au(111) electrode in 0.1 M H₂SO₄. Well developed bands appear at 3500 cm⁻¹ and between 1615 and 1650 cm⁻¹, which could be assigned to OH-stretching and HOH-bending

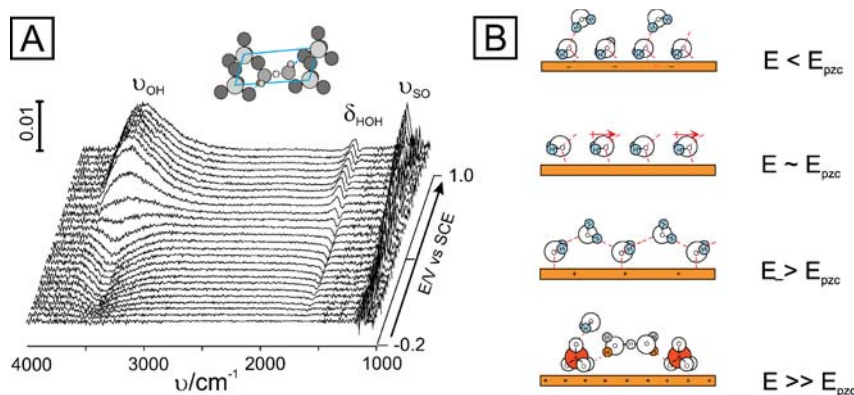


Fig. 4 **A** Series of infrared spectra of Au(111-20 nm)/0.05 M H₂SO₄ as a function of potential. The spectra were acquired during a potential sweep (5 mV s^{-1}) between -0.2 V and 1.0 V vs. SCE. The reference potential is at 0.25 V . **B** Proposed models of the interfacial structure at various characteristic potential regions [22]

vibrations of interfacial water. Around 0.240 V, which is close to the potential of zero charge, a third band appears which could be assigned to the ν_3 mode of specifically adsorbed sulfate. The shape and the characteristic frequencies of OH and HOH vibrations represent distinct potential-dependent changes within the electrical double layer, such as the transformation from weakly hydrogen-bonded water at a negatively charged surface to strongly hydrogen-bonded water at a positively charged electrode (Fig. 4B [22, 31]). Based on pH-dependent electrochemical, spectroscopic and in situ STM investigations we also propose that at higher positive potentials, where the ordered ($\sqrt{3} \times \sqrt{7}$) adlayer is formed, sulfate ions (coverage $\theta = 0.2$) are co-adsorbed with Zundel ions, H_5O_2^+ , in which one proton is shared between two water molecules. Adjacent sulfate species are bridged via hydrogen bonds along the main diagonal of the ($\sqrt{3} - \sqrt{7}$) unit cell. This alternating arrangement gives rise to a long range ordered 2D network of sulfate and water species interconnected by hydrogen bonds, and capable to form hydrogen bonds with second layer water species.

2.2

Au(100) in 0.05 M H_2SO_4

The phase behavior of Au(100) in aqueous H_2SO_4 and HClO_4 has been studied before [23, 32–34]. Figure 5 shows a typical current vs. potential curve of Au(100) in 0.05 M H_2SO_4 .

The first cycle started with a freshly flame-annealed (e.g. thermally reconstructed) Au(100)-(hex) electrode after immersion at -0.10 V (indicated as “START”, solid line). The corresponding large-scale STM-image (Fig. 1A) reveals the typical one-dimensional corrugation lines superimposed by a Moiré-pattern, which is due to a small rotation of the (hex)-structure with respect to the quadratic bulk lattice [35]. The quadratic symmetry of the underlying (1×1) lattice allows two, by 90° mutually rotated directions of the reconstructed domains. On carefully flame-annealed electrodes usually one terrace is covered by a single domain. The reconstruction lines of the top layer are either exactly aligned with the atomic rows of the quadratic lattice, or they are rotated by 0.8° . The latter case is shown in Fig. 5A. Details of the *hexagonal* arrangement of the individual gold atoms in this phase are illustrated in Fig. 5B (long range corrugation of (1.45 ± 0.05) nm periodicity, and ~ 0.05 nm height due to the structural misfit between the reconstructed surface and the bulk).

Scanning the electrode potential towards more positive values causes the “lifting” of the thermally induced reconstruction at potentials around the current peak P3 ($E_{\text{P}3} = 0.304$ V, $q_{\text{P}3}^{\text{M}} = 21 \mu\text{C cm}^{-2}$), and the Au(100)-(1×1) surface structure is formed. The excess of gold atoms of the preexisting (hex)-phase (24%) is expelled onto the surface and monatomic high gold islands are created [23, 32–34] (Fig. 5C). Similar as in the case of Au(111), sufficiently

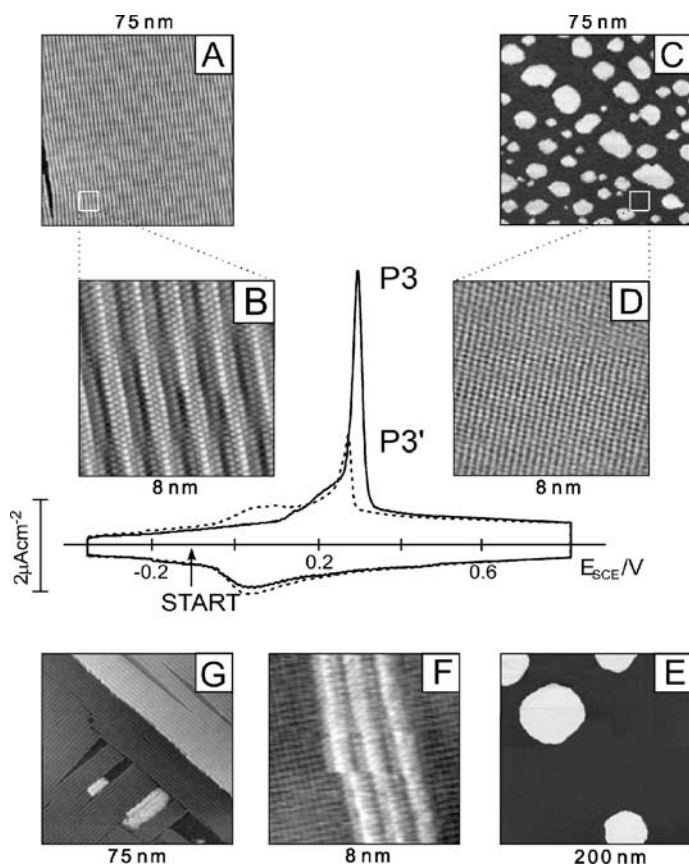


Fig. 5 Cyclic voltammograms for Au(100) in 0.05 M H_2SO_4 , scan rate 10 mV s^{-1} . The first scan as obtained with a flame-annealed, reconstructed electrode after immersion at -0.10 V is plotted as a *solid line*. The steady-state voltammogram is shown as a *dotted curve*. In-situ STM-images represent the substrate surface structure at various stages of the potentiodynamic experiment: **A** large-scale image of a thermally reconstructed Au(100)-(hex) surface, $E = -0.10 \text{ V}$; **B** atomic resolution of the reconstructed Au(100)-(hex) surface; **C** Au(100)-(1 \times 1) surface with monatomic high gold islands after lifting the surface reconstruction, $E = 0.55 \text{ V}$; **D** atomic resolution of the Au(100)-(1 \times 1) surface structure; **E** “electrochemically annealed” Au(100)-(1 \times 1) surface after 60 min at 0.55 V ; **F** atomic resolution image of three newly formed hexagonal reconstruction rows on Au(100)-(1 \times 1), $E = 0.0 \text{ V}$; **G** potential-induced reconstructed Au(100)-(hex) surface at $E = -0.20 \text{ V}$

long electrochemical annealing at positive potentials, for instance at 0.60 V , causes an increase of the average island size and simultaneously a significant decrease of their number (Fig. 5E). The rate of this electrochemical annealing process increases with potential and is higher for strongly specifically adsorbed anions. A typical high-resolution *square* lattice arrangement of sur-

face gold atoms under conditions, such as demonstrated in Fig. 5C,E, is shown in Fig. 5D.

Scanning the electrode potential towards more negative values, causes the charge (potential)-induced surface reconstruction to appear. Morphological details of the newly formed *hexagonal* “reconstruction stripes” within the metastable gold surface top layer of *square* symmetry at $E = 0.0$ V are depicted in Fig. 5F. The (hex)-structure is reformed to a large extent at sufficient negative potentials and long waiting times (Fig. 5G). Typically, this phase is characterized by a significantly higher defect density, and rather small domains rotated 90° with respect to each other. Both structure features also determine the negative shift of P3 during the second and each subsequent voltammetric cycle (dotted line in Fig. 5, $E_{p3'} = 0.278$ V).

Experiments on the time-dependence of the (hex) \rightarrow (1×1) transition demonstrate that the (1×1) phase is established clearly during a voltammetric scan with 10 mV s^{-1} . The reformation of the long-range order of the (hex)-structure, after once being lifted, requires a much longer time than is available within such a dynamic scanning regime (see also [23, 32]). The nucleation of the charge (potential)-induced reconstruction elements starts at substrate defects, such as steps and remaining gold islands, and is strongly dependent on the temporal history in the thermodynamic stability range of the (1×1) phase.

3

Molecular Self-Assembly Involving Directional Hydrogen Bonding

3.1

Introduction

We will present herein selected examples of potential (charge-)induced self-assembly of organic supramolecular nanostructures based on *non-covalent interactions* [36]. The spontaneous generation of organized structures depends on the design of individual molecular components capable of self-assembling into supramolecular entities. Self-assembly methods represent a unique potential to create well-defined functional structures with dimensions on the nanometer scale, and to control surface properties. In particular, the assembly of supramolecular structures via *hydrogen-bonding* has developed into a central theme for constructing a wide variety of molecular nanostructures in solution, in liquid crystals, in solid state and on surfaces [37]. Hydrogen bonds are formed when a donor (D) with an available acidic hydrogen atom is brought into direct contact with an acceptor (A). Hydrogen bonding is not random, but selective and controlled by the directional strength of intermolecular interactions [38]. It can be used to tune the spatial arrangement of functionalized molecules and ions in the solid state and

on surfaces. The structure and energetic features of hydrogen-bonding interactions have been extensively studied [39–44]. The choice of molecular shape and size, and especially the arrangement of hydrogen bonding donor and acceptor sites, are crucial to the correct tessellation of tailored supramolecular arrays.

In the following sections we will specifically focus on selected results obtained with aromatic carboxylic acids assembled on surfaces. These acids are commonly used as motif-controlling functional elements in crystal engineering. They can form hydrogen-bonding patterns that contain a center of symmetry, the dimer motif, and also aggregate in acentric one-dimensional chains, catemers, resulting from the formation of hydrogen bonds to two or more neighboring acids [44]. The dimer synthon has been used to assemble a variety of supermolecules due to its bidentate character, which increases the strengths of interactions considerably. For example, terephthalic acid (1,4-benzene dicarboxylic acid, TA) [45] and isophthalic acid (1,4-benzene dicarboxylic acid, IA) [46] form one-dimensional tapes and ribbons, respectively. Trimesic acid (1,3,5-benzene tricarboxylic acid, TMA) with its threefold molecular symmetry forms a two-dimensional network composed of characteristic honeycomb units [47–49]. The ~ 1.4 nm diameter cavities of the honeycombs are often employed to fabricate inclusion compounds [50, 51]. TMA represents a prototype material for supramolecular self-assembly. The acid and some analogue structure motifs have been used as template patterns to create a variety of nanostructures [52–57]. Functionalized TMA [58], its protonated forms [59], and its metal complexes [60, 61] were employed as unique building blocks in crystal and nanostructure engineering. The ordering at surfaces was studied under UHV conditions [62, 63] and at the solid–liquid interface [64–68]. Molecular self-assembly at surfaces is governed by the subtle balance between intermolecular and molecule–surface interactions, which can be tuned by the substrate material and the symmetry, the temperature or, at electrified interfaces, by the applied electrode potential. Dmitriev et al. [62] reported on Cu(100) at low temperatures (~ 200 K) the existence of 2D ordered adlayer islands composed of a honeycomb structure of TMA molecules in a planar orientation. Long-range order was not achieved due to kinetic limitations. At room temperature, deprotonation of the carboxyl groups leads to an upright adsorption geometry, where chemisorbed TMA molecules are anchored to the substrate through a carboxylate functionality. The upright molecules order in striped islands. Barth et al. also explored the molecular assembly of metal–organic coordination networks of TMA and related aromatic carboxylic acids on well-defined metal surfaces in ultrahigh vacuum [69]. Griessl et al. [63] reported on HOPG at 25 K up to room temperature the coexistence of two hexagonal ring structures composed of TMA with hydrogen bonds formed either between two (honeycomb pattern) or three (flower structure) adjacent molecules.

Alternatively, the adsorption-triggered self-assembly of TMA [64, 66–68] and of many other monomeric precursors [21, 70–72] can be explored on well-defined metal surfaces in an electrochemical environment. This approach offers the advantage, in comparison to a UHV-based environment, that formation, properties and structural transitions of a wide variety of 2D supramolecular adlayers can be tuned (and equilibrated!) by the applied electrode potential, and subsequently characterized by structure-sensitive in-situ techniques in real space and real time [21, 70]. Ishikawa et al. reported for Au(111)/0.1 M HClO₄ a honeycomb-type (8 × 8) 2D network of flat oriented TMA molecules, which transform at higher potentials into a close-packed structure of hydrogen-bonded TMA dimers [65]. Under similar experimental conditions, Su et al. found three ordered TMA adlayers [66]. A quasi-hexagonal (4 × 4) phase of planar oriented molecules at low coverages and negative charge densities changes via a mixed (5 × 2√3) adlayer into a high coverage striped phase at rather high positive potentials. The latter is ascribed to perpendicularly adsorbed TMA molecules coordinated with one or two deprotonated carboxylate groups to the positively charged electrode.

In the following paragraphs we will describe results of a comprehensive electrochemical study employing cyclic voltammetry, STM and ATR-SEIRAS on the potential-controlled assembly and on structure transitions of TMA adlayers on Au(111) electrodes in 0.1 M H₂SO₄. For comparison we will also discuss data for benzoic acid (BA), isophthalic acid (IA) and terephthalic acid (TA).

3.2

TMA on Au(111) in 0.1 M H₂SO₄

3.2.1

Overview Data

Figure 6 shows a typical current vs. potential curve of Au(111)-(1 × 1) in 0.05 M H₂SO₄ in the presence of 3 mM TMA recorded with a scan rate of 10 mV s⁻¹. Under these conditions TMA is completely protonated (pK₁ = 2.1, pK₂ = 4.1, pK₃ = 5.18) [73].

Four characteristic potential regions (labeled I, IIa–c, III and IV in a sequence from lower to higher potentials), which are separated by the distinct current peaks P1/P1', P2/P2' and weak, rather broad additional peaks, can be distinguished. The stability range of I is delimited at negative potentials by the onset of hydrogen evolution. After a broad region II, region III evolves, which is strongly dependent on scan rate and surface preparation (between P1/P1' and P2/P2'). A broad current maximum P3/P3' at more positive potentials leads finally to the low capacitance region IV (saturation capacitance ~ 10 μF cm⁻²). Upon increasing the potential further, the stability range of

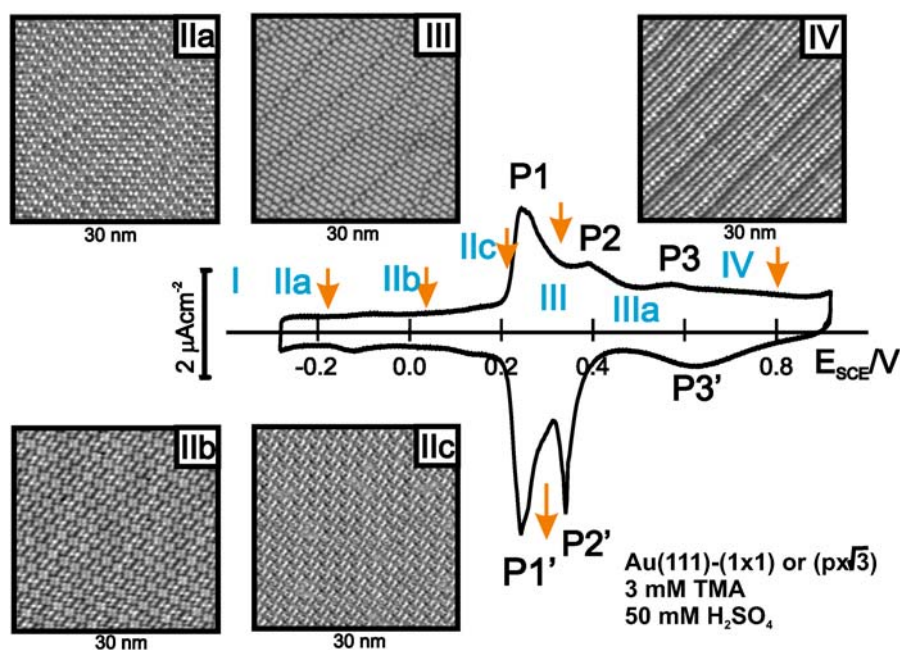


Fig. 6 Steady state voltammogram for Au(111)-(1 × 1)/ 0.05 M H₂SO₄ in the presence of 3 mM TMA. The stability regions of the various adlayer phases are labeled I, IIa–c, III and IV, scan rate 10 mV s⁻¹. These adlayers are illustrated with typical in-situ STM images: (IIa) hexagonal honeycomb phase, $E_s = -0.18$ V; (IIb) ribbon-type motif, $E_s = 0.03$ V; (IIc) herringbone motif, $E_s = 0.21$ V; (III) hydrogen-bonded linear dimers, $E_s = 0.34$ V; (IV) ordered chemisorbed striped phase of TMA at $E_s = 0.80$ V. Tunneling currents were below 200 pA [67]

IV is delimited by the competing adsorption of OH⁻ and the onset of gold oxidation.

Steady state in-situ STM measurements were performed to explore structural details of the various stages of the electrochemical experiment. We observed no changes of the ideally terminated hexagonal Au(111)-(1 × 1) substrate geometry, but five distinctly different supramolecular adlayer motifs depending on the applied potential and the assembly conditions (Fig. 6). Three long-range ordered adlayer structures were found in region II, which we shall label honeycomb (structure IIa), ribbon-type (structure IIb) and herringbone-type (structure IIc) pattern. Region III is composed of strongly correlated chains of linear rows with characteristic translational domain boundaries. No ordered pattern was found at potentials between the current peaks P2/P3 and P2'/P3'. A striped phase with regular features at $E > P3$ (P3') appears in potential region IV. Structural details of the five ordered TMA adlayers will be discussed next.

3.2.2

Structure Details of the Various TMA Adlayers on Au(111)-(1 × 1)

Hexagonal Honeycomb Phase IIa

Depositing TMA ($c > 0.2$ mM) from sulfuric acid solution on Au(111)-(1 × 1) at potentials more negative than 0.00 V, e.g. at a negatively charged electrode surface, gives rise to large domains (> 100 nm) of a long-range ordered honeycomb pattern. The latter represents a hexagonal network with equal-size cavities. The rarely observed domain boundaries appear frizzy and do not strictly follow characteristic symmetry directions of the underlying Au(111) substrate surface indicating a high mobility of TMA monomers and a rather weak adsorbate–substrate corrugation potential. Once formed the TMA adlayer IIa is stable until the onset of hydrogen evolution at $E < -0.30$ V, and at positive potentials up to the current peak P1 (Fig. 6). We note that the same honeycomb structure of TMA is also observed on the reconstructed Au(111)-(p × √3) gold surface, without a preferential alignment to the substrate surface crystallography.

High-resolution in-situ STM images (Fig. 7A) reveal that the honeycomb pattern is composed of six bright, separately resolved triangular features, which are assigned to individual TMA molecules, and a dark depression in the center of the assembly. Their triangular contrast pattern with a characteristic side length of $l \approx 0.7$ – 0.8 nm and the comparison with the molecular structure of TMA [47] suggest a planar surface orientation. The positions of the symmetrically arranged carboxyl groups in individual TMA molecules are clearly resolved. Adjacent carboxyl groups of each two neighboring TMA units appear to be aligned. Cross section profiles reveal an apparent corrugation height of the bright spots ranging between 0.10 to 0.15 nm, and a value of 0.05 nm for the 1.2 nm in diameter dark, but somewhat streaky hole in the center. The former represent typical values for physisorbed, planar oriented aromatic molecules with the π -system of the phenyl ring oriented parallel to the substrate surface [74–78]. The planar orientation of TMA in potential region II is also supported by the results of an in-situ ATR-SEIRAS study (see below [68]).

The highly symmetrical motif shows a characteristic repeat distance of (1.70 ± 0.08) nm. The experimentally determined rhombohedral unit cell with $a = b = (1.70 \pm 0.08)$ nm and $\alpha = (60 \pm 5)^\circ$ is composed of two TMA molecules and gives rise to a coverage $\Gamma_{\text{IIa}}(\text{ex}) = (1.3 \pm 0.1) \times 10^{-10}$ mol cm $^{-2}$ (Fig. 7A). These data correspond to $A_{\text{IIa}}(\text{ex}) = (1.25 \pm 0.10)$ nm 2 as approximate area per molecule (Table 1). The characteristic lengths of the unit cell vectors are close to six times the gold diameter ($6 \times |a_{\text{Au}}| = 1.73$ nm). Together with the absence of long-range corrugations (indicative of a Moiré or dislocation pattern) in the TMA phase IIa we deduce that the molecular layer is commensurate with the substrate and that individual molecules reside at

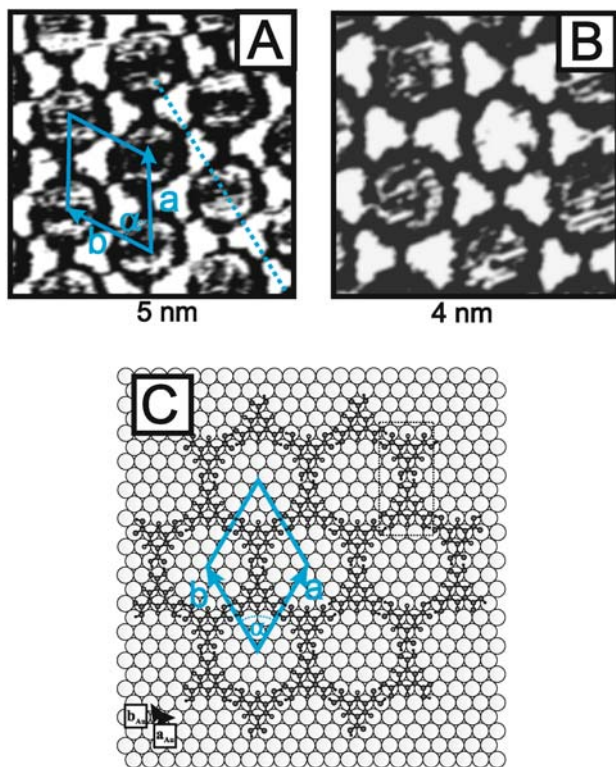


Fig. 7 **A** High-resolution in-situ STM image of the hexagonal honeycomb phase IIa of TMA on Au(111)|0.05 M H₂SO₄ in the presence of 3 mM TMA, $E_s = -0.10$ V, $i_T = 70$ pA. The primitive unit cell is indicated. **B** TMA guest molecule positioned in the center of a honeycomb-type hexagonal TMA host lattice, $E_s = -0.10$ V, $i_T = 70$ pA. **C** Proposed packing model of TMA in IIa. The unit cell and a centro-symmetric dimer motif are indicated. The parameters of the unit cell are summarized in Table 1 [67]

distinct adsorption sites. Based on literature data [76, 78, 79] and a recent *ab initio* calculation employing density functional theory [80], we propose that the aromatic phenyl rings of the TMA molecules are preferentially bound to high symmetry threefold hollow sites of the substrate lattice. This assumption suggests a nearly perfect alignment of the (6 × 6) honeycomb-type TMA adlayer to adjacent [110] symmetry directions of the substrate surface. Using vectors of the primitive gold lattice, a_{Au} and b_{Au} (Fig. 7C) with $|a_{\text{Au}}| = |b_{\text{Au}}| = 0.2885$ nm as basis one obtains in matrix notation:

$$\begin{pmatrix} a \\ b \end{pmatrix} = \begin{pmatrix} 6 & 6 \\ 0 & 6 \end{pmatrix} \begin{pmatrix} a_{\text{Au}} \\ b_{\text{Au}} \end{pmatrix}.$$

The parameters of the corresponding unit cell are summarized in Table 1.

Table 1 Characteristic dimensions of the unit cell parameters of the various TMA adlayers. The experimentally determined values are given in the first line, the model parameters are summarized in the second line

Adlayer	a [nm]	b [nm]	α [°]	Area A [nm ²]	Coverage Γ [10 ¹⁰ mol cm ⁻²]
Honeycomb IIa	1.70 ± 0.08	1.70 ± 0.08	60 ± 5	1.25 ± 0.10	1.3 ± 0.1
	1.73	1.73	60		
Ribbon-type IIb	3.57 ± 0.20	1.92 ± 0.10	80 ± 5	0.84 ± 0.05	2.0 ± 0.1
	3.6	2.02	76	0.88	1.9
Herringbone motif IIc	3.30 ± 0.15	4.10 ± 0.15	84 ± 5	0.75 ± 0.05	2.2 ± 0.2
	3.25	4.04	87.5	0.73	2.3
Linear dimers III	1.43 ± 0.05	1.18 ± 0.05	63 ± 5	0.75 ± 0.02	2.2 ± 0.1
	1.44	1.15	60	0.72	2.3
Chemisorbed phase IV	0.86 ± 0.05	2.15 ± 0.20	86 ± 8	0.46 ± 0.05	3.6 ± 0.4
	0.865	2.00	90	0.43	3.8

The comparison of our experimental observations with crystal structure data [47] indicates that the supramolecular honeycomb motif is determined by the hexagonal arrangement of hydrogen-bonded dimers between adjacent carboxyl groups. Each of the three carboxylic acid groups forms two hydrogen bonds with its neighbors. This results in a total of six OH···O hydrogen bonds per TMA molecule, which leads to a strong in-plane stability of the network. The dimer synthon represents the most prevalent hydrogen-bonded pattern formed by aromatic carboxylic acids in solid state [44–47]. Experimentally, we estimate 0.26 nm as the average length of the OH···O hydrogen bonds. This value is typical for the hydrogen-bonding pattern of carboxylic acid dimers [45–47, 49, 81]. In the crystal structure of bulk α -polymorph trimesic acid, 1.4 nm diameter holes of the honeycomb exist resulting in a TMA–TMA distance of 1.97 nm through the mesh center and an OH···O bond length of 0.27 nm [47]. The dimensions of the TMA network in the potential region IIa, e.g. at a negatively charged Au(111) electrode, are slightly smaller. This observation could be attributed to the relaxation of the hydrogen bonds in the presence of the electron gas of the charged metal surface. The notion is supported by comparing related hydrogen-bonded assemblies of TMA on different substrate surfaces. Heckl et al. reported on HOPG under UHV conditions [63] and in heptanoic acid [82] a regular physisorbed network with $a = b = (1.72 \pm 0.10)$ nm and $\alpha = (60 \pm 1)^\circ$ as characteristic dimensions of the unit cell. Dmitriev et al. found on Cu(100) substrates at 205 K in UHV small islands of a distorted honeycomb pattern with TMA–TMA distances through the mesh center of $a = 2.04$ nm and $b = 2.28$ nm [56]. Ishikawa et al. [65] obtained for the assembly of 0.1 mM TMA on Au(111)-($p \times \sqrt{3}$)/0.1 M HClO₄ an expanded honeycomb pattern with a hexagonal

unit cell of $a = b = 2.3$ nm and $\alpha = 60^\circ$, which is composed of two molecules. Su et al. [66] reported under similar experimental conditions a hydrogen-bonded network, which could be represented by a rhombohedral unit cell with $a = b = 1.15$ nm and $\alpha = 60^\circ$, just containing one molecule. Comparing the properties of the hexagonal honeycomb phase IIa found in the present study with the various open TMA assemblies on other substrate surfaces in solution and under UHV conditions demonstrates that the driving force for the self-assembly process and the dominating intermolecular interactions are the hydrogen bonds between two carboxylic groups of adjacent TMA molecules. However, interactions of the molecular π -orbitals with the substrate surface, with solvent molecules or electrolyte ions of the solution phase modify this effect and cause distinct changes [62, 63, 65, 66].

The open six-fold honeycomb structure with a 1.2 nm diameter “hole” in the center of the ring may also act as a nanoscale host system with pre-defined sites for guest molecules [49, 63, 82, 83]. The formation of size-selective inclusion complexes may significantly increase the packing stability of the hydrogen-bonded pattern. In aqueous electrolyte and in the absence of specific adsorption of anions the cavities appear streaky (Fig. 7A). These observations are attributed to the high mobility and/or transient adsorption of either water or solute molecules [84]. This interpretation is supported by the absence of similar features in TMA adlayers prepared in UHV [62, 63]. Increasing the solution concentration of TMA above 1 mM allows incorporating individual flat-lying physisorbed TMA molecules having a finite residence time in the organic host lattice (Fig. 7B). The guest species appear disk-like with an apparent corrugation of approximately 0.10–0.15 nm. No triangular features were resolved. The size and shape of the TMA guest molecules indicate no specific interaction, such as directional hydrogen bonds, with the host skeleton. Their smeared-out appearance, in comparison to the regular triangular shape of the two-dimensional host lattice molecules, indicates a rotation of the TMA guest being significantly faster than the acquisition time of the STM image. A similar interpretation was suggested for coronene incorporated into a TMA host lattice [82].

Ribbon-Type Motif IIb

Depositing TMA from aqueous electrolyte at higher concentrations ($c > 1.0$ mM) under potential control in 0.00 V $< E < 0.20$ V reveals large domains of a new two-dimensional assembly pattern of TMA on Au(111)-(1 × 1) as well as Au(111)-(p × $\sqrt{3}$) (Figs. 6, 8).

One identifies alternating parallel rows of squares and rhombohedral motifs. Each subunit is composed of four bright spots, which are assigned to individual flat-lying TMA molecules. High-resolution images (Fig. 8B) illustrate their regular shape, and an apparent corrugation height of 0.10–0.15 nm. The nearest neighbor distance of the square motif within one row is esti-

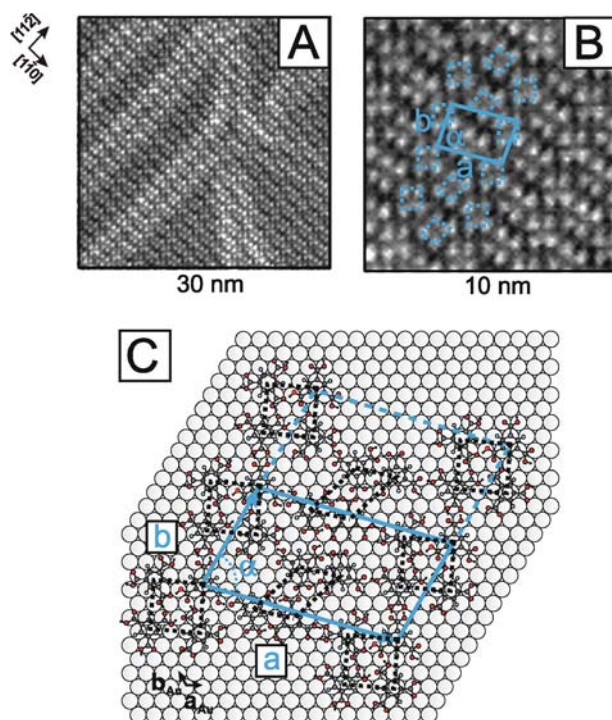


Fig. 8 **A** Large scale and **B** high-resolution image of I Ib on Au(111)-(1 × 1)/0.05 M H₂SO₄ in the presence of 3 mM TMA, $E_s = 0.03$ V, $i_T = 150$ pA. The characteristic quadratic and rhombohedral structure elements as well as the primitive unit cell are indicated. **C** Proposed packing model of TMA in I Ib. The parameters of the unit cell are summarized in Table 1 [67]

mated to $b = (1.92 \pm 0.10)$ nm, and between two adjacent rows of squares to $a = (3.57 \pm 0.20)$ nm. The enclosed angle α amounts to $(80 \pm 5)^\circ$. Within one row, the square units are rotated by $(30 \pm 3)^\circ$, as referenced to the main direction of the row. The derived unit cell contains eight individual, flat-lying TMA molecules, which are arranged in alternating rows of quadratic four-mer motifs and parallel dimers in rhombohedral subunits. The area per molecule is estimated to $A_{\text{I Ib}}(\text{ex}) = (0.84 \pm 0.05) \text{ nm}^2$, which corresponds to a coverage $\Gamma_{\text{I Ib}}(\text{ex}) = (2.00 \pm 0.10) \cdot 10^{-10} \text{ mol cm}^{-2}$. Adjacent dimers appear to be aligned with the upper right and the upper left, respective the lower right and the lower left TMA molecules in the squared sub-motif at each corner. The tetramer arrangement is attributed to the formation of a hydrogen-bonded closed loop between the four carboxyl groups of one unit. Similar motifs were reported for the crystal structures of chloroacetic acids [85] and for the self-assembly of 5,10,15,20-tetrakis-(4-carboxylphenyl)-21H,23H-porphyrin (TCPP) on HOPG [86]. The suggested tetrameric configuration of TCPP was attributed to a compromise between optimal intermolecular hydro-

gen bonding, maximization of 2D packing and substrate–adsorbate interaction to minimize surface free energy [53, 86]. Crystallographic studies show that the four-mer close-loop motif of carboxylic groups is stabilized by incorporation of water molecules [87, 88], or short chain alcohols [88, 89]. Returning to the arrangement of dimers in alternating rows of rhombohedral-type subunits one may assume the typical centrosymmetric motif composed of two carboxyl groups of two neighboring aligned TMA molecules [39, 44], or, alternatively, a macrocyclic dimer as formed by four carboxylic groups arranged in 1,3-positions of two adjacent TMA molecules [57]. We hypothesize the preference of macrocyclic dimers. In this approach, we considered the planar orientation of TMA in region IIb [68], the experimentally determined unit cell parameters, space filling arguments and an attempt to maximize the number of intermolecular hydrogen bonds. Each dimer unit is then allowed to form two respective three hydrogen bonds to adjacent TMA molecules of the tetramer unit. The bond lengths $\text{OH} \cdots \text{O}$ vary between 0.25 to 0.29 nm with estimated bond angles of 150 to 180°, typical for strong respective medium strong hydrogen bonding [81].

Experiments with reconstructed $\text{Au}(111)\text{-(p} \times \sqrt{3})$ electrodes illustrate that the quadratic four-mer motifs are aligned with the $[11\bar{2}]$ and the $[1\bar{1}0]$ directions of the substrate surface. Based on ab-initio calculations [80] and experimental results of flat oriented aromatic molecules [62, 75, 76] we further assume a preferential location of the TMA phenyl ring at or close to energetically favorable threefold hollow sites of the hexagonal substrate lattice. Combining both boundary conditions with the above-described properties of a 2D ordered molecular network, we propose the model depicted in Fig. 8C for the adlayer IIb. Using vectors of the primitive gold lattice, a_{Au} and b_{Au} one obtains in matrix notation

$$\begin{pmatrix} a \\ b \end{pmatrix} = \begin{pmatrix} 10 & -4 \\ 7 & 7 \end{pmatrix} \begin{pmatrix} a_{\text{Au}} \\ b_{\text{Au}} \end{pmatrix}.$$

The model shows typical lengths and angles of intermolecular hydrogen bonding, and nearly all TMA molecules of the unit cell occupy threefold substrate coordination sites. The model is in good agreement with the results derived from the experimental images (Table 1, Fig. 8B).

Herringbone Motif IIc

Transient desorption of the ribbon-type motif IIb upon excursion to positive potentials and immediate return to potentials around 0.20 V, e.g. just negative of the capacitive current peaks labeled P1' respective P1, allows one to create a new two-dimensional long-range assembly of TMA (Figs. 6, 9).

High-resolution images reveal a regular arrangement of dimers composed of two triangular units with typical properties of planar-oriented TMA molecules (side length $\sim 0.7\text{--}0.8$ nm, apparent corrugation height of $(0.10 \pm$

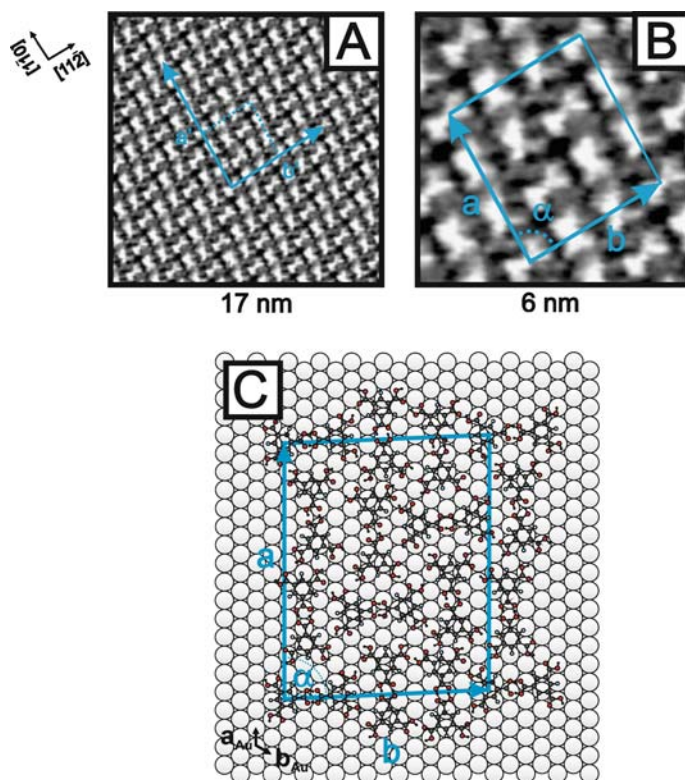


Fig. 9 **A** Large-scale in-situ STM image of the herringbone-type motif IIC of TMA on Au(111)-(1 × 1)/0.05 M H₂SO₄ in the presence of 3 mM TMA, $E_s = 0.20$ V, $i_T = 270$ pA. The lattice vectors a' and b' are indicated. **B** High-resolution image of IIC on Au(111)-(1 × 1), $E_s = 0.18$ V, $i_T = 120$ pA. The experimental unit cell is outlined. **C** Proposed packing model of TMA in IIC. The parameters of the unit cell are summarized in Table 1 [67]

0.02) nm). The length of one dimer-type unit in the STM contrast pattern along the main axis is estimated to (1.4 ± 0.2) nm. These observations and the comparison with the honeycomb motif IIA described before indicate that the dimers are stabilized by centrosymmetric hydrogen bonds between two carbonyl groups of adjacent TMA molecules [39, 44]. Next we define two adlayer directions by introducing the vectors a' and b' (Fig. 9A). Individual dimers are arranged with their main axis either parallel (represented by “-”) or perpendicular (represented by “|”) to the introduced adlayer directions. Parallel to the lattice vector a' the one-dimensional assembly of TMA dimer units follows the motif “...-|-|-|-...”. Parallel to b' we identify the motif “...-||-||-...”. The careful inspection of high-resolution STM images demonstrates that an assembly of four dimers of “|-|-” along a' and of “-||-” along b' identify the unit cell of the herringbone-type TMA adlayer IIC. The characteristic di-

mensions along a' and b' are estimated as $a = (4.10 \pm 0.15)$ nm, $b = (3.30 \pm 0.15)$ nm separated by an angle $\alpha = (84 \pm 5)^\circ$. The complex unit cell is formed by 18 TMA molecules arranged in a regular 2D pattern of centrosymmetric dimers. The area per molecule amounts to $A_{\text{IIc}}(\text{ex}) = (0.75 \pm 0.05)$ nm², and the resulting coverage is given by $\Gamma_{\text{IIc}}(\text{ex}) = (2.2 \pm 0.15) 10^{-10}$ mol cm⁻². This value is almost 70% higher than the coverage of the honeycomb network IIa, and only slightly higher than the value of the ribbon-type assembly IIb.

The distances and angles between dimers of the same row as well as of adjacent rows are compatible with the existence of a complex 2D hydrogen-bonded network. The dimer motif may be considered as a structural element in three-mer respective four-mer macrocycles representing motifs of up to four possible intermolecular hydrogen bonds between carboxyl groups of neighboring TMA molecules [39, 44, 53, 63, 83, 85, 86]. A tentative model of the adlayer IIc assumes that the phenyl rings of the TMA molecules are preferentially located in or nearby high symmetry sites of the hexagonal Au(111)-(1 × 1) substrate. Experimentally we could not determine the exact positions of the aromatic rings with respect to the substrate geometry. Taking the latter assumption, the properties of the experimentally derived unit cell, and the geometrical restrictions for dimer, three-mer respective four-mer hydrogen-bonding assemblies [53, 86] we propose the model drawn in Fig. 9C for the herringbone-type TMA phase IIc. With the primitive vectors of the gold lattice, a_{Au} and b_{Au} , one obtains in matrix notation

$$\begin{pmatrix} a \\ b \end{pmatrix} \begin{pmatrix} 14 & 0 \\ 7 & 13 \end{pmatrix} \begin{pmatrix} a_{\text{Au}} \\ b_{\text{Au}} \end{pmatrix},$$

The model implies a compromise between intermolecular interactions due to hydrogen bonding and adsorbate–substrate interactions to minimize the surface free energy. It is in agreement with the properties of the experimentally observed unit cell (Table 1), and maximizes the number of flat-lying TMA molecules localized in “close-to” high coordination threefold hollow sites of the Au(111) surface. The model proposes that the a' direction of the unit cell is aligned with the $[1\bar{1}0]$ substrate direction. The b' vector is misaligned by 2.5° with respect to the $[11\bar{2}]$ direction of Au(111). The experimentally observed “-||-” and “|- -|” motifs are clearly recognized as subunits of the model structure. The lengths of the hydrogen bonds OH···O in the dimer units are typically (0.26 ± 0.01) nm with bond angles of $(180 \pm 5)^\circ$. The lengths of the hydrogen bonds in the three-mer and four-mer units appear elongated up to 0.30 nm with estimated angles varying between 150° and 180° .

The herringbone structure IIc dissolves at positive potentials when passing the current peak P1' in the cyclic voltammograms (Fig. 6). On the other hand, it is stable at negative potentials until $E \leq -0.20$ V.

Hydrogen-Bonded Dimer Motif III

The potential-controlled deposition of TMA ($c > 1 \text{ mM}$) in $0.20 \text{ V} \leq E \leq 0.40 \text{ V}$, e.g. in the range marked by the current peaks P1/P1' and P2/P2' in the cyclic voltammograms (Fig. 6), triggers the assembly of TMA dimers in

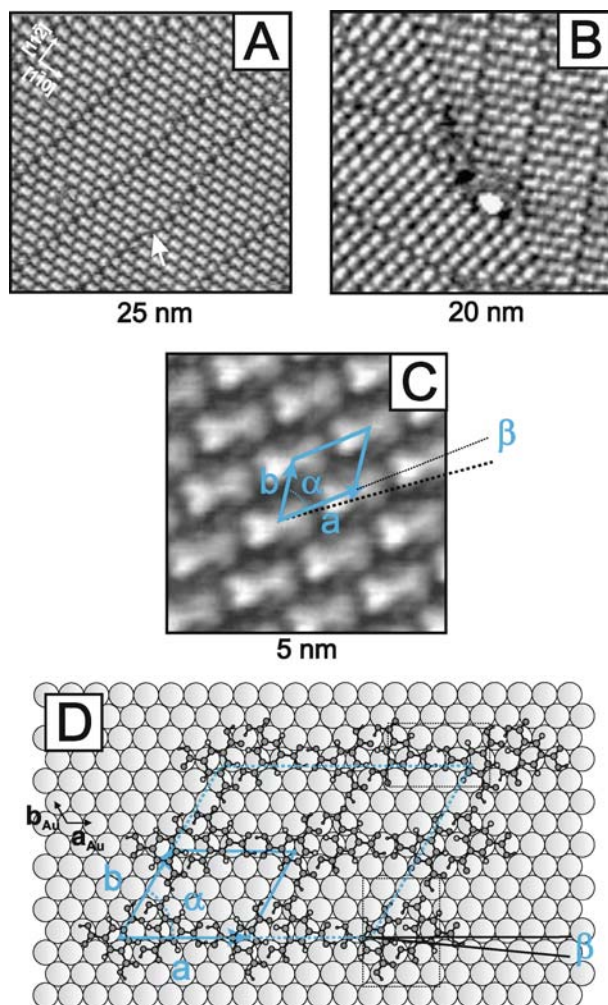


Fig. 10 **A** Translational and rotational **(B)** domain boundaries in a large-scale in-situ STM image of the hydrogen-bonded dimer motif III of TMA on Au(111)-(1 × 1)/0.05 M H₂SO₄ in the presence of 3 mM TMA, $E_s = 0.33 \text{ V}$, $i_T = 111 \text{ pA}$. The *arrow* in **A** marks a characteristic kink site at a translational domain boundary. **C** High-resolution image of III on Au(111)-(1 × 1), $E_s = 0.30 \text{ V}$, $i_T = 200 \text{ pA}$. The primitive unit cell is indicated. **D** Proposed packing model of TMA in III [67]

quasi-linear rows (Fig. 10). The field in the electrical double layer is expected to be small because the electrode bears a rather low excess charge in this potential region. The new adlayer emerges from an initially disordered phase, which slowly transforms, according to a nucleation and growth mechanism, into large two-dimensional islands of the assembly motif III.

Characteristic translational and rotational domain boundaries were found (Fig. 10A,B). The rotation angles between adjacent domains were $(120 \pm 5)^\circ$ or $(240 \pm 5)^\circ$ thus reflecting the hexagonal symmetry of the substrate surface. Within one adlayer island one often observes several, typically straight and parallel translation domain boundaries. Occasionally we found kink sites causing steps and a rotation of the domain boundary by 45° . Identical adlayer structures were detected on Au(111)- (1×1) and Au(111)- $(p \times \sqrt{3})$. The latter studies indicate that translational domain boundaries often extend over several tens of nanometers and are closely aligned to the $[11\bar{2}]$ direction of the substrate. The width of the corresponding domains in $[1\bar{1}0]$ direction is determined by two up to ten characteristically shaped protrusions aligned in parallel and highly correlated one-dimensional chains. Closer inspection (Fig. 10C) reveals that they are composed of two triangular features with the typical properties of a planar oriented TMA molecule (side length 0.7–0.8 nm, apparent corrugation height $\sim (0.08 \pm 0.01)$ nm). Assigning the corners of the triangular spots to the positions of the three carboxyl groups in individual TMA molecules we conclude on the existence of hydrogen-bonded centrosymmetric dimers [39, 44]. TMA dimers within one chain and of entire two-dimensional domains point in the same direction. The centers of these dimers are aligned with the $[1\bar{1}0]$ lattice direction. The center-to-center separation is estimated to $a = (1.43 \pm 0.05)\text{nm} \approx 5 \times |a_{\text{Au}}|$. Moreover, the molecular axis of individual TMA dimers is rotated by $\beta = (5 \pm 2)^\circ$ with respect to the chain direction (Fig. 10D). Linear chains of dimers are separated by an inter-row distance of 1.05 ± 0.04 nm. The nearest neighbor distance between the dimer centers of adjacent rows is estimated to 1.18 ± 0.05 nm $\approx 4 \times |a_{\text{Au}}|$. The regular arrangement of these dimers defines a characteristic second adlayer direction, rotated $(63 \pm 5)^\circ$ with respect to $[1\bar{1}0]$. The derived unit cell, which contains two TMA molecules, is indicated in Fig. 10C (Table 1). The corresponding area per molecule and coverage were estimated to $A_{\text{III}}(\text{ex}) = 0.75 \pm 0.02$ nm² and $\Gamma_{\text{III}}(\text{ex}) = (2.2 \pm 0.1)10^{-10}$ mol cm⁻², respectively. The experimental observations can be rationalized by the directional nature of hydrogen bonding. Molecular modeling reveals that the regular arrangement of dimers within one linear row may involve hydrogen-bonded macrocyclic dimers formed between four carboxyl groups of two adjacent TMA units. This motif is known to support the assembly of TMA in planar sheets in three-dimensional supramolecular assemblies [57]. Adjacent TMA molecules of the one-dimensional chains appear to be connected by hydrogen bonds in an alternating arrangement of centrosymmetric and macrocyclic dimers. Single hydrogen bonds may exist between molecules of parallel rows. This hy-

pothesis is supported by the observation that the positions of dimers within one domain appear to be very stable, not frizzy and highly correlated [84]. Neighboring molecular rows at translational domain boundaries are not in the registry. They are in interstitial positions and contain, in an alternating arrangement, TMA monomers with a broken centrosymmetric hydrogen bond. The experimentally observed registry between the linear dimer motif III and the substrate surface suggests a commensurate (5×4) TMA adlayer structure. Using vectors of the primitive gold lattice one obtains in matrix notation

$$\begin{pmatrix} a \\ b \end{pmatrix} \begin{pmatrix} 0 & 5 \\ 4 & 4 \end{pmatrix} \begin{pmatrix} a_{\text{Au}} \\ b_{\text{Au}} \end{pmatrix}.$$

We further assume that the phenyl rings of the TMA molecules are located in threefold hollow sites of Au(111). The corresponding model is depicted in Fig. 10D (Table 1). We notice that the substrate-adsorbate interaction (π -ring in threefold hollow sites) reduces the distance between the TMA centers of one centrosymmetric dimer by approximately 10%. The model predicts further the misalignment of the dimer axis by -5° with respect to the $[1\bar{1}0]$ substrate direction, which results from the directional nature of hydrogen bonds in the alternating arrangement of centrosymmetric and macrocyclic dimers.

Chemisorbed Striped TMA Adlayer IV

Increasing the electrode potential to higher values, e.g. past the current peak P2 in Fig. 6, causes the transformation of phase III previously assigned to hydrogen-bonded linear dimers of TMA. This process starts at adlayer defects on terraces, but most frequently on translational domain boundaries. These local sites are composed of planar-oriented TMA monomers (Fig. 11A,B). The latter are less strongly stabilized by the two-dimensional hydrogen-bonded network in region III. Subsequently, the linear dimers dissolve anisotropically line-by-line. The dissolution rate parallel to the chains of linear dimers, which are aligned to the $[1\bar{1}0]$ substrate direction, is faster than the process perpendicular to these rows. Initially, a transient disordered chemisorbed adlayer is formed (Fig. 11F) composed of rather fragile and irregular one-dimensional features. These features start to align with time and at higher positive potentials into the ordered chemisorbed striped phase IV.

Complementary IR-spectroscopic investigations revealed that this transition involves an orientation change of TMA molecules from planar to perpendicular, accompanied by the deprotonation of *one* COOH-group that is chemically bound to the positively charged electrode [68].

A long-range ordered and rather fragile new phase labeled IV starts to emerge with time (Fig. 12). Individual domains of 50–100 nm size exhibit a characteristic arrangement of alternating bright and dark stripes. Often one observes neighboring domains mutually rotated by integer multiples of 30°

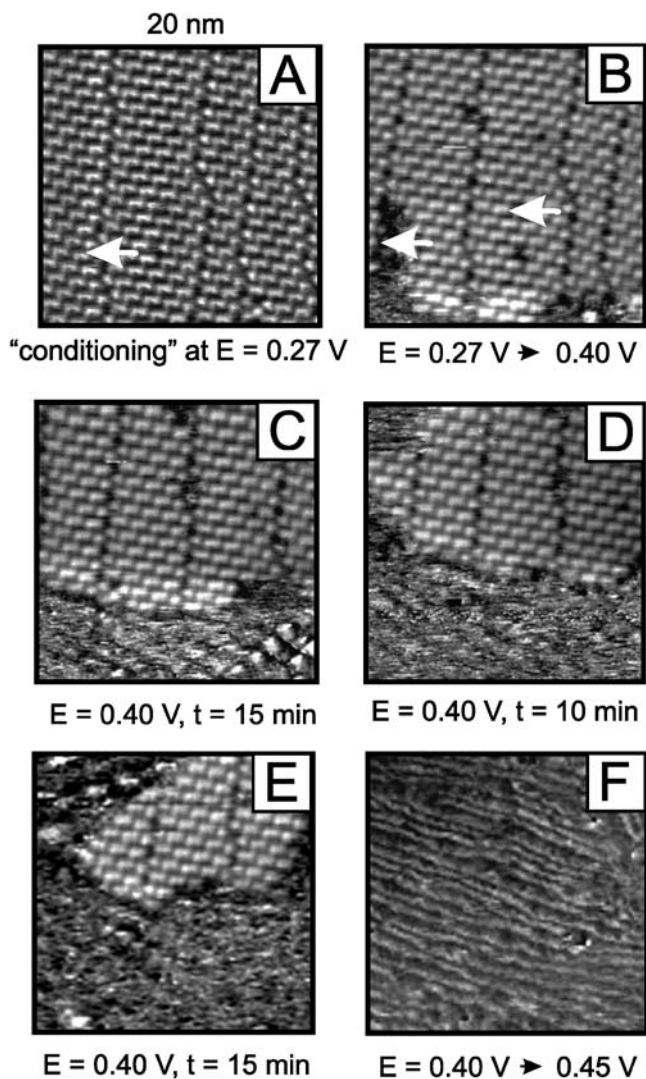


Fig. 11 Sequence of STM images ($20 \times 20\text{ nm}^2$) for Au(111)/0.05 M H_2SO_4 in the presence of 3 mM TMA after a potential step from $E_s = 0.27\text{ V}$ (stability range of the linear dimer phase III) to $E_s = 0.45\text{ V}$ (stability range of a transient disordered chemisorbed stripe phase), $i_T = 82\text{ pA}$. *White arrows* indicate the formation of active sites of the structural transformation [67]

indicating a commensurate registry of the adlayer with the hexagonal substrate surface. The striped domains appear to be aligned with one of the [110] substrate directions on Au(111)-(1 × 1). High-resolution images such as shown in Fig. 12B reveal details of the striped phase. Rows of identically aligned bright dots (trace i) are separated by alternating rows of parallel-

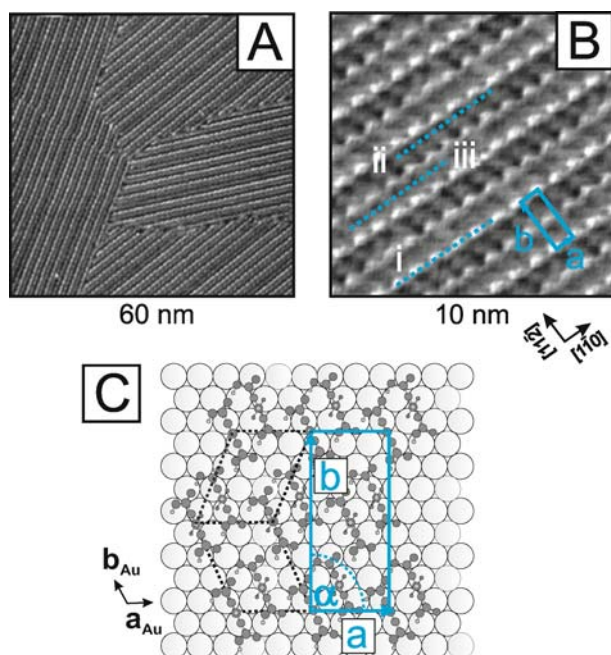


Fig. 12 **A** Large-scale in-situ STM image of the chemisorbed striped TMA adlayer IIIb on Au(111)-(1 × 1)/0.05 M H₂SO₄ in the presence of 3 mM TMA, $E_s = 0.70$ V, $i_T = 60$ pA. **B** High-resolution image of IV on Au(111)-(1 × 1), $E_s = 0.70$ V, $i_T = 77$ pA. The primitive unit cell is indicated. **C** Proposed packing model of TMA in IV. The parameters of the unit cell are summarized in Table 1 [67]

aligned light gray (trace iii) respective dark gray (trace ii) ellipsoidal-like features of 0.7–0.9 nm length. Their axis is tilted by 60–70° with respect to the main row directions. Cross section profiles reveal asymmetric main maxima and smaller side maxima with characteristic repeat distances of (0.86 ± 0.05) nm, e.g. neighboring features are approximately three lattice constants apart. The apparent corrugation height is estimated as 0.20–0.40 nm. Adjacent rows of bright dots appear to be slightly darker while every other row is identical and exactly aligned. The interspacing rows of light and dark features exhibit rather broad maxima of similar periodicity with an apparent corrugation height of 0.05–0.15 nm. A rectangular repeat motif with $a = (0.86 \pm 0.05)$ nm ($\approx 3|a_{\text{Au}}|$) parallel and $b = (2.15 \pm 0.20)$ nm ($\approx 4\sqrt{3}|a_{\text{Au}}|$) perpendicular to the bright rows could be identified (Fig. 12B, Table 1). The different STM contrast pattern and the increase of the apparent corrugation height in region IV indicate an orientation change from flat lying to a tilted and/or upright standing configuration accompanied with major changes in the substrate–adsorbate interaction potential. Tunneling may involve molecular σ and π states [90].

The surface orientation was explored in a comprehensive steady state and time-resolved study employing surface-enhanced infrared reflection absorption spectroscopy (ATR-SEIRAS). The detailed study is presented in [68]. Here we only focus on selected main results (Fig. 13). No TMA-related spectral features were found at $E < 0.40$ V supporting the notion of flat orientated molecules. In the potential region IV, e.g. for $E > 0.40$ V, three distinct positive-going IR bands appear in the presence of 3 mM TMA at 1720 – 1735 cm^{-1} , around 1375 cm^{-1} , and at 1300 – 1320 cm^{-1} (Fig. 13A). Comparison with solid state and solution spectra [91, 92] supported the assignment of these spectral features to the following TMA vibrations: the stretching mode of C=O in COOH ($\nu_{\text{C=O}}$), the symmetric stretching mode of O–C–O in COO^- ($\nu_{\text{s(OCO)}}$), e.g. a deprotonated carboxylate group, and the stretching mode of C–OH in COOH ($\nu_{\text{C-OH}}$), respectively. A correlation analysis demonstrates that both sets of vibrations originate from the same molecule. Simultaneously, co-adsorbed isolated and strongly hydrogen-bonded water was detected. The intensities of the TMA bands increase with positive potential, reach their

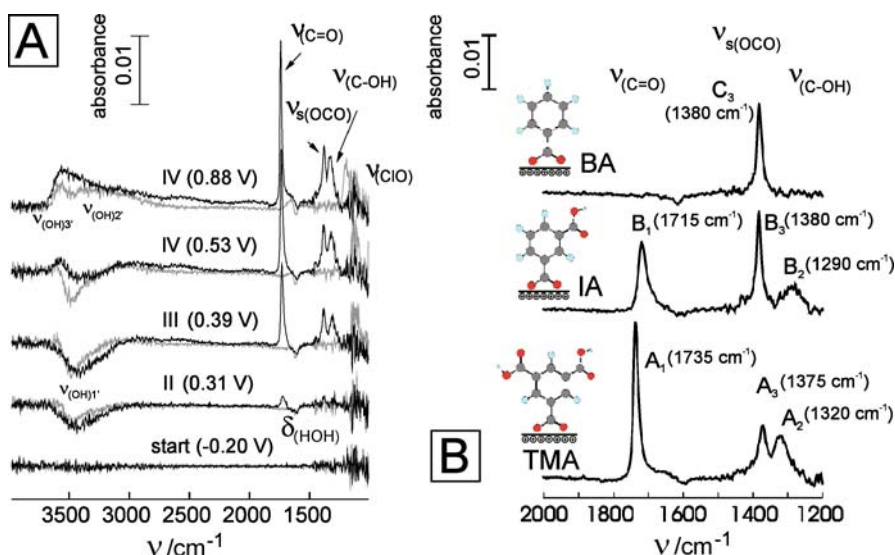


Fig. 13 **A** Selected SEIRA spectra of Au(111-25 nm)/0.1 M HClO₄ in the absence (gray traces) and in the presence of 3 mM TMA (black traces) recorded simultaneously during a positive-going potential from -0.20 to 0.90 V, scan rate 10 mV s^{-1} . The background spectra were measured at -0.20 V. The data represent different potential regions of the various adlayer phases of TMA: start (-0.20 V), IIa (0.11 V), IIb (0.39 V), IV (0.53 V) and IV (0.88 V). **B** Equilibrium SEIRA spectra of TMA (3 mM), isophthalic acid (IA, saturated solution) and benzoic acid (BA, 3 mM) in 0.05 M H₂SO₄ obtained at 0.80 V in region IV. The reference spectra were taken at $E = -0.20$ V. The insets illustrate the derived interfacial orientations of the three molecules chemisorbed on a positively charged Au(111-25 nm) film electrode [68]

maximum in the chemisorbed region IV, and decrease to zero during the subsequent negative going scan. Referring to the surface selection rule of SEIRAS that only vibrations with dipole changes perpendicular to the local surface can be observed [93], we conclude that perpendicularly oriented TMA molecules could be chemisorbed onto the positively charged electrode surface via one or two deprotonated carboxylate groups. An orientation change from flat lying to an upright standing conformation takes place following deprotonation of the TMA carboxyl group(s) due to the strong interaction of the negatively charged carboxylate ion with the positively charged electrode. TMA forms a distinct chemisorption bond. The corresponding gain in chemisorption energy with the upright geometry is assumed to compensate for the loss of the π -bonding upon reorientation of the flat lying species. Carboxylate formation is a typical finding on a positively charged electrode surface in contact with aqueous electrolyte [94–96]. To resolve the issue on surface coordination, a comparative study of TMA with benzoic acid (BA) and isophthalic acid (IA) was carried out in the high coverage region [68]. These carboxylic acids have different numbers of identical carboxyl groups but similar conjugated structures. Figure 13B shows typical SEIRAS equilibrium spectra of the three molecules at $E = 0.80$ V. The comparative correlation and intensity analysis of the observed carboxylate modes and of the vibrations attributed to protonated carboxyl groups provide clear evidence for deprotonation and surface coordination of only one carboxylate group of TMA. The remaining two protonated carboxyl side groups are directed toward the electrolyte and may form intermolecular hydrogen bonds. Based on calculations and experimental evidence for related systems [62, 94–100] we suggest that the surface-bound carboxylate group is centered at two-fold short bridge sites. The carbon atom resides midway between two nearest-neighbor gold atoms, and the chemically bound oxygen atoms are equidistant from the surface. TMA forms a distinct chemisorption bond. The site-specificity, a consequence of a strong, localized surface–molecule bond and interaction through a single molecule functionality, contrasts with the behavior of the flat lying species with their multifunctional surface interaction [98]. The phenyl ring and the protonated carboxyl groups may undergo conformational rotations with respect to C–C bonds which allows forming a supramolecular network stabilized by intermolecular hydrogen involving the solution-directed carboxyl groups.

The analysis of potential-induced time-dependent SEIRAS experiments demonstrated [68] that the formation of chemisorbed TMA in phase IV proceeds in two steps: TMA molecules change their orientation from planar to perpendicular accompanied by the deprotonation of one carboxyl group after a potential step towards sufficiently high positive charge densities. In a subsequent and much slower process, the chemisorbed TMA molecules start to gradually align into a highly ordered two-dimensional network IV.

Based on complementary observations from in-situ STM and ATR-SEIRAS experiments we propose the model depicted in Fig. 12C for the adlayer of

chemisorbed TMA on Au(111)-(1 × 1) in the potential region IV. The structure is represented by a commensurate (3 × 4√3) unit cell. Using vectors of the primitive gold lattice, a_{Au} and b_{Au} as basis one obtains in matrix notation

$$\begin{pmatrix} a \\ b \end{pmatrix} \begin{pmatrix} 3 & 0 \\ 4 & 8 \end{pmatrix} \begin{pmatrix} a_{\text{Au}} \\ b_{\text{Au}} \end{pmatrix}.$$

The unit cell is composed of four molecules. The corresponding area per molecule and coverage were obtained to $A_{\text{IV(th)}} = 0.43 \text{ nm}^2$ and by $\Gamma_{\text{IV(th)}} = 3.8 \times 10^{-10} \text{ mol cm}^{-2}$, respectively. The bright dots along $[1\bar{1}0]$ are assigned to pairs of upright and parallel-aligned TMA molecules coordinated to the positively charged substrate surface via one deprotonated carboxylate group per molecule. The aromatic ring and the carboxylate group of one molecule assume a coplanar conformation. A 30° rotation of the carboxylate plane is suggested for the second TMA molecule of the pair. The surface-bound carboxylate groups of both molecular units are in registry with the direction of the hexagonal substrate in energetically favored bridge sites. The parallel orientation of the phenyl ring and their alignment with the rows of densely packed gold atoms within one pair is supported by the possible formation of intermolecular hydrogen bonds involving the solution directed protonated carboxyl groups. In this arrangement the parallel phenyl rings of one dimer are separated by 0.375 nm ($= 3/4\sqrt{3}|a_{\text{Au}}|$), and the distance between the displaced centers of the carboxylate groups amounts to 0.38 nm ($= 1/2\sqrt{7}|a_{\text{Au}}|$). Nearest neighbor parallel rows of bright dots, which appear slightly darker in the experimental STM image, are also assigned to pairs of upright TMA molecules, exhibiting just the reverse alignment of phenyl ring and coordinating carboxylate. The two types of alternating molecular rows are separated by 1 nm ($= 2\sqrt{3}|a_{\text{Au}}|$) in $[11\bar{2}]$ direction. The bright features in neighboring rows representing pairs of molecules are mutually shifted by 0.43 nm ($= 3/2|a_{\text{Au}}|$) along the $[1\bar{1}0]$ direction. This arrangement enables still the existence of inter-row hydrogen bonding. Each TMA molecule may form up to four hydrogen bonds with molecules (“or molecular dimers”) within the same and of neighboring rows, thus giving rise to a supramolecular ladder-type network. Hydrogen bond lengths ranging between 0.26 to 0.30 nm are estimated. The interspacing rows of light gray and dark gray ellipsoidal features between the rows of bright dots, as illustrated in the STM contrast pattern in Fig. 12B, might result from aligned carboxyl groups and/or mutually shifted phenyl rings of pairs of dimers.

3.3

Self-Assembly of Other Aromatic Carboxylic Acids on Au(111)-(1 × 1)

The interplay of hydrogen-bonded dimers and substrate–adsorbate coordination is a general property of aromatic carboxylic acids on low index gold single crystal electrodes.

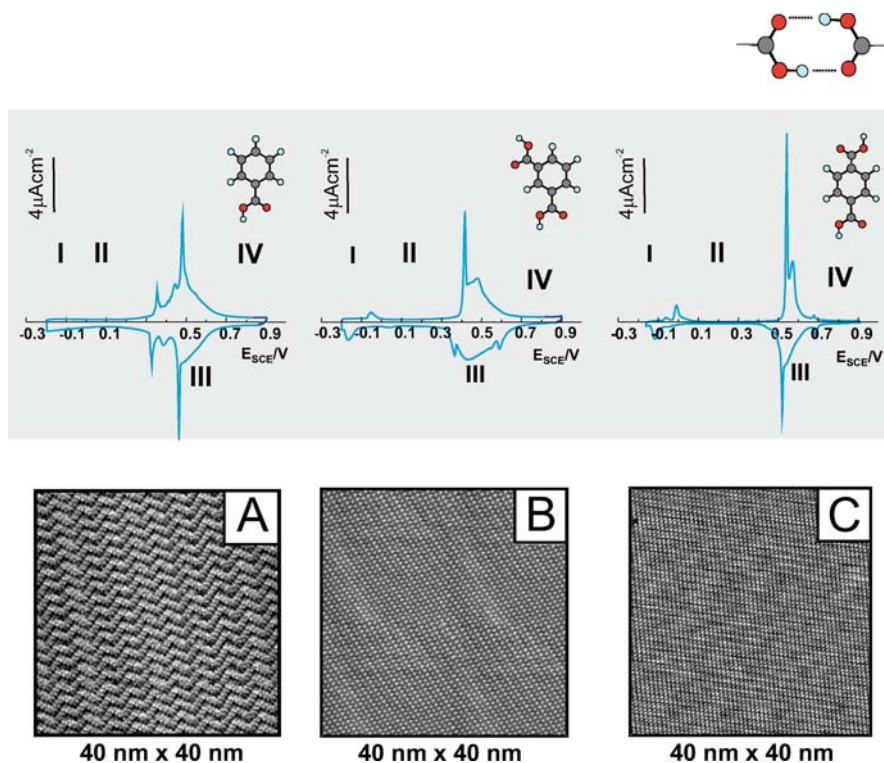


Fig. 14 Cyclic voltammograms (0.1 M HClO_4 , 10 mV s^{-1}) and large-scale in-situ STM images of 12 mM BA (A) 0.5 mM IA (B) and a saturated solution of TA (C) on $\text{Au}(111)-(1 \times 1)$. Four characteristic potential regions labeled I to IV are indicated. The large-scale STM images represent physisorbed adlayers of type II ($i_T = 20\text{--}200\text{ pA}$, $E = 0.10\text{ V}$)

The cyclic voltammograms of BA, IA and terephthalic acid (TA) in 0.1 M HClO_4 (Fig. 14) show four characteristic potential regions labeled I to IV, which are separated by more or less distinct current peaks. A disordered adlayer I at the most negative potentials and at low coverages is followed by a two-dimensional physisorbed film II, which undergoes a complex re-orientation accompanied with a partial charge transfer transition III until, at sufficiently positive potentials a chemisorbed adlayer IV is formed due to substrate–adsorbate coordination of one deprotonated carboxylate group with the positively charged electrode. Structure details of the highly ordered adlayers in regions II and IV are illustrated in Figs. 15 and 16, respectively.

BA forms for solute concentrations higher than 3 mM at a negatively charged $\text{Au}(111)-(1 \times 1)$ surface an ordered adlayer of quadratic motifs composed of four planar oriented and mutually hydrogen-bonded BA molecules (macrocyclic tetramers). These molecules interact with each other via intermolecular hydrogen bonds [101, 102]. A unit cell with the following charac-

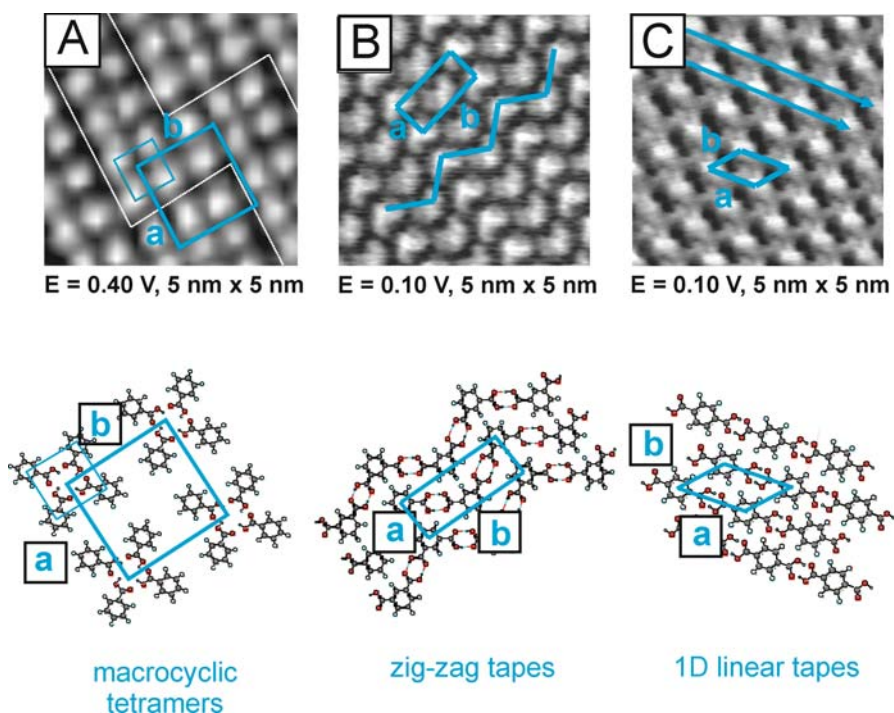


Fig. 15 High-resolution in situ STM images of the planar-oriented physisorbed adlayers of type II of BA (**A**), IA (**B**) and TA (**C**) on Au(111)-(1 × 1); $i_T = 20\text{--}200 \text{ pA}$ and $E = 0.1 \text{ V}$. The corresponding molecular models are shown in the lower panels. Parameters of the indicated unit cells are summarized in Table 2

Table 2 Characteristic dimensions of the experimental unit cell parameters of the physisorbed adlayers II of aromatic carboxylic acids

Adlayer	a [nm]	b [nm]	α [°]	Area A [nm ²]	Coverage Γ [10 ¹⁰ mol cm ⁻²]
BA	1.55 ± 0.1	1.58 ± 0.1	85 ± 8	0.61 ± 0.10	2.7 ± 0.3
	1.44	1.50	90	0.54	3.0
IA	0.74 ± 0.05	1.70 ± 0.08	90 ± 5	0.63 ± 0.05	2.6 ± 0.2
	0.75	1.73	90	0.65	2.6
TA	1.01 ± 0.08	0.76 ± 0.10	50 ± 8	0.59 ± 0.05	2.8 ± 0.3
	1.0	0.82	45	0.58	2.6

teristic dimensions is identified $a = (1.55 \pm 0.10) \text{ nm}$, $b = (1.58 \pm 0.10) \text{ nm}$ and $\alpha = (85 \pm 8)^\circ$. The cell contains four molecules, which gives rise to a coverage of $\Gamma_{\text{IIBA}} = (2.7 \pm 0.3) \times 10^{-10} \text{ mol cm}^{-2}$. The characteristic data and the corresponding model parameters are summarized in Fig. 15A and Table 2. In case

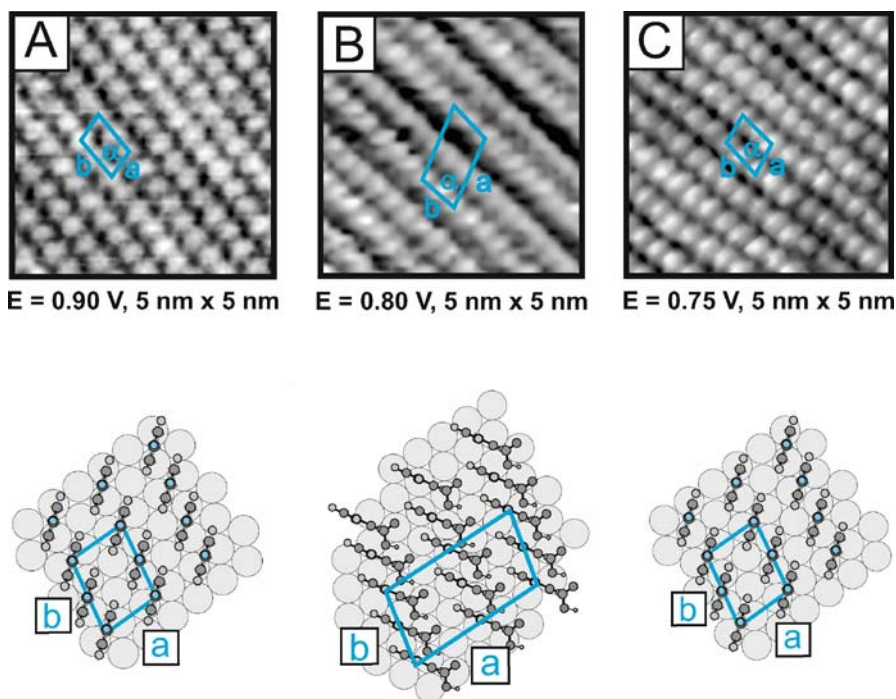


Fig. 16 High-resolution in situ STM images of the chemisorbed adlayers of type IV, formed by substrate–adsorbate coordination, of BA (A), IA (B) and TA (C) on Au(111)-(1 × 1); $i_T = 5\text{--}50$ pA and $E = 0.8$ V. The corresponding molecular models are shown in the lower panels. Parameters of the indicated unit cells are summarized in Table 3

Table 3 Characteristic dimensions of the experimental unit cell parameters of the chemisorbed adlayers IV of aromatic carboxylic acids

Adlayer	a [nm]	b [nm]	α [°]	Area A [nm ²]	Coverage Γ [10 ¹⁰ mol cm ⁻²]
BA	0.58 ± 0.05	0.8 ± 0.08	74 ± 5	0.22 ± 0.03	7.5 ± 0.5
	0.58	0.76	79	0.22	7.5
IA	1.50 ± 0.08	0.80 ± 0.08	75 ± 5	0.29 ± 0.05	5.7 ± 0.2
	1.44	0.76	79	0.27	6.1
TA	0.56 ± 0.05	0.76 ± 0.08	80 ± 5	0.21 ± 0.035	7.9 ± 0.5
	0.58	0.76	79	0.22	7.5

of IA and TA we observed zig-zag tapes and 1D linear dimers, which nicely reflect the key pattern of the 3D crystal structures of both acids [45, 46]. Figure 15B,C illustrates high-resolution STM images of both adlayers, the derived structure models and the corresponding unit cells. The parameters are summarized in Table 2. These motifs of self-organization by hydrogen bond-

ing are determined by the number and position of the carboxylic groups and rather little by direct interactions with the substrate if the adlayers are allowed to equilibrate. With this knowledge controlled engineering to incorporate functional guest molecules into tailored host lattices appears to be possible at electrified solid–liquid interfaces.

Application of a high positive charge (potential) results for all three acids in a change in orientation and the formation of a substrate–adsorbate complex with just one deprotonated carboxylic acid group being in direct contact to the electrode surface (Fig. 16) [68]. BA and TA form densely packed stacking rows with intermolecular distances ranging between 0.4 to 0.5 nm. IA shows a more structured stacking row pattern, which is rationalized by the surface coordination of one carboxylate group, while the other, undissociated carboxyl group is capable to form a strongly correlated hydrogen-bonded network with neighboring molecules. The unit cells and the corresponding structure models are shown in Fig. 16. All parameters are summarized in Table 3. The detailed analysis follows a similar strategy as that described for TMA in the previous paragraph [103].

4

Molecular “Self-Assembly” Involving Covalent Bond Formation

4.1

Introduction

The understanding of the relationships between molecular structure of tailored organic molecules, their hierarchical organization in assemblies chemically bound to surfaces and interfaces as well as their functionality represent fundamental topics of current interest [104, 105]. In the following we shall focus on so-called chemisorbed, “self-assembled” monolayers (SAM), which are distinctly different from the physisorbed, hydrogen-bonded adlayers discussed in the previous paragraph. Following a historical development we will use the terminus self-assembled monolayers herein exclusively as molecular assemblies formed by chemisorption of an active surfactant onto a solid surface [106–108]. We will specifically focus on selected results with aromatic SAMs on Au(111) electrodes at solid–liquid interfaces.

SAMs offer design flexibility both at the individual molecular and at the materials level (“surface engineering”), and represent model systems to explore specific interactions and reactions at surfaces and interfaces [106–108]. Assemblies of thiol-based organic molecules “self-assembled” on metal substrates are a special class of SAM’s. These adsorbates are composed of one or two thiol-anchor groups, custom-designed alkyl or phenyl spacer units and, in some cases, incorporated tailored functionalities [106, 109–111]. The application of SAMs covers diverse areas such as adhesion [112], lubri-

cation [113], microfabrication [110], bioenergetics [114], corrosion [115], fundamental electrochemistry [116] and metal deposition [117] as well as the emerging field of nanoelectronics [118–120]. Of particular interest is their ability to control charge transfer in metal–molecular hybrid systems [121, 122].

Most fundamental studies on electrochemical and electrical properties of organosulfur compounds focused on aliphatic thiols [106, 107, 116, 118–129]. Aromatic thiols have been investigated far less [106, 111, 128, 130–132]. However, the vision of a molecular level electronics has triggered an active research interest in aromatic thiol-based molecular rods and functional building blocks of single molecules and tailored assemblies (cf. [133]). The rigid aromatic system offers a unique control of structure and local molecular functionality. Furthermore, the absence of conformational disorder (employing the concept of commensurability of intra-assembly planes [134]) may lead to stable and low-defect, molecularly engineered model surfaces. With reference to the unique structure properties of 4,4'-dialkyl-substituted biphenyls [135], 4-methyl-4'-(*n*-mercaptoalkyl)biphenyls (BP*n*) represent a particularly interesting group of molecular building blocks for the construction of hierarchical molecular assemblies at surfaces. The molecules consist of an aromatic biphenyl moiety with an aliphatic spacer unit of variable length between the annular system and the sulfur anchoring group. Buck, Zharnikov and Wöll described in a series of spectroscopic [136, 137] and scanning tunneling microscopy (STM) studies [138–141] under UHV conditions and in air the structure and assembly of BP*n* adlayers on polycrystalline gold and silver surfaces. The three groups reported a pronounced odd-even effect with a denser molecular packing for BP*n* with $n = \text{odd}((2\sqrt{3} \times \sqrt{3})$ [138–141] unit cell), in comparison to the less favorable packing with $n = \text{even}((5\sqrt{3} \times 3)$ and $(6\sqrt{3} \times 2\sqrt{3})$ unit cells) [138–140]. They also found that these structure differences lead to a periodic odd-even alteration of the reductive desorption behavior [142, 143] as well as in the stability against organic exchange by other thiols [144].

In the following sections we will present selected results on the structure, electrochemical and electrical properties of BP*n*'s ($n = 1-6$) immobilized

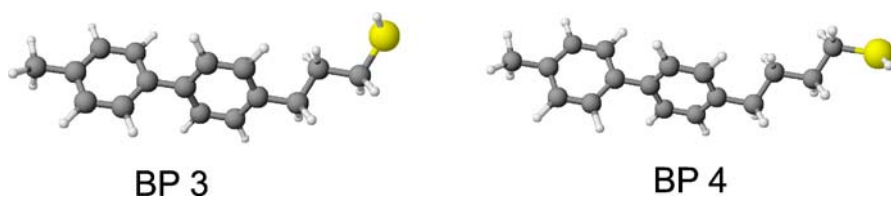


Fig. 17 Molecular structures of 4-methyl-4'-(3-mercaptopropyl) biphenyl (BP3) and of 4-methyl-4'-(3-mercaptobutyl) biphenyl (BP4)

on well-defined Au(111)-(1 × 1) single crystal electrodes employing STM and STS, cyclic voltammetry and chronoamperometry [145, 146].

4.2

Structure of BPn Adlayers on Au(111)-(1 × 1)

The structure properties of the prepared BPn monolayers on Au(111)-(1 × 1) were monitored by high-resolution STM studies in mesitylene. In the following we report key results obtained after assembly of BPn from 0.1 mM ethanolic solution at 90 °C for 12 h. The results of the complete STM/STS studies were published in [146].

Figure 18A shows a large-scale STM image of BP3, a typical representative of the investigated molecular class with an odd number of (CH₂)-spacer units. Individual terraces are covered by large domains of a uniform adlayer. Within the terraces, monatomically deep depressions with a typical size of 5–10 nm and a depth of 0.25 nm were identified. They are evenly distributed on flat terraces. Depletion was found in the neighborhood of step sites due

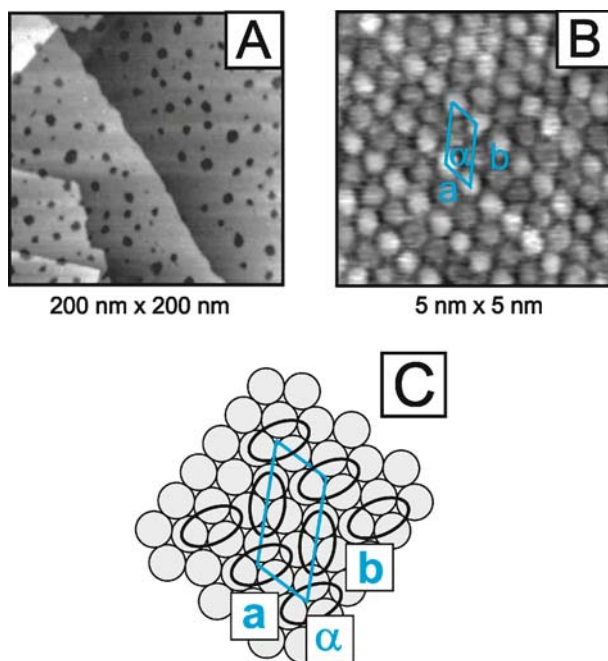


Fig. 18 **A** Large-scale and **B** high-resolution STM images of the $(\sqrt{3} \times 2\sqrt{3})$ adlayer of BP3 on Au(111)-(1 × 1) in mesitylene. Tunneling conditions: $E_{\text{bias}} = -0.55$ V, $i_T = 70$ pA. The unit cell is indicated in **(B)**. Panel **C** illustrates a top view of the structure model of the $(\sqrt{3} \times 2\sqrt{3})$ overlayer of BP3 (ellipsoids) on Au(111)-(1 × 1) (gray circles). Complete details of the structure analysis are given in [146]

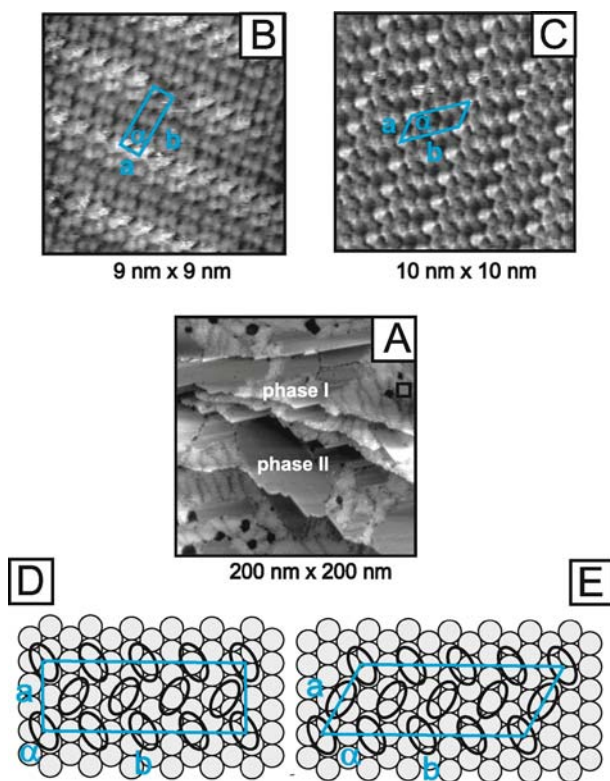


Fig. 19 **A** Large-scale and high-resolution STM image of the coexisting **B** ($3 \times 5\sqrt{3}$) and **C** ($2\sqrt{3} \times 5\sqrt{3}$) adlayers of BP4 on Au(111)-(1×1) in mesitylene. Tunneling conditions: $E_{\text{bias}} = -0.5$ V, $i_T = 40$ pA. The panels **D** and **E** represent top view structure models of the ($3 \times 5\sqrt{3}$) and ($2\sqrt{3} \times 5\sqrt{3}$) overlayers of BP4 (ellipsoids) on Au(111)-(1×1) (gray circles). The unit cells are indicated. The parameters are discussed in the text, and more details are presented in [146]

to coarsening and thermal annealing processes [147]. High-resolution experiments (Fig. 18B) revealed a hexagonal pattern of molecular size protrusions arranged in alternating dark and bright rows. The dimensions of the unit cell were estimated from height profiles as $a = (0.52 \pm 0.02)$ nm, $b = (1.03 \pm 0.05)$ nm and $\alpha = (58 \pm 4)^\circ$ corresponding to a ($\sqrt{3} \times 2\sqrt{3}$) structure with two BP3 molecules per unit cell (Fig. 18B,C). The resulting area per molecule is obtained as $A_{\text{ex}} = 0.23$ nm² ($A_{\text{model}} = 0.22$ nm²) which gives a coverage of $\Gamma_{\text{ex}} = 7.3 \times 10^{-10}$ mol cm⁻² ($\Gamma_{\text{model}} = 7.7 \times 10^{-10}$ mol cm⁻²). This observation is in agreement with LEED and ex-situ STM experiments recently reported by Azzam et al. [138–140]. Careful inspection of the entire organic adlayer revealed no additional co-adsorbed structures. Similar results were also obtained with BP5 [146].

In contrast, the adlayers fabricated with BPn's having an even number of (CH₂)-units exhibit coexisting phases. Figure 19 demonstrates, as an example, a typical large-scale scan of BP4 on Au(111)-(1 × 1). On the same terrace one observes areas of bright contrast (phase I) and areas of dark contrast (phase II), occasionally coexisting with monatomically deep holes. Domain boundaries between the two phases are not sharp, but no large regions of disorder exist between them. High-resolution measurements reveal that phase I is represented by a regular array of protrusions, which are assigned to individual BP4 molecules. The suggested repeat pattern is estimated to $a = (0.86 \pm 0.05)$ nm, $b = (2.45 \pm 0.12)$ nm separated by an enclosed angle $\alpha = (93 \pm 5)^\circ$, which is consistent with a $(3 \times 5\sqrt{3})$ commensurate unit cell composed of eight BP4 molecules [138–140, 146], $\Gamma_{\text{ex}} = 6.3 \times 10^{-10}$ mol cm⁻² ($\Gamma_{\text{model}} = 6.1 \times 10^{-10}$ mol cm⁻²; Fig. 19B,D). The analysis of phase II gives $a = (1.04 \pm 0.07)$ nm, $b = (2.46 \pm 0.10)$ nm and $\alpha = (61 \pm 4)^\circ$, which leads to a $(2\sqrt{3} \times 5\sqrt{3})$ unit cell of eight BP4 species and an area per molecule $A_{\text{ex}} = 0.28$ nm² ($A_{\text{model}} = 0.27$ nm², Fig. 19C,E) [146]. The corresponding coverage is calculated to $\Gamma_{\text{ex}} = 5.9 \times 10^{-10}$ mol cm⁻¹ ($\Gamma_{\text{model}} = 6.1 \times 10^{-10}$ mol cm⁻²). The unit cell is smaller than the $(2\sqrt{3} \times 6\sqrt{3})$ structure recently proposed by Azzam et al. [138–140]. The bright protrusions define molecular rows, which align with the short direction of the unit cell in both phases. Interestingly, rows representing adjacent neighboring phases are often perpendicular with respect to each other. Coexistence of a majority $(2\sqrt{3} \times 5\sqrt{3})$ phase with a more complex $(3 \times n\sqrt{3})$ structure was also observed for adlayers of the even numbered molecules BP2 and BP6 assembled at 90 °C for 12 h from ethanolic solution [138–140, 146].

4.3

Selected Electrochemical Properties of BPn Adlayers on Au(111)-(1 × 1)

Figure 20A shows, as an example, a series of current-voltage curves for BP4 in 0.1 M NaOH and 0.1 M HClO₄, respectively. Three characteristic potential intervals labeled I, II and III, which are separated by the current peaks P1 and P2/P2', can be readily distinguished. The stability region of I, which is assigned to the double layer range, is delimited at negative potentials by the onset of reductive desorption (peak P1) and at positive potentials by the oxidative desorption of BP4 (peak P2).

Double Layer Properties

In a typical experiment a dry, freshly prepared Au(111)-(1 × 1) electrode modified with a BP4 monolayer was brought in contact with the electrolyte at $E = 0.0$ V (vs. SCE) establishing a hanging meniscus configuration in an oxygen-free environment. Scanning the electrode potential in $-0.50 \text{ V} \leq E \leq 0.10 \text{ V}$ (in 0.1 M NaOH) or in $-0.10 \text{ V} \leq E \leq 0.50 \text{ V}$ (in 0.1 M HClO₄) revealed

a capacitance of $2.4 \mu\text{F cm}^{-2}$, rather independent of the electrolyte. As compared to bare Au(111)-(1 × 1), the BP4-covered electrode exhibits a markedly reduced charging current, and an almost potential independent behavior in a wide potential range, which is characteristic for thin organic adlayers with a low dielectric constant blocking ion transfer and solvent penetration.

The adlayer capacitance C is decreasing with increasing chain length of the alkyl spacer group. The plot $1/C$ vs. number of CH_2 -units yields a straight line with a slope of $(0.023 \pm 0.004) \text{ cm}^2 \mu\text{F}^{-1}$ and an intercept $(0.34 \pm 0.02) \text{ cm}^2 \mu\text{F}^{-1}$ ($\sigma = 0.95$). This linear correlation quantitatively agrees with previously reported capacitance data for alkanethiols on Au(poly) electrodes [148]. However, a more detailed inspection reveals that the adlayer capacities of BPn's with $n = \text{odd}$ (even) are slightly lower (higher) than the theoretical values predicted by the results of the linear regression analysis described above. This trend is in agreement with the higher (lower) packing density and the lower tilt angle of the biphenyl moiety of BPn, $n = \text{odd}$ (even) adlayers on Au(111) [138–140].

An alternative way to determine the interfacial capacitance is based on the so-called “immersion method” [149–151]. We adopted this technique here to explore thermodynamic properties of a well-defined Au(111)-(1 × 1) electrode modified with an aromatic self-assembled monolayer. The following strategy is applied: The dry, BP4-covered Au(111)-(1 × 1) electrode is brought under potential control and in the absence of oxygen in contact with the electrolyte forming a hanging meniscus without wetting the walls of the electrode. Figure 20B illustrates two current transients recorded at $E = -0.40 \text{ V}$ and at $E = -0.20 \text{ V}$. The current decreases (increases) steeply, reaches a minimum (maximum) and subsequently decays exponentially to zero. The charging current through the interface is either negative or positive and varies systematically with the electrode potential chosen. The charge consumed is attributed to building up the electrochemical double layer at the respective immersion potentials. The full and open circles in Fig. 20A represent the charge density vs. potential curve, as obtained by integration of a series of systematically recorded current–time transients for two different electrolytes in $-0.70 \text{ V} \leq E \leq 0.70 \text{ V}$. The plot is linear with a slope of $(2.2 \pm 0.2) \mu\text{F cm}^{-2}$, which is in excellent agreement with the voltammetric data reported above. The zero crossing at $E = (-0.30 \pm 0.01) \text{ V}$ represents an estimation of the potential of zero charge (E_{pzc}) of the BP4-covered Au(111)-(1 × 1) electrode. This value is significantly more negative than E_{pzc} of the bare supporting electrolyte (cf. $E_{\text{pzc}} = 0.240 \text{ V}$ published for Au(111)-(1 × 1) in 0.01 M HClO_4 [152]). Similar values of E_{pzc} were also obtained for all BPn, $n = 1-6$ [145]. For comparison, Sondag-Huethorst and Fokkink [153, 154] reported $E_{\text{pzc}} = -0.450 \text{ V}$ for self-assembled monolayers of alkanethiols on Au(poly), independent on the length of the alkyl chain, employing the Wilhelmi plate technique. Becka and Miller et al. found for similar systems $E_{\text{pzc}} = -0.40 \text{ V} \pm 0.20 \text{ V}$ based on impedance measurements in dilute electrolytes [155]. Iwami et al. determined E_{pzc} of

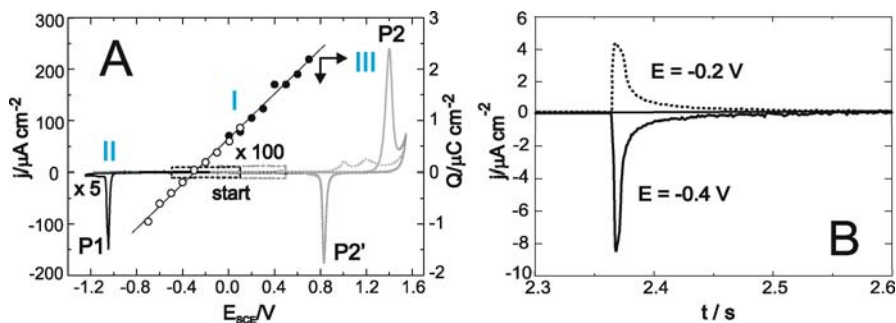


Fig. 20 **A** Typical single scan current vs. potential curves for the reductive desorption (black traces, region labeled II) and for the oxidative desorption (gray traces, region labeled III) of a monolayer of BP4 assembled on Au(111)-(1 × 1) in 0.1 M NaOH and 0.1 M HClO₄, respectively. Scan rate 10 mV s⁻¹. Contact with the electrolyte was always established under strict potential control in hanging meniscus configuration at $E = 0.00$ V. The dashed black and gray curves represent voltammograms in the double layer region as recorded after immersion and stabilization either in alkaline or in acidic electrolyte. The dotted gray trace in potential region III illustrates the second anodic scan measured after the first oxidative desorption trace. The open and filled circles symbolize the charges derived from immersion experiments in 0.1 M NaOH (○) and 0.1 M HClO₄ (●) at various potentials. The solid line was obtained from a linear regression analysis (see text for further details). **B** Typical immersion i - t traces as recorded in 0.1 M NaOH for a freshly prepared and dry BP4 monolayer on Au(111)-(1 × 1) at $E = -0.40$ V (solid line) and $E = -0.20$ V (dotted line) [145]

alkanethiol-modified Au(111) single crystal electrodes applying the sessile drop method [158]. These authors reported values of E_{pzc} ranging between -0.34 V and -0.56 V (vs. SCE). We may conclude that there is reasonable agreement between the estimated values of E_{pzc} for the thiol-based monolayers without polar head groups.

Reductive Desorption

The stability of the BP4 adlayer at negative potentials is limited by the so-called “reductive desorption”. The first potential scan (in 0.1 M NaOH) with a rate of 10 mV s⁻¹ leads to a sharp, slightly asymmetric cathodic current peak at -1.053 V (FWHM ~ 0.024 V, Fig. 20A). Decreasing the scan rate shifts the peak potential to more positive values. The pronounced peak was only observed during the first potential scan with a freshly prepared sample, and exhibits no anodic counterpart. Subsequent multiple cycling of the electrode potential in -1.20 V $< E \leq -0.20$ V did not reveal any reductive desorption features. The organic monolayer is entirely removed and does not re-adsorb. Similar observations were reported previously for alkanethiols of moderate chain lengths on gold electrodes [156–158]. Current integration yields a charge $q_{BP,red} = (73 \pm 5)$ μC cm⁻². This reductive desorption charge

was corrected by fitting to the baseline before and after the reduction peak in $E_{P1} - 0.10 \text{ V} < E < E_{P1} + 0.10 \text{ V}$, or by subtracting the current of the corresponding second potential scan.

Referring to the coverage of BP4, $\Gamma_{\text{ex}} = (5.9\text{--}6.3) \cdot 10^{-10} \text{ mol cm}^{-2}$ as estimated from STM studies and assuming the commonly accepted one-step one-electron process [116, 156]



to be valid, a charge of 57 to 61 $\mu\text{C cm}^{-2}$ is predicted. This value is smaller than $q_{\text{BP,red}} = (73 \pm 5) \mu\text{C cm}^{-2}$, the charge obtained by integration of the prominent desorption peak, which indicates a substantial double layer contribution of $(14 \pm 5) \mu\text{C cm}^{-2}$ to the total charge balance. The latter could be estimated roughly by referring to the shift in E_{pzc} due to BP4 adsorption from 0.24 V [159] to -0.30 V , which leads to $dq \approx 15 \mu\text{C cm}^{-2}$, a value close to the one observed in our experiment.

The potential of reductive desorption shifts with increasing length of the alkylspacer ($n = 1\text{--}6$) toward more negative values and shows a characteristic odd-even fine structure (Fig. 21A).

The time dependence of reductive desorption was explored by single potential step experiments (from E_i to E_f). Selected transients (dotted lines) for freshly prepared BP3 monolayers on Au(111)-(1 × 1)/0.1 M NaOH are displayed in Fig. 21B. The traces are characterized by an initial exponential decay ($t < 5 \text{ ms}$, $q < 5 \mu\text{C cm}^{-2}$), followed by a well-developed maximum, i_{max} at t_{max} , which increases and shifts towards shorter times with more nega-

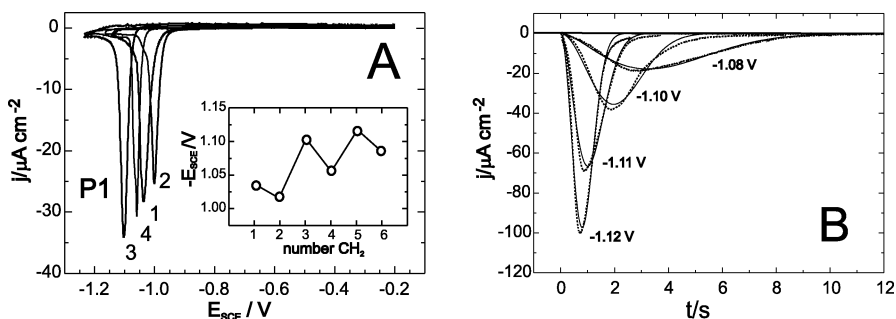


Fig. 21 **A** Single voltammetric scans of the reductive desorption for BP1 to BP4 monolayers on Au(111)-(1 × 1) in 0.1 M NaOH after immersion at 0.00 V, scan rate 10 mV s^{-1} (only traces at $E < -0.20 \text{ V}$ are shown). The insets illustrate the chain length dependence of the potentials of reductive desorption for the investigated organic adlayers. **B** Experimental i - t traces (dotted lines) of the reductive desorption recorded for freshly prepared monolayers of BP3 (**A**) after immersion at 0.0 V, stabilization, and subsequently stepping the potential from $E_i = -0.90 \text{ V}$ (waiting time $t_{\text{wait}} = 30 \text{ s}$) to various final potential E_f , which are indicated in the figure. The solid curves represent the numerical fits calculated according to the models represented by Eq. 3 [145]

tive final potentials E_f . The current decays to zero if E_f is chosen sufficiently far from the onset of hydrogen evolution. No significant dependence on the choice of E_i (in $-0.90 \text{ V} \leq E_i \leq -0.40 \text{ V}$) and on the waiting time at E_i was found for ordered and annealed BP3 adlayers. The initial part of the transient is attributed to the double layer charging of the thiol-coated electrode. The major segment is assigned to the reductive desorption of the organic monolayer. The main cathodic current has two contributions, which are not separated, the Faraday current due to thiol reduction and the capacitive current due to the formation of the double layer of the uncoated gold electrode. The integrated charges of the current–time transients are in good agreement to those obtained from single sweep voltammetry. Maxima in the desorption transients of self-assembled thiol adlayers and anodic sulfide films have been attributed to a hole nucleation and growth process [160–162] or to an irreversible desorption based on a Frumkin-type isotherm assuming attractive lateral interaction forces [163]. The latter model requires a homogeneous distribution of equal sites, which is not supported by our STM investigations [146]. Wano et al. [164] demonstrated for a self-assembled monolayer of hexanethiol on Au(111) in 0.01 M KOH, based on in-situ STM measurements, that the reductive desorption starts from defects of the adlayer such as domain boundaries or missing rows and edges of vacancy islands, and proceeds by a hole nucleation and growth process with the desorbed thiolate molecules diffusing toward the bulk electrolyte. Morin et al. [160, 161] pointed out that the application of the hole nucleation and growth model implies that the reductive removal of the thiol monolayer is assumed to start by the diffusion of cations into the etching centers (“defect sites”), which expand via the reduction of chemisorbed thiols at their edges upon further exposure to solvent molecules and electrolyte counter ions.

In a first attempt to interpret the reductive adsorption transients of BP-based self-assembled monolayer’s, we analyzed the experimental data displayed in Fig. 21B with the diagnostic Avrami equation (Eq. 2), which is based on the Bewick–Fleischmann–Thirsk model of (hole) nucleation and growth [165, 166]

$$i(t) = k_1 t^{(k_3-1)} \exp(-k_2 t^{k_3}) , \quad (2)$$

with $k_1 = q_{\text{BP,red}} \times k_2 \times k_3$, k_2 being a coefficient which combines the rates of (hole) nucleation and growth; k_3 reflects the dimensionality and the nature of the nucleation process, and $q_{\text{BP,red}}$ corresponds to the total charge involved in the reductive desorption process. The model assumes cylinder-like hole nuclei with a height equal to the thickness of the monolayer, which grow at constant rate radially and parallel to the electrode surface. Non-linear regression analysis of Eq. 2 to the experimental reductive desorption transients for BP3 (Fig. 21B) results in Avrami exponents k_3 ranging between 2 and 3. Non-integer values of k_3 can be modeled by the exponential law of one-step

nucleation in combination with a linear growth law [166]

$$i = k'_1 \left(t - 1/k'_2 \left(1 - \exp(-k'_2 t) \right) \right) \exp \left(-k'_3 \left(t^2 - 2t/k'_2 + 2/k'_2{}^2 \left(1 - \exp(-k'_2 t) \right) \right) \right), \quad (3)$$

with $k'_1 = -2k'_3 \times q_{\text{BP,red}}$, k'_2 as the hole nucleation rate and k'_3 a constant related to the growth process.

The comparison of the experimental data for BP3 (dotted trace in Fig. 21B) and the results of the non-linear regression fit of Eq. 3 (solid lines in Fig. 21B) show excellent agreement [145]. Additional confidence for the validity of the model expressed by Eq. 3 is given by the charge balance $q_{\text{BP,red}}$ as derived from chronoamperometric and voltammetric experiments. The values of $q_{\text{BP,red}}$ estimated with both techniques are nearly identical. We further notice that the nucleation rate k'_2 as investigated for final potentials E_f in $-1.12 \text{ V} \leq E_f \leq -1.08 \text{ V}$ shows no significant potential dependence while the growth parameter k'_3 increases significantly with more negative final potentials E_f . This result indicates that pre-existing defects within the one-component BP3 adlayer (“etching centers”) act as primary hole nucleation centers. Similar trends could be observed with BP5. More complex hole nucleation and growth transients were found for the dissolution of the BP4 and BP6 adlayer, which is caused by the coexistence of two or more structures [145].

Oxidative Desorption

The stability limit of the BP4 monolayer on Au(111)-(1 × 1) at positive potentials was investigated in 0.1 M HClO₄. The first cycle revealed a constant capacitive charging current up to 1.20 V, implying the blocking of the onset of gold surface oxidation (Fig. 20A). The inhibition effect of the aromatic BP4 adlayer is much stronger than previously reported for aliphatic thiols in acidic solution [167]. At $E > 1.20 \text{ V}$ a broad anodic peak P2 with a maximum at 1.40 V develops (FWHM $\sim 70 \text{ mV}$, scan rate 10 mV s^{-1}). The latter is followed by an additional increase in current, which might be related to the formation of a complex gold oxide film [168]. The charge corresponding to P2 as derived from three independent measurements amounts to $q_{\text{ox}} = (2050 \pm 80) \mu\text{C cm}^{-2}$. This value accounts for contributions from the oxidative adsorption of the BP4 adlayer as well as from gold oxidation. Reversing the direction of the potential scan gives rise to a cathodic peak P2' at 0.832 V with $a_{\text{re}} = (740 \pm 30) \mu\text{C cm}^{-2}$. The latter is only slightly higher, 10 to 15%, than typical charges of the reduction of the gold surface oxide for a well-prepared Au(111)-(1 × 1) electrode in 0.1 M HClO₄ [169]. The second potential scan (dotted gray line in Fig. 20A) leads to the voltammeter profile of a bare Au(111) electrode having a low density of surface defects with typical charges for surface oxidation and reduction [168]. We may conclude that the BP4 adlayer is completely desorbed during the first oxidation scan,

and no significant amount of BP4 or reaction products could re-adsorb. In consequence, the upper limit of the charge attributed to the oxidative desorption of BP4 is estimated as $q_{\text{BP,ox}} = q_{\text{ox}} - q_{\text{re}} \sim (1310 \pm 80) \mu\text{C cm}^{-2}$. Similar data were obtained for all BPn's. The oxidative desorption of these molecules involves a complex electrooxidation process. FTIR measurements in 0.1 M KOH [170] and 0.1 M HClO₄ [171] suggested the breaking of the C–S bond, oxidation of the sulfur to (H)SO₄⁽²⁾⁻ and the formation of RCOO⁻ respectively further oxidation to CO₂ are suggested. The multi-step reaction mechanism involves up to 18 electrons [157]. However, its detailed nature is not yet understood [145].

4.4

Electrical Properties of BPn Adlayers – An STS Study

Distance Tunneling Characteristics

The electronic characteristics of the BPn self-assembled monolayers were studied by measuring current–distance and current–voltage characteristics in 1,3,5-trimethylbenzene (TMB) employing a gold STM-tip/BPn/Au(111)-(1 × 1) configuration. Immediately after measuring a STS spectrum high-resolution STM images were recorded to ensure the structural integrity of the SAMs underneath the tip.

Figure 22 shows typical current–distance curves in a semilogarithmic representation recorded in $10 \text{ pA} \leq i_{\text{T}} \leq 20 \mu\text{A}$ for BP3. The shapes of the curves for the other BPn's are rather similar. The data plotted in Fig. 22 represent the average of 50 approaching traces. For illustration, selected individual curves of the low current range, $10 \text{ pA} < i_{\text{T}} \leq 100 \text{ nA}$, are shown as inset Fig. 22A. The tunneling current i_{T} increases with decreasing distance between the Au tip and the Au(111)-(1 × 1) surface. The entire plot $\log i_{\text{T}}$ vs. Δz is not linear. However, three linear regions labeled I, II and III could be identified for BP3 (BP4 data are given in brackets): I – $i_{\text{T}} < 100 \text{ pA}$ ($i_{\text{T}} < 100 \text{ pA}$); II – $200 \text{ pA} \leq i_{\text{T}} < 200 \text{ nA}$ ($200 \text{ pA} \leq i_{\text{T}} < 5 \mu\text{A}$); III – $i_{\text{T}} > 600 \text{ nA}$ ($i_{\text{T}} > 5 \mu\text{A}$). We notice that individual $i_{\text{T}}-\Delta z$ approaching curves exhibit small but characteristic current steps at $i_{\text{T}} \geq 5 \mu\text{A}$, which are accompanied by the evolution of current plateaus with values ranging between 10 to 20 μA for $E_{\text{bias}} = -0.200 \text{ V}$ (the dotted blue lines in Fig. 22). The occurrence of these steps is not exactly reproducible. STM images recorded immediately after one $i_{\text{T}}-\Delta z$ trace in the high current range demonstrate the formation of isolated monatomic gold islands with a diameter of 1–2 nm (Fig. 22B). Considering a bias voltage of -0.200 V one would expect a current of 15.6 μA for a single Au–Au atom conductance channel [172]. The experimental data are rather close to this value. Therefore, we attribute the observations at $i_{\text{T}} > 5 \mu\text{A}$ to the formation of single Au–Au nanocontacts. Defining this point of jump-to-contact as zero distance between the tip and the substrate surface, an absolute distance

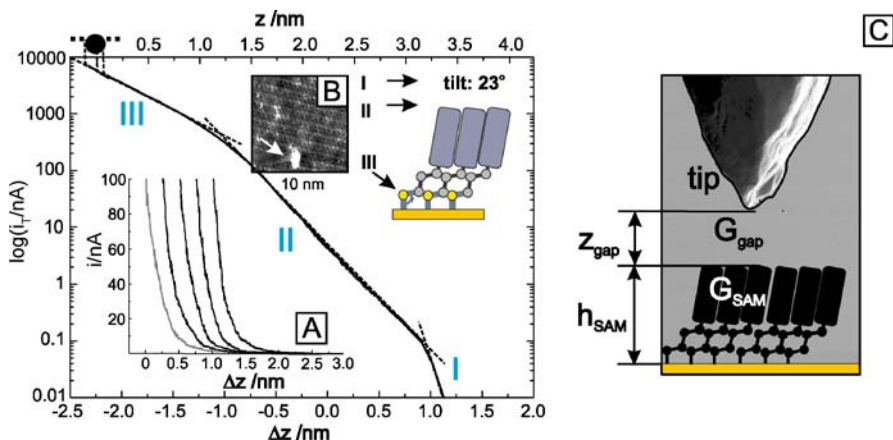


Fig. 22 Current–distance curve for the $(\sqrt{3} \times 2\sqrt{3})$ adlayer of BP3 on Au(111)-(1 × 1) in a semi-logarithmic representation. The whole plot is obtained by superposition of two sets of i_T – Δz measurements carried out in the ranges $10 \text{ pA} \leq i_T \leq 100 \text{ nA}$ (dashed blue line) and $3 \text{ nA} \leq i_T \leq 20 \text{ }\mu\text{A}$ (dotted blue line). The blue arrows indicate the overlapping region. The relative distance scale Δz was chosen by defining $\Delta z = 0$ at $i_T = 3 \text{ nA}$ and $E_{\text{bias}} = -0.200 \text{ V}$. Fifty individual approaching curves were averaged. The position of quantum point contact is marked by the black point. The insert **A** shows, as examples, selected individual curves measured in the low current range. The traces are shifted along the Δz axis for better display. The insert **B** represents an image of the $(\sqrt{3} \times 2\sqrt{3})$ BP3 adlayer recorded immediately after an individual i – Δz trace in the high current range leading to direct contact between the gold STM tip and the adsorbate-modified Au(111)-(1 × 1) surface. The white arrow marks the formation of a monatomically high gold island. **C** Two-layer tunneling junction model. The STM tunnel junction is composed of two distinct layers: the solution (TMB) gap and the BP adlayer [146]

scale is introduced (top z -axis in Fig. 22). The uncertainty of this calibration is estimated to be less than 0.5 nm.

In an attempt to quantify the recorded current–distance characteristics we adapt a two-layer model for coherent non-resonant electron tunneling, originally proposed by Bumm et al. [173] (Fig. 22C). The assumption of a non-resonant mechanism is supported by the generally accepted values of the energy differences between the HOMO and the LUMO orbitals, which are $\sim 5 \text{ eV}$ for the phenyl ring and $\sim 7 \text{ eV}$ for the aliphatic alkyl chain [122]. The STM junction is assumed to be composed of two distinct layers – the solution (TMB) gap and the SAM. Each layer is characterized by a transconductance G , such as

$$G_{\text{gap}} = A \exp(-\alpha_D z_{\text{gap}}), \quad (4)$$

and

$$G_{\text{SAM}} = B \exp(-\beta_D h_{\text{SAM}}), \quad (5)$$

where α_D and β_D are decay constants, z_{gap} and h_{SAM} are the layer thicknesses, and the prefactors A and B are the respective contact conductances. The film thickness h_{SAM} is an intrinsic property. Based on STM (see above) and spectroscopic studies [174], h_{SAM} is estimated as 1.70 nm for BP3 and 1.65 nm for BP4. The solution gap thickness is controlled by the position of the STM tip. Because the transconductance is an electron tunneling probability one obtains for the two-layer junction

$$G = G_{\text{gap}}G_{\text{SAM}} = AB \exp(-\alpha_D z_{\text{gap}} - \beta h_{\text{SAM}}) . \quad (6)$$

Equation 6 is approximated by introducing the absolute tip distance z and an effective decay constant κ_{eff}

$$G = AB \exp(-\kappa_{\text{eff}}z) , \quad (7)$$

where z represents the absolute distance. Equation 4 reduces to h_{SAM} if $z_{\text{gap}} = 0$. For $z > h_{\text{SAM}}$, the measured tunneling current depends on $(-\alpha z_{\text{gap}} - \beta h_{\text{SAM}})$ with a dominant contribution of $(-\alpha z_{\text{gap}})$ at high tunneling resistances.

The analysis of the experimental data plotted in Fig. 22A leads for $i_T < 100$ pA (region I) to $(10.4 \pm 0.8) \text{ nm}^{-1}$ as decay constants κ_{eff} for BP3. We obtain, based on the Wentzel-Kramer-Brillouin approximation and assuming a rectangular tunneling barrier between two identical electrodes [175], an effective barrier height of $(1.05 \pm 0.15) \text{ eV}$. Referring to the absolute distance scale z and comparison with the film thickness h_{SAM} indicate a weakly interacting STM tip positioned well above the organic adlayer. The effective decay constant κ_{eff} of the bare Au-tip/TMB/Au(111)-(1 × 1) junction was obtained to $(10 \pm 1) \text{ nm}^{-1}$. This value is slightly higher compared to the BPn modified substrate surface indicating that the tunneling in region I is dominated by the solution gap.

The values of κ_{eff} , as derived from the linear region II of the $\log i_T$ vs. Δz plots, amount to $(4.6 \pm 0.7) \text{ nm}^{-1}$. The value of the corresponding barrier height ϕ_{eff} is $(0.19 \pm 0.06) \text{ eV}$. The lower values of κ_{eff} and ϕ_{eff} in region II, as compared to I, indicate a higher transconductance of the Au-tip/BPn/Au(111)-(1 × 1) junctions. Referring to the absolute distance scale z (top axis in Fig. 22) and to the heights of the BP3 SAM, we conclude on a strong electronic coupling between tip and sample, even before establishing physical contact. In comparison to experiments carried out under UHV conditions, we did not observe a *sudden* change in slope of the $\log i_T$ vs. Δz characteristics upon formation of a contact between the STM and the SAM [128, 176]. The surrounding aromatic solvent is proposed to act as a mediator at short distances. The STM tip moves from its initial z position at $\Delta z = 0$ (region I) toward the substrate surface at a fixed bias until it penetrates into the organic adlayer. Under those conditions z_{gap} approaches zero and the transconductance G is dominated by the contribution of G_{SAM} . The value of κ_{eff} for BP3 in region II is within the range $4 \text{ nm}^{-1} \leq \kappa_{\text{eff}} \leq 7 \text{ nm}^{-1}$.

This range is rather typical for non-resonant electron tunneling through π -bonded molecules [121], as documented in STM and CP-AFM studies under UHV and under ambient conditions [177–180], by electron transport experiments employing Hg/SAM/Ag junctions [181] and adlayer-confined redox couples [182].

An additional decrease of the effective decay parameter κ_{eff} and of the corresponding barrier height is observed in the high current range (region III), just prior to the formation of Au–Au nanocontacts. We speculate that these findings are related to increasing contact forces causing the mechanical compression and/or distortion of the BPn adlayer, which might lead to the local destruction of the SAM [183, 184]. Higher compression forces may also cause a significant decrease of the barrier for direct (through space) tip–sample tunneling, which opens an additional electron transport channel [185].

Region III is more pronounced developed for the slightly thicker and more densely packed (25%) BP3 adlayer, as compared to BP4. The tilt angle of the biphenyl moiety, as referred to the surface normal, is significantly smaller for the former. This is also reflected in the observation that, in constant current mode and at a fixed bias potential, the absolute tip–substrate distance z appears to be slightly larger in the presence of BP3. Similar trends were also observed for the other BPn molecules ($n = 2$ –6).

Current–Bias Voltage Characteristics

The just-described distance-tunneling characteristics were complemented by current–bias voltage experiments employing long-range ordered BPn adlayers. Typical data for BP3 are plotted in Fig. 23.

Two distinct starting conditions were chosen: (i) The Au tip was positioned above the organic monolayer ensuring weak interactions (region I with $i_T = 60$ pA) and $E_{\text{bias}} = -0.200$ V, cf. curve 1 in Fig. 23). (ii) The Au tip was placed immediately in contact or penetrating into the BPn adlayer, which leads to a strong electronic coupling (region II with $i_T = 3$ nA or larger and $E_{\text{bias}} = -0.200$ V, cf. curves 2–4 in Fig. 23).

The i_T – E_{bias} curves are almost symmetric and linear at low bias voltages (Fig. 23A). The estimated tunneling resistance of the Au-tip/BPn/Au(111)-(1 × 1) junction follows the same trend as discussed in the analysis of the distance tunneling characteristics. The current increases exponentially at higher bias voltages. The experimental data can be qualitatively represented by the Simmons tunneling model [187] in $-0.500 \text{ V} \leq E_{\text{bias}} \leq 0.500 \text{ V}$.

For i_T – E_{bias} traces recorded with a setpoint in region II ($i_T = 3$ nA and $E_{\text{bias}} = -0.200$ V) one estimates values of z and ϕ_{eff} ranging between 1.5 to 2.5 nm and 0.4 to 0.8 eV for BP3. The values for ϕ_{eff} are somewhat higher than those extracted from i_T – Δz characteristics.

Systematic deviations occur at higher bias voltages. All i_T – E_{bias} traces exhibit a distinct asymmetry. The origin of the asymmetry can be attributed to

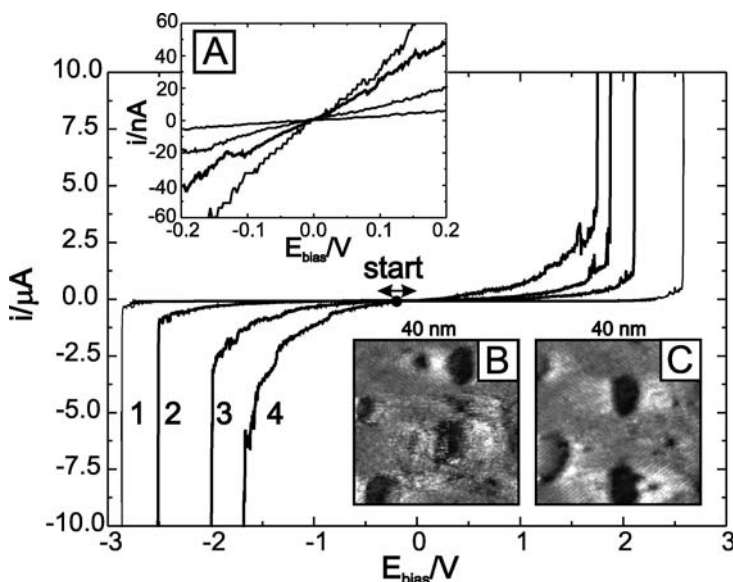


Fig. 23 Current–voltage curves of the $(\sqrt{3} \times 2\sqrt{3})$ adlayer of BP3 on Au(111)-(1 \times 1) in TMB recorded at various vertical positions of the Au STM tip. Each *curve* plotted represents the average of more than 20 individual traces. The *curves* are composed of a negative and of a positive bias voltage scan (scan rate 2 V s^{-1}), which started always after equilibration of the junction at $E_{\text{bias}} = -0.200 \text{ V}$ and at a present tunneling current i_{T0} : (1) – tip positioned outside the BP3 adlayer with $i_{T0} = 60 \text{ pA}$ (this curve, shown as a *dashed line*, was recorded with a custom-made preamplifier [186]). (2)–(4) – tip positioned in contact or penetrating into the adlayer with $i_{T0} = 3 \text{ nA}$, and subsequently moving the tip closer towards the adlayer by 0 nm (2), 0.3 nm (3) and 0.6 nm (4) before the voltage scan was activated. We refer to the top axis of the current–distance characteristics shown in Fig. 22 for a calibration of the absolute tip position. The *inset A* illustrates a magnification of the linear region of the $i_{T}-E_{\text{bias}}$ curves. The panels **B** and **C** show images of the BP3 adlayer recorded immediately after a bias potential excursion close to the negative or to the positive break down potentials, respectively. The initial setpoint was $i_{T0} = 3 \text{ nA}$ [146]

the intrinsic asymmetry of the BPn molecules as well as to an unequal coupling in the STM junction (weak coupling between the STM tip and BPn; strong coupling between Au(111) and BPn due to chemisorption) [188].

The discontinuous decrease (increase) of the tunneling current at large negative (positive) bias potentials corresponds to the dielectric breakdown of the BPn adlayers [128, 183, 184, 189]. We have imaged the respective SAM's before, during (the x - y scan was briefly interrupted for the acquisition of the spectroscopic trace) and immediately after the $i_{T}-E_{\text{bias}}$ measurements in order to explore the mechanism of this process (cf. inserts in Fig. 23). The topographic studies were carried out in constant current mode choosing a setpoint current of 60 pA, e.g. the Au tip is positioned above the BPn SAM. Satisfactory images could still be recorded up to 5 nA. However, stronger tip–

sample interactions due to tip penetration into the organic monolayer caused a significant increase of the noise level.

The combined STM and STS measurements revealed no changes of the BPN adlayer structures if the bias potential sweep was restricted to values 0.500 V below (above) the critical break down potentials (BDP). Excursion to higher values leads to streaky images and irreversible changes of the adlayer. Upon reaching the positive or negative BDP one observes locally, e.g. within the adlayer region polarized by the near field of the STM tip, dark depressions and occasionally small monatomic high gold islands (inserts in Fig. 23). These features point to a mechanism of field-induced dissociation and desorption [128]. The absolute values $|E_{\text{bias}}|$ of the negative BDP are higher than the corresponding positive ones, which reflects the asymmetry of the STM junction. Decreasing the tip-sample distance leads to a systematic decrease of the absolute values of the negative and of the positive BDP. This trend is rationalized by the local perturbation of the 2D long-range order of the adlayer upon tip penetration. Based on the experimentally accessible breakdown potentials and the absolute tip-sample distance, which is obtained from $i_{\text{T}}-\Delta z(z)$ experiments (Fig. 22), we estimated the electric field strength of the dielectric break down: rather independent of the initial tip position (region I or region II with $i_{\text{T}} \leq 5$ nA) we obtained $-(0.95 \pm 0.05) \times 10^9$ V m⁻¹ and $(0.85 \pm 0.05) \times 10^9$ V m⁻¹ for the negative and the positive branch of the $i_{\text{T}}-E_{\text{bias}}$ plot of BP3, respectively. This interpretation is supported by a comparison with aliphatic alkanethiols. A critical threshold electric field strength of $\sim 2 \times 10^9$ V m⁻¹ was reported based on different experimental approaches, such as STM [128], CP-AFM [184] and Hg/SAM/Ag-junctions [189]. The values for the electrically insulating aliphatic molecules are higher than those estimated with aromatic biphenyls in the present case.

5

Charge Transport in Single Au/Molecule/Au Junctions at Electrified Solid-Liquid Interfaces

5.1

Introduction

The ability to measure and to control charge transport across nanometer-scale metal-molecule-metal junctions represents a key step toward the realization of molecular-based electronics [190–192]. Various experimental approaches have been employed to study molecular junctions in two- and three-terminal configurations. These include scanning probe microscopies (STM, STS, CP-AFM) [193–208], crossed-wire junctions [209], mechanical [210–215] and electromigration [216, 217] break junctions, nanopores [218] and mercury drop electrodes [219]. Approaches in condensed media, and in par-

ticular in an electrochemical environment, offer unique opportunities to *measure* and to *control* charge transport across single molecule junctions. The measured current represents both, the electrical contact to the external circuit and the functional state of the tailored molecule.

Employing in-situ STM or a planar nanogap electrode configuration and the concept of “*electrolyte gating*” [207, 219–224], several groups demonstrated in pioneering studies transistor- and diode-like functions with high current amplification and rectification ratios [225–234]. These examples include porphyrines [207, 235], viologen-type molecular wires [228, 231, 236, 237], aniline and thiophen oligomers [225–227, 238, 239], metal transition complexes [230, 240, 241], carotenes [242], nitro-derivatives of oligophenylene ethynylene [243, 244] and ferrocene [245, 246], perylene tetracarboxylic diimide [232–234] and the redox protein azurin [229, 247–249]. Most of these studies refer to Au (or Pt)/molecule/Au junctions constructed in a vertical STM configuration or a planar assembly of molecular-size nanoelectrodes in aqueous electrolyte and at ambient conditions [191, 192, 225–227]. Albrecht et al. [241] introduced ionic liquids. First studies with substituted aliphatic α,ω -alkane derivatives by Leary [250] and Chen et al. [251], and aromatic 1,4-diaminobenzene-type molecular wires by Venkataraman et al. [252] at solid-liquid interfaces illustrate the potential of chemical control, e.g. the effect of electron-donating respective -withdrawing substituents or variable anchoring groups on the conductance signatures of single molecular junctions.

Kuznetsov and Ulstrup initialized recently a discussion on the importance of conformational dynamics and electrical double layer effects on charge transport characteristics in single metal/redox-molecule/metal tunneling junctions [237, 253]. Tao et al. explored the stability and break down of Au-thiol contacts, and addressed quantitatively local ionic and electron heating in single junctions composed of redox-inactive molecules [254].

The electronic levels of (single) redox-species in electrochemical metal/molecule/metal tunneling junctions are strongly coupled to the nuclear environmental motion, extending to both local molecular modes and to the liquid (or solid) electrolyte environment [248, 253, 255]. The following scenarios of interfacial electron transfer in a nanoscale electrochemical metal/redox molecule/metal configuration have been proposed [248, 253, 255]:

1. *superexchange via off-resonance levels*,
2. *resonance tunneling* [256–258],
3. *non-coherent two-step electron transfer* with complete vibration relaxation [259, 260] or
4. *two-step electron transfer with partial vibration relaxation* [255, 261–263].

Schmickler [264] and Nitzan [265] considered explicitly structural fluctuations and the role of water molecules in the gap. A recent stochastic model of Schmickler and Kuznetsov [266] treats fluctuations of the redox level in the tunneling gap explicitly.

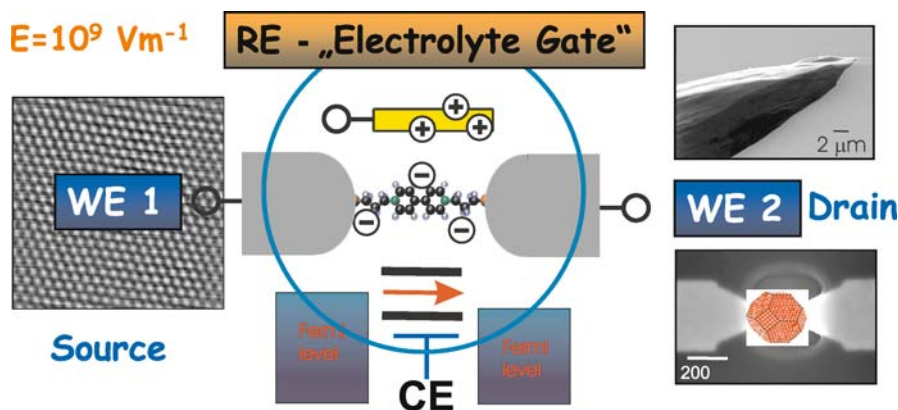


Fig. 24 Principle of “electrolyte gating”. Tuning of the Fermi levels of WE 1 and WE 2 relative to the molecular levels enables measuring of current–voltage (i – E) characteristics i vs. $(E_{WE1} - E_{WE2})$ at fixed E_{WE1} or E_{WE2} , i vs. E_{WE1} or E_{WE2} at fixed bias $(E_{WE1} - E_{WE2})$ as well as barrier height profiles i vs. distance of tailored molecular junctions in a vertical SPM – configuration respective horizontal nanoelectrode assemblies

Experimentally accessible relations of (i) the source–drain current (between the two working electrodes) and the (source–drain) bias at fixed potential of one working electrode (or gate voltage with respect to the reference electrode) and of (ii) the source–drain current and the potential of one working electrode at fixed bias provide diagnostic criteria to distinguish between different mechanisms of charge transport and switching [248, 253, 255]. Important experimental observables are, in principle, also accessible from temperature-dependent studies [191, 267, 268]. However, the application of this approach to single molecule experimental studies at electrified solid|liquid interfaces is rather unexplored at present.

In the following two paragraphs we present first a STM method to create and to measure charge transport characteristics in metal–molecule–metal junctions. The approach will be illustrated based on a case study with α,ω -alkanedithiols attached to gold contacts [208]. Then we will discuss redox-active junctions in an electrochemical environment with viologen-type molecules bound either to one (asymmetric configuration) or to both (symmetrical configuration) adjacent electrodes [231, 236, 269].

5.2

Charge Transport in Single Au/Alkanedithiol/Au Junctions—An STM Approach

Charge transport in Au|alkanedithiol|Au junctions was measured with a variety of techniques. These include mechanically controlled break junctions (MCBJ) [213], STM [205, 208, 270–275] and conducting AFM break

junctions [202, 203, 276] as well as STM-controlled point contact measurements [228, 277]. The latter group of methods is particularly attractive because the technique is applicable to different environments, such as gas and solution phases as well as UHV conditions. Approaches differ in the following criteria: (i) formation of reproducible contacts between a molecule and two probing electrodes, (ii) access to “signatures” of single molecules, (iii) details of the statistical data analysis.

In order to improve the experimental reproducibility, Xu and Tao [205] have begun to analyze the statistical properties of conductance traces, which show the conductance over a control parameter, measuring the electrode separation. Such current–distance traces were obtained from the repeated formation and breaking of a large number of individual molecular junctions formed between a gold STM tip and a gold substrate in a solution containing molecules [205]. The procedure was adopted and modified by several other groups [228, 231, 270–274]. The statistical interpretation of the individual conductance–distance traces is mostly based on the analysis of conductance plateaus [205, 213, 228, 231, 272, 274] that leads to the construction of conductance histograms. Alternative approaches involve the logarithmic analysis of entire transients [213, 270, 278] or the rapid conductance drop in the last step [271].

Figure 25 shows a schematic representation of the STM-based contact junctions approach as developed in our group [208]. Single junction conductance data were obtained from current–distance traces employing either

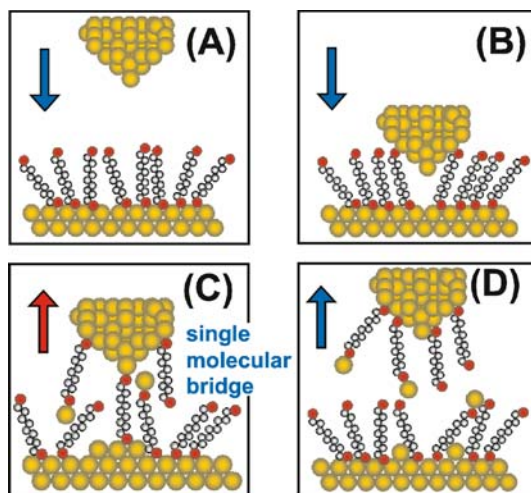


Fig. 25 Schematic representation of the STM-type “contact junction” approach applied in the present study. **A** Approach, **B** formation of molecular contacts, **C** pulling and **D** breaking [208]

a single channel preamplifier (0.1, 1.0 or 10 nA/V) or a dual multi-channel preamplifier stage capable of recording currents in $1 \text{ pA} \leq i_T \leq 210 \text{ }\mu\text{A}$ simultaneously [186]. The following sequence was applied (Fig. 25): A sharp gold STM tip, with imaging capability at atomic resolution, was brought to a preset tunneling position, typically defined by $i_T = 50$ or 100 pA and E_{bias} ranging between ± 0.010 and $\pm 0.300 \text{ V}$ (Fig. 25A). Subsequently, the STM feedback was switched off, and the tip approaches the adsorbate-modified substrate surface at constant x - y position (Fig. 25B). The approach was stopped before reaching point contact with the gold surface (“gently touching”) by choosing an upper threshold current of $0.2G_0E_{\text{bias}}$ ($G_0 = 77 \text{ }\mu\text{S}$). These settings still ensure rather strong interactions between the gold tip and the α,ω -alkanedithiol adlayer. After a dwelling time of 100 ms, sufficient to create molecular junctions between tip and substrate, the tip was retracted at a rate of $5\text{--}10 \text{ nm s}^{-1}$ until a lower threshold position was reached. The entire cycle is typically repeated more than 1,000 times.

The retraction or pulling curves were recorded with high resolution in $1 \text{ pA} < i_T < 100 \text{ nA}$. We observed three types of transient curves [208]. Type I curves are exponential and represent direct electron tunneling between the gold tip and the substrate without molecular junctions being formed. The percentage of these decay curves was 50% when performing the experiment in 1,3,5-trimethylbenzene (TMB) containing 0.1 mM alkanedithiol. Type II curves are non-monotonic and noisy, which could be attributed to mechanical instabilities. The percentage of these curves was around 10%. Traces of type I and II were rejected in the further analysis of the experimental data. The remaining type III conductance traces are monotonic and non-exponential. Figure 26 illustrates typical examples for 0.1 mM nonanedithiol (ND) in TMB. These curves exhibit single plateaus or series of plateaus with a typical length of $0.04\text{--}0.15 \text{ nm}$, which are separated by abrupt steps of 50 up to 3 nA. The current steps are assigned to the breaking of individual respective multi-molecular ND junctions previously formed between the gold STM tip and the substrate surface. The percentage of type III conductance traces varied between 40 and 10%. Similar observations were reported previously by Li et al. [275]. Control experiments in pure TMB displayed almost exclusively (98%) exponentially decaying traces. No evidence of current steps resembling type III traces was found.

The statistical analysis of the plateau currents of type III conductance traces was carried out by constructing histograms. These histograms showed characteristic current peaks. Their analysis allows identification of three different sequences of equally spaced maxima. They are attributed to low, L, medium, M, and high, H, conductance junctions. The current within each series scales *approximately* linearly with the number of peaks. The first peak of each sequence is attributed to a single molecular junction. The corresponding currents depend also linearly on the applied bias voltage, at least up to $\pm 0.200 \text{ V}$ (cf. insets in Fig. 27A,B). These correlations lead to the following

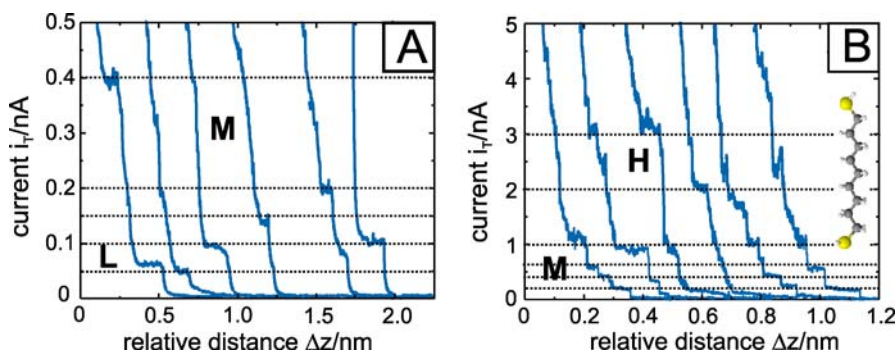


Fig. 26 **A** Current–distance retraction curves recorded with a gold STM tip (low current channel with a preamplifier limit of 1 nA) for 0.1 mM 1,9-nonanedithiol in 1,3,5-trimethylbenzene on Au(111)-(1 × 1), at $E_{\text{bias}} = 0.10$ V. The setpoint current before disabling the feedback was chosen at $i_{T0} = 100$ pA. The pulling rate was 4 nm s^{-1} . **B** Same conditions as in **A**, except that the preamplifier limit was chosen at 10 nA. The dotted lines represent characteristic regions of the low, mid and high currents

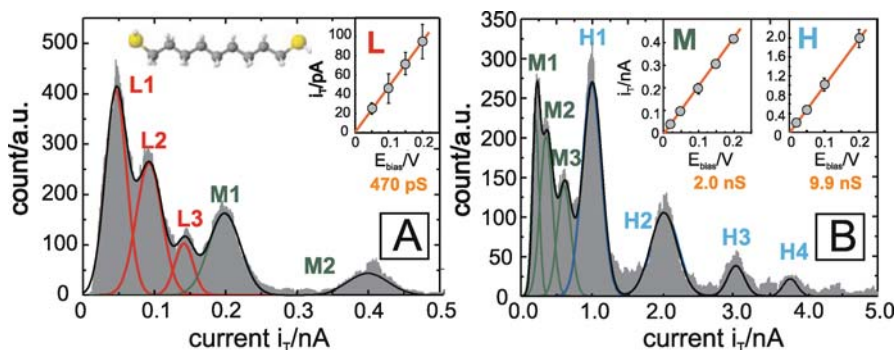


Fig. 27 Conductance histograms constructed from values of the plateaus of type III “stretching” curves for Au/1,9-nonanedithiol/Au junctions. **A** 1,600 out of 4,300 traces employing a 1 nA (max) preamplifier; **B** 1,100 out of 4,300 traces recorded with the 10 nA (max) preamplifier. All other conditions are identical to those in Fig. 26. We notice that the low conductance sequence could only be resolved with the high sensitive preamplifier. The insets in **A** and **B** show that the current within each series scales approximately linearly with the number of peaks [208]

conductance values of the three specific single molecule Au/ND/Au junctions: $(0.47 \pm 0.03) \text{ nS}$ (L), $(2.0 \pm 0.2) \text{ nS}$ (M) and $(9.9 \pm 0.9) \text{ nS}$ (H).

Following the same experimental protocol one also obtains multi-peak conductance histograms for 1,5-pentanedithiol (PD), 1,6-hexanedithiol (HD), 1,8-octanedithiol (OD) and 1,10-decanedithiol (DD) in TMB.

Figure 28 shows the semi-logarithmic plot of the conductance versus molecular length. The latter is expressed as the number of CH_2 -units. The

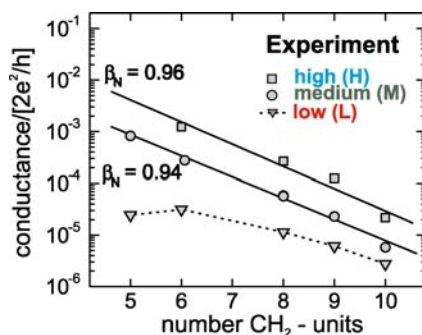


Fig. 28 Chain length dependence of the single junction Au-alkanedithiol-Au conductivity in a semilogarithmic representation. The three sets of conductance values – high (H), medium (M) and low (L) – are shown as *squares*, *circles* and *triangles*. The *straight lines* were obtained from a linear regression analysis with decay constants β_N defined per methylene unit (CH_2) [208]

H- and M-conductance values follow a simple tunneling model given by $G = G_c \exp(-\beta_N n)$ with decay constants β_N of (0.96 ± 0.15) and (0.94 ± 0.05) , respectively. These values of β_N are in agreement with literature data on the M- and/or H-conductances of single junctions Au|alkanedithiol|Au [205, 271, 275] as well as for the electron transfer through compact and aligned monolayers of alkanethiols using nanopores [279], mercury contacts [181, 280, 281], CP-AFM [184] or redox probes [282, 283]. The low conductance data give a rather poor linear correlation with a decay constant $\beta_N \sim (0.45 \pm 0.09)$, distinctly different from the H- and M-sequences. However, we notice that the estimated value β_N is rather close to that reported by Haiss et al. [277].

To provide insight into the multiple peak series observed experimentally, DFT-based calculations of alkanedithiols coupled to Au electrodes were carried out. Calculations were performed for different configurations of an “*extended molecule*” composed of an n -alkanedithiol of variable chain lengths ($n = 4-10$) bridged between two pyramids of $\sim 40-55$ Au atoms (Fig. 29). These clusters model the contact region of the gold electrodes. Molecular conformation and contact geometries have been varied. Examples are *gauche* and *trans* conformation of the alkyl chain with the sulfur atoms bridged to one or two gold atoms and/or combinations of them. Conductances have been calculated within the Landauer approach [208].

The comparison of the experimental data with the quantum chemical simulations leads to the following conclusions [208]: The mid conductance junctions M represent an all-*trans* conformation of the alkyl chains with the sulfur atoms bound in *atop* position to a single gold atom. All *trans* chains with sulfur atoms bound to two gold atoms in *bridge* position represent the high conductance junctions H, a factor four larger than the former. The low

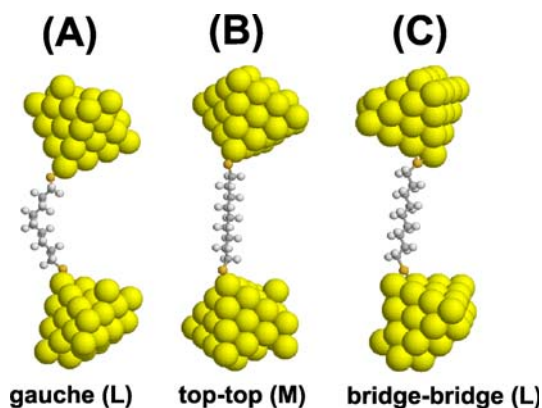


Fig. 29 Three typical arrangements of a single alkanedithiol molecule bridged between Au electrodes as used for the conductance calculations. **A** 1,9-Nonanedithiol (ND) with one gauche defect and both terminal sulfur atoms coordinated in atop position (low, L), **B** ND in all-trans conformation and atop–atop coordination (medium, M), **C** all-trans ND in a bridge–bridge coordination (high, H)

conductance junctions could be attributed to a sequence of gauche isomers with atop binding sites (cf. Fig. 29).

The agreement between experiment and theory is also reflected by the calculated chain length dependencies of the different junctions as well as the constructed histograms, which reproduce all essential features of the experiment well.

5.3

Electrolyte Gating in (Single) Molecule Junctions Containing Redox-Active Viologen Derivatives

The development of the methodology to measure single molecule electron transport in metal–molecule–metal configurations motivated applications in an electrochemical environment employing the concept of electrolyte gating [207, 219–223] (cf. Sect. 5.1). An applied gate voltage drops across the double layer at the electrolyte–source (drain) electrode interface, the electrolyte between the gate electrode and the source (drain) electrodes (WE 1, WE 2), as well as the reference electrode–electrolyte interface (the latter is constant). Since the current between the gate and the source (drain) electrode is negligible, the voltage drop in the electrolyte approaches zero. The effective gate–molecule distance is thus determined by the double layer thickness at the electrode–electrolyte interface, which is typically of the size of a few solvated ions. The electrolyte gating ensures a strong coupling due to low contact resistances, thin adjacent double layers (< 1 nm) and high mobility of the charge carriers (ions). The field in the electrochemical double

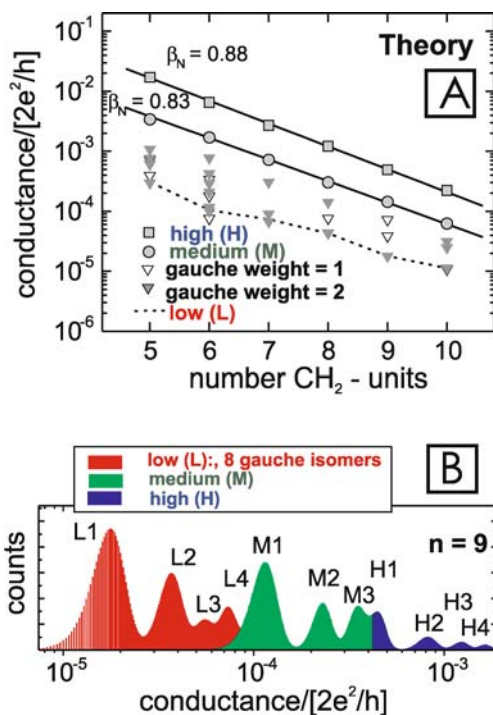
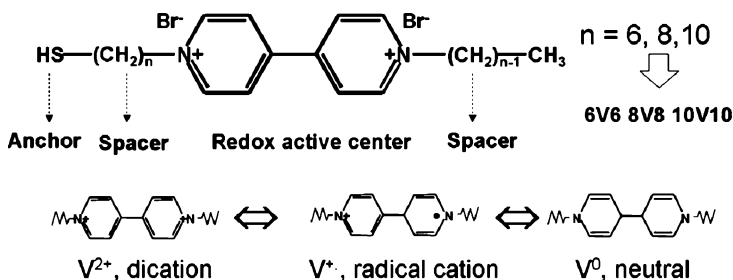


Fig. 30 **A** Calculated conductance values of the Au/ n -alkanedithiol/Au junctions vs. number n of methylene units in a semilogarithmic representation. The straight lines are based on the linear regression analysis. The high (H, filled squares) and medium (M, filled circles) values were directly obtained for the arrangements of molecular bridges depicted in Fig. 29C,B. The conductances of many different, non-equivalent *gauche* isomers cover the window below the medium values. **B** Example of a simulated conductance histogram for a molecule with $n = 9$ units. Extracting the positions of the lowest conductance peaks leads to the dashed line drawn in Fig. 29A. Further details of the histogram construction are given in [208]

layer (EDL) is close to the gate field required to significantly change the current through a molecule, according to first principle calculations by di Ventura et al. [284, 285].

As an example we will describe STM-based experiments employing gold junctions (symmetric and asymmetric) modified with N,N' -bis(6-thiohexyl)-4,4'-bipyridinium bromide (HS-6V6-SH) or N -hexyl- N' -(6-thiohexyl)-4,4'-bipyridinium bromide (HS6V6), which are composed of the redox-active 4,4'-bipyridinium cation V^{2+} (viologen) as a core, two flexible alkyl spacer units attached to each ring nitrogen with either two or one terminal SH anchoring groups. The latter ensures chemical surface immobilization.

We have chosen HS6V6 and HS-6V6-SH because the viologen core V^{2+} is easily reduced forming the radical-cation $V^{+\cdot}$ and the neutral form



Scheme 1 Molecular structure and redox reactions of viologen

V^0 [286–288]. The first oxidation-reduction $V^{2+} \leftrightarrow V^{+}$ is completely reversible in bulk solutions as well as immobilized on various surfaces. The redox-active unit has been incorporated as a “backbone” component in self-assembled monolayers [289–292], or in a nanometer scale electronic switch [293] and various functional materials [294, 295]. For a detailed characterization of the macroscopic electrochemical and structure properties of the various viologen-type adlayers on solid electrodes we refer to [231, 296] and the literature cited therein.

The Liverpool group recently pioneered electron transport studies with a single molecule wire containing the V^{2+} core unit bound symmetrically between the tip of an STM and a gold substrate [228, 237, 293, 297, 298]. This work was extended by the Jülich/Bern group in a strictly electrochemically controlled environment and combined with in-situ structure studies [231, 236, 269, 296]. Based on the statistical analysis of a large number of current-distance ($i_T - \Delta z$) and current-time ($i_T - t$) traces both groups demonstrated that junction conductance increases upon the potential-induced transition from the stable dication V^{2+} to the radical cation V^{+} state.

Figure 31 shows a typical cyclic voltammogram for a Au(111)-(1 × 1) electrode modified with two distinct concentrations of *N,N'*-bis(6-thiohexyl)-4,4'-bipyridinium bromide in 0.05 M $KClO_4$, pH ~ 7. The low coverage curve is represented by the solid line, the high coverage trace by the dashed curve. The two peaks P1 ($E = -0.470$ V) and P1' ($E = -0.450$ V) correspond to the reversible electron transfer between the viologen dication and the radical cation $V^{2+} \leftrightarrow V^{+}$ [231, 236, 287]. The peak-to-peak separation is rather constant, and the peak heights scale linearly with scan rate. These observations indicate a fairly reversible process. The coverages were estimated to be $\Gamma_L(CV) = (1.2 \pm 0.2) \times 10^{-10}$ mol cm^{-2} for the low coverage and $\Gamma_H(CV) = (3.8 \pm 0.2) \times 10^{-10}$ mol cm^{-2} for the high coverage phase, respectively. The latter points to a perpendicular or tilted viologen surface orientation. In-situ STM images of the high coverage phase of HS-6V6-SH are rather disordered and show characteristic monatomic deep holes (Fig. 31D). Similar results were obtained with high coverage adlayers of the other HS-*nVn*-SH viologen adlayers [231]. A highly ordered striped adlayer of planar oriented

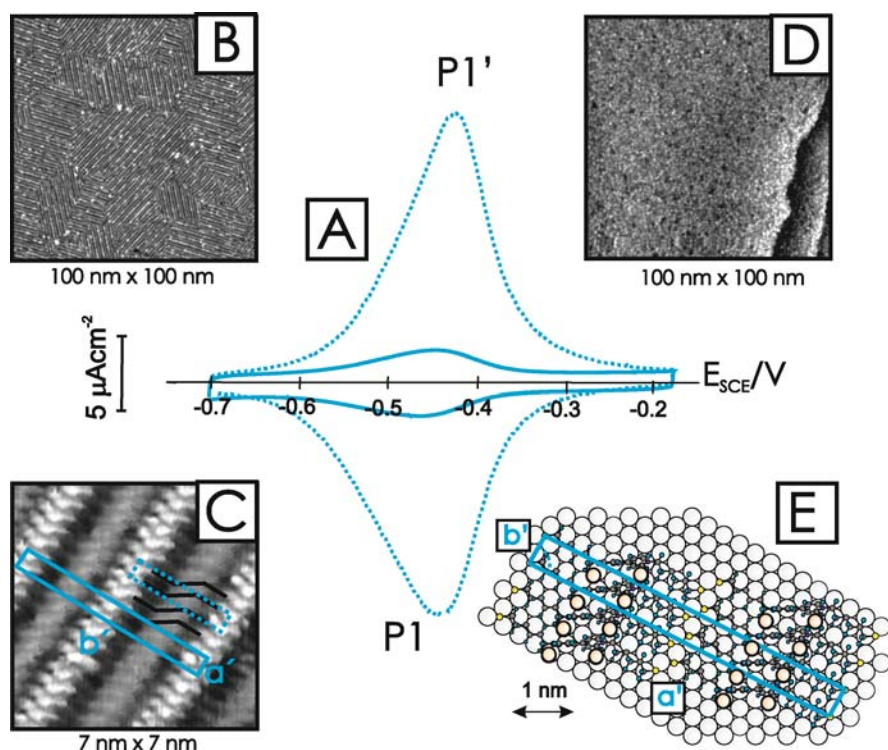


Fig. 31 **A** Cyclic voltammogram of a Au(111)-(1 × 1) electrode in 0.05 M KClO₄, pH ~ 7, modified with a low coverage (*solid line*) and a high coverage (*dotted line*) adlayer of HS-6V6-SH for the reversible one-electron oxidation/reduction between the viologen dication V²⁺ and the radical cation V^{+•} form. **B** Large-scale in-situ STM image of the low coverage striped phase of HS-6V6-SH, $E_S = -0.25$ V, $E_{bias} = -0.10$ V, $i_T = 60$ pA; **C** high-resolution image of the striped phase, $E_S = -0.35$ V, $E_{bias} = 0.08$ V, $i_T = 40$ pA; **D** high-coverage adlayer of HS-6V6-SH, $E_S = -0.25$ V, $E_{bias} = -0.09$ V, $i_T = 60$ pA; **E** proposed packing model of the ordered striped phase

molecules is formed at low coverages in -0.70 V $\leq E \leq -0.20$ V, e.g. within the stability ranges of V²⁺ and V^{+•}, respectively (Fig. 31B) [231]. The stripes are not uniform. Bright and dark contrast patterns alternate. Individual domains are anisotropic and rather small. Their size ranges typically between 10 and 20 nm. Neighboring domains with sharp boundaries are mutually rotated by multiples of 120° indicating registry with the underlying hexagonal substrate surface. High-resolution experiments (Fig. 31C) reveal details of the molecular adlayer. Rows of bright dots are separated by parallel rows of dark gray and light gray ellipsoidal-like segments. The latter are tilted by $(60 \pm 5)^\circ$ with respect to the main row direction. A cross section analysis reveals that parallel rows of the same type are separated by (2.7 ± 0.3) nm for HS-6V6-SH. The periodicity between identical features within

one row is estimated to be (0.50 ± 0.05) nm ($= \sqrt{3}a_{\text{Au}}$). The dark rows are assigned to the positions of the alkyl chains in a fully extended all-trans conformation with the molecular axis parallel to the surface plane. The gray rows are attributed to the viologen moieties. The bright dots are assigned to the positions of the terminal sulfur functionalities [231]. Using the vectors of the primitive gold lattice, a_{Au} and b_{Au} (Fig. 31E), a commensurate unit cell

$$\begin{pmatrix} a \\ b \end{pmatrix} \begin{pmatrix} 18 & 1 \\ -1 & 2 \end{pmatrix} \begin{pmatrix} a_{\text{Au}} \\ b_{\text{Au}} \end{pmatrix},$$

which gives rise to $|a'| = 5.35$ nm, $|b'| = 0.5$ nm enclosing an angle $\alpha' = 87^\circ$ is suggested. The unit cell contains one HS-6V6-SH molecule. The area per molecule is obtained to $A_{\text{L}}(\text{STM}) = 1.24$ nm², which corresponds to a coverage of $\Gamma_{\text{L}}(\text{STM}) = 1.34 \times 10^{-10}$ mol cm⁻². This value is in good agreement with $\Gamma_{\text{L}}(\text{CV}) = (1.2 \pm 0.2) \times 10^{-10}$ mol cm⁻² obtained from cyclic voltammetric experiments at low coverages. A similar analysis was also carried out for the low coverage adlayer of the monothiol HS-6V6-SH. The results do not differ significantly from those of the monothiol [231].

Employing an in-situ STM/STS configuration and a low coverage HS-6V6-SH adlayer current–distance characteristics were recorded to explore electron transport properties of single molecule junctions Au/HS-6V6-SH/Au in an electrochemical environment (cf. Figs. 24 and 25). These traces are non-monotonic and exhibit single or a series of characteristic plateaus with a typical length of 0.05–0.2 nm, which are separated by abrupt steps [231, 236]. These steps are assigned to the breaking of individual respective multimolecular viologen-type junctions previously formed between the gold STM tip and the substrate surface. The statistical analysis of these conductance traces leads to plateau current histograms (Fig. 32A). Compared to studies with alkanedithiols, only a single series of peaks corresponding to one, two or three HS-6V6-SH molecules in the gap was observed. The first peak in the plot is attributed to the conductance current of a single molecular junction. Repeating this experiment for different substrate, E_{S} , and tip polarizations, E_{T} , gives the potential dependence of a single molecular conductance of HS-6V6-SH junctions (Fig. 32B). The conductance is constant in the potential range of the stable dication V^{2+} . A value of 1.05 nS is estimated. However, the conductance increases by ca. 50% upon the potential induced transition to the radical cation state $V^{+\cdot}$. This is attributed to the higher electron density and the higher degree of conjugation of the radical cation [231]. Quantum chemical calculations of Bagrets et al. suggest additional contributions from the interaction of the tunneling electron with molecular vibrations [299].

The electrochemical experiments with symmetric Au/HS-6V6-SH/Au junctions were complemented by studies in asymmetric tunneling junctions

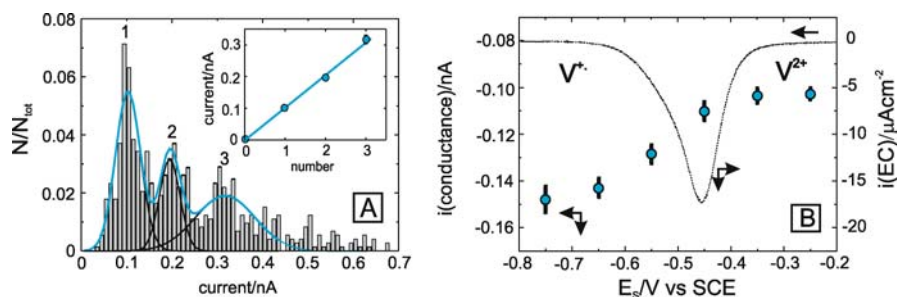


Fig. 32 **A** Histogram constructed from values of the plateau currents of a series of more than 500 individual i - Δz pulling curves for molecular junctions Au(T)/HS-6V6-SH/Au(S) recorded at $E_S = -0.250$ V and $E_T = -0.150$ V. The peak positions were determined by Gaussian fits (black lines) to the histogram peaks (blue line as the sum of the Gaussians). The inset shows the linear correlation between current and peak number. **B** represents a plot of the single molecule conductance currents of Au(T)/HS-6V6-SH/Au(S) junctions vs. the substrate potential E_S at fixed bias ($E_S - E_T$) = -0.100 V. The sign convention of the bias voltage gives the negative conduction currents. Each data point was obtained from histograms similar to the one in Fig. 32A. The dotted line corresponds to the macroscopic current-voltage curve for the reduction of $V^{2+} \rightarrow V^{+}$ (cf. cyclic voltammograms in Fig. 31) [231]

with the redox molecule HS-6V6-H chemically bound either to the Au tip or the Au(111) substrate surface [231, 269]. Figure 33A,B illustrates the principle: After establishing the tunneling junctions, the STM feedback was switched off. Subsequently, the tunneling current was recorded as a function of the tip voltage while keeping the bias voltage, $E_{\text{bias}} = E_S - E_T$, constant. In other words, the Fermi levels of tip and substrate were shifted relative to the discrete molecular levels. In both cases, e.g. a viologen-modified tip or substrate, an enhanced tunneling current with a well-defined maximum close to the equilibrium potential E_0 of the redox couple was observed (Fig. 33C). This maximum shifts with increasing bias voltage E_{bias} towards more negative tip (substrate) potentials.

The careful analysis of the experimental data within the framework of the developed theories of interfacial electron transfer in a nanoscale electrochemical metal/redox molecule/metal configuration led to the conclusion that the experimentally observed enhanced tunneling current i_{enh} (Fig. 33D) could be represented best by a two-step electron transfer process accompanied with partial vibrational relaxation. This model was developed by Kuznetsov and Ulstrup and is represented by the following theoretical formalism [255, 261, 262, 300]

$$i_{\text{enh}} = e\kappa\rho(eE_{\text{bias}}) \frac{\omega}{2\pi} \left(\frac{\exp\left(\frac{e}{4\lambda kT}(\lambda + \xi\eta - \gamma E_{\text{bias}})^2\right)}{+ \exp\left(\frac{e}{4\lambda kT}(\lambda - \xi\eta - \gamma E_{\text{bias}} + E_{\text{bias}})^2\right)} \right)^{-1}. \quad (8)$$

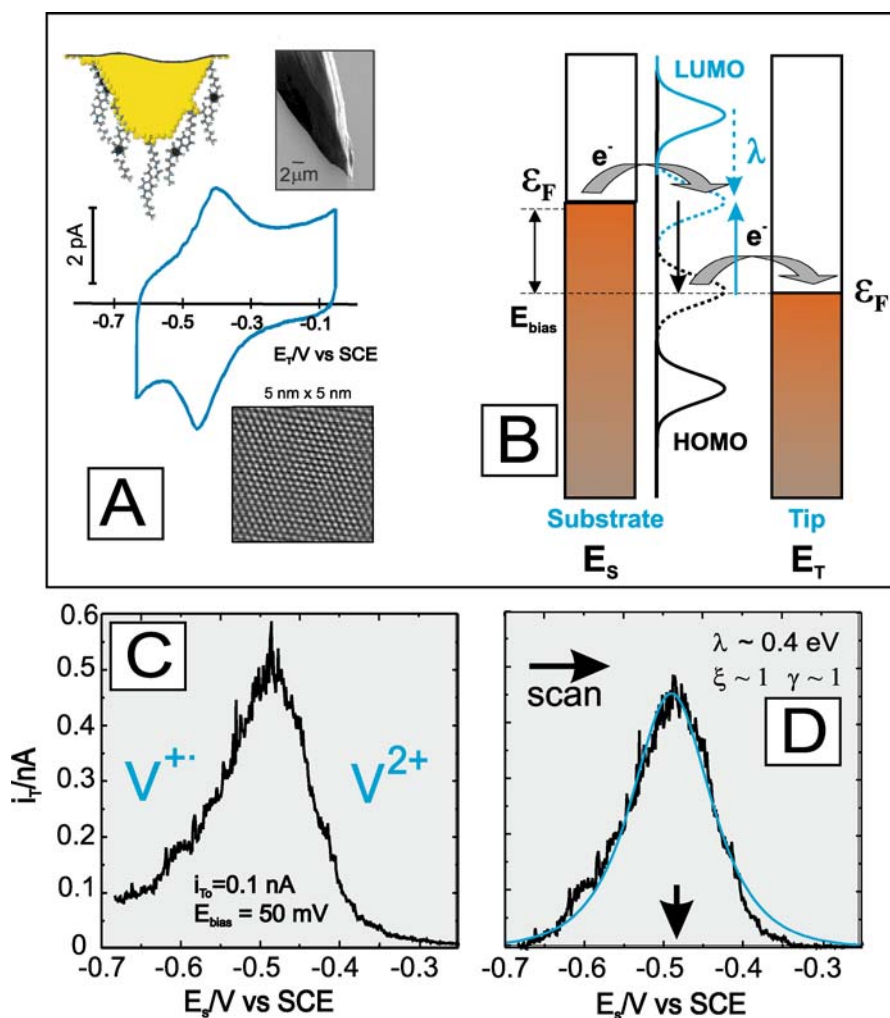


Fig. 33 **A** Set-up of the redox-mediated tunneling experiment with a viologen-modified Au tip; **B** schematic energy level diagram of a two-step ET process mediated by a redox-active molecule. The electron is transferred from the Fermi level of the substrate (*left*) e_{F_s} to the LUMO of the molecule and after partial vibrational relaxation to the Fermi level of the tip e_{F_t} (*right*). **C** Average i_T vs. E_s curves recorded in constant bias spectroscopy mode, $i_{T0} = 0.1$ nA, $E_{bias} = 0.050$ V. The sweep started in the stability region of $V^{+\bullet}$; **D** average constant bias spectroscopy curve **C** after baseline correction. The *blue line* represents the fit using Eq. 8 with $\lambda = 0.42$ eV, $\xi = 1.0$, $\gamma = 1.0$ [269]

Here, e is the elementary charge, κ the electronic transmission coefficient, ρ the density of electronic states in the metal near the Fermi level, ω is the characteristic vibration frequency, $\eta = E_s - E_0$ is the overpotential, k is the Boltzmann constant and T the temperature. ξ and γ , both ranging between

0 and 1, are model parameters describing the shift of the effective electrode potential at the reactive center with the variation of η and E_{bias} , respectively.

Figure 33D illustrates the fit of the model expressed by Eq. 8 to the enhanced tunneling current vs. substrate potential characteristics (i_{enh} vs. E_S). I_{enh} was obtained from the experimental data plotted in Fig. 33C after baseline correction. The particular experiment led to reorganization energies $\lambda = 0.42$ eV of the radical cation $V^{+\cdot}$. The values of ξ and $\gamma \sim 1$ indicate a complete potential drop at the reactive viologen center with the variation of η and E_{bias} . For further details we refer to [269].

Complementary EC-STs experiments were carried out in variable bias mode with a fixed substrate potential $E_S = -0.2$ V and the tip potential E_T varied in a wide range. The resulting ($i_T - E_T$)_{ES} curve (Fig. 34) is asymmetric. For $E_T > E_S$ (i.e., $E_{\text{bias}} < 0$) and at small positive values of E_{bias} , a nearly linear current response was observed, which is characteristic for direct tunneling at a fixed gap geometry. The dashed line in Fig. 34 represents the fit to the linear part. An enhanced exponential-like tunneling response is observed at $E_T \leq -0.25$ V. The on/off ratio between the negative and the corresponding positive branches of the i_T vs. E_T curve at $|E_{\text{bias}}| = 0.4$ V is ca. 20.

Equation 8 was compared to the experimental data after subtraction of the linear response contribution due to direct tunneling. The baseline was evaluated by the extrapolation of the linear part of the experimental curve. This approximation neglects the different electronic transmission of V^{2+} and $V^{+\cdot}$ in the respective off-resonance states and attributes the observed effect to

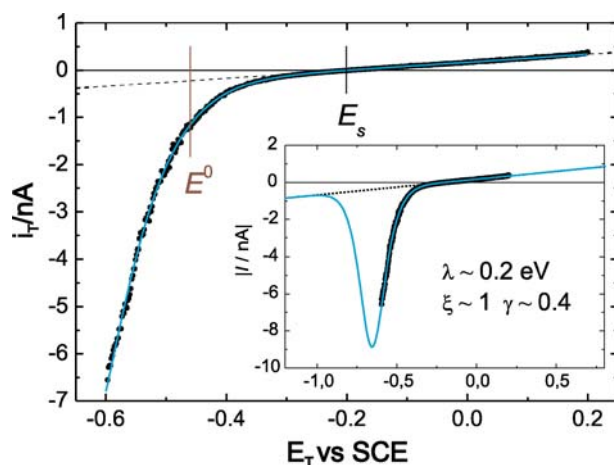


Fig. 34 i_T vs. E_T curve recorded in variable bias spectroscopy mode (points), an expected linear current response of the direct tunneling (dashed line) and a fit of the tunneling enhancement (Eq. 8, solid curve). The inset shows the same data and a simulated curve in a wider potential range assuming that the 2-step ET model with partial vibrational relaxation is valid [269]

redox-mediated tunneling only. The resulting theoretical curve is shown in Fig. 34 [269]. Similar as for constant bias mode, the estimated value of ξ is close to 1. The estimated value of $\lambda = 0.2$ eV is also in agreement with the one obtained from constant bias spectroscopy when starting the trace in the stability range of the V^{2+} [269].

Finally we note that the asymmetric configuration is distinctly different from the symmetric Au/molecule/Au configuration. The latter exhibits modifications of the junction conductance due to structure changes of the redox-active unit, while the former exhibits a maximum of the tunneling current due to the coexistence of the oxidized and the reduced forms. As shown for the quantitative analysis of viologen-based tunneling junctions, the maximum is often close to the equilibrium potential E_0 of the redox pair. The observed enhancement of the tunneling current in an electrochemical environment is not restricted to viologen-based junctions. Qualitative similar phenomena were also reported for several other systems, such as, derivatives of ferrocene [245], organometallic complexes [230, 240, 241, 301] and porphyrins [207] respective metallo-proteins [229, 247–249]. These experimental approaches offer a novel and unique strategy to explore electron transfer processes and related phenomena at the single molecular level at electrified solid–liquid interfaces.

6

Concluding Comments

Combined electrochemical, in-situ STM and spectroscopic measurements revealed a detailed molecular level understanding of structure formation and self-assembly of selected organic monolayers on well-defined solid–liquid interfaces. The results presented demonstrate the interplay of molecular structure, substrate geometry and electrode potential. It involves specific adsorbate–adsorbate and adsorbate–substrate interactions, such as electrostatic forces, π -stacking, van der Waals forces, intermolecular hydrogen bonding and partial charge transfer. We emphasize the difference between spontaneous self-assembly of physisorbed adlayers and the assembly of monolayers involving the formation of covalent bonds to the substrate surface. We demonstrate that the understanding of these complex co-operative mechanisms offers exciting possibilities to modify metal surfaces via substrate–adsorbate and/or ion–adsorbate co-ordination, molecular recognition (“key–lock”-principle and/or “host–guest” chemistry and physics) and self-organization employing the *electrode potential* as active *tool* and/or *detector*. Structural, electrical and mechanical properties and functions of single molecules and ions in template structures are now accessible. We report on the construction of symmetric and asymmetric metal/(single) molecule/metal junctions to explore charge transport and redox switching in

an electrochemical environment. The various scanning probe microscopies offer a powerful group of methods to study these novel phenomena at a local level in-situ with unprecedented resolution in real space and, under some circumstances, in real time. The combination with other high-resolution structure-sensitive techniques will soon lead to fascinating in-situ reactivity studies at solid-liquid interfaces at the molecular/atomistic level. These experiments may guide the way towards single molecule and cluster electrochemistry, which is of fundamental importance, but also bears a unique potential for many novel applications in various other fields, such as molecular electronics, bio- and chemosensors, molecular catalysis etc.

Acknowledgements The present work was supported by the Volkswagen Foundation, the Research Center Jülich, the University of Berne and the Deutsche Forschungsgemeinschaft. R.A. and I.P. acknowledge support of the German Academic Exchange Agency (DAAD). G.S. thanks the Alexander von Humboldt Foundation for a fellowship. We would also like to thank A. Blaszczyk, M. Mayor, M. Homberger and U. Simon for discussions and the synthesis of the viologen and the biphenyl derivatives.

References

1. Lehn J-M (1995) *Supramolecular Chemistry: Concepts and Perspectives*. Wiley-VCH, Weinheim
2. Whitesides GM (2002) *Science* 295:2418–2421
3. Leininger S, Olenyuk B, Stang PJ (2000) *Chem Rev* 100:853–908
4. Barth JV, Costantini G, Kern K (2005) *Nature* 437:671–679
5. Desiraju GR (2002) *Acc Chem Res* 35:565–573
6. Kaifer AE, Gómez-Kaifer M (1999) *Supramolecular Chemistry*. Wiley-VCH, Weinheim
7. Wandlowski T (2003) *Fundamentals of Nanoelectronics*. Lectures of the 34th IFF Spring School; Jülich
8. Heath JR, Ratner MA (2003) *Phys Today* 5:43–46
9. Moore G (1965) *Electron Mag* 4:19–22
10. Iwasita T, Nart F (1997) *Progr Surf Sci* 55:271–340
11. Wandlowski T, Ocko BM, Magnussen OM, Wu S, Lipkowski J (1996) *J Electroanal Chem* 409:155–164
12. Wu S, Lipkowski J, Magnussen OM, Ocko BM, Wandlowski T (1998) *J Electroanal Chem* 446:67–77
13. Hamelin A (1995) Harmony of electrochemical results, in situ STM observations and in situ SXRS data at gold|aqueous solution interfaces. In: Gewirth AG, Siegenthaler H (eds) *Nanoscale Probes of the Solid/Liquid Interface*. Kluwer, Dordrecht, pp 285–306
14. Kolb DM, Schneider J (1986) *Electrochim Acta* 31:929–936
15. Zei MS, Lehmpfuhl G, Kolb DM (1985) *Surf Sci* 221:23–34
16. Friedrich A, Pettinger B, Kolb DM, Lüpke G, Steinhoff R, Marowsky G (1989) *Chem Phys Lett* 163:123–128
17. Wang J, Ocko BM, Davenport AJ, Isaacs HS (1992) *Phys Rev B* 46:10321–10338
18. Magnussen OM (1993) PhD Thesis, University of Ulm
19. Gao X, Hamelin A, Weaver MJ (1991) *J Chem Phys* 95:6993–6996

20. Tao NJ, Lindsay SM (1992) *Surf Sci* 274:L546–L552
21. Dretschkow T, Wandlowski T (2003) Structural transitions in organic adlayers – A molecular view. In: Wandelt K, Thurgate S (eds) *Solid–Liquid Interfaces: Macroscopic Phenomena – Microscopic Understanding*. Springer, Berlin, pp 259–321
22. Wandlowski T, Ataka K, Pronkin S, Diesing D (2006) *Electrochim Acta* 49:1233–1247
23. Kolb DM (1996) *Prog Surf Sci* 51:109–173
24. Chambliss DD, Wilson RJ (1991) *J Vac Sci Technol B* 9:928–932
25. Barth JV, Brune H, Ertl G, Behm RJ (1990) *Phys Rev* 42:9307–9318
26. Randler R (1995) Diploma Thesis, University of Ulm
27. Magnussen OM, Hageböck J, Hotlos J, Behm RJ (1992) *Faraday Discuss Chem Soc* 94:329–338
28. Eden GJ, Gao X, Weaver MJ (1994) *J Electroanal Chem* 375:357–366
29. Dretschkow T, Wandlowski T (1997) *Ber Bunsenges Phys Chem* 101:749–756
30. Cuesta A, Kleinert M, Kolb DM (2000) *PhysChemChemPhys* 2:5684–5690
31. Ataka K, Osawa M (1998) *Langmuir* 14:951–959
32. Magnussen OM, Hotlos J, Behm RJ, Batina N, Kolb DM (1993) *Surf Sci* 296:310–332
33. Gao X, Edens GJ, Hamelin A, Weaver MJ (1993) *Surf Sci* 296:333–342
34. Batina N, Dakkouri AS, Kolb DM (1994) *J Electroanal Chem* 370:87–94
35. Ocko BM, Wang J, Davenport A, Isaacs H (1990) *Phys Rev Lett* 65:1466–1469
36. Lehn JM (1995) *Supramolecular Chemistry*. Wiley-VCH, Weinheim
37. Atwood LJ, Davies JED, MacNicol DD, Vögtle F, Lehn JM (eds) (1996) *Comprehensive Supramolecular Chemistry*. Pergamon, New York
38. Etter MC (1990) *Acc Chem Res* 23:120–126
39. Desiraju GR (1989) *Crystal Engineering*. Elsevier, Amsterdam
40. Ward MD, Hollingsworth MD (eds) (1994) *Chem Mater* 6
41. Jeffrey GA, Saenger W (1991) *Hydrogen Bonding. Biological Structures*. Springer, Berlin
42. Subramanian S, Zaworotko MJ (1994) *Coord Chem Rev* 137:357–401
43. MacDonald JG, Whitesides GM (1994) *Chem Rev* 94:2383–2420
44. Melendez R, Hamilton AD (1998) *Topics Curr Chem* 198:97–129
45. Bailey M, Brown CJ (1967) *Acta Crystallogr* 22:387–391
46. Alcalá R, Martínez-Carrera S (1969) *Acta Crystallogr B* 25:5–19
47. Duchamp DJ, March RE (1972) *Acta Crystallogr B* 28:1671–1677
48. Zaworotko MJ (2001) *Chem Commun* 1:1–138
49. Herbststein FH (1987) *Top Curr Chem* 140:107–139
50. Herbststein FH (1996) 1,3,5-Benzene-tricarboxylic acid. In: Atwood JL; MacNicol DD, Vögtle F, Lehn JM (eds) *Comprehensive Supramolecular Chemistry, Vol 6*. Pergamon, New York, p 61
51. Herbststein FH, Kapon M, Maor I, Reisner GM (1981) *Acta Crystallogr B* 37:136–142
52. De Feyter S, Gasquiere A, Klapper M, Müllen K, De Schryver FC (2003) *Nano Lett* 3:1485–1488
53. De Feyter S, De Schryver FC (2003) *Chem Soc Rev* 32:139–150
54. Rabe JP, Buchholtz S (1991) *Science* 253:424–427
55. Eichhorst-Gerner K, Stabel A, Moessner G, Declerq D, Valiyaveetil S, Enkelmann V, Müllen K, Rabe JP (1996) *Angew Chem Int Ed* 35:1492–1495
56. Lin N, Dmitriev A, Weckesser J, Barth JV, Kern K (2002) *Angew Chem Int Ed* 41:4779–4783
57. Ermer O, Neudörfl J (2001) *Chem Eur J* 7:4961–4980
58. Kolotuchin SV, Fenlon EE, Wilson SR, Loweth CJ, Zimmerman SC (1996) *Angew Chem Int Ed* 34:2654–2657

59. Melendez RE, Sharma CVK, Zaworotko MJ, Bauer C, Rogers RD (1996) *Angew Chem Int Ed* 35:2213–2215
60. Yaghi OM, Li G, Li H (1995) *Nature* 378:703–706
61. Gutschke SOH, Molinier M, Powell AK, Winpenny REP, Wood PT (1996) *Chem Commun* 823–824
62. Dmitriev A, Lin N, Weckesser J, Barth JV, Kern K (2002) *J Phys Chem B* 106:6907–6912
63. Griessl S, Lackinger M, Edelwirth M, Hietschold M, Heckl W (2002) *Single Molecule* 3:25–31
64. Feyter S, De Schryver FC (2005) *J Phys Chem B* 109:4290–4302
65. Ishikawa Y, Ohira A, Sakata M, Hirayama C, Kunitake M (2002) *Chem Commun* 2652–2653
66. Su GJ, Zhang HM, Wan LJ, Bai CL, Wandlowski T (2004) *J Phys Chem B* 108:1931–1937
67. Li Z, Wang LJ, Han B (2005) *Langmuir* 21:6915–6928
68. Han B, Li Z, Pronkin S, Wandlowski T (2004) *Can J Chem* 82:1481–1494
69. Spillmann H, Dmitriev A, Lin N, Messina P, Barth JV, Kern K (2003) *J Am Chem Soc* 125:10725–10728
70. Wandlowski T (2003) Phase transitions in two-dimensional adlayers at electrode surfaces: Thermodynamics, kinetics and structural aspects. In: Gileadi E, Urbakh M (eds) *Encyclopedia of Electrochemistry*. Wiley, pp 383–467
71. Yoshimoto S (2006) *Bull Chem Soc Jpn* 79:1167–1190
72. Wang D, Wan LJ (2007) *J Phys Chem C* 111:16109–16130
73. Dean JA (ed) (1985) *Lange's Handbook of Chemistry*. Mc Graw–Hill, New York, pp 5–42
74. Lippel PH, Wilson RJ, Miller MD, Wöll C, Chiang S (1989) *Phys Rev Lett* 62:171–174
75. Chiang S (1997) *Chem Rev* 97:1083–1096
76. Sautet P (1997) *Chem Rev* 97:1097–1116
77. Böhringer M, Morgenstern K, Schneider WD, Berndt R, Mauri F, de Vita A, Car R (1999) *Phys Rev Lett* 83:324–327
78. Yuan HJ, Lu J, Wan LJ, Bai CL (2004) *J Phys Chem B* 108:11251–11255
79. Barth JV, Weckesser J, Trimarchi G, Vladimirova M, de Vita A, Cai C, Brune H, Günter P, Kern K (2002) *J Am Chem Soc* 124:7991–8000
80. Atoderesi T, Blügel S (2005) personal communication
81. Steiner T (2002) *Angew Chem* 114:50–113
82. Griessl SJ, Lackinger M, Jamitzky F, Markert T, Hietschold M, Heckl W (2004) *Langmuir* 20:9403–9407
83. Desiraju GR (1995) *Angew Chem Int Ed* 34:2311–2327
84. Sumetskii M, Kornyshev AA (1993) *Phys Rev B* 48:17493–17506
85. Kanter JA, Roelofsen G (1976) *Acta Cryst B* 32:3328–3331
86. Lei SL, Wang C, Yin SX, Wang HN, Xi F, Liu HW, Wan LJ, Bai CL (2001) *J Phys Chem B* 105:10838–10841
87. Herbstein FH, Marsh RE (1977) *Acta Cryst B* 33:2358–2367
88. Chatterjee S, Pedireddi VR, Ranganathan A, Rao CNR (2000) *J Mol Struct* 520:107–115
89. Dale SH, Elsegood MRJ, Richards SJ (2004) *Chem Commun* 1278–1279
90. Frederick BG, Chen Q, Leibsle FM, Lee MB, Kitching KJ, Richards NV (1997) *Surf Sci* 394:1–25
91. Arenas JF, Marcos JI (1979) *Spectrochim Acta* 35A:355–361
92. Gonzalez-Sanchez F (1957) *Spectrochim Acta* 12:17–25
93. Osawa M (1997) *Bull Chem Soc Jpn* 70:2861–2880
94. Ikezawa Y, Sekiguchi R, Kitazume T (2000) *Electrochim Acta* 46:731–736
95. Noda H, Wan LJ, Osawa M (2001) *Phys Chem Chem Phys* 3:3336–3342
96. Noda H, Ataka K, Wan LJ, Osawa M (1999) *Surf Sci* 427/428:190–194

97. Frederick BG, Ashton MR, Richardson NV, Jones TS (1993) *Surf Sci* 292:33–46
98. Frederick BG, Leibsle FM, Haq S, Richardson NV (1996) *Surf Rev Lett* 3:1523–1546
99. Casarin M, Granozzi G, Sambì M, Tondello E (1994) *Surf Sci* 307–309:95–100
100. Ortega-Lorenzo M, Baddeley CJ, Muryn C, Raval R (2000) *Nature* 404:376–379
101. De Feyter S, Gasquiere A, Abdel-Mottaleb MM, Grim PCM, de Schriver FC, Meiners C, Siffert M, Valiyaveetil S, Müllen K (2000) *Acc Chem Res* 33:520–531
102. Kolotuchin SV, Thiessen PA, Fenton EE, Wilson SR, Loweth CJ, Zimmerman SC (1999) *Chem Eur J* :2537–2547
103. Li Z, Han B, Wandlowski T (2008) *Electrochim Acta*, in preparation
104. Swalen JD, Allara DL, Andrade JD, Chandross EA, Garoff S, Israelachvili J, McCarthy IJ, Murray R, Pease RF, Rabold JF, Wynne KJ, Yu H (1987) *Langmuir* 3:932–950
105. Iwamoto M, Chen-Xu W (2001) *The Physical Properties of Organic Monolayers*. World Scientific Publishers, Singapore
106. Ulman A (1996) *Chem Rev* 96:1533–1554
107. Schreiber F (2004) *J Phys Condens Matter* 16:R881–R900
108. Wilbur J, Whitesides GM (1999) Self-assembly and self-assembled monolayers in micro- and nanofabrication. In: Timp G (ed) *Nanotechnology*. Springer, New York, pp 331–342
109. Nuzzo RG, Allara DL (1983) *J Am Chem Soc* 105:4481–4483
110. Smith RK, Lewis PA, Weiss PS (2004) *Prog Surf Sci* 75:1–68
111. Love JC, Estroff LA, Kribel JK, Nuzzo RG, Whitesides GM (2005) *Chem Rev* 105:1103–1170
112. Mrksich M, Chen CS, Xia Y, Dike LE, Ingber DE, Whitesides GM (1996) *Proc Natl Acad Sci USA* 93:10775–10778
113. Ahn HS, Cuong PD, Park S, Kim YW, Lim JC (2003) *Wear* 255:819–825
114. Zhang J, Chi Q, Kuznetsov AM, Hansen AG, Wackerbarth H, Christensen HEM, Andersen JET, Ulstrup J (2002) *J Phys Chem B* 106:1131–1152
115. Whelan CM, Kinsella M, Ho HM, Maex K (2004) *J Electrochem Soc* 151:B33–B39
116. Finklea HO (1996) Electrochemistry of organized monolayers of thioles and related molecules on electrodes. In: Bard AJ (ed) *Electroanal. Chem.*, Vol 19. Dekker, New York, pp 109–335
117. Baunach T, Ivanova V, Kolb DM, Boyen HG, Ziemann P, Büttner M, Oelhafen P (2004) *Adv Mater* 16:2024–2028
118. Mantooth BA, Weiss PS (2003) *Proc IEEE* 91:1785–1802
119. Cuniberti G, Fagas G, Richter K (eds) *Introduction to Molecular Electronics*. Springer, Berlin
120. Nichols R (ed) (2006) *Molecular Wires and Nanoscale Conductors – Fundamentals and Applications*. Faraday Discuss 131
121. Salomon A, Cahen D, Lindsay SM, Tomfohr J, Engelkes VB, Frisbie CD (2003) *Adv Mater* 15:1881–1890
122. McCreery RL (2004) *Chem Mater* 16:4477–4496
123. Porter MD, Bright TB, Allara DL, Chidsey CED (1987) *J Am Chem Soc* 109:3559–3568
124. Chidsey CED (1991) *Science* 251:919–922
125. Becka A, Miller C (1992) *J Phys Chem* 96:2657–2668
126. Finklea HO, Handschew DD (1992) *J Am Chem Soc* 114:3173–3181
127. Holmlin RE, Haag R, Chabinyc MI, Ismagilov RF, Cohen AC, Terfort A, Rampi MA, Whitesides GM (2001) *J Am Chem Soc* 123:5075–5085
128. Yang G, Liu G (2003) *J Phys Chem B* 107:8746–8759
129. Li X, He J, Hihath J, Xu B, Lindsay SM, Tao NJ (2006) *J Am Chem Soc* 126:2135–2141
130. Ulman A (2001) *Acc Chem Res* 34:855–863

131. Sikes HD, Smalley JF, Dudek SP, Cook AR, Newton MD, Chidsey CED, Feldberg SW (2001) *Science* 291:1519–1523
132. Azzam JW, Bashir A, Terfort A, Strunskus T, Wöll C (2006) *Langmuir* 22:3647–3655
133. Adams DM, Brus L, Chidsey CED, Creager S, Creutz C, Kagan CR, Kamat PV, Lieberman M, Lindsay S, Marcus RA, Metzger RM, Michel-Beyerle ME, Miller JR, Newton MD, Rollison DR, Sankey O, Schanze KS, Yardely J, Zhu X (2003) *J Phys Chem B* 107:6668–6697
134. Ulman A, Scaringe RP (1992) *Langmuir* 8:894–897
135. Foster JS, Frommer JF (1988) *Nature* 333:542–545
136. Rong HT, Frey S, Yang YJ, Zharnikov M, Buck M, Wühn M, Wöll C, Helmchen G (2001) *Langmuir* 17:1582–1593
137. Heister K, Rong HT, Buck M, Zharnikov M, Grunze M, Johanson LSO (2001) *J Phys Chem* 105:6888–6894
138. Azzam W, Cyganik P, Witte G, Buck M, Wöll C (2003) *Langmuir* 19:8262–8270
139. Cyganik P, Buck M (2004) *J Am Chem Soc* 126:5960–5961
140. Cyganik P, Buck M, Azzam W, Wöll C (2004) *J Phys Chem B* 108:4989–4996
141. Cyganik P, Buck M, Wilton-Ely JDET, Wöll C (2005) *J Phys Chem B* 109:10902–10908
142. Long YT, Rong HT, Buck M, Grunze M (2002) *J Electroanal Chem* 524/525:62–67
143. Thom I, Buck M (2005) *Surf Sci* 581:33–46
144. Felgenhauer T, Rong HT, Buck M (2003) *J Electroanal Chem* 550/551:309–319
145. Aguilar-Sanchez R, Su GJ, Homberger M, Simon U, Wandlowski T (2007) *J Phys Chem C* 111:17409–17419
146. Su GJ, Aguilar-Sanchez R, Li Z, Pobelov I, Homberger M, Simon U, Wandlowski T (2007) *ChemPhysChem* 8:1037–1048
147. Cavalleri O, Hirstein A, Bucher JP, Kern K (1996) *Thin Solid Films* 284/285:392–395
148. Iwami A, Hobora D, Yamamoto M, Kakiuchi T (2004) *J Electroanal Chem* 564:77–83
149. Frumkin AN, Petrii OA, Damaskin BB (1980) Potential of zero charge. In: Bockris JOM, Conway BE, Yeager E (eds) *Comprehensive Treatise of Electrochemistry*, Vol 1. Plenum Press, New York, pp 221–290
150. Sokolowski J, Czajkowski JM, Turowska M (1990) *Electrochim Acta* 35:1393–1398
151. Cuesta A (2004) *Surf Sci* 572:11–22
152. Kolb DM, Schneider J (1986) *Electrochim Acta* 31:929–936
153. Sondag-Huethorst JAM, Fokkink LGJ (1992) *Langmuir* 8:2560–2566
154. Sondag-Huethorst JAM, Fokkink LGJ (1994) *J Electroanal Chem* 367:49–57
155. Becka AM, Miller C (1993) *J Phys Chem* 97:6233–6239
156. Widrig CA, Chung C, Porter MD (1991) *J Electroanal Chem* 319:335–359
157. Yang DF, Wilde CP, Morin M (1996) *Langmuir* 12:6570–6577
158. Imbayashi SI, Lida M, Hobara D, Feng ZO, Niki K, Kakiuchi T (1997) *J Electroanal Chem* 428:33–38
159. Chen A, Lipkowski J (1999) *J Phys Chem B* 103:682–691
160. Yang DF, Morin MJ (1997) *Electroanal Chem* 429:1–5
161. Yang DF, Morin MJ (1998) *Electroanal Chem* 441:173–181
162. Retter U, Kant W (1995) *Thin Solid Films* 256:89–93
163. Calvente JJ, Kovacova Z, Sanchez MD, Andreu R, Fawcett WR (1996) *Langmuir* 12:5696–5703
164. Wano H, Uosaki K (2001) *Langmuir* 17:8224–8228
165. Harrison JA, Thirsk HR (1971) The fundamentals of metal deposition. In: Bard AJ (ed) *Electroanal. Chem*, Vol 5. Dekker, New York, pp 67–121
166. Wandlowski T (2002) Phase transitions. In: Gileadi E, Urbakh M (eds) *Encyclopedia of Electrochemistry*, Vol 1. VCH, Weinheim, pp 383–467

167. Esplandiú MJ, Hageström H, Kolb DM (2001) *Langmuir* 17:828–838
168. Conway BE (1995) *Prog Surf Sci* 49:331–452
169. Wandlowski T, Pronkin S, Berna A, Hara M (2008) in preparation
170. Yang DF, Mazanai HA, Morin M (1997) *J Phys Chem B* 101:1158–1166
171. Ye S, Haba T, Sato Y, Shimazu K, Uosaki K (1999) *PhysChemChemPhys* 1:3653–3659
172. Landauer R (1957) *IBM J Res Dev* 1:223–230
173. Bumm LA, Arnold JJ, Dunbar TD, Allara DL, Weiss PS (1999) *J Phys Chem B* 103:8122–8127
174. Rong HT, Frey S, Yang YJ, Zharnikov M, Buck M, Wühn M, Wöll C, Helmchen G (2001) *Langmuir* 17:1582
175. Dawydov AS (ed) (1976) *Quantum Mechanics*. Pergamon Press, Oxford
176. Wakamatsu S, Fuji S, Akiba U, Fujihira M (2003) *Ultramicroscopy* 97:19
177. Wold DJ, Haag R, Rampi MA, Frisbie CD (2002) *J Phys Chem B* 106:2813–2816
178. Wakamatsu S, Fuji S, Akiba U, Fujihira M (2003) *Ultramicroscopy* 97:19–26
179. Wakamatsu S, Akiba U, Fujihira M (2002) *Jpn J Appl Phys* 41:4998–5002
180. Lüssem B, Müller-Meskamp L, Karthäuser S, Waser R, Homberger M, Simon U (2006) *Langmuir* 22:3021–3027
181. Holmlin RE, Haag R, Chabynyc ML, Ismagilov RF, Cohen AE, Terfort AE, Rampi MA, Whitesides GM (2001) *J Am Chem Soc* 123:5075–5085
182. Sachs SB, Dudek SP, Hsung RP, Sita LR, Smalley JF, Newton MD, Feldberg SW, Chidsey CED (1997) *J Am Chem Soc* 119:10563–10564
183. Cui XD, Zarate X, Tomfohr J, Sankey OF, Primak A, Moore AL, Moore TA, Gust D, Harris G, Lindsay SM (2002) *Nanotechnology* 13:5
184. Wold DJ, Frisbie CD (2001) *J Am Chem Soc* 123:5549–5556
185. Davis JJ, Wang N, Morgan A, Zhang TT, Zhao JW (2006) *Faraday Discuss* 131:167–179
186. Meszaros G, Li C, Pobelov I, Wandlowski T (2007) *Nanotechnology* 18:424004
187. Simmons JG (1963) *J Appl Phys* 34:1793–1800
188. Datta S, Tian W, Hong SH, Reifenberger R, Henderson JL, Kubiak CP (1997) *Phys Rev Lett* 79:2530–2533
189. Haag R, Rampi MA, Holmlin RE, Whitesides GM (1999) *J Am Chem Soc* 121:7895–7906
190. Aviram A, Ratner MA (1974) *Chem Phys Lett* 29:277–283
191. Tao NJ (2006) *Nat Nanotechnol* 1:173–181
192. Chen F, Hihath J, Huang Z, Li X, Tao N (2007) *Annu Rev Phys Chem* 58:535–564
193. Donhauser ZJ, Mantooth BA, Kelly KF, Bumm LA, Monnell JD, Tapleton JJ, Price DW Jr, Rawlett AM, Allara DL, Tour JM, Weiss PS (2001) *Science* 292:2303–2307
194. Andres RP, Datta S, Janes DB, Kubiak CP, Reifenberger R (2001) The design, fabrication and electronic properties of self-assembled molecular nanostructures. In: Nalwa HS (ed) *Handbook of Nanostructured Materials and Nanotechnology*, Vol 3. AP, New York, p 180
195. Gimzewski JK, Joachim C (1999) *Science* 283:1683–1688
196. Lu X, Hipps KW, Wang XD, Mazur U (1996) *J Am Chem Soc* 118:7197–7202
197. Scudiero L, Barlow DE, Hipps KW (2000) *J Phys Chem B* 104:11899–11905
198. Scudiero L, Barlow DE, Mazur U, Hipps KW (2001) *J Am Chem Soc* 123:4073–4080
199. Scudiero L, Barlow DE, Hipps KW (2002) *J Phys Chem B* 106:996–1003
200. Repp J, Meyer G, Paavilainen S, Olsson FE, Persson M (2006) *Science* 312:1196–1199
201. Temirov R, Lassise A, Anders B, Tautz FS (2008) *Nanotechnology* 19:065401
202. Wold DJ, Haag R, Rampi MA, Frisbie CD (2002) *J Phys Chem B* 106:2813–2816
203. Cui XD, Primak A, Zarate X, Tomfohr J, Sankey OF, Moore AL, Moore TA, Gust D, Harris G, Lindsay SM (2001) *Science* 294:571–574

204. Fan F-RE, Yang J, Cai L, Price DW Jr, Dirk SM, Kosynkin DV, Yao Y, Rawlett AM, Tour JM, Bard AJ (2002) *J Am Chem Soc* 124:5550–5560
205. Xu B, Tao NJ (2003) *Science* 301:1221–1223
206. Huang Z, Chen F, D'Agosta R, Bennett PA, Ventra MD, Tao N (2007) *Nat Nanotechnol* 2:698–703
207. Tao NJ (1996) *Phys Rev Lett* 76:4066–4069
208. Li C, Pobelov I, Wandlowski T, Bagrets A, Arnold A, Evers F (2008) *J Am Chem Soc* 130:318–326
209. Seferos DS, Trammell SA, Bazan GC, Kushmerick JG (2005) *Proc Natl Acad Sci USA* 102:8821–8825
210. Reed MA, Zhou C, Muller CJ, Burgin TP, Tour JM (1997) *Science* 278:252–254
211. Kergueris C, Bourgoin J-P, Palacin S, Esteve D, Urbina C, Magoga M, Joachim C (1999) *Phys Rev B* 59:12505–12513
212. Reichert J, Ochs R, Beckmann D, Weber HB, Mayor M, V Löhneysen H (2002) *Phys Rev Lett* 88:176804
213. Gonzalez MT, Wu S, Huber R, Van der Molen SJ, Schönenberger C, Calame M (2006) *Nano Lett* 6:2238–2242
214. Huber R, Gonzalez MT, Wu S, Langer M, Grunder S, Horhoiu V, Mayor M, Bryce MR, Wang C, Jitchati R, Schönenberger C, Calame M (2008) *J Am Chem Soc* 130:1080–1084
215. Lörtscher E, Cizek JW, Tour J, Riel H (2006) *Small* 2:973–977
216. Park J, Pasupathy AN, Goldsmith JI, Chang C, Yaish Y, Petta JR, Rinkoski M, Sethna JP, Abruña HD, McEuen PL, Ralph DC (2002) *Nature* 417:722–725
217. Van der Zant HSJ, Osorio EA, Poot M, O'Neill K (2006) *Phys Stat Sol B* 243:3408–3412
218. Chen J, Reed MA, Rawlett AM, Tour JM (1999) *Science* 286:1550–1552
219. Tran E, Duati M, Whitesides GM, Rampi MA (2006) *Faraday Discuss* 131:197–203
220. White HS, Kittleson GP, Wrighton MS (1984) *J Am Chem Soc* 106:5375–5377
221. Meulenkamp EA (1999) *J Phys Chem B* 103:7831–7838
222. Krüger M, Buitelaar MR, Nussbaumer T, Schönenberger C, Forro L (2001) *Appl Phys Lett* 78:1292–1293
223. Rosenblatt S, Yaish Y, Park J, Gore J, Sazonova V, McEuen PL (2002) *Nano Lett* 2:869–872
224. Corni S (2007) *IEEE Trans Nanotechnol* 6:561–570
225. He H, Zhu J, Tao NJ, Nagahara LA, Amlani I, Tsui R (2001) *J Am Chem Soc* 123:7730–7731
226. He HX, Li XL, Tao NJ, Nagahara LA, Amlani I, Tsui R (2003) *Phys Rev B* 68:045302
227. Chen F, He J, Nuckolls C, Roberts T, Klare JE, Lindsay S (2005) *Nano Lett* 5:503–506
228. Haiss W, Van Zalinge H, Higgins SJ, Bethell D, Höbenreich H, Schiffrin DJ, Nichols RJ (2003) *J Am Chem Soc* 125:15294–15295
229. Alessandrini A, Salerno M, Frabboni S, Facci P (2005) *Appl Phys Lett* 86:133902
230. Albrecht T, Guckian A, Ulstrup J, Vos JG (2005) *Nano Lett* 5:1451–1455
231. Li Z, Han B, Meszaros G, Pobelov I, Wandlowski T, Blaszczyk A, Mayor M (2006) *Faraday Discuss* 131:121–143
232. Xu B, Xiao X, Yang X, Zang L, Tao N (2005) *J Am Chem Soc* 127:2386–2387
233. Li X, Hihath J, Chen F, Masuda T, Zang L, Tao N (2007) *J Am Chem Soc* 129:11535–11542
234. Li C, Mishchenko A, Li Z, Pobelov I, Wandlowski T, Li XQ, Würthner F, Bagrets A, Evers F (2008) *J Phys Condens Matter* 20:374122
235. Yoshimoto S, Tada A, Suto K, Narita R, Itaya K (2003) *Langmuir* 19:672–677
236. Li Z, Pobelov I, Han B, Wandlowski T, Blaszczyk A, Mayor M (2007) *Nanotechnology* 18:044018

237. Haiss W, Albrecht T, Van Zalinge H, Higgins SJ, Bethell D, Höbenreich H, Schiffrin DJ, Nichols RJ, Kuznetsov AM, Zhang J, Chi Q, Ulstrup J (2007) *J Phys Chem B* 111:6703–6712
238. He J, Chen F, Lindsay S, Nuckolls C (2007) *Appl Phys Lett* 90:072112
239. Xu BQ, Li XL, Xiao XY, Sakaguchi H, Tao NJ (2005) *Nano Lett* 5:1491–1495
240. Albrecht T, Guckian A, Kuznetsov AM, Vos JG, Ulstrup J (2006) *J Am Chem Soc* 128:17132–17138
241. Albrecht T, Moth-Poulsen K, Christensen JB, Hjelm J, Bjørnholm T, Ulstrup J (2006) *J Am Chem Soc* 128:6574–6575
242. Visoly-Fisher I, Daie K, Terazono Y, Herrero C, Fungo F, Otero L, Durantini E, Silber JJ, Sereno L, Gust D, Moore TA, Moore AL, Lindsay SM (2006) *Proc Natl Acad Sci USA* 103:8686–8690
243. Xiao X, Nagahara LA, Rawlett AM, Tao N (2005) *J Am Chem Soc* 127:9235–9240
244. He J, Fu Q, Lindsay S, Ciszek JW, Tour JM (2006) *J Am Chem Soc* 128:14828–14835
245. Wassel RA, Credo GM, Fuierer RR, Feldheim DL, Gorman CB (2004) *J Am Chem Soc* 126:295–300
246. Xiao X, Brune D, He J, Lindsay S, Gorman CB, Tao N (2006) *Chem Phys* 326:138–143
247. Chi Q, Farver O, Ulstrup J (2005) *Proc Natl Acad Sci USA* 102:16203–16208
248. Alessandrini A, Corni S, Facci P (2006) *PhysChemChemPhys* 8:4383–4397
249. Chi Q, Zhang J, Jensen PS, Christensen HEM, Ulstrup J (2006) *Faraday Discuss* 131:181–195
250. Leary E, Higgins SJ, Van Zalinge H, Haiss W, Nichols RJ (2007) *Chem Commun* 3939–3941
251. Chen F, Li X, Hihath J, Huang Z, Tao N (2006) *J Am Chem Soc* 128:15874–15881
252. Venkataraman L, Park YS, Whalley AC, Nuckolls C, Hybertsen MS, Steigerwald ML (2007) *Nano Lett* 7:502–506
253. Kuznetsov AM, Medvedev IG, Ulstrup J (2007) *J Chem Phys* 127:104708
254. Huang Z, Chen F, Bennett PA, Tao N (2007) *J Am Chem Soc* 129:13225–13231
255. Zhang J, Chi Q, Kuznetsov AM, Hansen AG, Wackerbarth H, Christensen HEM, Andersen JET, Ulstrup J (2002) *J Phys Chem B* 106:1131–1152
256. Schmickler W, Widrig C (1992) *J Electroanal Chem* 336:213–221
257. Schmickler W (1993) *Surf Sci* 295:43–56
258. Schmickler W, Tao N (1997) *Electrochim Acta* 42:2809–2815
259. Kuznetsov AM, Ulstrup J (1991) *Chem Phys* 157:25–33
260. Kuznetsov AM, Ulstrup J (1994) *Surf Coat Technol* 67:193–200
261. Kuznetsov AM, Ulstrup J (2000) *J Phys Chem A* 104:11531–11540
262. Zhang J, Kuznetsov AM, Ulstrup J (2003) *J Electroanal Chem* 541:133–146
263. Zhang J, Chi Q, Albrecht T, Kuznetsov AM, Grubb M, Hansen AG, Wackerbarth H, Welinder AC, Ulstrup J (2005) *Electrochim Acta* 50:3143–3159
264. Schmickler W (1995) *Surf Sci* 335:416–421
265. Nitzan A (2001) *Annu Rev Phys Chem* 52:681–750
266. Kuznetsov AM, Schmickler W (2002) *Chem Phys* 282:371–377
267. McCreery RL (2004) *Chem Mater* 16:4477–4496
268. Wang W, Lee T, Reed MA (2004) *J Phys Chem B* 108:18398–18407
269. Pobelov I, Li Z, Wandlowski T (2008) *J Am Chem Soc* 10, in press
270. Ulrich J, Esrail D, Pontius W, Venkataraman L, Millar D, Doerr LH (2006) *J Phys Chem B* 110:2462–2466
271. Jang SY, Reddy P, Majumdar A, Segalman RA (2006) *Nano Lett* 6:2362–2367
272. Fujihira M, Suzuki M, Fujii S, Nishikawa A (2006) *PhysChemChemPhys* 8:3876–3884
273. Sek S, Misicka A, Swiatek K, Maicka E (2006) *J Phys Chem* 110:19671–19677

274. Wierzbinski E, Slowinski K (2006) *Langmuir* 22:5205–5208
275. Li X, He J, Hihath J, Xu B, Lindsay SM, Tao NJ (2006) *J Am Chem Soc* 128:2135–2141
276. Xu XB, Xiao XY, Tao NJ (2003) *J Am Chem Soc* 125:16164–16165
277. Haiss W, Nichols RJ, V. Zalinge H, Higgins SJ, Bethell D, Schiffrin D (2004) *J Phys Chem Chem Phys* 6:4330–4337
278. Venkataraman L, Klare JE, Nuckolls C, Hybertsen MS, Steigerwald ML (2006) *Nature* 442:904–907
279. Wan WY, Lee T, Reed MA (2003) *Phys Rev B* 68:0354161
280. Slowinski K, Chamberlain RV, Miller CJ, Majda M (1997) *J Am Chem Soc* 119:11910–11919
281. York RL, Nguyen PT, Slowinski K (2003) *J Am Chem Soc* 125:5948–5953
282. Chidsey CED (1991) *Science* 251:919–922
283. Smalley JF, Feldberg SW, Chidsey CED, Linford MR, Newton MN, Liu YP (1995) *J Phys Chem* 99:13141–13149
284. Di Ventra M, Pantelides ST, Lang ND (2000) *Appl Phys Lett* 76:3448
285. Di Ventra M, Lang ND, Pantelides ST (2002) *Chem Phys* 281:189
286. Michaelis L, Hill ES (1933) *J Gen Physiol* 16:859–873
287. Bird CL, Kuhn AT (1981) *Chem Soc Rev* 10:49–82
288. Monk PMS (1998) *The Viologens*. John Wiley and Sons, Chichester
289. Long HCD, Buttry DA (1990) *Langmuir* 6:1319–1322
290. Long HCD, Buttry DA (1992) *Langmuir* 8:2491–2496
291. Sagara T, Kaba N, Komatsu M, Uchida M, Nakashima N (1998) *Electrochim Acta* 143:2183–2193
292. Alvarado RJ, Mukherjee J, Pacsial EJ, Alexander D, Raymo FM (2005) *J Phys Chem B* 109:6164–6173
293. Gittins DI, Bethell D, Schiffrin DJ, Nichols RJ (2000) *Nature* 408:67–69
294. Lahav M, Heleg-Shabtai V, Wasserman J, Katz E, Willner I, Dürr H, Hu YZ, Bossmann SH (2000) *J Am Chem Soc* 122:11480–11487
295. Akiyama T, Inoue K, Kuwahara Y, Niidome Y, Terasaki N, Nitahara S, Yamada S (2005) *Langmuir* 21:793–796
296. Han B, Li Z, Wandlowski T, Blaszczyk A, Mayor M (2007) *J Phys Chem C* 111:13855–13863
297. Haiss W, Van Zalinge H, Höbenreich H, Bethell D, Schiffrin DJ, Higgins SJ, Nichols RJ (2004) *Langmuir* 20:7694–7702
298. Haiss W, Nichols RJ, Higgins SJ, Bethell D, Höbenreich H, Schiffrin DJ (2004) *Faraday Discuss* 125:179–194
299. Bagrets A, Arnold A, Evers F (2008) *J Am Chem Soc* 130:9013–9018
300. Zhang J, Kuznetsov AM, Medvedev IG, Chi Q, Albrecht T, Jensen PS, Ulstrup J (2008) *Chem Rev* 108:2737–2791
301. Albrecht T, Moth-Poulsen K, Christensen JB, Guckian A, Bjørnholm T, Vos JG, Ulstrup J (2006) *Faraday Discuss* 131:265–279

Subject Index

- Adsorbate-induced reconstructions 58
Alkanedithiol/Au junctions 233
Alkoxide infiltration 151, 154
5-Alkoxy-isophthalic acid derivatives 106
Alumina films, epitaxial 74
Amphiphilic ionic liquids (AILs) 163
Anthraquinone 125
Assembling units 49
Atomic layer deposition (ALD) 171
ATR-SEIRAS 187
Au surfaces, vicinal 71
Au(100), H₂SO₄ 191
Au(111), H₂SO₄ 188
Au(111)-(1×1), aromatic carboxylic acids,
self-assembly 212
Au/alkanedithiol/Au junctions, charge
transport 233
Au/molecule/Au junctions, charge
transport 231
Azobenzene, interconversion, UV 173
4,4'-Azobenzene dicarboxylic acid 19
- Benzene carboxylic acid 94
Benzene tribenzoic acid 114
Benzoic tricarboxylic acid (trimellitic acid)
(TMLA) 15, 182, 194
Bimodal porous silica, tailored 164
Biosensing polymer inverse opals 157
Biphenyl dicarboxylic acid (BDA) 18
1,4-Bis(4-pyridyl)benzene, Cu(100) 16
2,5-Bis(dodecyloxy)terephthalic acid 95
Block copolymer templating 161
Boron nitride nanomesh 66
Bovine serum albumin (BSA) 169
BPn adlayers, Au(111)-(1×1) 218
- Cage compounds 34
Carbamate 104
Carbon-based networks 149
- Carboxylates 9
Charge transport 181
Chemical vapor deposition 144, 152
Clean surfaces, reconstructions 55
Cobalt-dicarbonitrile superlattices,
Ag(111) 20
Cobalt phthalocyanine, Au(788) 69
Colloid templating, multiple-size 162
Colloidal crystals 136, 141
Colloidal films/crystals, fabrication 139
Computational modeling 26
Conformational pseudopolymorphism
103
Coordination systems, linear 16
Coordinatively unsaturated sites 3
Copper-carboxylate 13
Coronene 111
Crystal engineering 89
Crystals, colloidal 136, 141
– two-dimensional 88
Cu-phthalocyanine 120
Cu-TMA (1,3,5-benzoic tricarboxylic acid)
13
Current-induced tunneling spectroscopy
(CITS) 34
Cyclothiopen 112
- Dehydrobenzo[12]annulenes 116
Density functional theory (DFT),
metal-TMA 26
Desorption, oxidative 225
– reductive 222
Deposition temperature 60
Diamino triazine derivative 107
Diamond inverse opals 153
Dicarbonitrile nanomesh, Ag(111) 28
Dicarbonitrile-polyphenyl 21
2,5-Dihydroxybenzohydroquinone
(DHBQ), Cu(II) 35

- 9,10-Dimethoxyanthracene 125
 1,3-Dinonadecanoylbenzene 103
 DNA/diazo resin 159
- Electrochemical deposition 153
 Electrochemistry 181
 Electrolyte gating 232, 238
 Electropolymerization 157
 Ethene monolayer, Cu₃Pt(111) 52
 Ethene-1,2-diyl-bisbenzoic acid 19
- Fe-biphenolate networks, Ag(111)/Cu(100) 20, 24
 Fe-carboxylates 15
 Fe-TMA 14
 Fe-TPA 14, 78
 Films, epitaxial inorganic 61
 Fluorene 114
 Foldamers 93
 Forces, directional, control 93
 Functionality complementarity 92
- Ge opal 153
 Graphene layers, Ir(111) 61
 Grid-of-grids network 33
- Herringbone/chevron pattern 56, 67, 202
 Hexabenzocoronene 118
 Hexabenzocoronene 61
 Hexabenzocoronene-anthraquinone 125
 1-Hexadecyl-3-methylimidazolium chloride 163
 Hierarchical structure 136
 Highly oriented pyrolytic graphite (HOPG) 33, 100
 Honeycomb networks 20, 114, 194
 HOPG 33, 100
 Hydrogels 159
 Hydrogen bonding 93
- Interface science 1
 Inverse opal 136
 Ionic liquid templating 163
 Iron oxide films, epitaxial 77
 Island arrays, self-organized growth, Fe/Co 23
 Isophthalic acid (ISA) (1,3-benzenedicarboxylic acid) 94
- Kagomé lattices 19
- Layers, epitaxial inorganic 61
 – epitaxial organic 66
 Local deposition, confined 167
- Macropores 137
 Manganese-carboxylate 19
 Manganese porphyrins 127
 Melt infiltration 152
 Merocyanine dye dweivatives 106
 Mesopores 237
 Meso-tetradodecylporphyrins 123
 Metal deposition, electrochemical 148
 – electroless 147
 Metal films, epitaxial 59, 71
 Metal ion arrays (MIAs) 33
 Metal ion–ligand assemblies, solid–liquid interface 30
 Metal oxide-based networks 154
 Metal precursor infiltration/transformation 147
 Metal surfaces 1
 – reconstructed 67
 – templates 66
 Metal-based networks 145
 Metal-directed assembly 1
 Metal-carboxylates, Cu surfaces 13
 Metal–ligand coordination 96
 Metal–organic coordination networks (MOCNs) 17, 79
 Metal-phthalocyanine 7
 Metal-porphyrin 7
 4-Methyl-4'-(*n*-mercaptoalkyl)biphenyls on Au(111) 182, 187, 217
 Metalloporphyrin nanoarchitectures 12
 Metallosupramolecular engineering, in vacuo, solid surfaces 8
 Migration (rotation) energy barrier 8
 Molecular electronics 125
 Molecular self-assembly, directional hydrogen bonding 193
 Monodendron 110
 Monolayers 39, 50, 52, 88, 124, 216
 Multilayers 124
- N/Cu(100) 72
 Nanomeshes, metal–organic honeycomb 21
 Nanoparticle codeposition/infiltration 146
 Nonanedithiol 235

- Octadecyltrimethylammonium chloride 163
- Oligo(phenylene ethynylene) 111
- Opal infiltration, semiconductor nanoparticles 150
- Optoelectronics 171
- Oxide reduction 152, 155
- Oxide surfaces, templates 74
- PAHs, electron-poor 125
- Particle film formation, strategies 140
- Perylene bisimide derivatives 106
- Perylenetetracarboxylic-dianhydride 50
- Phenyl octane-graphite 96
- 2,2'-bipyridine, Pd(OAc)₂ 30
- Phthalocyanines 7
- Phthalic acid (PA)
(1,2-benzenedicarboxylic acid) 94
- Polybenzene carboxylate 24
- Polycyclic aromatic hydrocarbons (PAHs) 125
- Polymer-based networks 155
- Polymerization, reactivity 126
- Polymorphism 103
- Polyoxometalates (POMs) 34
- Poly(dimethyl siloxane) (PDMS) stamp micromolding 161
- Poly(methyl methacrylate) (PMMA) 139
- Poly(thiophene-*co*-3-thiophenemethanol) copolymer inverse opal, biotinylation 169
- Pores, 2D 112
- alkyl chains 116
- hydrogen bonds 113
- Porous networks 136
- hierarchical 160
- Porous particles 165
- Porphyrins 7
- PS inverse opal 159
- Pt(100)-hex reconstruction 57
- PTCDA monolayers, self-assembled 50
- Pyrazine derivatives 106
- Pyridine-Cu-pyridine 23
- 4-[*trans*-2-(Pyrid-4-ylvinyl)]benzoic acid (PVBA) 13
- Quinacridone 98
- Reactivity, 2D 125
- Relaxation 56
- Replica 136
- Replica formation, porous 143
- Salophen 31
- Salt infiltration 151, 155
- Scanning tunneling microscopy (STM) 1, 4, 11, 88, 90, 181
- Scanning tunneling spectroscopy (STS) 181
- Self assembly 181
- molecular, covalent bonds 216
- Self-assembled monolayers (SAMs) 39, 50, 52, 88, 216
- Semiconductor networks 149
- Sensing platforms 168
- Shape complementarity 92
- Silica inverse opal, gold nanoparticles 170
- Single molecules 181
- Solid-liquid interfaces, electrified 231
- metal ion-ligand assemblies 30
- Solvent-evaporation-mediated direct physical casting (SEDPC) 163
- STM 1, 4, 11, 88, 181
- Supramolecular chemistry/engineering 1, 88
- Surface coordination chemistry 1
- Surface engineering 216
- Surfaces, vicinal 57
- Surfactant templating 163
- Tecton 97
- Template generation, strategies 55
- Template removal 144
- Template-assisted assembly 50
- Template-controlled assembly 51
- Templates 136
- 2D 52
- metal surfaces 66
- oxide surfaces 74
- self-assembly 47
- Terephthalic acid (TTA) (1,4-benzenedicarboxylic acid) 94
- Terphenyl-1,4-dicarboxylic acid (TDA) 18
- Tetracyanoethylene, Cu(100) 17
- Tetrakis-(4-carboxylphenyl)-21H,23H-porphyrin (TCPP) 201
- Tetrapropylammonium hydroxide (TPAOH) 163

- Tetra-pyridyl-porphyrin (TPyP) 11
Tetrathiofulvalene 100
Titania 76
TMA 94, 115, 182, 194
– Au(111) H₂SO₄ 195
TMA adlayers, Au(111)-(1×1) 197
Trimellitic acid (TMLA) 15, 182, 194
Trimesic acid (TMA) 94, 115, 182, 194
1,3,5-Trimethylbenzene (TMB) 226,
235
- 1,3,5-Tris(10-carboxydecyloxy)benzene
120
1,3,5-Tris(4-pyridyl)-2,4,6-triazine 115
Ultra-high vacuum (UHV) 5, 90
Vicinal surfaces 57, 68
Viologen derivatives, redox-active 238
Wall functionalization 165